

**EGE UNIVERSITY GRADUATE SCHOOL OF
APPLIED AND NATURAL SCIENCES**

(MASTER OF SCIENCE THESIS)

**CRYSTALLIZATION KINETICS OF
POLYCAPROLACTONE (PCL)-CLAY COMPOSITE
FILMS WITH OLEIC ACID/AND GLYCEROL MONO
OLEATE ADDITIVES AND PRODUCT PROPERTIES**

Tansel KAHRAMAN

Advisor : Assoc. Prof. Dr. Serap CESUR

Co-advisor : Prof. Dr. Devrim BALKÖSE

Chemical Engineering Department

Department Code : 603.02.00

Presentation Date : 07.02.2013

Bornova-İZMİR

2013

Tansel KAHRAMAN tarafından yüksek lisans tezi olarak sunulan ‘‘Crystallization Kinetics of Polycaprolactone (PCL)-Clay Composite Films with Oleic Acid/and Glycerol Mono Oleate Additives and Product Properties’’ bařlıklı bu alıřma E.Ü. Lisansüstü Eđitim ve Öđretim Yönetmeliđi ile E.Ü. Fen Bilimleri Enstitüsü Eđitim ve Öđretim Yönergesi'nin ilgili hükümleri uyarınca tarafımızdan deđerlendirilerek savunmaya deđer bulunmuş ve 07 řubat 2013 tarihinde yapılan tez savunma sınavında aday oybirliđi/oyokluđu ile bařarılı bulunmuřtur.

Jüri Üyeleri:

İmza

Jüri Bařkanı : Do. Dr. Serap CESUR

Raportör Üye : Prof. Dr. Saadet YAPAR

Üye : Y.Do.Dr. Sekin ERDEN

ÖZET**OLEİK ASİT/ VE GLİSEROL MONO OLEAT KATKILI
POLİKAPROLAKTON (PCL)-KİL KOMPOZİT FİMLERİN
KRİSTALİZASYON KİNETİĞİ VE ÜRÜN ÖZELLİKLERİ**

KAHRAMAN, Tansel

Yüksek Lisans Tezi, Kimya Mühendisliği Anabilim Dalı

Tez danışmanı: Doç. Dr. Serap CESUR

Tez ikinci danışmanı: Prof. Dr. Devrim BALKÖSE

Şubat 2013, 157 sayfa

Bu projenin amacı biyobozunur ve toksik olmayan bir polimer olarak PCL'in inorganik ve organik katkılarla karakterizasyon ve kristalizasyonunun incelenmesidir. İnorganik madde olarak kil, organik madde olarak oleik asit ve Gliserol mono oleat (GMO) kullanılmıştır. Kompozit filmler çözgen döküm yöntemi ile hazırlanmış ve çözücü olarak diklorometan kullanılmıştır.

Kompozit filmlerin kristalizasyon kinetikleri izotermal ve izotermal olmayan koşullar altında incelenmiştir. İzotermal koşullar için tüm filmler 100 °C'den 40 °C'ye ani olarak soğutulmuş ve 1 saat boyunca kristallendirilmiştir ve kristalizasyon kinetik parametreleri Avrami modeli ile hesaplanmıştır. Avrami sabiti, n , 1,86 - 2,66 değerleri arasında değişmiştir ve kristal büyümesinin 2 boyutlu olduğu anlaşılmıştır. Büyüme hız sabiti, K , değerleri hesaplanmış ve yalnız oleik asit katkısının kristalizasyonu hızlandırdığı, fakat yalnız GMO katkısının yavaşlattığı görülmüştür. Kil ve organik katkı içeren kompozit filmlerin, katkısız PCL'e göre, kristalizasyon hızını yavaşlattığı izlenmiştir. İzotermal olmayan koşullarda kristalizasyon 2, 5, 10 ve 20 °C/dak. soğutma hızları seçilerek gerçekleştirilmiştir. Kristalizasyon kinetik parametreleri Avrami Jeziorny, Ozawa, Liu-Mo ve Lauritzen Hoffmann metodları ile hesaplanmıştır ve izotermal olmayan koşullar altında, %3 kil katkısının kristallik derecesini arttırdığı ve kristallemeyi hızlandırdığı belirlenmiştir. Ayrıca kompozit filmlerin kristallenme yarı zamanları soğutma hızı arttıkça azalmıştır. Kristalizasyon aktivasyon enerjileri Kissenger ve Augis-Bennett modelleri ile hesaplanmıştır. %3 kil katkısının kompozit filmlerin kristalizasyon enerjilerini düşürdüğü ve kil katkısının çekirdeklendirici ajan olarak etki gösterdiği anlaşılmıştır. Seçilen kompozit filmler, izotermal olmayan koşullar altında ısıtma-soğutma kontrollü Polarize Optik Mikroskop (POM) ile analiz edilmiştir. Elde edilen

görüntüler kil katkılı filmlerin daha küçük kristallerden oluştuğu, oleik asitin kristal boyutunu arttırdığı anlaşılmıştır. Bir de yüksek oranda kil katkısının erime sıcaklığını arttırdığı ve oleik asit katkısının kristallenmeyi hızlandırdığı anlaşılmıştır.

Kompozit filmlerin ürün özellikleri FTIR, SEM, optik tensiyometre, XRD ve çekme test analiz cihazları ile incelenmiştir. FTIR analizi sonucunda PCL ve kil'e ait karakteristik pik değerleri görülmüştür. SEM fotoğraflarından kompozit filmlerin gözenekli bir yapıya sahip olduğu ve katkı maddeleri ile değişkenlik gösteren yüzey özellikleri gösterilmiştir. Optik tensiyometre ölçümleri sonucunda organik katkılar ile yüzeydeki kontak açısının azaldığı ve ıslanabilirliğin arttığı anlaşılmıştır. XRD analizleri sonucunda kil yapılarının tabakalar halinde kompozit filmler içinde dağıldığı anlaşılmıştır. Ayrıca kristal yapı da incelenmiştir ve kil katkısı ile kristal kalınlığının arttığı anlaşılmıştır. Kompozit filmlerin mekanik çekme özellikleri incelenmiş ve PCL'in esnek bir yapıya sahip olduğu, bunun kil ve organik katkılar ile esnek ve mukavemetli bir yapının oluşturduğu anlaşılmıştır. Pukanszky modeli ile PCL-kil arayüzeyindeki uyumluluk incelenmiştir ve organik katkının PCL-kil arayüzeyinde uyumlaştırıcı etki yarattığı tespit edilmiştir.

Termal ve biyobozunur özellikler sırasıyla TGA ve toprakta bozunma testleri ile incelenmiştir. Termal bozunma sıcaklığının ve bozunma sonrası kalan kül miktarının kil katkısı ile arttığı anlaşılmıştır. Termal aktivasyon enerji değerleri Brodio modeli ile hesaplanmıştır ve oleik asit katkısı ile GMO katkılı filmlere göre daha az yanıcı filmler elde edildiği anlaşılmıştır. Simüle toprakta biyobozunurluk testleri 9 ay boyunca sürdürülmüştür. Test öncesi ve sonrası yapılan XRD ve FTIR analizlerinden öncelikle filmlerin amorf yapılarının bakteriler tarafından sindirildiği anlaşılmıştır. Katkılar PCL'in biyobozunurluğunu hızlandırmıştır.

Deneysel ve istatistiksel analiz sonuçları PCL kristalizasyonunun izotermal ve izotermal olmayan koşullar altında inorganik ve organik katkılarla kontrol edilebildiğini göstermiştir. Kristallik ve ürün özellikleri arasında ilişki fiziksel, yapısal ve mekanik, izotermal ve izotermal olmayan koşullarda kristalizasyon kinetikleri ve bozunma mekanizmaları ile açıklanmaya çalışılmıştır. Bu yeni kompozit malzemeler iyileştirilmiş özellikleri ile aktif ambalaj, ilaç salınım sistemleri, doku mühendisliği ve kalp-damar operasyonlarında kullanılabilir.

Anahtar Kelimeler: Biyobozunur PCL, kil katkılı kompozit filmler, izotermal kristalizasyon kinetiği, izotermal olmayan kristalizasyon kinetiği.

ABSTRACT**CRYSTALLIZATION KINETICS OF POLYCAPROLACTONE (PCL)-
CLAY COMPOSITE FILMS WITH OLEIC ACID/AND GLYCEROL
MONO OLEATE ADDITIVES AND PRODUCT PROPERTIES**

KAHRAMAN, Tansel

Master Thesis, Chemical Engineering Department

Advisor: Assoc. Prof. Dr. Serap CESUR

Co-advisor: Prof. Devrim BALKÖSE

February 2013, 157 pages

In this project, crystallization and characterization of PCL, as biodegradable and non-toxic polymer, is aimed with inorganic and organic additives. Clay is used as inorganic, oleic acid and glycerol mono oleate (GMO) are used as organic additives. The composite films are prepared by solvent casting method and dichloromethane is used as the solvent.

Crystallization of the composite films is investigated under isothermal and nonisothermal conditions. All composite films are quenched cooled from 100 °C to 40 °C for 1 h under isothermal conditions and the crystallization kinetics is evaluated by Avrami model. Avrami exponent, n , values change between 1.86-2.66, which show fast and 2 dimensional crystallization. Growth rate constant, K , is calculated which shows that oleic acid alone accelerates and GMO alone slows down the nucleation step of the crystallization. But for composites with clay and organic additives, K values obtained are lower than the value of neat PCL. Nonisothermal crystallization test was performed for selected samples. Four different cooling rates are selected as 2, 5, 10 and 20 °C/min The results are evaluated by Avrami Jeziorny, Ozawa, Liu-Mo and Lauritzen Hoffmann models. The results show that 3% wt. clay addition increase the degree of crystallinity and accelerate the crystallization. Also crystallization half time of the composite films are decreased with increasing cooling rate. The crystallization activation energies are calculated by Kissinger and Augis-Bennett models. 3% clay contained composite films have lower the activation energy values which shows that clay act as nucleating agent. Polarized optical microscope (POM) analysis is carried out with hot stage under nonisothermal conditions for selected composite films. The pictures showed that clay contained composite films have tiny crystals and organic additives cause increasing of crystal size. Also high

load of clay is increased the melting temperature and oleic acid addition is accelerated the crystallization.

Product properties of the composite films are analyzed by FTIR, SEM, Optical Tensiometer, XRD, tensile test analyzer. FTIR spectra of the composite films show both characteristic PCL and clay infrared bands. In the SEM pictures, porous structure of the composite films and variation of surface structure with additives can be seen. Optical tensiometer measurements indicated that contact angle values are decreased with organic additives and this increases the wettability of the films. PCL has a hydrophobic property and organic additives decrease the hydrophobicity of PCL. From the XRD analysis, intercalated structure of the clay contained composite films is observed. The crystal structure is also analyzed and increasing crystal thickness with clay addition has been seen. Tensile properties of the composite films were analyzed. PCL has flexible tensile property and the composite films gain strength and flexibility with clay and organic additives addition. The compatibility of PCL and clay is examined by Pukanszky's model, and it is obtained that organic additives are good compatibilizers for PCL-clay contained composite films.

Thermal and biodegradation properties are analyzed by TGA and soil burial test, respectively. Thermal degradation temperatures and amount of ash values are increased with clay addition. Thermal degradation activation energies evaluated by Brodio's model and the results showed that less flammable composite films were observed with oleic acid addition by comparison with GMO. Meanwhile, the biodegradation test was carried out with soil burial tests for 9 months. The results of XRD patterns and FTIR spectra of before and after soil burial test of samples were also indicated that first amorphous regions of the films were digested by bacteria. The biodegradation of PCL films are accelerated by additives.

Experimental and statistical analysis results showed that the crystallization of PCL can be controlled with inorganic and organic additives under isothermal and nonisothermal conditions. The relations between crystallinity and product properties as physical, structural and mechanical, isothermal and nonisothermal crystallization kinetics and degradation mechanism were tried to be obtained. These new composite materials can be used in active packaging, drug delivery systems, tissue engineering and cardiovascular surgery applications with improved product properties.

Key Words: Biodegradable PCL, clay contained composite films, isothermal crystallization kinetics, nonisothermal crystallization kinetics.

dedicated to

*...to whom has contribution to my
crystallization and growth process...*

ACKNOWLEDGEMENT

I owe sincere thankfulness to my research advisor, Assoc. Prof. Dr. Serap Cesur and co-advisor Prof. Devrim Balköse, who made me believe in myself and guided me through the whole process of dissertation writing. I am sure that this dissertation would not have been possible without their support, understanding and encouragement I felt when working on my research paper.

The thesis has been supported by Ege University Scientific Research Project Fund with project BAP 11/ MÜH / 041 and TÜBİTAK with project 110M157. I am greatly thankful to Izmir Institute of Technology for allowing me to use of their test labs and equipments. I owe my deepest gratitude to İYTE Geothermal Energy Research and Application Center for isothermal DSC analysis; Assist. Prof. Dr. Ali Durmuş and Nur İslam Karşahin for nonisothermal DSC analysis; Prof. Dr. Funda Tihminlioğlu and Prof. Dr. Metin Tanoğlu for contact angle measurements; Prof. Dr. Ahmet Yemenicioğlu for mechanical characterization tests; Ass. Prof. Dr. Mehmet Sarıkanat and Ass. Prof. Dr. Seçkin Erden for Polarized Optical Microscopic tests; Yelda Küçüköksel and Beyza Aysan for biodegradation tests. Also I would like to give my special thanks to Prof. Dr. Mustafa Demircioğlu and Prof. Dr. Saadet Yapar for their creative and useful advises.

I owe my deepest gratitude to Fatma Üstün, Ahmet Kurul, Nazil Karaca, Hale Oğuzlu and Okan Akın for their valuable help. I also thank to Dr. Burcu Alp, as a member of our TÜBİTAK project team, for her valuable help. I would never forget the help I got from my extraordinary friends Emre Koç, Olcay Doğukan Aydın, Sercan Ekşi, Can Çelik, Eren Bostancı, Yücel Güngör, Melike Sancak, Umur Duman and Fatih Dönmez for their moral support during my thesis.

I am also pleased to thank everyone who supported me from my department in Robert Bosch A.Ş.. Especially I would like to thank for understanding of my department manager Hamdi Ayayüksel, our team leader Ferhat Şengül and colleagues Neşe Yenigün, Şükrü Nal, Alper Kaya and Barkın Arak.

The Master study was one of the most productive parts of my life and my family provided me the greatest support, comprehension and motivation. I would like to thank my father İsmail Kahraman, my mother Ş. Aynur Kahraman, my brother Ersel Kahraman and our new family member Tuğba Kahraman for all support and encouragement.

TABLE OF CONTENTS

	<u>Pages</u>
ÖZET	v
ABSTRACT	vii
ACKNOWLEDGEMENT	xi
TABLE OF FIGURES	xvi
LIST OF TABLES	xxiv
NOMENCLATURE	xxvii
1. INTRODUCTION	1
2. LITERATURE, LAYER SILICATE and BIODEGRADABLE POLYMERIC COMPOSITES	4
3. CRYSTALLIZATION OF POLYMERS	16
3.1. Melting Point Calculation, Florry Huggings and Thomson Gibbs models ..	16
3.2. Theories in Crystal Morphology and Crystal Geometry	20
3.3. Crystallization Kinetics Models	32
3.3.1. Primary nucleation kinetics models	33
3.3.2. Secondary nucleation kinetics model: Lauritzen Hoffman	38
3.4. Effective Activation Energy of Crystallization	41

TABLE OF CONTENTS (continued)

	<u>Pages</u>
4. EXPERIMENTAL	44
4.1. Materials.....	44
4.2. Method	44
4.2.1. PCL polymeric composite film preparation by solvent casting.....	44
4.2.2. DSC analysis	45
4.2.3. Investigation of crystallization kinetics by a polarized optical microscope .	47
4.2.4. Product properties	48
4.2.5. Experimental design and statistical analysis.....	52
5. RESULTS AND DISCUSSION	53
5.1. DSC Analysis	53
5.1.1. Melting point measurements of PCL composite films and prediction models	53
5.1.2. Degree of crystallinity and statistical analysis.....	58
5.1.3. Crystallization kinetics	65
5.2. Crystallization Activation Energy	94
5.3. Crystal Morphology and Growth Rate Kinetics	97

TABLE OF CONTENTS (continued)

	<u>Pages</u>
5.4. Product Properties	101
5.4.1. Density	101
5.4.2. Structural properties	107
5.4.3. Mechanical properties	116
5.4.4. Degradation results	123
6. CONCLUSION	143
7. RECOMMENDATIONS	146
REFERENCES	147
CURRICULUM VITAE	154
APPENDICES	

TABLE OF FIGURES

<u>Figures</u>	<u>Pages</u>
2.1 Generalized tensile stress - strain curve for polymeric materials (Blaga, 1973).	6
2.2 Tensile stress-strain curves for four types of polymeric material (Blaga, 1973).	7
2.3 Tensile modulus vs. clay concentration for crosslinked polyester nanocomposites (Bharadwaj et al., 2002).	8
2.4 Effect of MMT content on yield strength of nylon 6 nanocomposites (Manias, 2001).	9
2.5 Stress – Strain curves for PCL and two composites at a crosshead speed of 130 mm/min; a) PCL/30B (95/5), b) PCL/93A (95/5), c) PCL	9
2.6 Dependence of Young’s modulus on the clay content for PCL (Lepoittevin et al., 2002).	10
2.7 Tensile strength of 80% PLLA - 20% PCL with various contents of OMMT prepared by solution casting and melt blending (Hoidy et al., 2010).	10
2.8 TGA curves of the degradation of neat PS and PS + 10% clay at a heating rate 5 °C min ⁻¹ in air and nitrogen (Vyazovkin et al., 2004).	12
2.9 Temperature dependence of the weight loss under an air flow for unfilled PCL and PCL-nanocomposites containing 1,3,5 and 10 wt. % of MMT.	12
2.10 Relationship between the rate of degradation in soil and crystallinity of PCL (Mochizuki and Hayashi, 1999).	13
2.11 Weight retention as a function of degradation time for PCL/RH eco-composites in soil suspension system (Zhao et al., 2008).	15
3.1 Rate of crystallization rises to a maximum between T _g and T _m .	16
3.2 Quenched sample of silicone copolymer being heated from below T _g . Recrystallization between T _g and T _m increases stiffness, which then appears when T _m is exceeded.	17
3.3 Simple model of crystal lamella (Gedde, 1995).	18

TABLE OF FIGURES (continued)

<u>Figures</u>	<u>Pages</u>
3.4 Macroscopic single crystal.	20
3.5 Crystallization of macromolecules. i) polymerization followed by crystallization; ii) crystallization during polymerization.	21
3.6 Schematic of orientation induced by crystallization (The first three drawings illustrate the orientation and crystallization of random coils while the last two drawings show the growth of folded chain kebab around the central shish).	21
3.7 (a) Keller model for crystallization; (b) Hermann & Gerngross model (Flory, 1962; Geil, 1963).	23
3.8 Single crystals of polyethylene after evaporation of tetrachloroethylene solvent. Pleats form due to crystal collapse.	24
3.9 (A) Schematic of a Switchboard model, showing the surface of a lamella, interlamellar region and tie chains between the lamella. (B) originally proposed model for melt crystallization in polymers.	24
3.10 (i) Smooth surface model; (ii) Rough surface model; (iii) Erstarrungs model (solidification model): (a) chain conformation in the melt state; (b) alignment of suitable conformations into the crystal.	25
3.11 Calculation of degree of crystallinity of PCL from XRD pattern by Gaussian function.	26
3.12 A melting process for the case of a highly crystalline polymer which is slowly heated through its melting temperature.	27
3.13 DSC thermograms of PCL and of selected PCL/clay nanocomposites after isothermal crystallization at 45 °C. Number refers to clay weight concentration; 0* is the DSC thermogram of nonisothermal crystallized (-10 °C/min) pure PCL (Di Maio et al., 2004).	28
3.14 The relationship between o-MMT content and T _g of composite (Ke and Yongping, 2005).	29

TABLE OF FIGURES (continued)

<u>Figures</u>	<u>Pages</u>
3.15 POM photographs taken during cooling by 1 °C.min ⁻¹ for (a) pure PCL and (b) PCL/SiO ₂ 2.5 wt.% nanocomposite.....	30
3.16 POM images of (a) PCL and (b) 0.5 wt % PCL/c-MWNT composites after melting at T _{max} = 90 °C and then quenching to T _c = 46 °C.	30
3.17 Polarizing microscope images of (A) neat PCL; (B) PCL with 1 wt% clay; (C) PCL with 2 wt% clay and (D) PCL with 4 wt% clay.	31
3.18 Utilization of isothermal crystallization data by DSC measurements (Rattaa et al., 2000).....	35
3.19 The characteristic Avrami plots obtained by isothermal crystallization experiments for a polyamide (Rattaa et al., 2000).....	35
3.20 Schematic of regime analysis (Mark, 2007).	39
3.21 Types of Crystal Nuclei (a) Primary nucleus (b) Secondary Nucleus (c) Tertiary Nucleus.	39
3.22 Schematic presentation of the temperature dependencies for the growth rate (dash line) and the effective activation energy (solid line). The E _A value turns negative when crystallization occurs at temperatures above T _{max} (Vyazovkin and Dranca, 2006).....	42
4.1 Temperature profile for isothermal crystallization experiments.	46
4.2 Temperature profiles for nonisothermal crystallization experiments.....	47
4.3 Water drop for contact angle measurement.	49
4.4 Intercepts of a lattice plane (hkl) on the unit cell vectors a, b, c. $ON = d_{hkl}$ =interplanar spacing.....	50
4.5 2 ² design with center points (Montgomery, 1997).....	52
5.1 DSC heating and cooling profiles of neat PCL film; a- isothermal conditions, b- nonisothermal conditions.	54

TABLE OF FIGURES (continued)

<u>Figures</u>	<u>Pages</u>
5.2 Variation of first and second melting points obtained from isothermal DSC analysis of PCL composite films depend on additive concentration; a and c- Clay & Oleic acid; b and d-Clay & GMO.	56
5.3 Variation of melting point temperatures of PCL composite films from nonisothermal DSC analysis.	57
5.4 Variation of degree of crystallinity of PCL composite films obtained from isothermal DSC analysis depend on additive concentration; a- DOC from first melting peak for Clay-Oleic acid, b- DOC from first melting peak for Clay-GMO, c- DOC from second melting peak for Clay-Oleic acid, d- DOC from second melting peak for Clay-GMO.....	61
5.5 Variation of degree of crystallinity of PCL composite films obtained solvent casting from X-Ray analysis depend on additive concentration; a-Clay-Oleic acid, b-Clay-GMO.....	62
5.6 a. Variation of degree of crystallinity of PCL composite films obtained from nonisothermal DSC analysis of second melting peak at different cooling rates depend on additive concentration; b. Crystallization temperatures of composite films for each cooling rate.	63
5.7 Statistical evaluation of isothermal DSC experiments for studying isothermal crystallization kinetics at 40 °C a. variation of 1 st melting temperature; b. variation of 2 nd melting temperature; c. Degree of crystallinity of solvent cast films; d. Degree of crystallinity of the melt crystallized films.	64
5.8 DSC exotherm of 1 wt% clay contained composite films with variation of oleic acid.....	66
5.9 Time dependent relative crystallinity of 1 wt% clay contained composite films with variation of oleic acid.....	66
5.10 Avrami plot of 1 wt% clay contained composite films with variation of oleic acid.....	67
5.11 Variation of Avrami constant values of composite films a. Clay and Oleic Acid; b. Clay and GMO.....	69

TABLE OF FIGURES (continued)

<u>Figures</u>	<u>Pages</u>
5.12 Variation of growth rate constant values of composite films a. Clay and Oleic Acid; b. Clay and GMO.	70
5.13 Variation of crystallization half time values of composite films a. Clay and Oleic Acid; b. Clay and GMO.	71
5.14 Statistical evaluation results of; a- Avrami exponent, n ; b- Growth rate constant, K ; c- Crystallization half time, $t_{1/2}$	72
5.15 Temperature dependent nonisothermal crystallization exotherms of neat PCL with different cooling rates.....	74
5.16 Time dependent relative crystallinity percent of neat PCL with different cooling rates.....	74
5.17 Avrami Jeziorny plot for neat PCL with different cooling rates.....	75
5.18 Variation of nonisothermal Avrami Jeziorny crystallization model results; a – Avrami Jeziorny exponent, n ; b – Growth rate constant, Z_c ; c – Crystallization half time, $t_{1/2}$	77
5.19 Relative crystallinity percent of neat PCL film, X_t , versus temperature at different cooling rates.	78
5.20 Ozawa plot of neat PCL.....	79
5.21 a- Variation of Ozawa exponent, b- rate constant $K(T)$ of selected PCL composite films at various temperatures.....	81
5.22 Liu Mo plot for neat PCL.	82
5.23 Variation of Liu Mo parameters; a – Liu Mo constant, a ; b – Cooling rate value, $\ln F(T)$	84
5.24 Lauritzen Hoffman plot of neat PCL.....	86
5.25 Variation of overall crystallization rate constants; a – Regime II; b – Regime III.....	90
5.26 Variation of crystallization rate; a – Regime II; b – Regime III.....	91

TABLE OF FIGURES (continued)

<u>Figures</u>	<u>Pages</u>
5.27 Variation of growth crystal surface free energy; a – Regime II; b – Regime III.	92
5.28 Variation of; a – R constant; b – Transition temperature from Regime III to II.	93
5.29 Kissinger plots of nonisothermally crystallized selected samples.	95
5.30 Augis–Bennett plots of nonisothermally crystallized selected samples.	95
5.31 Comparison of crystallization activation energies calculated from different models.	96
5.32 POM micro photos of neat PCL with 2 °C/min cooling rate.	98
5.33 POM micro photos of PCL_C0.1_O3 with 2 °C/min cooling rate.	98
5.34 POM micro photos of PCL_C3_O5 with 20 °C/min cooling rate.	99
5.35 The variation of density values of composite films measured by Archimedes method depend on additive concentration.	103
5.36 Variation of measured contact angle of composite films depend a-Clay–Oleic acid; b-Clay–GMO concentration.	105
5.37 Variation of measured surface tension of composite films depend a-Clay–Oleic acid; b-Clay–GMO concentration.	106
5.38 FTIR spectra of organoclay.	107
5.39 FTIR spectra of the composite films; 1-Neat PCL; 2- 0.1 wt% clay; 3- 0.4 wt% clay; 4- 1 wt% clay; 5- 3 wt% clay.	108
5.40 Effects of increasing different organic additives (top row: Oleic acid, bottom row: GMO) concentration on surface morphologies of PCL composite films by SEM analysis.	109
5.41 Effects of 1 wt% clay contained PCL composite films with increasing different organic additives (top row: Oleic acid, bottom row: GMO) concentration on surface morphologies by SEM analysis.	109

TABLE OF FIGURES (continued)

<u>Figures</u>	<u>Pages</u>
5.42 XRD analysis of neat PCL, clay, 3 wt% clay contained composite films.	111
5.43 SEM picture of ruptured PCL_C3_OA0 from tensile test.....	111
5.44 Variation of degree of crystallinity values of composite; a-Clay-Oleic acid; b-Clay-GMO.....	113
5.45 Variation of crystal thickness values of composite; a-Clay-Oleic acid; b-Clay-GMO.	114
5.46 Variation of degree of crystallinity by central point statistical model.	115
5.47 Strain - stress diagram of neat PCL film.	116
5.48 Variation of Young Modulus of PCL composite films with additive concentration; a-Clay-Oleic acid; b-Clay-GMO.	118
5.49 Variation of Yield Points of PCL composite films with additive concentration; a-Clay-Oleic acid; b-Clay-GMO.	119
5.50 Variation of Tensile Strength of PCL composite films with additive concentration; a-Clay-Oleic acid; b-Clay-GMO.	120
5.51 Variation of Elongation values of PCL composite films with additive concentration; a-Clay-Oleic acid; b-Clay-GMO.	121
5.52 Variation of Pukanszky constant values of PCL composite films depend on additive concentration.	122
5.53 TGA thermogram of organoclay.	123
5.54 Variation of degradation beginning temperature of composite films; a- Clay-Oleic Acid; b – Clay-GMO.	126
5.55 Variation of remaining ash amount of composite films; a- Clay-Oleic Acid; b – Clay-GMO.....	127
5.56 Degradation activation energy obtained from Broido Model of composite films depend on additive concentration; a-Clay - Oleic acid, b- Clay – GMO.....	128

TABLE OF FIGURES (continued)

<u>Figures</u>	<u>Pages</u>
5.57 Variation of weight loss values after 3 months; a-Clay-Oleic acid; b-Clay-GMO.	133
5.58 Variation of weight loss values after 5 months; a-Clay-Oleic acid; b-Clay-GMO.	134
5.59 Variation of weight loss values after 9 months; a-Clay-Oleic acid; b-Clay-GMO.	135
5.60 Variation of thickness of the composite films for before soil burial and after 3, 5 and 9 months of soil burial.	136
5.61 Variation of $A_{\text{amorphous}}/A_{\text{crystalline}}$ ratio of the composite films for before soil burial and after 3, 5 and 9 months of soil burial.	137
5.62 Photographs of degradation progress of neat PCL with increasing organic addition before soil burial and after 3, 5 and 9 months of soil burial.	138
5.63 Photographs of degradation progress of 0.1% clay contained PCL films with increasing organic addition before soil burial and after 3, 5 and 9 months of soil burial.	139
5.64 Photographs of degradation progress of 0.4% clay contained PCL films with increasing organic addition before soil burial and after 3, 5 and 9 months of soil burial.	140
5.65 Photographs of degradation progress of 1% clay contained PCL films with increasing organic addition before soil burial and after 3 and 5 months of soil burial, they are completely degraded in 9 months.	141
5.66 Photographs of degradation progress of 3% clay contained PCL films with increasing organic addition before soil burial and after 3 and 5 months of soil burial, they are completely degraded in 9 months.	142

LIST OF TABLES

<u>Tables</u>	<u>Pages</u>
2.1 Stress - strain curve with the association of polymer properties (Blaga, 1973). .6	
3.1 Avrami exponents for various types of crystal growth geometry's (Rattaa et al., 2000).	36
3.2 Theoretical values of n and K for different morphologies and nucleation mechanisms (Mark, 2007).	40
4.1 Contents of composite films prepared with clay, oleic acid and GMO.....	45
5.1 Melting temperatures of solvent cast films (T_{m1}) and films crystallized at 40 °C (T_{m2}) from Isothermal DSC analysis and calculated melting points from model equations.....	55
5.2 The second melting temperatures of films which are melt crystallized by cooling at different rates.....	57
5.3 Degree of crystallinity % values (DOC%) of PCL composite films obtained from isothermal DSC analysis.	59
5.4 Degree of crystallinity % values (DOC) and crystallization temperatures of PCL composite films obtained from nonisothermal DSC analysis at different cooling rates.	60
5.5 Central point samples for isothermal DSC results and levels for statistical evaluation.	60
5.6 Model equations by statistical evaluation.	64
5.7 Central point samples for isothermal DSC results and levels for statistical evaluation.	67
5.8 Crystallization kinetics parameters of PCL composite films obtained by Avrami model.	68
5.9 Model equations obtained by the statistical evaluation.	72
5.10 Nonisothermal crystallization kinetics parameters (n , Z_c) and crystallization half time ($t_{1/2}$) obtained by Avrami Jeziorny Model.	76

LIST OF TABLES (continued)

<u>Tables</u>	<u>Pages</u>
5.11 Nonisothermal crystallization kinetics parameters (m , $K(T)$) and regression coefficients values obtained by Ozawa Model.....	80
5.12 Comparison of isothermal and nonisothermal crystallization kinetics parameter (a , $\ln F(T)$) and regression coefficient values obtained by Liu Mo Model.....	83
5.13 Variation of overall crystallization growth rate G_0 , crystallization rate K_g , growth crystal surface free energy σ_e of nonisothermal crystallized composite films obtained by Lauritzen Hoffman Model were calculated according to Regime IIb and to Regime III. The ratio of regime rate constant is $R (K_{g,III}/K_{g,II})$ and regime transition temperature is $T_{II \rightarrow III}$	87
5.14 Variation of overall crystallization growth rate G_0 , crystallization rate K_g , growth crystal surface free energy σ_e of nonisothermal crystallized composite films obtained by Lauritzen Hoffman Model were calculated according to Regime II and to Regime III. The ratio of regime rate constant is $R (K_{g,III}/K_{g,II})$ and regime transition temperature is $T_{II \rightarrow III}$	88
5.15 Variation of overall crystallization growth rate G_0 , crystallization rate K_g , growth crystal surface free energy σ_e of nonisothermal crystallized composite films obtained by Lauritzen Hoffman Model were calculated according to Regime II and to Regime III. The ratio of regime rate constant is $R (K_{g,III}/K_{g,II})$ and regime transition temperature is $T_{II \rightarrow III}$	89
5.16 Crystallization activation energy values obtained from Kissinger and Augis Bennet for nonisothermally crystallized selected PCL composite films.	94
5.17 Melting and crystallization start temperatures of the films obtained by POM analysis.....	100
5.18 Density values of composite films.	102
5.19 Contact angle and surface tension value of composite films.....	104
5.20 Characteristic FTIR infrared bands for neat PCL.	108
5.21 XRD analysis results of PCL composite films.	112

LIST OF TABLES (continued)

<u>Tables</u>	<u>Pages</u>
5.22 Mechanical properties and polymer additive interaction parameter B values calculated from Pukanszky Model of PCL films.	117
5.23 Thermal degradation results of PCL composite films.	125
5.24 Weight loss values of composite films followed by 9 months.	130
5.25 Thickness of the composite films measured for 9 months.	131
5.26 $A_{\text{amorphous}}/A_{\text{crystalline}}$ ratio of the composite films for 9 months.	132

NOMENCLATURE

a	Ratio of the Avrami exponent n to the Ozawa exponent m (n/m)
a	Filler–matrix interaction constant
B	A measure of the peak width, the full width at half maximum FWHM (2θ)
B	An interaction parameter that is related to the macroscopic characteristics of the filler–matrix interface and interphase
B^*	Slope of Pukanszky plot
d_{hkl}	The distance between planes (nm)
E	The molar-attraction constants
Ea	Activation energy (kJ/mol)
$F(T)$	The value of cooling rate
G	Overall growth rate
G_0	Growth rate constant (cm/s)
k	Avrami rate constant (containing the nucleation and the growth parameters (min^{-1}))
k_0	Preexponential factor
K_g	Nucleation rate constant (K^2)
$K(T)$	Function of cooling rate for nonisothermal crystallization by Ozawa model
m	Ozawa exponent (depends on the crystal growth)
M_w	Molecular weight of repeating polymer chain (g/mol)
n	The diffraction order in Scherrer equation
n	Avrami exponent (depends on the mechanism of nucleation and on the form of crystal growth)
t	Crystal thickness (nm)
$t_{1/2}$	Crystallization half time [min]

c	Crystallization peak temperature ($^{\circ}\text{C}$)
T_d	Degradation onset temperature ($^{\circ}\text{C}$)
T_g	Glass transition temperature ($^{\circ}\text{C}$)
T_m	Melting temperature ($^{\circ}\text{C}$)
T_m^0	Equilibrium melting point ($^{\circ}\text{C}$)
T_{∞}	$T_g - 30(^{\circ}\text{K})$
X_c	Degree of crystallinity
X_t	Relative degree of crystallinity
U^*	Activation energy for segmental jump rate in polymers (1500 cal/mol)
V_u	The molar volume of the polymer repeat unit (mol/lt)
Z_c	Parameter characterizing the kinetic of nonisothermal crystallization by Avrami Jeziorny's model
Z_t	Rate constant in the nonisothermal crystallization process
β	Heating rate ($^{\circ}\text{C}/\text{min}$)
ΔG	The change in free energy on melting (J)
ΔG^*	The surface-independent change in free energy (J)
ΔH_u	The heat of fusion per polymer repeat unit (J)
σ_i	The specific surface free energy of surface i with area A_i (J)
v_1	The volume fraction of the solvent
χ	The polymer-solvent interaction parameter

1. INTRODUCTION

Poly(ϵ -caprolactone) (PCL) is an aliphatic polyester with crystallinity around 45%, exhibiting a glass transition temperature at about -60°C and a melting point ranging between $59\text{-}66^{\circ}\text{C}$. PCL has been approved by the Food and Drug Administration (FDA) as a material used in the human body as sutures, drug delivery device, or tissue scaffold due to its biocompatibility, biodegradability and nontoxicity. PCL belongs to the class of synthetic biodegradable polymers. PCL is a linear, hydrophobic and partially crystalline polyester that can be slowly consumed by micro-organisms. Its physical properties and commercial availability makes it a good substitute for conventional nonbiodegradable polymers used not only for common applications but also for specific areas such as medicine and agriculture (Acierno et al., 2005; Avella et al., 2006; Elzein et al., 2004; Fukushima et al., 2010; Luduena et al., 2007; Ludueña et al., 2008; She et al., 2007; Skoglund and Fransson, 1996; Wang et al., 2009; Wong and Baji, 2007; Woodruff and Hutmacher, 2010; Yingwei et al., 2005).

Polymer-clay nanocomposite (PCN) was discovered at Toyota Central Research and Development Laboratory, Inc. in 1985, and since its discovery, interests in PCN has grown tremendously to the extent that the number of papers on PCNs published in major journals was claimed to exceed 500 in 2005 alone. The primary reason that PCNs have generated so much interest in industry and academe is the perceived benefits that PCNs possess relative to traditional materials. These benefits include efficient reinforcement, improved stiffness (modulus of elasticity), strength, thermal endurance, flame resistance, improved barrier properties, improved abrasion resistance, reduced shrinkage and altered stress, and altered electrical, electronic, and optical properties with silicate loadings as low as 1–4 vol% (Aloisi et al., 2010; Di Maio et al., 2004; Gopakumar et al., 2002; Homminga et al., 2006; Luduena et al., 2007; Maiti et al., 2002; Okada and Usuki, 2006; Wu et al., 2007).

The crystallization process significantly influences polymer properties through the crystal structure and morphology established during the phase transition from the viscous molten state to the semicrystalline solid state (Acar et al., 2007; Chen et al., 1997; Skoglund and Fransson, 1996; Wang et al., 2009). The final polymeric material properties are dependent on the morphology generated during their processing. In this stage, the filler in polymeric-based composite materials may act as a nucleating agent and effect thus the crystallization behavior. So, the knowledge of the parameters affecting crystallization is crucial for the optimization of the processing conditions and the properties of the end product (Acierno et al., 2005; Durmus et al., 2009; Mitchell and Krishnamoorti, 2005; Perez and Alvarez, 2009; Vyazovkin et al., 2005;

Wang and Dong, 2006; Wu et al., 2004). As a semi-crystalline polymer, the final properties of PCL, such as mechanical properties and biodegradability, are strongly correlated with the extent of crystallization, crystalline morphology and crystalline texture. PCL crystallization rate is lower than that of conventional polymers. It has been reported that when clay, multi-walled carbon nanotube, and hydroxyapatite were introduced into PCL to form nanocomposites, the crystallization rate of PCL was enhanced (Di Maio et al., 2004; Gan et al., 1997; Grozdanov et al., 2007; Huang et al., 2010; Jana and Cho, 2010; Liu et al., 2010; Lovera et al., 2007).

The crystallization behavior of nylon 6 based melt processed nanocomposites have extensively been analyzed both in isothermal and non-isothermal condition with the DSC (Acar et al., 2007; Di Maio et al., 2004; Durmus et al., 2009; Fornes and Paul, 2004; Labidi et al., 2010; Mersmann, 2001; Papageorgiou et al., 2005; Skoglund and Fransson, 1996). The authors evidenced that, at very low levels of clay, the crystallization kinetics of the nanocomposites were dramatically increased. This behavior is commonly observed in particulate filled polymers: at low filler concentration the filler-polymer interfaces act as heterogeneous nucleating sites, hence increasing the nucleation rate and, therefore, the crystallization kinetics; at higher filler content, diffusion of polymer chains to the growing crystallites is hindered and the overall crystallization rate is reduced. Other authors have reported different behaviors in nanocomposites crystallization (Di Maio et al., 2004; Gopakumar et al., 2002; Kim et al., 2004; Labidi et al., 2010; Lee and Park, 2011; Nam and Ray, 2003).

In this work, the motivation arises from the lack of literature since there is no study related to improvement of PCL crystallinity behavior by using both organic and inorganic additives. Therefore, this study attempts not only to control the crystallization behavior of PCL by using both inorganic additive as clay and organic additives as oleic acid and glycerol monooleate, but also to design PCL composite materials with desired product properties for several application areas by solvent casting technique. Moreover, the other objective is to characterize the prepared composite films in order to estimate the ranges of application of composite films as a medical in tissue, drug delivery, dental and packaging and to understand the mechanism under melt crystallization.

This study also aimed to provide the crystallization process as a whole wherein the details of the formation of crystals, various models, thermodynamics and kinetics of crystallization process and product properties. Furthermore thermal and soil burial degradation mechanisms are also focused in this study. The chapters of this thesis can be summarized as follows:

In Chapter 2, literature survey are reviewed according to biodegradable polymers, PCL based composites, preparation methods, clay contained PCL composite films and their compatibility according to product properties, thermal and biological degradation mechanism with soil burial.

In Chapter 3 includes thermodynamic consideration of crystallization, melt crystallization, crystallinity, crystal morphology, polymer crystallization kinetics models, correlations for additives, crystallinity and product properties. The kinetics of crystallization is introduced under isothermal and nonisothermal conditions with the help of a wide range of models determine the final physical properties of the product. The correlation of crystallinity with various properties is also represented. For kinetics evaluation, the basic hypotheses of various models, as well as their relative drawbacks are also underlined.

Chapter 4 describes the materials used in the preparation of composite films, experimental procedure of the preparation of composite films and explains the characterization techniques for PCL composite films.

Chapter 5 includes all results obtained for solvent casted PCL composite films. This chapter indicates the product properties, crystallization kinetics under isothermal and nonisothermal conditions and thermal and soil burial degradation. This chapter also indicates statistical analysis of some results with factorial design with central point model.

2. LITERATURE, LAYER SILICATE and BIODEGRADABLE POLYMERIC COMPOSITES

Traditionally, polymeric materials have been filled with synthetic or natural inorganic compounds in order to improve their properties, or simply to reduce cost. Conventional fillers are materials in the form of particles (e.g. calcium carbonate), fibers (e.g. glass fibers) or plate-shaped particles (e.g. mica). However, although conventionally filled or reinforced polymeric materials are widely used in various fields, it is often reported that the addition of these fillers imparts drawbacks to the resulting materials, such as weight increase, brittleness and opacity (Alexandre and Dubois, 2000; Fischer, 2003; Giannelis, 1996; Lagaly, 1999; Varlot et al., 2001). Nanocomposites, on the other hand, are a new class of composites, for which at least one dimension of the dispersed particles is in the nanometer range. Depending on how many dimensions are in the nanometer range, one can distinguish isodimensional nanoparticles when the three dimensions are on the order of nanometers, nanotubes or whiskers when two dimensions are on the nanometer scale and the third is larger, thus forming an elongated structure, and, finally, layered crystals or clays, present in the form of sheets of one to a few nanometers thick and hundreds to thousands nanometers in extent. Among all the potential nanocomposite precursors, those based on clay and layered silicates have been most widely investigated, probably because the starting clay materials are easily available and because their intercalation chemistry has been studied for a long time (Gorrasi et al., 2002).

Polymer-layered silicate nanocomposites, which are the subject of the present contribution, are prepared by incorporating finely dispersed layered silicate materials in a polymer matrix (Fischer, 2003). However, the nanolayers are not easily dispersed in most polymers due to their preferred face to face stacking in agglomerated tactoids. Dispersion of the tactoids into discrete monolayers is further hindered by the intrinsic incompatibility of hydrophilic layered silicates and hydrophobic engineering plastics. Therefore, layered silicates first need to be organically modified to produce polymer-compatible clay (organoclay). In fact, it has been well-demonstrated that the replacement of the inorganic exchange cations in the cavities or “galleries” of the native clay silicate structure by alkylammonium surfactants can compatibilize the surface chemistry of the clay and a hydrophobic polymer matrix (LeBaron et al., 1999).

Thereafter, different approaches can be applied to incorporate the ion-exchanged layered silicates in polymer hosts by in situ polymerization, solution intercalation or simple melt mixing. In any case, nanoparticles are added to the matrix

or matrix precursors as 1–100 μm powders, containing associated nanoparticles. Engineering the correct interfacial chemistry between nanoparticles and the polymer host, as described previously, is critical but not sufficient to transform the micron-scale compositional heterogeneity of the initial powder into nanoscale homogenization of nanoparticles within a polymeric nanocomposite (Vaia and Wagner, 2004). Therefore, appropriate conditions have to be established during the nanocomposite preparation stage.

The resulting polymer-layered silicates hybrids possess unique properties – typically not shared by their more conventional microscopic counterparts – which are attributed to their nanometer size features and the extraordinarily high surface area of the dispersed clay (Alexandre and Dubois, 2000; Fischer, 2003; Giannelis, 1996; Lagaly, 1999; Varlot et al., 2001). In fact, it is well established that dramatic improvements in physical properties, such as tensile strength and modulus, heat distortion temperature and gas permeability, can be achieved by adding just a small fraction of clay to a polymer matrix, without impairing the optical homogeneity of the material. Most notable are the unexpected properties obtained from the addition of stiff filler to a polymer matrix, e.g. the often reported retention (or even improvement) of the impact strength. Since the weight fraction of the inorganic additive is typically below 10%, the materials are also lighter than most conventional composites (Ginzburg et al., 2000; Osman et al., 2004). These unique properties make the nanocomposites ideal materials for products ranging from high-barrier packaging for food and electronics to strong, heat-resistant automotive components (Balazs et al., 1999). Additionally, polymer-layered silicate nanocomposites have been proposed as model systems to examine polymer structure and dynamics in confined environments (Lincoln et al., 2001).

Mechanical properties of polymers such as ductility, hardness, brittleness, strength or forcefulness are determined by stress - strain tests. A typical stress-strain curve is shown in Figure 2.1. Stress strain curve with the association of polymer properties are given in Table 2.1 and various stress-strain curves for plastics are shown in Figure 2.2.

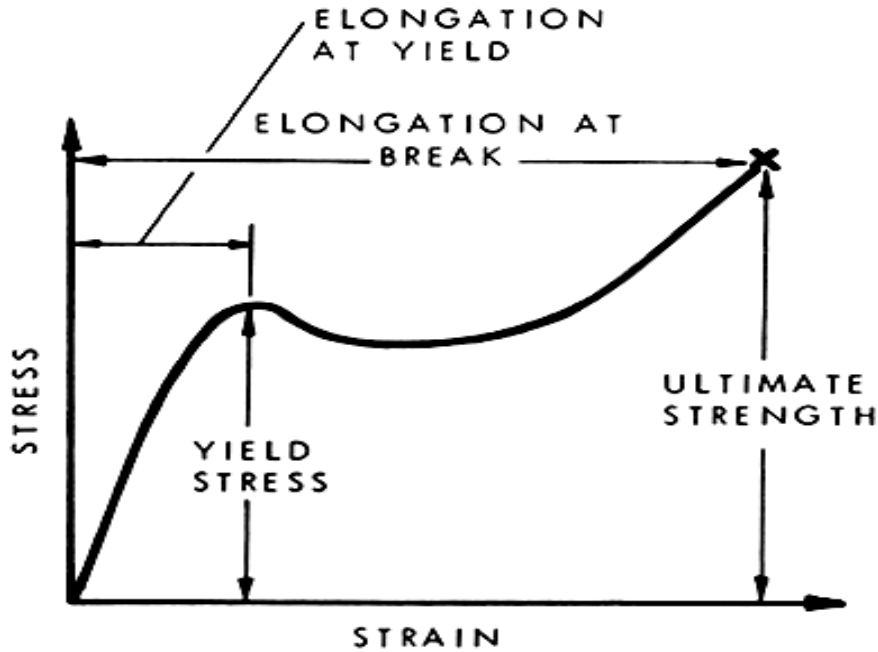


Figure 2.1 Generalized tensile stress - strain curve for polymeric materials (Blaga, 1973).

Table 2.1 Stress - strain curve with the association of polymer properties (Blaga, 1973).

Definition of Polymer	Stress-Strain Curve Properties			
	Young Modulus [N/mm ²]	Yield Stress [N/mm ²]	Strength	Elongation at break [mm]
Ductile and poor	low	low	low	medium
Ductile and strong	low	low	high	high
Hard and brittle	high	-	medium	low
Hard and forceful	high	high	high	medium
Hard and strong	high	high	high	high

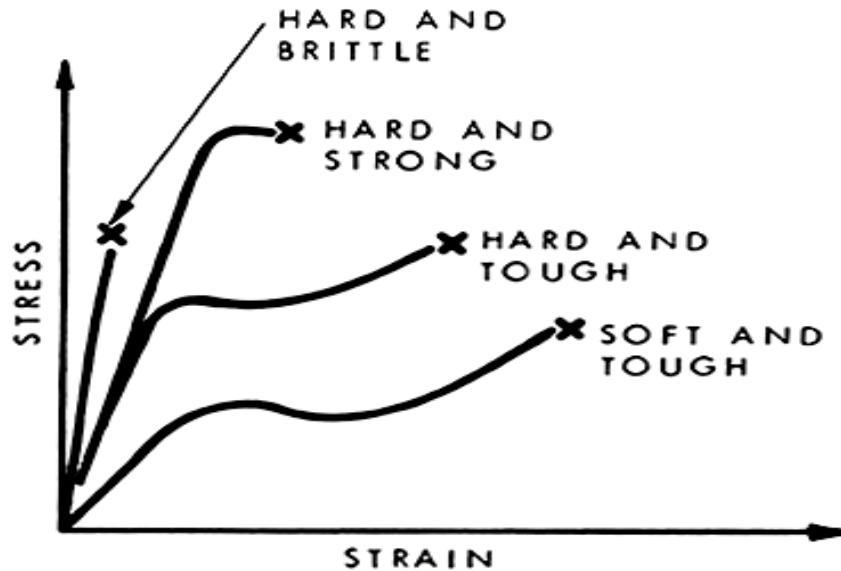


Figure 2.2 Tensile stress-strain curves for four types of polymeric material (Blaga, 1973).

In general, the addition of an organically modified layered silicate in a polymer matrix results in significant improvements of Young's modulus. For example, PCL nanocomposite containing 10 wt.% ammonium-treated montmorillonite (MMT) shows an increase from 216 to 390MPa, while in another study, Young's modulus was increased from 120 to 445MPa with addition of 8 wt.% ammonium treated clay in PCL (Gorrasi et al., 2002; Pantoustier et al., 2002).

However, exceptions to this general trend have been reported. As shown in Figure 2.3, in crosslinked polyester/organomodified clay nanocomposites, the modulus decreases with increasing clay content; in fact, the drop for the 2.5 wt.% nanocomposite was greater than expected. To explain this phenomenon, it was proposed that the intercalation and exfoliation of the clay in the polyester resin serve to effectively decrease the number of crosslinks from a topological perspective. The origin of the greater drop in properties of the 2.5 wt.% nanocomposites may be traced to the morphology; i.e. it was observed that the sample showed exfoliation on a global scale compared to the nanocomposite containing 10 wt.% clay, indicating that the crosslinking density is inversely proportional to the degree of exfoliation (Bharadwaj et al., 2002).

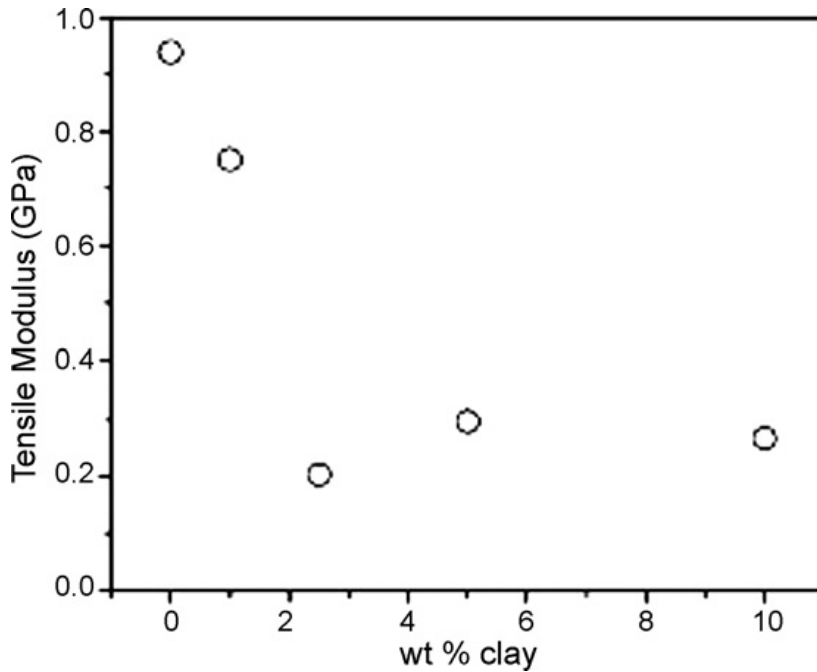


Figure 2.3 Tensile modulus vs. clay concentration for crosslinked polyester nanocomposites (Bharadwaj et al., 2002).

The effect of polyamide (PA6) molecular weight and MMT content on nanocomposite tensile modulus is researched (Manias, 2001). The addition of organoclay leads to a substantial improvement in stiffness for the composites based on each of the three PA6 samples examined, i.e. LMW, MMW and HMW (low, medium and high molecular weight, respectively). Interestingly, the stiffness increases with increasing matrix molecular weight at any given concentration, even though the moduli of the neat PA6s are all quite similar. Similar trends with respect to the level of organoclay content and molecular weight are evident in the yield strength results (Figure 2.4).

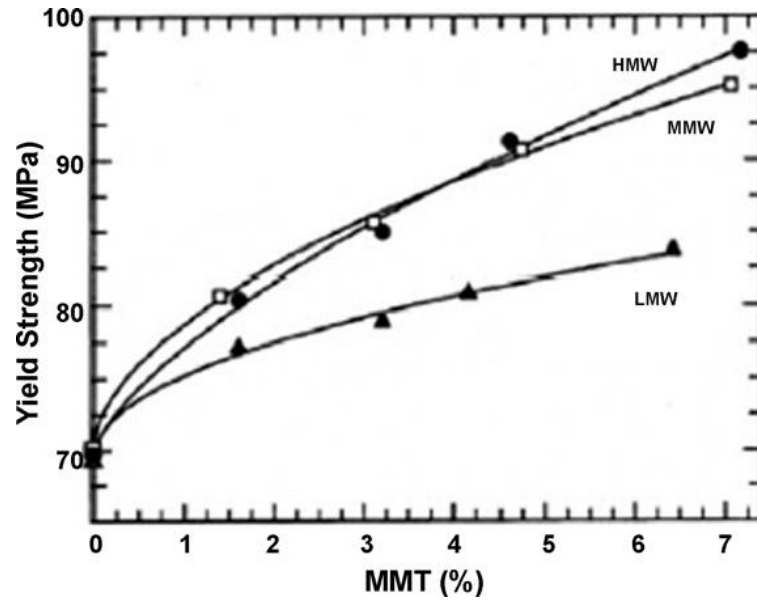


Figure 2.4 Effect of MMT content on yield strength of nylon 6 nanocomposites (Manias, 2001).

As shown in Figure 2.5, PCL with organomodified clay nanocomposites show good interaction between polymer - clay and barrier and mechanical properties of nanocomposites were improved with low amount of additive (Di Maio et al., 2004).

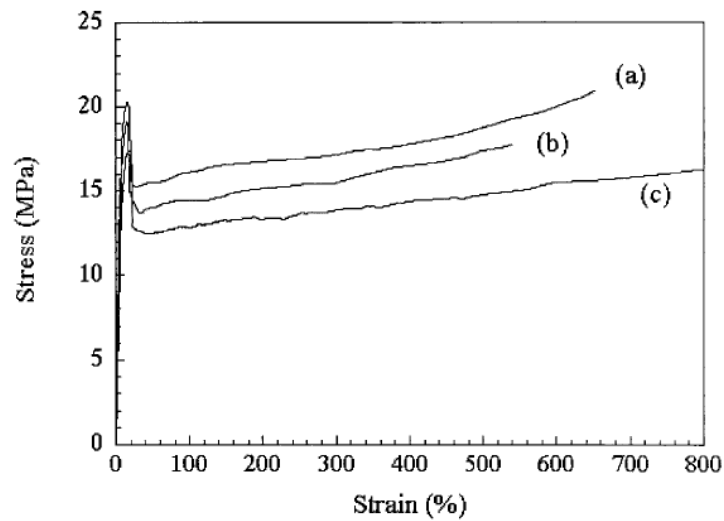


Figure 2.5 Stress – Strain curves for PCL and two composites at a crosshead speed of 130 mm/min; a) PCL/30B (95/5), b) PCL/93A (95/5), c) PCL

Young's modulus of PCL composites are improved with organomodified MMT addition (Lepoittevin et al., 2002). Also no correlation is observed between PCL-non modified MMT composites (MMT-Na) (Figure 2.6).

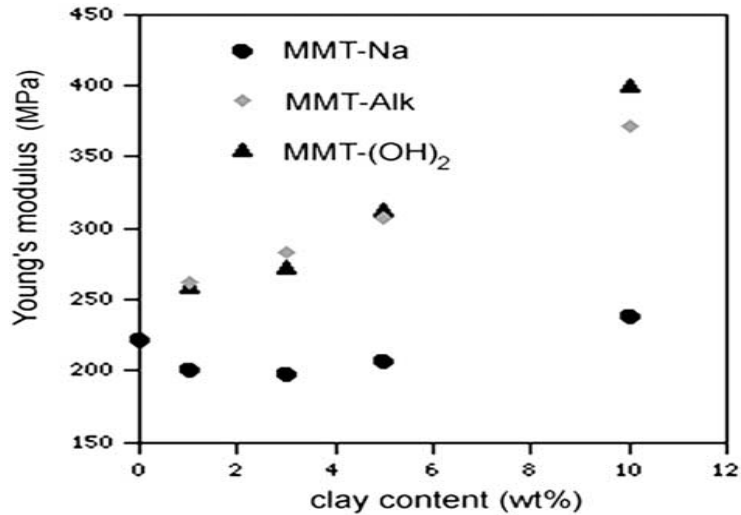


Figure 2.6 Dependence of Young's modulus on the clay content for PCL (Lepoittevin et al., 2002).

Tensile properties of polymeric materials can be improved in different degrees if nanocomposites are formed with layered silicates (Hoidy et al., 2010). The tensile strengths of hybrid films with different OMMT contents are shown in Figure 2.7. Also solvent cast composite films have less tensile properties than melt blending.

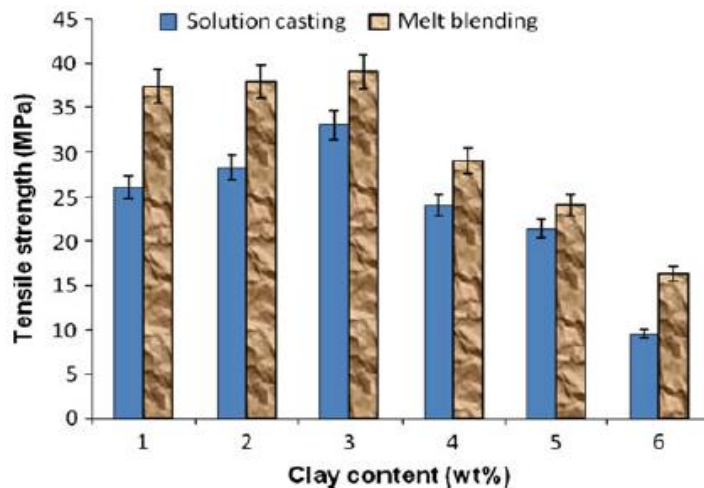


Figure 2.7 Tensile strength of 80% PLLA - 20% PCL with various contents of OMMT prepared by solution casting and melt blending (Hoidy et al., 2010).

Tensile yield stress of composites can be predicted by using Pukanzky model (Eq. 2.1);

$$\sigma_{yc} / \sigma_{ym} = \frac{1 - \phi_f}{1 + 2.5\phi_f} \exp(B\phi_f) \quad 2.1$$

The parameter B is an interaction parameter that is related to the macroscopic characteristics of the filler–matrix interface and interphase. σ_{yc} and σ_{ym} denote the tensile yield stress of composite and matrix, respectively. The first term in Eq. 2.1 is related to the decrease in effective load bearing cross-section, and the second one is concerned with the interfacial interaction between filler and matrix. Interfacial interaction depends on the area of the interphase, and the strength of the interaction as shown in Eq. 2.2.

$$B = (1 + A_f \rho_f t) \ln(\sigma_{yi} / \sigma_{ym}) \quad 2.2$$

where t , σ_{yi} , A_f and ρ_f are the thickness of the interface, strength of interaction, the specific surface area and density of the filler, respectively.

The effect of interfacial interactions on the mechanical properties of polypropylene (PP)/natural zeolite composites was investigated under dry and wet conditions by Pukanszky model (Metin et al., 2003). The tensile properties of the composites determined as a function of the filler loading and the concentration of the coupling agents were found to vary with surface treatment of zeolite. Improvements of the mechanical properties of treated silane contained composites were reported.

The thermal stability of polymeric materials is usually studied by thermogravimetric analysis (TGA). The weight loss due to the formation of volatile products after degradation at high temperature is monitored as a function of temperature (and/or time). When heating occurs under an inert gas flow, a non-oxidative degradation occurs, while the use of air or oxygen allows oxidative degradation of the samples (Krishnamoorti and Giannelis, 1997; Ray and Okamoto, 2003).

Generally, the incorporation of clay into the polymer matrix was found to enhance thermal stability by acting as a superior insulator and mass transport barrier to the volatile products generated during decomposition, as well as by assisting in the

formation of char after thermal decomposition (Becker et al., 2004; Krishnamoorti and Giannelis, 1997; Ray and Okamoto, 2003).

The thermal degradation of a Polystyrene (PS) nanocomposite with that of the virgin polymer was compared under nitrogen and air (Vyazovkin et al., 2004). As seen in Figure 2.8 in both nitrogen and air the decomposition temperature of nanocomposites increased by 30–40 °C. The authors also observed that the virgin polymer degrades without forming any residue, whereas the nanocomposite (as expected) leaves some residue.

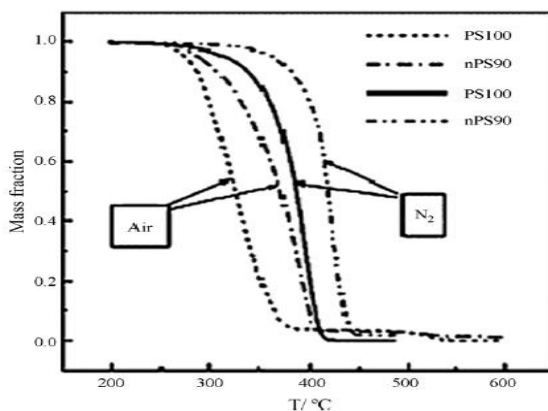


Figure 2.8 TGA curves of the degradation of neat PS and PS + 10% clay at a heating rate 5 °C min⁻¹ in air and nitrogen (Vyazovkin et al., 2004).

Thermal degradation behaviours of the PCL-clay nanocomposites were examined (Lepoittevin et al., 2002). Results showed that thermal properties of the PCL composites enhanced with low amount of clay addition (Figure 2.9).

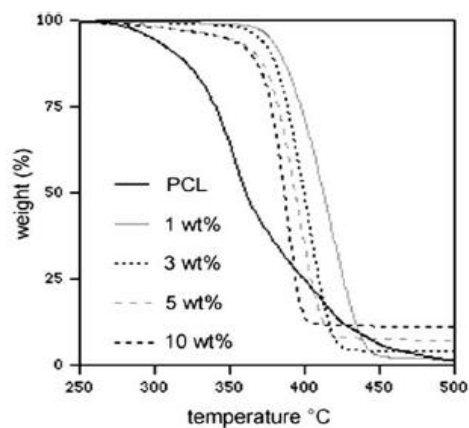


Figure 2.9 Temperature dependence of the weight loss under an air flow for unfilled PCL and PCL-nanocomposites containing 1,3,5 and 10 wt. % of MMT.

Degradation of PCL by soil has been studied recently in simulated soil (Mochizuki and Hayashi, 1999). In soil burial, biodegradation rates were observed from weight loss of the polymers.

PCL fibers were degraded under environmental conditions including soil burial (Mochizuki and Hayashi, 1999). The extent of degradation was examined by weight loss, loss of mechanical properties, such a tensile strength and ultimate elongation decreases, and visual observations by scanning electron microscopy. The rate of degradation was found to depend on the draw ratio and crystallinity of the PCL fibers with surface erosion of amorphous regions more readily than crystalline regions. Relationship between the rate of degradation in soil and crystallinity of PCL is shown in Figure 2.10. In terms of the degradation mechanism of PCL fiber breakdown, biodegradation seems to be the dominant reaction, which is a hydrolysis reaction catalyzed by enzymes secreted by microorganisms.

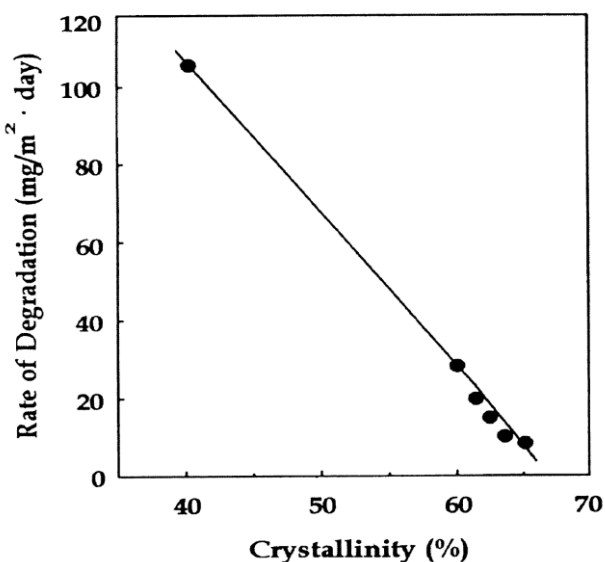


Figure 2.10 Relationship between the rate of degradation in soil and crystallinity of PCL (Mochizuki and Hayashi, 1999).

The thermal degradation activation energy is calculated by Brodio model. Mathematical expression of Brodio's model (Eq. 2.3) is as follows:

$$\log(-\log(1-\alpha)) = -\frac{E_a}{RT} + \ln \frac{(RT_m^2)}{\beta E_a} \quad 2.3$$

where $(1 - \alpha)$ is the fraction of number of initial molecules not yet decomposed, T is the peak temperature of derivative curve of TGA, T_m is maximum melting peak

temperature, R is the gas constant, β is heating rate and E_a is the activation energy can be calculated from the plot of $\log(-\log(1 - \alpha))$ versus $1/T$.

Thermal degradation activation energies of nanoclay filled nylon6 composite films were evaluated (Pashaei and Syed, 2011). The nanofiller contained composite films show lower degradation activation energy. This shows that addition of the nanofiller was improved the thermal degradation properties of nylon6.

PCL biodegradation in soil burial resulted in almost equivalent rate for unirradiated PCL and irradiated PCL at 160 kGy (containing 80% of gel). After 6 months, about 60% weight losses were achieved. For soil burial test, since controlling of microbial populations and environment changes by season are difficult, effect of morphology on degradation did not appear clearly. From these findings, it is concluded that biodegradation easily occurs even for PCL introduced crosslinking structure by irradiation (Davis and Song, 2006).

Seretoudi et al. (2002) were buried a prepared poly(ethylene succinate)/poly(ϵ -caprolactone) (PESu/PCL) block copolymers in soil. It is reported that observation of the biodegradation rates from weight loss constitutes a practical problem since PESu and its copolymers with PCL are waxy materials and the soil sticks on the film surface. These soil granules were very difficult to remove and therefore in all cases an increase in weight after soil burial was found. PCL film remained stable with no visible signs of biodegradation (Seretoudi et al., 2002).

An interesting aspect of nanocomposite technology is the enhancement in biodegradability, often reported after nanocomposite formation. Tetto et al. first presented results on the biodegradability of nanocomposites based on PCL, reporting that the PCL/MMT nanocomposites showed improved biodegradability compared with pure PCL (Tetto and Steeves, 1999).

Zhao et al. reported presence of rice husk fillers can accelerate the degradation of the PCL matrix in the ecomposites (Figure 2.11), and this acceleration effect becomes more pronounced with the increase of rice husk content (Zhao et al., 2008).

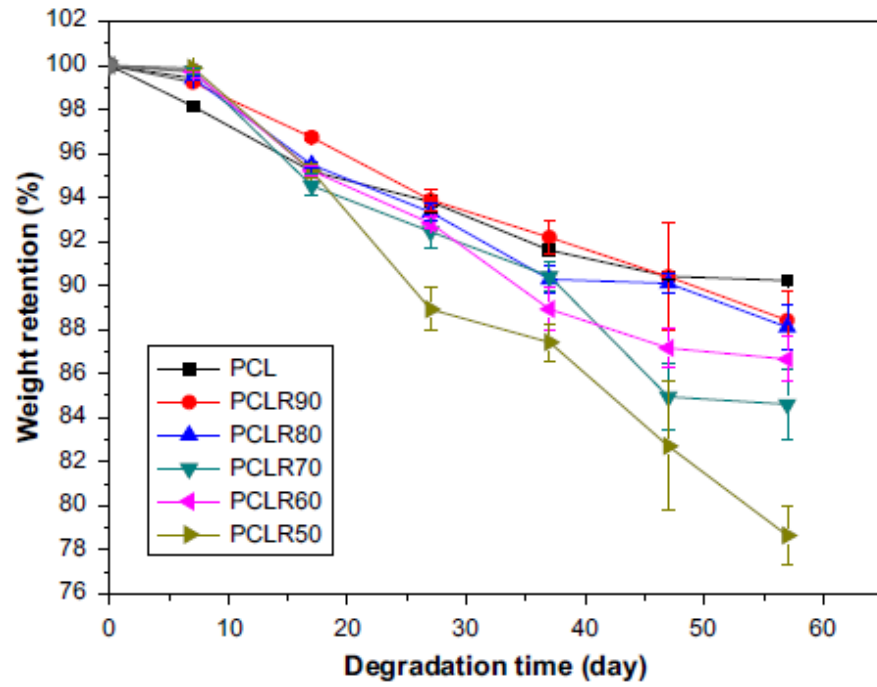


Figure 2.11 Weight retention as a function of degradation time for PCL/RH ecomposites in soil suspension system (Zhao et al., 2008).

3. CRYSTALLIZATION OF POLYMERS

3.1. Melting Point Calculation, Florry Huggings and Thomson Gibbs models

For the most polymers, there is a single temperature at which the onset of segmental motion occurs; it is termed the glass transition temperature, T_g . Similarly, for those polymers which crystallize to any extent, there is a single melting temperature, T_m . However, in both the amorphous and crystalline phases, additional rearrangements or relaxation processes can occur. For partially crystalline materials, T_m is always greater than T_g . The rate of polymer crystallization increases as the temperature is lowered from T_m . However, no crystallization takes place effectively below T_g . Consequently, the maximum rate of crystallization occurs at a temperature between T_m and T_g (Figure 3.1) (Rodriguez, 1987).

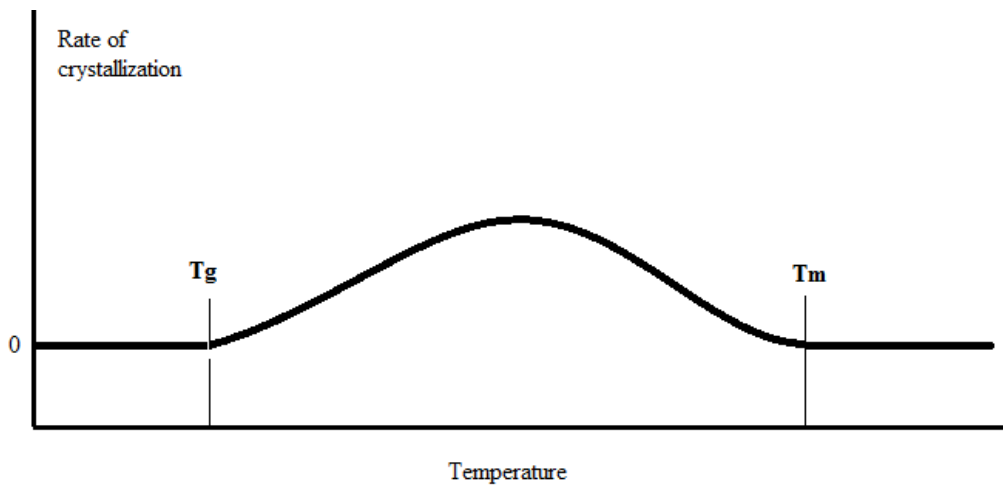


Figure 3.1 Rate of crystallization rises to a maximum between T_g and T_m .

If a sample of molten polymer is quenched rapidly to a temperature below T_g , a metastable glass may be obtained. Warming the sample just above T_g can increase crystallinity, making the sample stiffer. A glassy polymer is heated, becoming progressively softer as the temperature increases, suddenly stiffens, and then softens again as the T_m is approached (Figure 3.2).

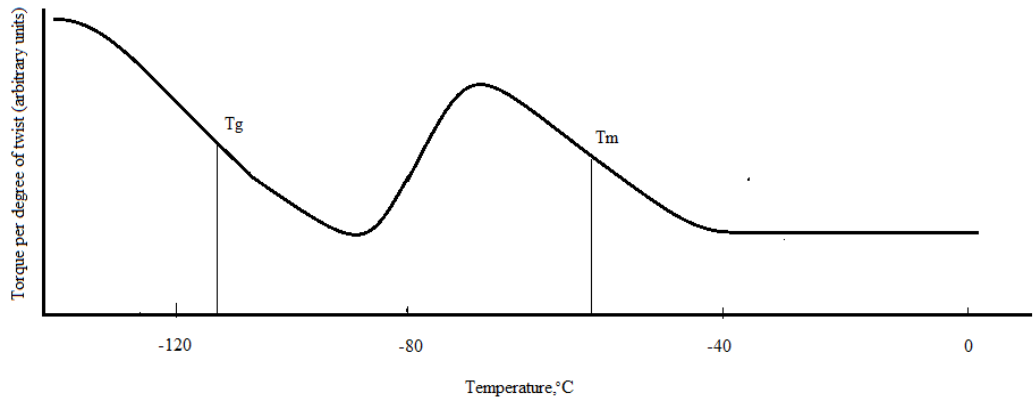


Figure 3.2 Quenched sample of silicone copolymer being heated from below T_g . Recrystallization between T_g and T_m increases stiffness, which then appears when T_m is exceeded.

Melting point of T_m of a polymer usually is more properly termed a melting range, because a single specimen consists of more than one molecular weight and more than one crystal size. Decreasing either molecular weight or crystal size lowers T_m somewhat. Besides the disappearance of opacity (seen by transmitted light) and polymer orientation (seen by transmitted polarized light), T_m can be characterized by the abrupt change in specific volume V that occurs. Chain stiffness also has an effect on T_m .

Adding a solvent to a polymer decreases the T_m in a manner predictable by the equation 3.1:

$$\frac{1}{T_m} - \frac{1}{T_m^0} = \frac{R}{\Delta H_u} \frac{V_u}{V_1} (\nu_1 - \chi \nu_1^2) \quad 3.1$$

where V_u is the molar volume of the polymer repeat unit, ΔH_u is the heat of fusion per polymer repeat unit, V_1 is the molar volume of the solvent, ν_1 is the volume fraction of the solvent, R is the gas constant, T_m^0 is the melting point of the pure polymer, χ is the polymer-solvent interaction parameter and calculated from equation 3.2:

$$\chi = \beta_1 + \frac{V_1}{RT} (\delta_1 - \delta_2)^2 \quad 3.2$$

where δ_1 and δ_2 relate to the solvent and polymer respectively. β_1 is the lattice constant, usually 0.35 ± 0.1 .

One of the important relationships for crystalline polymers is the Thompson-Gibbs (*TG*) equation which relates melting point and crystal thickness (Gedde, 1995). The change in free energy on melting (ΔG) is given by equation 3.3:

$$\Delta G = \Delta G^* + \sum_{i=1}^n A_i \sigma_i \quad 3.3$$

where ΔG^* is the surface-independent change in free energy and σ_i is the specific surface free energy of surface i with area A_i . At equilibrium:

$$\Delta G = 0 = \Delta G^* + \sum_{i=1}^n A_i \sigma_i \quad 3.4$$

Polymer crystals are lamella-shaped and the two fold surfaces greatly dominate the total surface energy term (Figure 3.3).



Figure 3.3 Simple model of crystal lamella (Gedde, 1995).

The surface-independent term is equal to:

$$\Delta G^* = \Delta g^* AL_c \rho_c \quad 3.5$$

where ρ_c is the density of the crystal phase. Since both Δh and Δs can be regarded as temperature-independent, the specific bulk free energy change (Δg^*) is given by;

$$\Delta G^* = \Delta h^0 - T_m \Delta s^0 = \Delta h^0 \left(1 - \frac{T_m}{T^0}\right) = \Delta h^0 \left(\frac{T_m^0 - T_m}{T_m^0}\right) \quad 3.6$$

if Eq. 3.6 is inserted in Eq.3.5, the following equation is obtained:

$$\Delta G^* = \Delta h^0 (T_m^0 - T_m) \frac{AL_c \rho_c}{T_m^0} \quad 3.7$$

The total area of the four lateral surfaces is small compared to the area of the fold surfaces and their contribution to the total surface free energy of the crystal can be neglected:

$$\sum_i^n A_i \sigma_i \approx 2\sigma A \quad 3.8$$

Combination of Eqs 3.4, 3.7 and 3.8 gives:

$$\Delta h^0 (T_m^0 - T_m) \frac{AL_c \rho_c}{T_m^0} = 2\sigma A \quad 3.9$$

$$(T_m^0 - T_m) = \frac{2\sigma A T_m^0}{AL_c \rho_c \Delta h^0} = \frac{2\sigma T_m^0}{L_c \rho_c \Delta h^0} \quad 3.10$$

which may be simplified to the Thompson-Gibbs equation:

$$T_m = T_m^0 \left(1 - \frac{2\sigma}{L_c \rho_c \Delta h^0}\right) \quad 3.11$$

The Thompson-Gibbs equation predicts a linear relationship between melting point and the reciprocal of crystal thickness (L_c). However, in order to obtain the correct crystal thickness from experimental melting-point data, crystal thickening has to be inhibited. This can be accomplished by selective crosslinking of the amorphous component by radiation or by controlled rapid heating.

3.2. Theories in Crystal Morphology and Crystal Geometry

The crystallization of polymers can be broadly classified under three groups as crystallization during polymerization, Crystallization induced by orientation and Crystallization under quiescent conditions:

Crystallization during Polymerization: A special attribute to this kind of polymerization is the formation of macroscopic single polymer crystal (Figure 3.4) (Stejny et al., 1979).



Figure 3.4 Macroscopic single crystal.

During such a process the monomers forming a crystal can be joined up into chains by solid state polymerization, while the original “monomer” crystals are preserved. The final polymer crystal is obtained due to the chemical reactions at the gas/solid or liquid/solid interface and not just as a consequence of the change in physical state of the material as is observed in normal crystallization process (Wegner, 1979). The final properties of crystals formed by such a method can be very interesting.

The mechanism of this process can be seen in Figure 3.5, which is of two types as:

- a. the simultaneous polymerization and crystallization;
- b. the successive polymerization and crystallization.

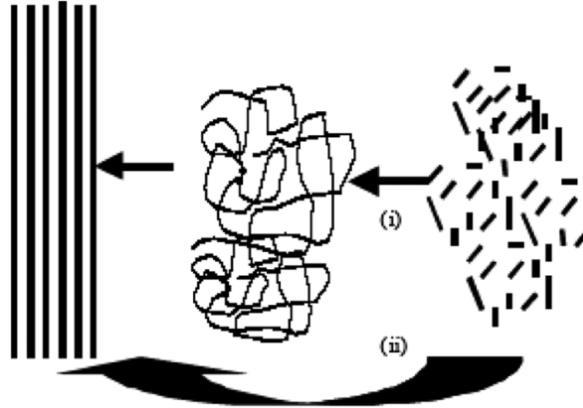


Figure 3.5 Crystallization of macromolecules. i) polymerization followed by crystallization; ii) crystallization during polymerization.

In (a), the primary and secondary bonds are set at the same time, and in (b), the polymerization and crystallization sites can be separated. Thus, the nature of the polymer segments as yet uncrystallized becomes important (Pennings, 1967).

Crystallization Induced by Orientation: The process as shown in Figure 3.6 can be described as stretching of long chains to form fibrous crystals.

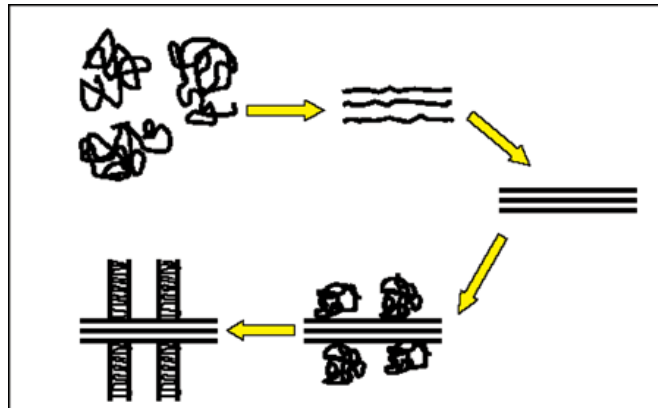


Figure 3.6 Schematic of orientation induced by crystallization (The first three drawings illustrate the orientation and crystallization of random coils while the last two drawings show the growth of folded chain kebab around the central shish).

In fact, this is the underlying process governing the formation of fibers though any perfectly smooth and completely elongated chain morphology, as illustrated in the schematic, is difficult to attain under the most perfect of circumstances. During the stretching, the distortion of chains from their most probable conformation results; hence, a decrease in conformational entropy takes place. If this deformation is

maintained in this lower conformational entropy state, then less conformational entropy needs to be sacrificed by transforming to the crystalline state. This decrease in total entropy of fusion allows the crystallization to occur at higher temperatures than will take place under quiescent conditions (Mandelkern, 1964).

Also crystallization in an already oriented polymer results in reduction in retractive force, which is inversely proportional to number of statistical elements and the magnitude of end-to-end distance. So, the reduction in force results due to a lesser number of statistical units available in amorphous regions and also because the end-to-end distance of the amorphous units is smaller than the end-to end distance in the crystal. Melting of such crystals leads to contraction, and crystallization leads to elongation. Thus, microscopic dimensional changes and changes in retractive force can be related to the crystal-liquid phase transformation (Mandelkern, 1964). Normally, the formation of such fibrous morphology is accompanied by formation of an epitaxial layer over and around the inner fiber giving rise to the so-called “shish-kebab” kind of morphology (Pennings, 1967).

Crystallization under Quiescent Conditions: Crystallization of long-chain flexible molecules of sufficient structural regularity is widely observed under quiescent conditions for a large number of macromolecules of both synthetic and natural origin. This type of crystallization is classified into two general types (Mandelkern, 1964).

1. Crystallization from dilute solutions which provide a more fundamental avenue for structural analysis of polymer crystal.
2. Crystallization from melt is often closer to pragmatic use of the polymer of interest though it adds an additional degree of difficulty to the fundamental structural studies.

During the crystallization from melt, the nucleation, growth and kinetics of development of these crystalline regions characteristics are directly linked to the understanding of the morphological details of these crystalline regions. On this account, there have been various models proposed over the past five decades—each involving considerable amount of controversy and debate, much of that debate persisting even to date. These models are elucidated next. The type of morphology can, however, be first classified into two broad classes the fringed micelle model and lamellar type of morphology. The model for lamellar morphology themselves differ on the basis of the nature of the fold surface, type of reentry of the chains and on accounts of presence of an intermediate region for the chain traveling from the crystal to the amorphous phase.

The Fringed Micelle Model: Hermann, Gerngross and Abitz first conceived this model in 1930 to explain the structure of gelatins, while the model was later more fully expanded (Flory, 1962; Geil, 1963). This model is based on the idea that part of polymer segment (either in solution or in melt) aligned themselves together to form bundled crystalline regions (Figure 3.7). These bundles can then grow in the direction of chain axis by reeling in adjoining chain segments (of the chains already part of the crystal) into the crystalline region.

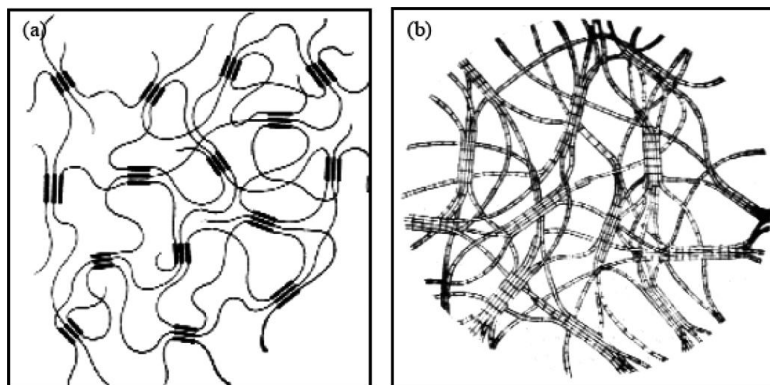


Figure 3.7 (a) Keller model for crystallization; (b) Hermann & Gerngross model (Flory, 1962; Geil, 1963).

Lateral growth of these crystalline regions can also take place by accretion of chain segments from the other molecules. The growth of these structures however is impeded by the presence of entanglements and strained regions, which then constitute the amorphous phase. The “fringes” are the regions of the chains traveling from the crystalline region to the amorphous regions. The crystalline regions then serve as physical crosslink.

Lamellar Models: It is a well-established and proven fact that a lamellar crystal is the fundamental structural form by which polymers most generally crystallize, a feature true for the vast majority of semicrystalline polymers crystallized from the bulk (i.e., from solution or from melt). The first report giving evidence of lamellar structures was by Storcks in 1938. He reported electron diffraction results on cast films of gutta-percha and concluded that the films contained microscopic crystals with the molecular axis less than 4% from normal to the plane of the film. He observed that while the electron diffraction results gave only reflections, the total length of the chains was much greater than the thickness of the films—a recognition that led him to first propose a chain-folded structure to explain the crystallization in such systems. Schlesinger and Leeper conducted similar experiments in 1953 on gutta-percha but this time using light microscopy and refractive index measurements.

Although both these studies were largely ignored, Jaccodine's report of single crystals of polyethylene in 1955 gained attention of several researchers who expanded on his work. In 1957, Till, Keller, and Fischer independently reported on the growth and identification of single crystals of polyethylene (Figure 3.8) (Prarthana and Vikrant, 2011).

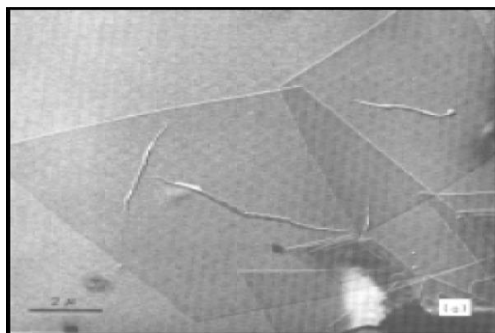


Figure 3.8 Single crystals of polyethylene after evaporation of tetrachloroethylene solvent. Pleats form due to crystal collapse.

Random Re-entry or "Switchboard" Folded Model: This model was first proposed by Flory, and consists of chains randomly folding back into the same lamella or even participating in adjoining lamellae (Figure 3.9) (Flory, 1985). The upper and lower surfaces consist of loops of varying sizes and the amount of adjacent reentry is small and not a necessity. The upper and lower surfaces may consist of transitional regions that constitute a diffuse phase boundary – their density being intermediate between the crystal and purely amorphous regions.

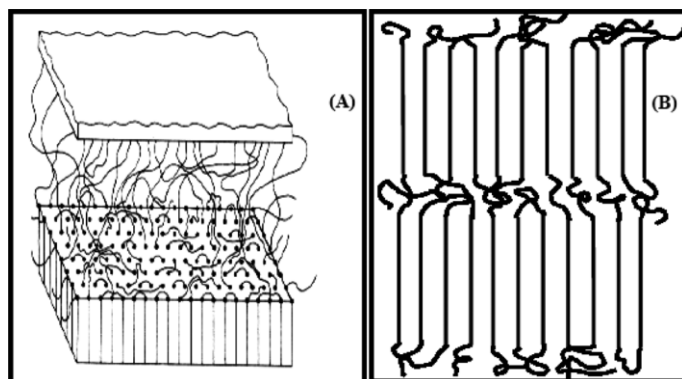


Figure 3.9 (A) Schematic of a Switchboard model, showing the surface of a lamella, interlamellar region and tie chains between the lamella. (B) originally proposed model for melt crystallization in polymers.

Adjacent Re-entry Chain-folded Models (Regular Folding):

(i) *Smooth surface model* (Hoffman and Lauritzen, 1961): This model is characterized by sharp phase boundary between the crystal and the amorphous phase. The mode of reentry of the chains is the adjacent neighbor with only a few exceptions due to multiple nucleation and chain-end defects. This is a very idealized visualization of the chain folding process (Figure 3.10 (i)).

(ii) *Rough surface model* (Hoffman and Lauritzen, 1961): The reentry of the chain is still in the nearest growth plane, though large variations in the fold length may exist on a local scale. Multiple nucleation and chain-end defects will further contribute to a rough surface. The overall phase boundary is no longer sharp, though local regions may still exhibit such character (Figure 3.10 (ii)).

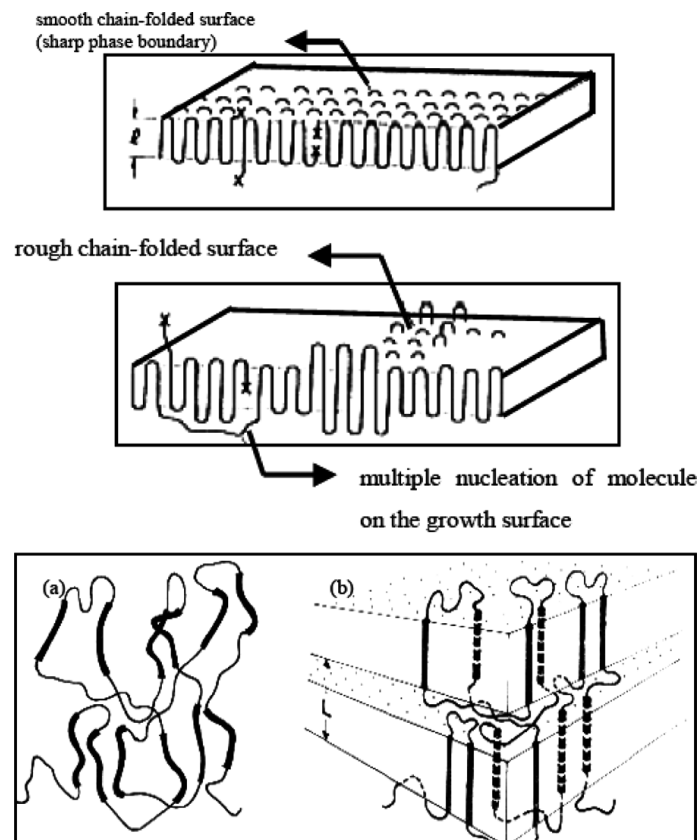


Figure 3.10 (i) Smooth surface model; (ii) Rough surface model; (iii) Erstarrungs model (solidification model): (a) chain conformation in the melt state; (b) alignment of suitable conformations into the crystal.

As the degree of crystallinity of a polymer affects its properties, accurately determining it is important. X-ray diffraction can be used to determine the degree of crystallinity of a sample. Thermal analysis techniques such as DSC can also be used. The two determinations may not necessarily be in agreement, and the reasons for this are complex.

Based on the diffraction pattern, the chain conformation, type and dimensions of crystal unit cell for different modifications can be well determined. Furthermore, the overlapping of reflections in these patterns hampers the determination of accurate unit cell dimensions and space group symmetry.

Unit cell of PCL was found to be orthorhombic with dimensions $a=7.496 \pm 0.002$, $b=4.974 \pm 0.001$, $c=17.297 \pm 0.023 \text{Å}$ (Bittiger and Marchessault, 1923).

Degree of crystallinity of the polymer is calculated from the ratio of the area of crystal peak to the total area of the peak of the XRD pattern. Figure 3.11 shows calculation of degree of crystallinity of PCL from XRD pattern by Gaussian function. The number 1 indicated that amorph phase whereas number 2, 3, and 4 crystal phase.

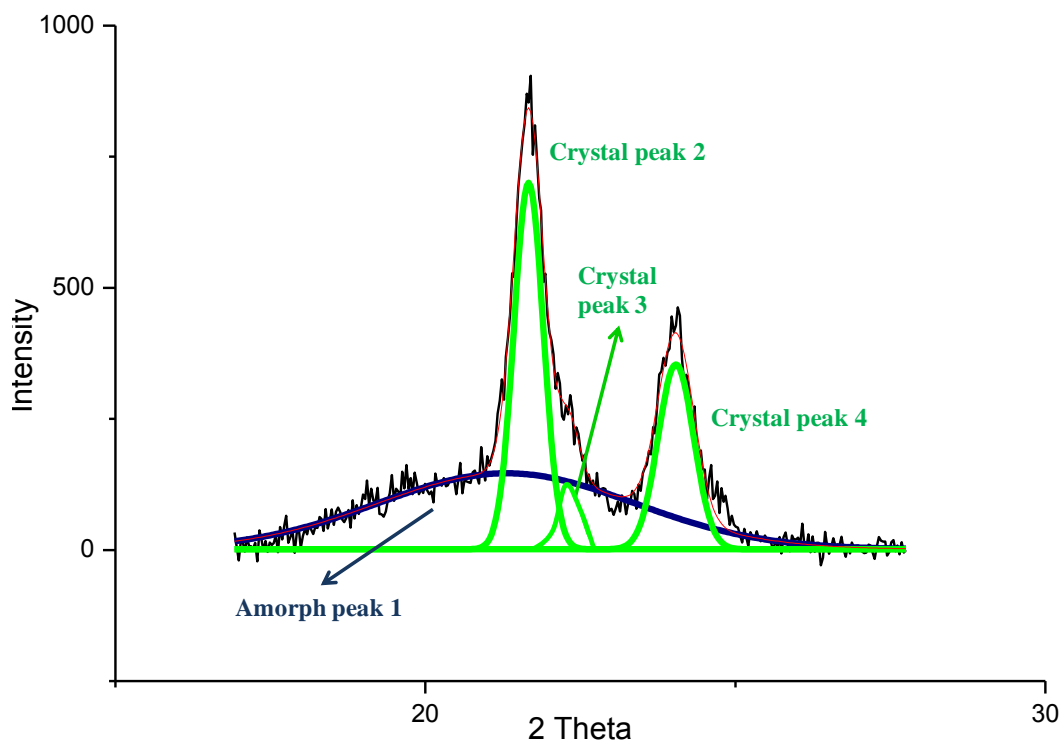


Figure 3.11 Calculation of degree of crystallinity of PCL from XRD pattern by Gaussian function.

Normally such materials have a high viscosity in the liquid state. When rapid cooling occurs to a temperature at which the crystalline state is expected to be the more stable, molecular movement is too sluggish or the geometry too awkward to take up a **crystalline** confirmation. Therefore the random arrangement characteristic of the liquid persists down to temperatures at which the viscosity is so high that the material is considered to be solid. The term glassy has come to be synonymous with a persistent non-equilibrium state. In fact, a path to the state of lowest energy might not be available. A melting process is illustrated in Figure 3.12 for a crystalline polymer which heated through its melting temperature. Besides, polymer crystallinity can be determined with DSC by quantifying the heat associated with melting (fusion) of the polymer. This heat is reported as **degree of crystallinity** by ratio against the heat of fusion for a 100% crystalline sample of the same material, or more commonly by ratio against a polymer of known crystallinity to obtain relative values.

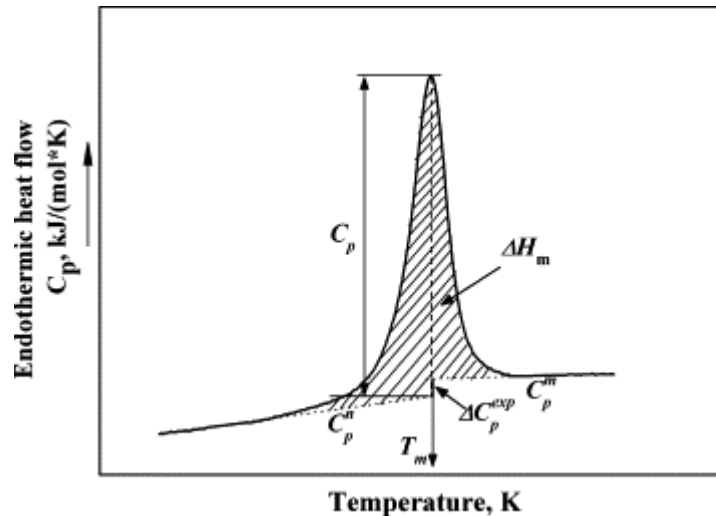


Figure 3.12 A melting process for the case of a highly crystalline polymer which is slowly heated through its melting temperature.

Crystal formation includes two stages, namely nucleation and crystal growth. However, although it is well established that nanometer sized clay platelets are effective nucleating agents, different effects have been reported on the linear growth rate and the overall crystallization rate, depending on the type of polymer (Mareaua, 2005).

As a semi-crystalline polymer, the final properties of PCL, such as mechanical properties and biodegradability, are strongly correlated with the extent of crystallization, crystalline morphology and crystalline texture. PCL crystallization rate is lower than that of conventional polymers and causes some trouble in injection

molding. It has been reported that when clay, multi-walled carbon nanotube, and hydroxyapatite were introduced into PCL to form nanocomposites, the crystallization rate of PCL was enhanced (Acierno et al., 2005).

For example, Maiti et al. found that although clay particles act as nucleating agents for the crystallization of a maleic anhydride grafted polypropylene (PP-MA) matrix, the linear growth rate and the overall crystallization rate are not significantly influenced by the presence of clay (Maiti et al., 2002).

Similarly, Di Maio et al. studied the isothermal crystallization of PCL/clay nanocomposites and noticed that the dispersed clay platelets act as nucleating agents in the PCL matrix, remarkably reducing the crystallization half time $t^{1/2}$. By DSC analysis after isothermal crystallization (Figure 3.13), the authors observed a reduction of the melting temperature with the increase of clay content, indicating a reduced degree of crystals perfection and degree of crystallinity. This was attributed to the confinement of chains and segments in the presence of clay, hindering the segmental rearrangement during crystallization and restricting the formation of perfect crystals in the polymer matrix (Di Maio et al., 2004).

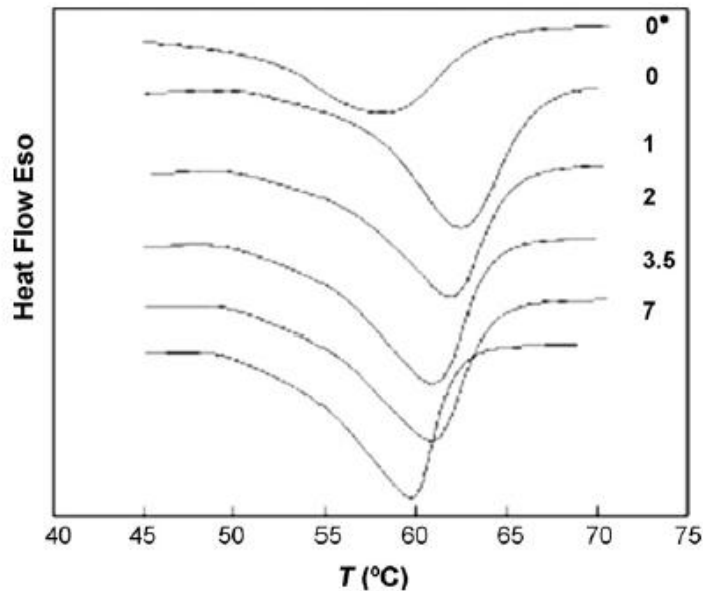


Figure 3.13 DSC thermograms of PCL and of selected PCL/clay nanocomposites after isothermal crystallization at 45 °C. Number refers to clay weight concentration; 0* is the DSC thermogram of nonisothermal crystallized (-10 °C/min) pure PCL (Di Maio et al., 2004).

Ke and Yongping conducted DSC analysis on intercalated PET/o-MMT nanocomposites. They found a reduction of T_g in the composite compared to the pure matrix, which they attributed to the plasticizing effect of organomodified MMT (o-MMT). However, they noticed that by increasing the o-MMT content the T_g is increased, as shown in Figure 3.14. Further, they observed that the cold crystallizing point of pure PET is 150 °C, while for the nanocomposite it decreases to 130 °C. This result shows that adding o-MMT into polyethylene terephthalate (PET) is favorable to its crystallization (Ke and Yongping, 2005).

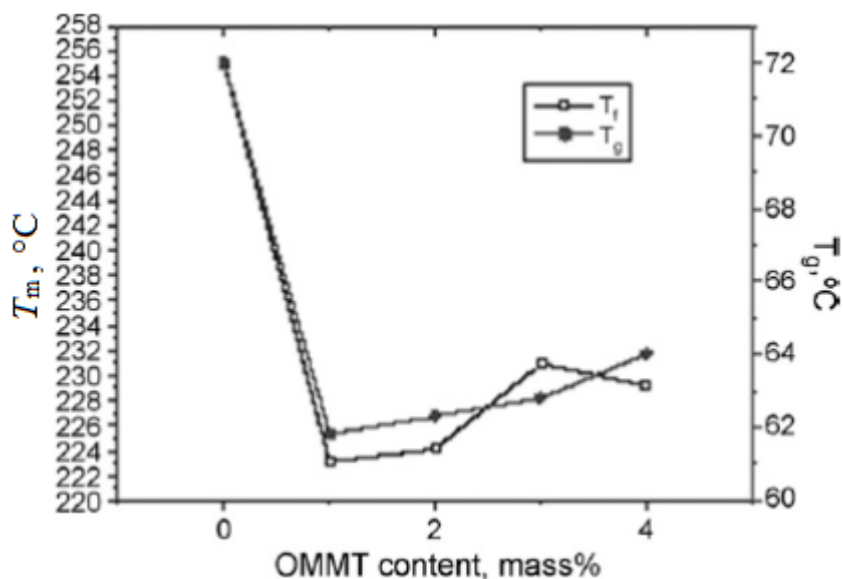


Figure 3.14 The relationship between o-MMT content and T_g of composite (Ke and Yongping, 2005).

Crystallization behavior of PCL/montmorillonite (MMT) was investigated (Homminga et al., 2006). The combination of surfactant modified MMT silicate layers, poly(ϵ -caprolactone) (PCL) and the adopted melt processing procedure result in intercalated nanocomposites in which the silicate layers act as nucleating agents for the crystallization of the PCL matrix and by which in turn the overall crystallization rate increases.

When the silica content was above 5 wt.%, the molecular weight of the polymer in the hybrids decreased, and the increase in the crystallisation rates was attributed to both the nucleating effect of the nanoparticles and the lower molecular weight. Also for the nanocomposites, spherulites appear at higher temperatures compared to pure PCL during cooling from the melt at a constant cooling rate. The activation energy was found to decrease upon increasing the filler content, showing that the crystallisation is favoured (Figure 3.15) (Vassiliou et al., 2007).

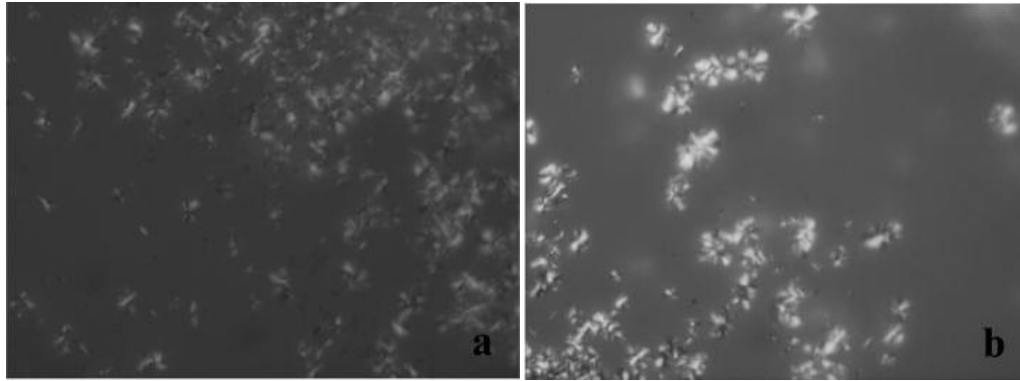


Figure 3.15 POM photographs taken during cooling by $1\text{ }^{\circ}\text{C}\cdot\text{min}^{-1}$ for (a) pure PCL and (b) PCL/SiO₂ 2.5 wt.% nanocomposite.

Isothermal crystallization behavior and crystalline structure of PCL/multiwalled carbon nanotube (MWNT) composites were investigated (Wu et al., 2009). PCL/MWNT composites were prepared via the mixing of a PCL polymer solution with carboxylic groups containing multiwalled carbon nanotubes (c-MWNTs). Optical microscopy was carried out with an optical microscope equipped with a hot stage and crossed polarizers. Polarized optical microscope (POM) micrographs of PCL and PCL/c-MWNT composites after melting at 90°C and then quenching to T_c (46°C) is shown in Figure 3.16. The addition of c-MWNTs to PCL induces heterogeneous nucleation at lower c-MWNT contents and then reduces the transportation ability of polymer chains during crystallization processes at higher MWNT contents.

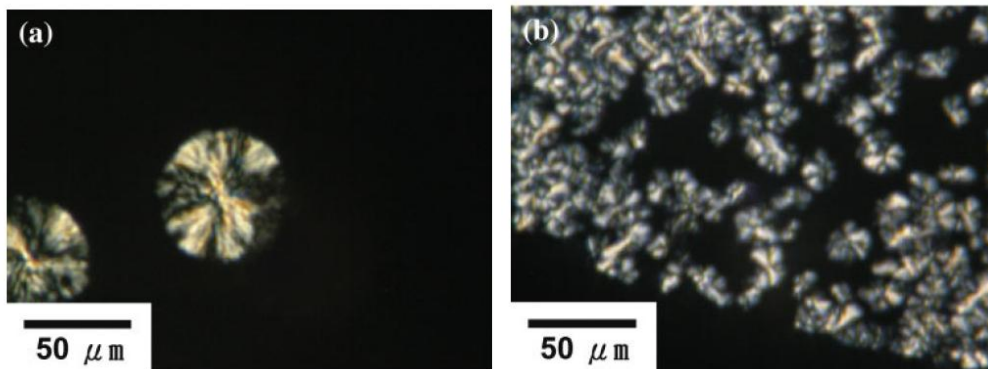


Figure 3.16 POM images of (a) PCL and (b) 0.5 wt % PCL/c-MWNT composites after melting at $T_{\text{max}} = 90\text{ }^{\circ}\text{C}$ and then quenching to $T_c = 46\text{ }^{\circ}\text{C}$.

Crystallization of PCL with organomodified MMT was researched by POM (Wu et al., 2009). The composite films were prepared with solvent casting method. The composite films were melted at 150°C and cooled to the room temperature and the results shown in Figure 3.17. The spherulites became gradually smaller with increasing the Na⁺-MMT content. The spherulites for PCL with 4% clay finally were converted into lamellar crystals, which confirms the nucleating effect of Na⁺-MMT on PCL.

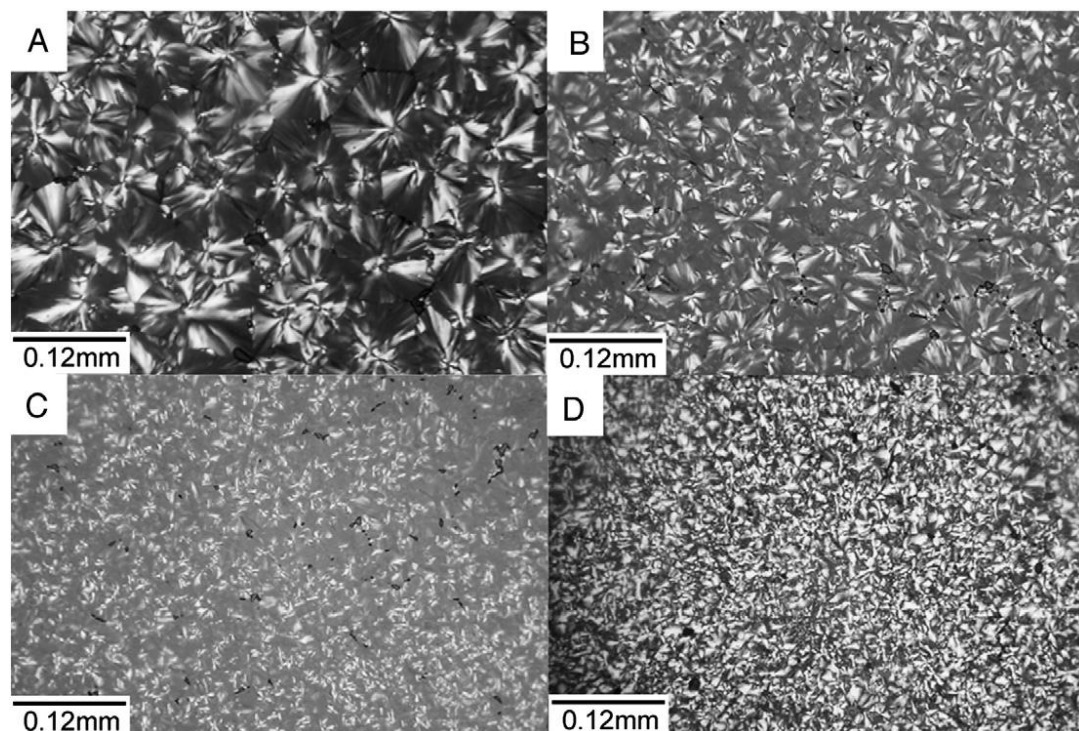


Figure 3.17 Polarizing microscope images of (A) neat PCL; (B) PCL with 1 wt% clay; (C) PCL with 2 wt% clay and (D) PCL with 4 wt% clay.

3.3. Crystallization Kinetics Models

There are several methods for studying crystallization kinetics of polymers, which fall into two general categories: bulk or volumetric analysis, and crystal growth analysis.

The physical and mechanical properties of crystalline polymers depend on the morphology, the crystals structure and on the degree of crystallinity behavior and the crystalline morphology of composites are affected by the presence of the additives (Chen et al., 1997; Di Maio et al., 2004; Durmus and Yalçınyuva, 2008; Homminga et al., 2006; Liu et al., 2010; Perez and Alvarez, 2009; Skoglund and Fransson, 1996). Researchers strongly remarked that at very low levels of inorganic additives such as clay, hydroxyapatite, starch etc., the crystallization kinetics of the nanocomposites were dramatically increased, with respect to extruded pure material. This behavior is commonly observed in particulate filled polymers. At low filler concentration, the filler polymer interfaces act as heterogeneous nucleating agent. The crystallization kinetics at higher filler content, diffusion of polymer chains to the growing crystallites is blocked and the overall crystallization rate is reduced by increasing the nucleation rate.

The formation of three-dimensional crystal structure from a disordered state begins with nucleation and involves the creation of a stable nucleus from the disordered polymer melt or solution. Depending on whether any second phase, such as a foreign particle or surface from another polymer, is present in the system, the nucleation is classified as homogenous nucleation (primary nucleation) or heterogeneous nucleation (secondary nucleation). In primary nucleation, creation of the stable nucleus by intermolecular forces orders the chains in a parallel array. As the temperature goes below the melting temperature T_m , the molecules tend to move toward their lowest energy conformation, a stiffer chain segment, and this will favor the formation of ordered chains and thus nuclei. Facilitating the formation of stable nuclei, secondary nucleation is also involved at the beginning of crystallization through heterogeneous nucleation agents, such as dust particles. In this section, studies on polymer crystallization kinetics have been classified as primary nucleation kinetics and secondary nucleation kinetics. The primary nucleation kinetics for isothermal conditions was investigated with Avrami model and secondary nucleation kinetics with the Lauritzen Hoffman model, for nonisothermal conditions with Avrami Jeziorny, Ozawa, and Liu Mo models and secondary nucleation kinetics with the Lauritzen Hoffman model.

3.3.1. Primary nucleation kinetics models

Primary crystallization kinetics are evaluated under isothermal with Avrami model and nonisothermal conditions with Avrami Jeziorny, Ozawa and Liu-Mo models.

3.3.1.1. Avrami model for isothermal crystallization

Kolmogoroff was the first to describe the consequences of nucleation and growth for the space covering by the formation of spherulites (Janeschitz, 2010). Later Avrami and Evans independently developed their theories, which meanwhile turned out to be essentially identical with Kolmogoroff's theory. Also Tobin developed a theory, which he considered as an improvement of Avrami's theory. Based on work of Avrami, the original derivations were simplified by Evans and rearranged for polymer crystallization by Meares and Hay. For the bulk crystallization of polymers, the crystallization kinetics can be represented as equation 3.12;

$$1 - X = e^{-V_t} \quad 3.12$$

where X is the degree of crystallinity and V_t is the volume of crystallization material, which should be determined by considering the following two cases: (a) the nuclei are predetermined, that is, they all develop at once on cooling the polymer, and (b) the crystals nucleate sporadically. For a spherical crystal in case (a);

$$dV_t = 4\pi r^2 L dr \quad 3.13$$

where r represents the radius of the spherical crystal at time t and L is the number of nuclei. Assuming the radius r grows linearly with time, and $r = \kappa t$. Integration of Eq. 3.13 and substitution into Eq. 3.12, one obtains;

$$1 - X = e^{-Kt^3} \quad 3.14$$

where K is the growth rate and equal to;

$$K = \left(\frac{4}{3}\right) \pi \kappa^3 L \quad 3.15$$

For sporadic nucleation, case (b), the argument is above followed, but the number of spherical nuclei is allowed to increase linearly with time at rate u . Then nucleation from time t_i to time t will create a volume increase of;

$$dV_i = \left(\frac{4}{3}\right)\pi\kappa^3(t-t_i)^3 u dt_i \quad 3.16$$

Integration of Eq. 3.16 between $t_i=0$ and t , and substitution into Eq. 3.12, one obtains;

$$1 - X = e^{-Kt^4} \quad 3.17$$

Where K is equal to;

$$K = \left(\frac{1}{3}\right)\pi\kappa^3 u \quad 3.18$$

The equations can be generalized by replacing the power of t with the Avrami exponent n ,

$$1 - X = e^{-Kt^n} \quad 3.19a$$

$$\ln[-\ln(1 - X(t))] = \ln K + n \ln t \quad 3.19b$$

The Avrami exponent n depends not only on the structure of the crystal but also on the nature of nucleation. It was assumed that the nucleation at the growth surface of the growing discs or spheres was the only governing factor in maintaining the growth rate G . In many instances, transport factors become rate determining in controlling the rate of growth. These kinds of problems involve a moving interface across which the transport phenomenon needs to be considered. Utilization of isothermal crystallization data by DSC measurements is shown in Figure Figure 3.18 and characteristic Avrami plot obtained from DSC measurement is shown in Figure Figure 3.19 (Rattaa et al., 2000).

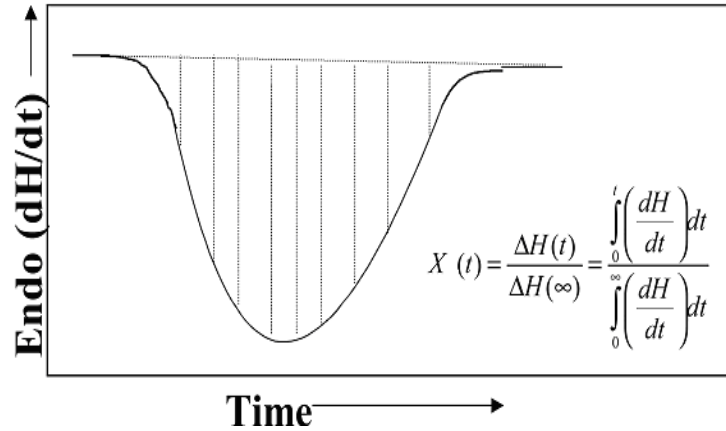


Figure 3.18 Utilization of isothermal crystallization data by DSC measurements (Rattaa et al., 2000).

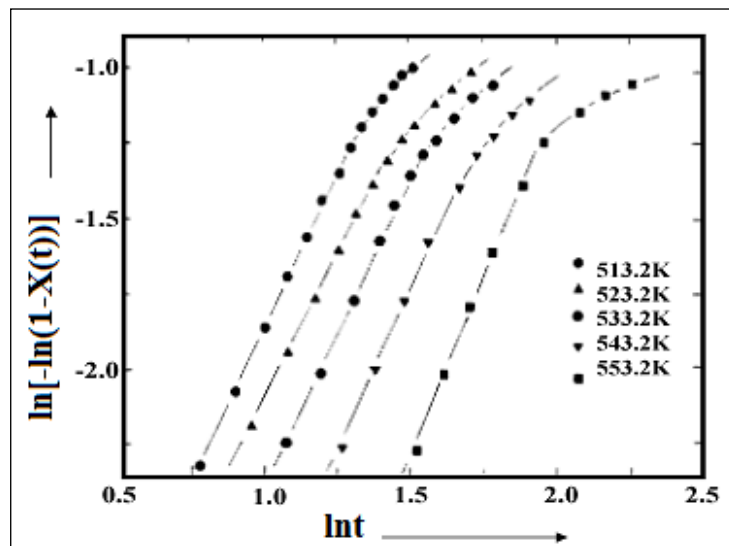


Figure 3.19 The characteristic Avrami plots obtained by isothermal crystallization experiments for a polyamide (Rattaa et al., 2000).

For isothermal crystallization, only two cases are of importance, namely the case, where the nuclei are there from the beginning, and the case, where the nucleation rate is constant and finite. In the first case one has a fixed number density of **athermal** nuclei or of heterogeneous nuclei, the latter being introduced by nucleation agents or impurities. In the second case the melt is clean, and sporadic nucleation of **thermal** nuclei is occurring. The critical point in both cases is the choice of time zero. In fact, the melt, which is originally kept at a temperature well above the equilibrium melting point, must be quenched fast enough to the temperature, where the crystallization is intended to happen. The time interval needed for the quench must be very short compared with the time required for the

crystallization process proper. Only under this condition time zero can readily be chosen within the time interval needed for the quench. In the case of sporadic nucleation the rate of formation of nuclei can be kept constant as long as the temperature is constant. In fact, this nucleation process occurs in the still uncovered volume of the sample (Hiemenz, 1984). The various Avrami exponents associated with different nucleation types and crystal geometry's are given in Table 3.1.

Table 3.1 Avrami exponents for various types of crystal growth geometry's (Rattaa et al., 2000).

Avrami Exponent	Crystal Geometry	Nucleation Type	Rate Determination Step
0.5	Rod	Athermal	Diffusion
1	Rod	Athermal	Nucleation
1.5	Rod	Thermal	Diffusion
2	Rod	Thermal	Nucleation
1	Disc	Athermal	Diffusion
2	Disc	Athermal	Nucleation
2	Disc	Thermal	Diffusion
3	Disc	Thermal	Nucleation
1.5	Sphere	Athermal	Diffusion
2.5	Sphere	Thermal	Diffusion
3	Sphere	Athermal	Nucleation
4	Sphere	Thermal	Nucleation

3.3.1.2. Avrami Jeziorny model for nonisothermal crystallization

The kinetics of nonisothermal crystallization are interpreted using the relative crystallinity as a function of temperature, $X(T)$, defined as

$$X(T) = \frac{\int_{T_0}^T \left(\frac{dH}{dT} \right) dT}{\int_{T_0}^{T_e} \left(\frac{dH}{dT} \right) dT} \quad 3.20$$

where H is the heat flow, is calculated for the nonisothermal DSC experiments. In the nonisothermal experiments described here the temperature is directly proportional to the cooling time ($t=(T_0-T)/\phi$) and an equivalent time dependent degree of crystallinity, $X(t)$. Based on the assumption that the crystallization temperature, T_c , is constant, the Avrami relation between the degree of crystallinity and the crystallization time was adapted to describe the nonisothermal crystallization by Mandelken;

$$X_c(t) = 1 - \exp[-Z_t \times t^n] \quad 3.21$$

$$\ln[-\ln(1 - X_c(t))] = n \times \ln t + Z_t \quad 3.22$$

where $X(t)$ is relative crystallinity, Z_t is the rate parameter in the nonisothermal crystallization process. In order to eliminate the effect of the cooling or heating rate $\phi = dT/dt$, the rate parameter characteristic of the kinetics of nonisothermal crystallization was modified by Jeziorny:

$$\log Z_c = \frac{\log Z_t}{\phi} \quad 3.23$$

With drawing the plot of $\ln[-\ln(1-X_c(t))]$ versus $\ln t$, the values of n and Z_t were determined from the slopes and intercepts, respectively. The parameter of Avrami exponent n describes the growing mechanism and geometry of crystallization, and the parameter Z_c describes the growth rate under the nonisothermal crystallization process.

3.3.1.3. Ozawa model for nonisothermal crystallization

The most used kinetics approach for nonisothermal crystallization process of semi crystalline polymers is Ozawa model. The Avrami model requires that crystallization occurs at quench cooling and constant temperature and that the nuclei grow as spherulites. From these assumptions, Ozawa deduced the following expression for the untransformed material fraction. It is based on the extended form of Avrami approximation assuming that the nonisothermal crystallization process could be composed of small isothermal steps. Ozawa equation is as follows:

$$X_c(t) = 1 - \exp\left(\frac{K(T)}{\phi^m}\right) \quad 3.24$$

$$\ln[-\ln(1 - X_c(t))] = \ln K(T) - m \times \ln \phi \quad 3.25$$

here, $X_c(t)$ is the relative crystallinity, $K(T)$ is the cooling crystallization function, which is a complicated function of nucleation and growth rates, ϕ is the absolute value of the cooling rate and m is the Ozawa exponent.

3.3.1.4. Lui Mo model for comparison of isothermal and nonisothermal crystallization

Another method developed by Liu and coworkers was also used to describe the nonisothermal melt-crystallization process. Liu and coworkers offered a new method combining the Avrami and Ozawa equations at a given value of $X(t)$ as follows:

$$\ln K(T) - m \times \ln \phi = \ln Z_t - n \times \ln t \quad 3.26$$

$$\ln \phi = \ln F(T) - \alpha \times \ln t \quad 3.27$$

where $F(T)=[K(T)/Z_t]^{1/m}$ refers to the value of the cooling rate, which has to be chosen at the unit crystallization time when the measured system amounts to a certain relative crystallinity; $K(T)$ is the crystallization rate parameter, and α is the ratio of the Avrami exponent n to the Ozawa exponent m ; that is, $\alpha = n/m$. It could be seen that $F(T)$ had a definite physical and practical meaning which means that high cooling rate is needed to reach this $X_c(t)$ in a unit time, which also indicates the difficulty in crystallization process. At a given degree of crystallinity, from the plots of $\ln \phi$ versus $\ln t$, the values of α and $F(T)$ could be obtained by the slopes and intercepts, respectively.

3.3.2. Secondary nucleation kinetics model: Lauritzen Hoffman

In reality, polymer crystallization is too complex to be described by a simple expression such as the Avrami equation. For example, the assumption in Avrami's expression that the volume does not change is inaccurate because the specimen tends to shrink during crystallization. In addition, secondary crystallization and crystal perfecting processes are not taken into account. There have been many attempts to develop theories to explain the important aspects of crystallization (Mark, 2007). The most widely accepted approach to the analysis of the linear crystal growth rates is the kinetic description due to Lauritzen and Hoffman.

Figure 3.20 and Figure 3.21 shows the Lauritzen–Hoffman theory analyzes the growth data according to competition between the rate of deposition of secondary nuclei (i) and the rate of lateral surface spreading (g), resulting in three different regimes. Regime I occurs when $i \ll g$ and may be found at very low supercoolings; in regime II, i is the order of g and occurs at moderate supercoolings; in regime III, $i > g$ and is found at very high supercoolings. Regime behavior varies from polymer to polymer. For example cis-polyisoprene shows all regimes (Mark, 2007). Also the regimes depend on the conditions of crystallization.

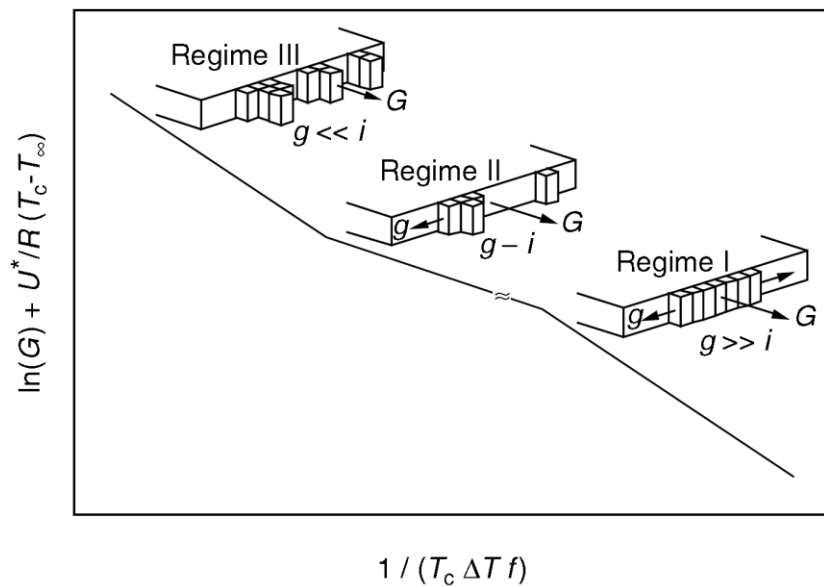


Figure 3.20 Schematic of regime analysis (Mark, 2007).

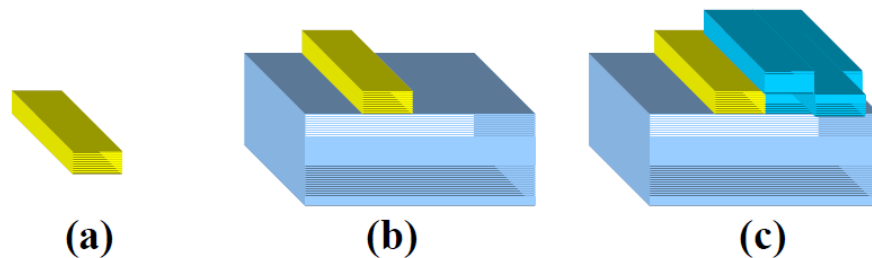


Figure 3.21 Types of Crystal Nuclei (a) Primary nucleus (b) Secondary Nucleus (c) Tertiary Nucleus.

The general expression of crystal growth as described by Lauritzen and Hoffman is:

$$G = G_0 \exp\left(-\frac{U^*}{R(T_c - T_\infty)}\right) \exp\left(-\frac{K_g}{T_c \Delta T f}\right) \quad 3.28$$

where G is the growth rate, G_0 is the growth rate constant; U^* is the activation energy for polymer diffusion; R is the gas constant; T_c is the crystallization temperature (K), $T_\infty = T_g - 30$ (K); ΔT =supercooling, $\Delta T = (T_m^0 - T_c)$; f =correction factor, $f = \frac{2T_c}{T_c + T_m^0}$; K_g is the nucleation rate constant given by;

$$K_g = \frac{j b_0 \sigma \sigma_e T_m^0}{k \Delta h_f} \quad 3.29$$

where b_0 is the width of the chain, σ is the lateral surface free energy, σ_e is the fold surface free energy, T_m^0 is the equilibrium melting temperature (K), k is the Boltzmann constant, and Δh_f is the heat of fusion. The parameter j is determined by the operating regime and is equal to 4 for regime I and III, and equal to 2 for regime II.

Theoretical values of n and K for different morphologies and nucleation mechanisms are tabulated in Table 3.2.

Table 3.2 Theoretical values of n and K for different morphologies and nucleation mechanisms (Mark, 2007).

Crystal growth shape	Nucleation mode	Avrami exponent (n)	Avrami rate constant (K) ^a
Rod	Heterogeneous ^b	1	$\dot{N}GA$
	Homogeneous ^c	2	$\dot{N}GA/2$
Disc	Heterogeneous	2	$\pi \dot{N}G^2 D$
	Homogeneous	3	$(\pi/3) \dot{N}G^3 D$
Sphere	Heterogeneous	3	$(4\pi/3) \dot{N}G^3$
	Homogeneous	4	$(\pi/3) \dot{N}G^3$
Sheaf	Heterogeneous	5	-
	Homogeneous	6	-

^a A is cross-sectional area of the rod; D is thickness of the disc; G is linear growth rate; N is nucleation density; and \dot{N} is nucleation rate.

^bHeterogeneous means that the nucleation density is constant.

^cHomogeneous, also named sporadic, means that the rate of nucleation is constant.

3.4. Effective Activation Energy of Crystallization

Several mathematical models have been proposed to calculate the activation energy of the crystallization process. In this study, the Kissinger and Augis–Bennett models were used. Figure 3.22 shows schematically a theoretical dependence of E_A on temperature. This dependence illustrates well the non-Arrhenius behavior that is reflected in the temperature dependence of E_A . The temperature, in its turn, determines the relative contributions of these processes to the growth rate and, therefore, the value of E . We call this value the effective activation energy to differentiate it from the true activation energy that represents the height of the energy barrier. As seen from Figure 3.22, the effective activation energy decreases with increasing the temperature of crystallization. There are two major temperature regions in this graph. In the melt crystallization region, the measurements are performed by cooling a polymer from above T_m . The rate of crystallization decreases with increasing temperature giving rise to negative values of E_A . The growth rate is predominantly determined by the nucleation rate in that region. The cold crystallization region is typically accessed by heating glassy polymers. The respective values of E_A are positive as the rate of crystallization increases with increasing temperature. In this region the growth rate is mostly determined by mass transport. The two regions are separated by the temperature of the maximum growth rate, T_{max} at which the value of E_A approaches zero. By performing crystallization in different temperature regions one can obtain practically any value of E from large positive to large negative numbers that clearly suggests that E_A is not an energy barrier of crystallization. (Vyazovkin and Dranca, 2006).

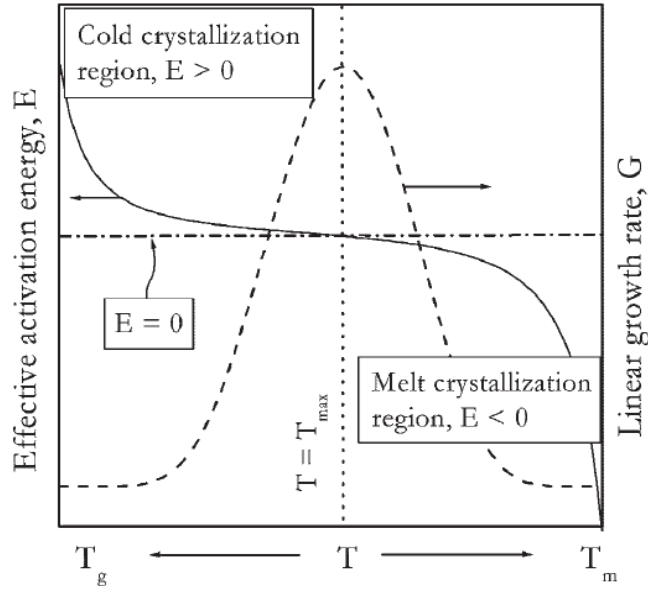


Figure 3.22 Schematic presentation of the temperature dependencies for the growth rate (dash line) and the effective activation energy (solid line). The E_A value turns negative when crystallization occurs at temperatures above T_{\max} (Vyazovkin and Dranca, 2006).

These models are based on the finite relationship between the peak temperatures T_c obtained from the nonisothermal crystallization exotherms and the heating/cooling rates.

Kissinger (Eq. 3.30) and Augis–Bennett (Eq. 3.31) equations can be described as follows:

$$\frac{d \left[\ln \left(\frac{\phi}{T_c^2} \right) \right]}{d \left[\frac{1}{T_c} \right]} = - \frac{\Delta E_A}{R} \quad 3.30$$

$$\frac{d \left[\ln \left(\frac{\phi}{T_0 - T_c} \right) \right]}{d \left[\frac{1}{T_c} \right]} = - \frac{\Delta E_A}{R} \quad 3.31$$

where ϕ is the cooling rate ($^{\circ}\text{C}/\text{min}$), T_c is the crystallization peak temperature ($^{\circ}\text{C}$), T_0 is the initial room temperature, ΔE_A is the activation energy of crystallization

process (kJ/mol), and R is the universal gas constant (8.314 kJ/mol K). When the parameter $\ln(\phi/T_c^2)$ or $\ln[\phi/(T_o-T_c)]$ is plotted against $1/T_c$, the slope of the curve gives the activation energy of the crystallization process. ΔE_A is negative because of exothermic nature of the transition from melt to crystalline state, and the negative activation energy values also imply that crystallization mechanisms are accelerated by decreasing the temperature.

4. EXPERIMENTAL

4.1. Materials

Polycaprolactone (**PCL**) (Aldrich; Mn:70000-90000) and dichloromethane (**DCM**) (Merck) were used for the preparation of the polymeric films. Organomodified Montmorillonite (OMMT) (Aldrich; clay surface modified with 25-30 wt. % methyl dihydroxyethyl hydrogenated tallow ammonium) and oleic acid (Riedel), and glyceryl monooleate (GMO) (Kimsan A.Ş) were used as additives for controlling the crystallization of PCL.

4.2. Method

4.2.1. PCL polymeric composite film preparation by solvent casting

PCL (4.2 g) was dissolved in 70 cm³ of DCM at room temperature and mixed by a magnetic stirrer. Then, OMMT and oleic acid (OA) or GMO were added into PCL solution with different concentrations and mixed further for 2 hours. In order to obtain the composite film, 10 mL of the mixture was poured into a petri dish with 10 cm diameter and it was waited for 12 hours in a hood to evaporate the solvent from the film as closed lids. After solvent was evaporated, PCL based composite film was obtained. Series of composite films were prepared by solvent casting to examine on the the product properties, crystallization and bidegradation the effects of OMMT, oleic acid, and GMO. All prepared samples and their codes were listed in Table 4.1.

The sample codes have this structure;

PCL_Inorganic Additive wt%_Organic Additive wt%

Therefore, PCL_IA0_OA0 shows the neat PCL for no inorganic and organic additives. Clay will be used as the inorganic additive and code C will be used for clay, as organic additives, Oleic acid as O or glyceril monooleate as G will be used in the composite codes. Therefore, PCL_C0.1_O3 is the composite with 0.1 wt% organomodified clay and 3 wt% oleic acid.

Table 4.1 Contents of composite films prepared with clay, oleic acid and GMO.

		Clay wt% (C)	Samples				Clay wt% (C)	Samples	
Oleic Acid (O)/ Glycerol monooleate (G) wt%	0	0	PCL_IA0_OA0		Oleic Acid (O)/ Glycerol monooleate (GMO) wt%	3	0	PCL_IA0_O3	PCL_IA0_G3
		0.1	PCL_C0.1_OA0				0.1	PCL_C0.1_O3	PCL_C0.1_G3
		0.4	PCL_C0.4_OA0				0.4	PCL_C0.4_O3	PCL_C0.4_G3
		1	PCL_C1_OA0				1	PCL_C1_O3	PCL_C1_G3
		3	PCL_C3_OA0				3	PCL_C3_O3	PCL_C3_G3
	1	0	PCL_IA0_O1	PCL_IA0_G1		5	0	PCL_IA0_O5	PCL_IA0_G5
		0.1	PCL_C0.1_O1	PCL_C0.1_G1			0.1	PCL_C0.1_O5	PCL_C0.1_G5
		0.4	PCL_C0.4_O1	PCL_C0.4_G1			0.4	PCL_C0.4_O5	PCL_C0.4_G5
		1	PCL_C1_O1	PCL_C1_G1			1	PCL_C1_O5	PCL_C1_G5
		3	PCL_C3_O1	PCL_C3_G1			3	PCL_C3_O5	PCL_C3_G5

4.2.2. DSC analysis

Crystallization kinetics, degree of crystallinity and melting point of PCL composite films were investigated by DSC. Isothermal crystallization were investigated all for prepared films whereas nonisothermal crystallization was only examined for some samples as PCL_IA0_OA0, PCL_IA0_O3, PCL_IA0_G3, PCL_C0.1_OA0, PCL_C0.1_O3, PCL_C0.1_G3, PCL_C0.1_O5, PCL_C3_OA0 and PCL_C3_O5.

4.2.2.1. Isothermal crystallization kinetics

Isothermal crystallization experiments were performed by DSC (TA instrument Q10). For DSC analysis, 6 mg samples were loaded on covered aluminum pan with nitrogen atmosphere (40mL/min), firstly heated with 10°C/min rate from room temperature to 100°C then waited for 10 minutes to delete the thermal memory. After that it was rapidly cooled to 40°C with liquid nitrogen (50°C/min as the cooling rate) and waited for 60 minutes at that temperature to observe the isothermal crystallization. After, the sample was cooled to 20°C with 10°C/min cooling rate, then heated again to 100°C with 10°C/min heating rate. The temperature profile followed for isothermal crystallization is given in Figure 4.1. Crystallization kinetics parameters were obtained from the isothermal crystallization peak area at 40°C by Avrami model.

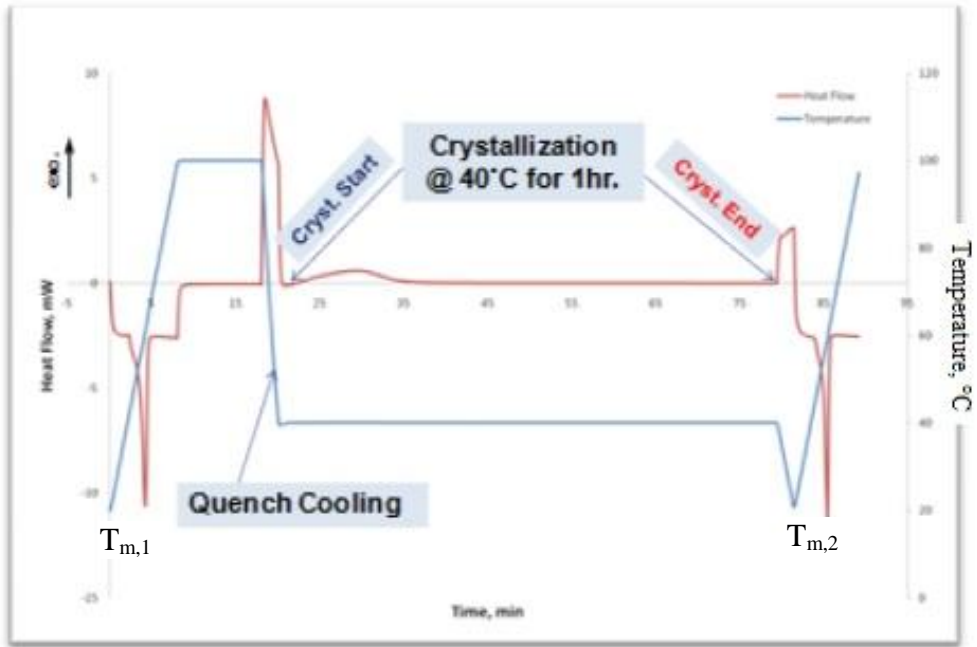


Figure 4.1 Temperature profile for isothermal crystallization experiments.

4.2.2.2. Nonisothermal crystallization kinetics

In order to investigate the effect of cooling rate on molten polymer crystallization, nonisothermal crystallization experiments were performed by SII Nanotechnology, ExStar DSC 6200. Samples of 6 mg were loaded on to covered aluminum pan with nitrogen atmosphere (50mL/min), firstly heated a 10°C/min rate from room temperature to 100°C, then waited for 5 minutes to delete the thermal memory. After that it was cooled with liquid nitrogen to 0°C at 2 and 5 °C/min cooling rates, -20°C at 10 and 20°C/min cooling rates and waited for 5 minutes, and then again heated to 100°C at 10°C/min heating rate. Samples were melted for the second time is to simulate the industrial extrusion process. Dynamic crystallization temperature profiles of polymeric composite films with different cooling rates are given in Figure 4.2.

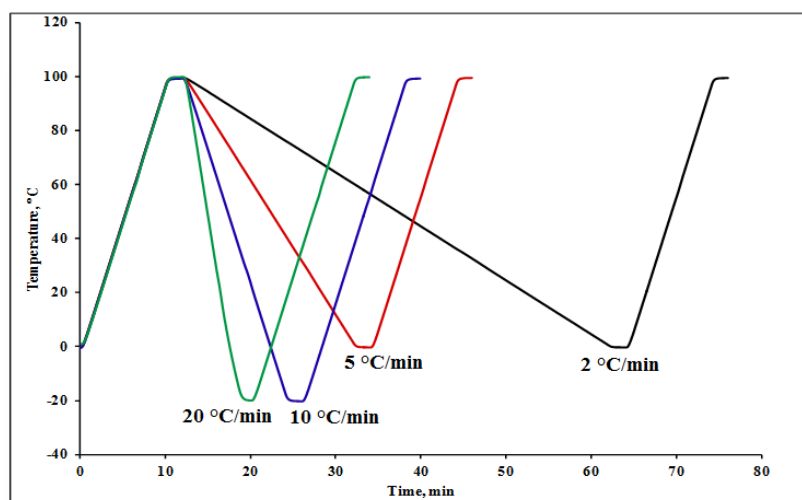


Figure 4.2 Temperature profiles for nonisothermal crystallization experiments.

4.2.3. Investigation of crystallization kinetics by a polarized optical microscope

Optical microscopy studies were carried out to obtain the spherulitic growth rate of PCL composite films. Spherulitic growth was analyzed by an optical microscopy with polarized light in reflected mode. Optical microscope (Olympus BX51/52-P) with a hot stage (Instec - Linkam THMS600) was used for the test. Samples were analyzed with different cooling rates. All samples were heated to 100 - 110 °C with 10 °C/min heating rate and held for 5 min. Melted composite films were cooled with 2, 5, 10 and 20 °C/min cooling rates to 0 °C. The second melting was carried out with 10 °C/min to heating rate 100 - 110 °C. Pictures of the spherulites were taken at several times with 200 times magnification.

4.2.4. Product properties

Product properties were investigated as physical, structural, and mechanical properties.

The density of the prepared biocomposite films was measured by a precision balance with Archimedes kit (Sartorius) and theoretically calculated. This application determines the density of solid substances using the buoyancy method. Composite films were cut as rectangle with 2x2 cm², then weighed as dry and wet. The temperature of the water was measured and recorded to find its density at that temperature. Density of the composite films was calculated by equation 4.1:

$$\rho_{experimental} = \frac{W_a \rho_{fl}}{0.99983G} + 0.0012 \quad 4.1$$

where w_a is the dry weight of the sample, ρ_{fl} density of water at measured temperature, G is the buoyancy of water obtained from Archimedes kit.

Theoretical density values of the composite films were calculated by equation 4.2.

$$\frac{1}{\rho_{theoretical}} = \sum \frac{x_i}{\rho_i} \quad 4.2$$

where x_i is the weight fraction of the pure substance, ρ_i is the density of the same substance.

Surface tension of the composite films was obtained from contact angle measurement by using Attension Theta Optical Tensiometer (Figure 4.3), KSV Instruments. Casting composite films were cut 1x5 cm² size for measurements. Droplet was 6 micro liters for each sample. Each test was repeated for 10 times and mean values and standart deviations are calculated. Contact angle value of the samples was obtained by its software. The average of the left and right angle summation was given as the contact angle of the sample.

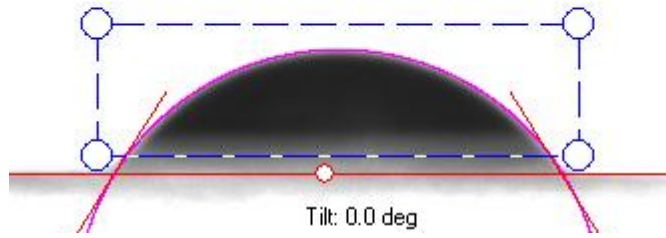


Figure 4.3 Water drop for contact angle measurement.

Surface morphology of the composite films was examined by scanning electron microscope (SEM-Philips XL30 SFEG). The samples were coated with gold for 30 seconds, then photographs were taken in various magnifications.

Functional groups of composite films were determined by Fourier Transform Infrared (FTIR-SHIMADZU FTIR-8400S) spectroscopy. Analysis was carried out in the wave number range from 4000 to 400 cm^{-1} at a resolution of 4 cm^{-1} using this spectrophotometer at room temperature.

Crystal structure of the composite films was identified by X-ray diffractometer (Philips Xpert-Pro) employing Ni-filtered Cu $K\alpha$ radiation, at a scanning rate of 6° min^{-1} with 2θ ranging from 10° to 60° to determine the crystal structure of the samples. Crystal thickness of PCL composite films was calculated from Debye Scherrer equation (equation 4.3)

$$t = \frac{\kappa\lambda}{B\cos\theta_B} \quad 4.3$$

Here K is a dimensionless constant that may range from 0.89 to 1.39 depending on the specific geometry of the scattering objects. For a perfect two-dimensional lattice, where every point on the lattice emits a spherical wave, numerical calculations yield the lower bound of 0.89 for K . A cubic three-dimensional crystal is best described by $K = 0.94$, while analytical calculations for a perfectly spherical object yield $K = 1.33$. It was taken as 0.9 in this study for calculation of crystal thickness from X-ray analysis of PCL composite films.

From X-ray diffraction pattern, calculation for d-spacing (also called interplanar spacing or lattice plane spacing), d_{hkl} , is simple in the case of crystals with orthogonal axes. Figure 4.4 shows the first plane away from the origin in a family of (hkl) planes. Unit cell of PCL was found to be orthorhombic with dimensions $d=7.496 \pm 0.002$, $b=4.974 \pm 0.001$, $c=17.297 \pm 0.023\text{\AA}$ by Bittiger and Marchessault (1923). For orthorhombic unit cell, d_{hkl} was calculated from equation 4.4 (Hammond, 2009). Calculation of d-spacing of PCL films h,k,l values were taken as 1.

$$d_{hkl} = \frac{1}{\sqrt{\left(\frac{h}{a}\right)^2 + \left(\frac{k}{b}\right)^2 + \left(\frac{l}{c}\right)^2}} \quad 4.4$$

$$\alpha=\beta=\gamma=90^\circ$$

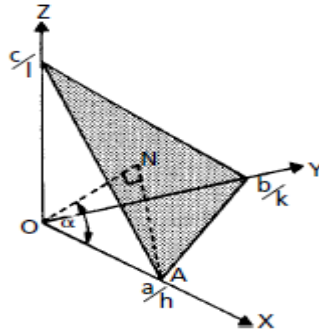


Figure 4.4 Intercepts of a lattice plane (hkl) on the unit cell vectors a , b , c . $ON = d_{hkl}$ =interplanar spacing.

Mechanical tests were done according to ASTM-D882 with the strain rate of 100 mm/min by tensile test analyser (TA-XT Plus texture analyzer). Samples were prepared as 1x10 cm and were waited at $23 \pm 2^\circ\text{C}$ and %50 relative humidity for 48 hours, before the mechanical tests. For each film mechanical tests were repeated 5 times and mean values and standart deviations were recorded.

Thermal behaviour of the composite films was characterized by TGA (Seteram LABSYS-TG) and DSC (TA-instrument DSC Q10). For TGA analysis, 10 mg samples were loaded into an alumina pan and heated with $10^\circ\text{C}/\text{min}$ rate with nitrogen atmosphere (40mL/min) from room temperature to 600°C .

For soil burial degradation tests, simulated soil was prepared according to literature (Rosa et al., 2005) that consisted of 23% loamy silt, 23% organic matter (cow manure), 23% sand and 31% distilled water (all w/w). Biodegradability was followed as based on weight loss, changes of amorph/crystal peak ratios by functional analysis and the appearences of the composite films. The specimens with $2 \times 2 \text{ cm}^2$

sizes were cut as 5 pieces for each composite film were weighed and buried, as 5 duplicates, in simulated soil at room temperature in two desiccators. Biodegradation was followed by every 2 weeks by measuring the weight losses, FTIR analysis and film thicknesses. The buried specimens were recovered, washed with distilled water, and dried at room temperature until there was no further variation in weight, after which they were then weighed, photographs are taken, then thicknesses of films were measured (Mitutoyo, Digimatic micrometer No: 293-821). Following weighting, the specimens were buried again in their respective containers. Then, degraded samples were investigated by FTIR spectroscopy (Perkin Elmer, Spectrum 100) every 4 weeks, but after FTIR analysis, they were kept for further analysis without burying again. The degree of crystallinities was measured for the degradation and at the end of the degradation experiments to check the variations caused by the soil burial degradation.

4.2.5. Experimental design and statistical analysis

The experimental results were evaluated by 2 level factorial design with center point method. In running a two-level factorial experiment, fitting the first- order model is usually anticipated, but it should be alerted to the possibility that the second- order model is really more appropriate. There is a method of replicating certain points in a 2^k factorial that will provide protection against curvature from second- order effects as well as allow an independent estimate of error to be obtained. The method consists of adding center points to the 2^k design. One important reason for adding the replicate runs at the design center is that center points do not affect the usual effect estimates in a 2^k design. When center points are added, it is assumed that the k factors are quantitative. To illustrate the approach, consider a 2^2 design with one observation at each of the factorial points $(-, -)$, $(+, -)$, $(-, +)$ and $(+, +)$ and center point observations at the $(0, 0)$. Figure 4.5 illustrates the situation (Montgomery, 1997).

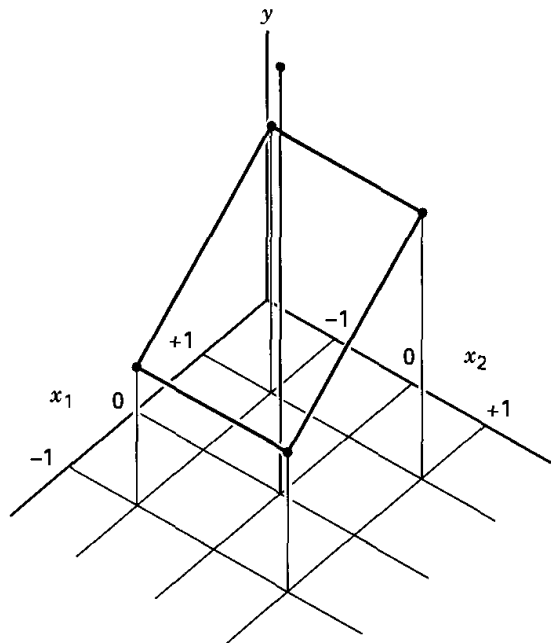


Figure 4.5 2^2 design with center points (Montgomery, 1997).

5. RESULTS AND DISCUSSION

5.1. DSC Analysis

The results obtained by DSC analysis for the first and second melting temperatures, isothermal and nonisothermal crystallization kinetics parameters are given in this section.

5.1.1. Melting point measurements of PCL composite films and prediction models

All isothermal and nonisothermal DSC analyses were performed. Isothermal and nonisothermal (with selected cooling rates) DSC thermograms are shown in Figure 5.1a-b. Melting points of the composite films are obtained from the maximum point of the first and second endotherms in the thermograms which are shown in Figure 5.1a as T_{m1} and T_{m2} .

Melting points from isothermal DSC analysis and calculated melting points from model equations are given in Figure 5.1. The first melting temperatures are mean value of both isothermal and nonisothermal DSC results which are also higher than second melting temperature values due to different crystallization mechanisms, melting from solution and melting from bulk of composite films (Rodriguez, 1987). The second melting temperature values are especially corresponding to the industrial extrusion process. The results are shown in Figure 5.2a-b-c-d.

To predict the effect of the liquid organic additives, theoretical melting point temperatures are calculated by Florry Huggins model (Eq. 3.1). Also the melting points are calculated by means of crystal thickness via Thomson-Gibbs model (Eq. 3.11). Calculated results show that the first melting temperatures decrease with increasing clay addition, but the organic additives slightly increase. The second melting temperatures which correspond the industrial extrusion process are lower than the first melting temperatures. The effects of clay and organic additives are not very dominant. Theoretical models give some hints about the mechanism but not completely match with quantitative experimental results.

Second melting points after non isothermal crystallization are given in Table 5.2. The values change between 53.27 (PCL_C0.1_O5, 10 °C/min) and 59.90 °C (PCL_C0.1_G3, 2 °C/min). The melting temperatures slightly decrease with organic additives. In Figure 5.3, some composite films show higher melting temperatures for lower crystallization cooling rates possibly due to forming of larger crystal sizes.

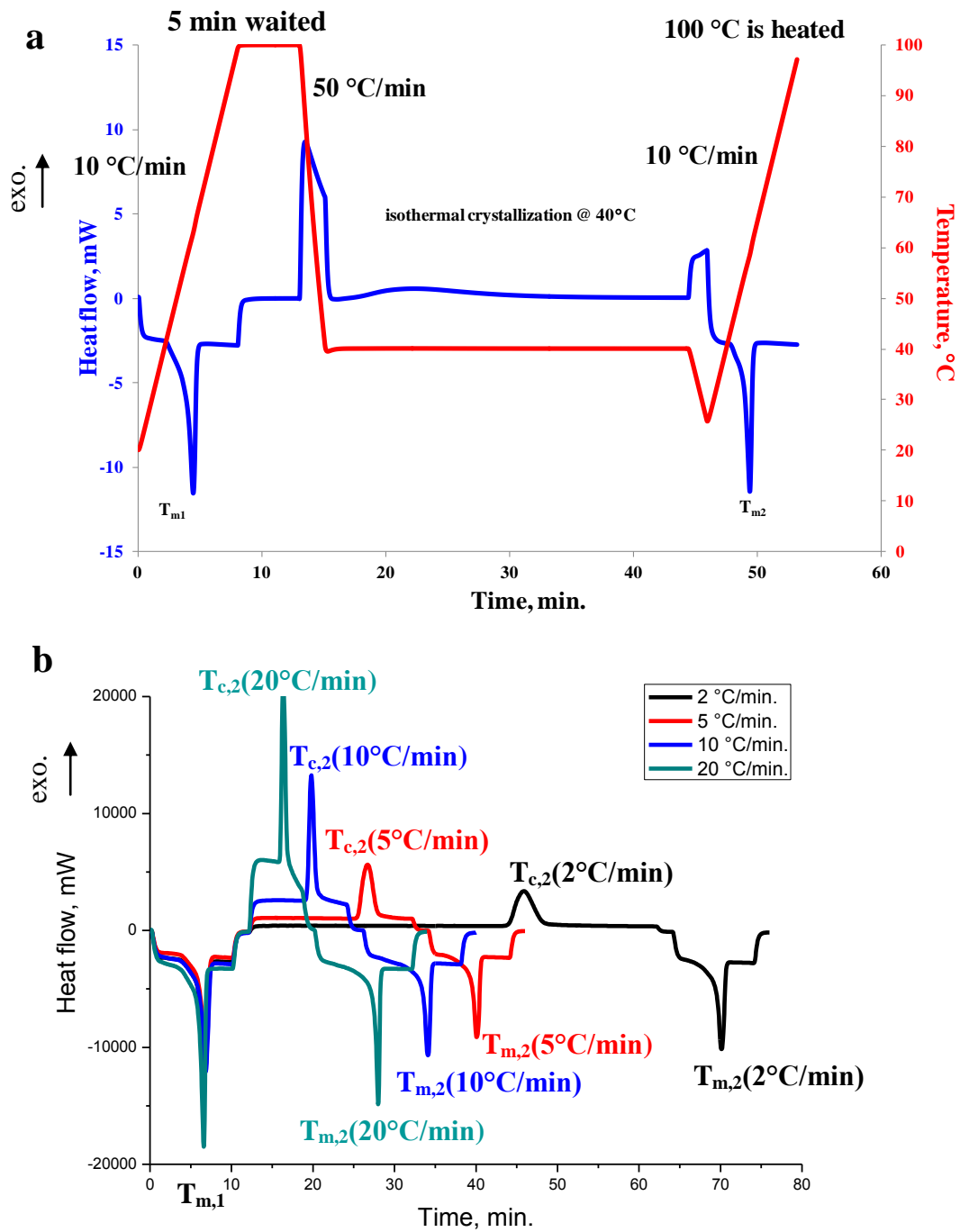


Figure 5.1 DSC heating and cooling profiles of neat PCL film; a- isothermal conditions, b- nonisothermal conditions.

Table 5.1 Melting temperatures of solvent cast films (T_{m1}) and films crystallized at 40 °C (T_{m2}) from Isothermal DSC analysis and calculated melting points from model equations.

Clay, % wt.	Organic Additive wt %	Melting temperatures of solvent cast films		Films crystallized @ 40°C		Florry Huggins Melting Point (°C)		Thomson Gibbs Melting Point (°C)	
		T_{m1} , °C		T_{m2} , °C		O	GMO	O	GMO
		O	GMO	O	GMO	O	GMO	O	GMO
0	0	62.68	62.68	58.48	58.48	-	-	59.68	59.68
	1	61.83	61.00	57.88	58.97	59.79	59.82	59.41	59.82
	3	63.42	60.93	56.43	58.25	59.37	59.48	59.79	59.77
	5	60.75	59.88	56.34	58.09	58.96	59.17	59.81	59.76
	0	61.53	61.53	59.13	59.13	-	-	59.88	59.88
0.1	1	60.95	62.47	58.72	58.84	59.79	59.82	59.93	59.74
	3	61.38	61.04	58.51	58.65	59.37	59.48	59.96	59.85
	5	57.49	61.15	58.23	58.35	58.96	59.17	59.83	59.83
	0	60.79	60.79	59.12	59.12	-	-	59.88	59.88
	1	60.11	62.38	58.83	58.78	59.79	59.82	59.77	59.83
0.4	3	59.31	61.83	58.13	58.55	59.37	59.48	59.88	59.81
	5	58.49	61.46	57.88	58.50	58.96	59.17	59.85	59.85
	0	60.31	60.31	59.07	59.07	-	-	59.88	59.88
	1	59.92	62.11	58.34	58.82	59.78	59.82	59.88	59.81
	3	59.96	61.72	59.07	58.48	59.36	59.48	59.83	59.85
1	5	58.35	61.92	57.81	58.44	58.95	59.17	59.83	59.81
	0	60.24	60.24	59.24	59.24	-	-	59.81	59.81
	1	60.03	62.34	58.84	58.95	59.78	59.82	59.85	59.85
	3	59.43	62.03	58.25	58.55	59.35	59.48	59.81	59.83
	5	62.39	61.69	58.23	58.58	58.93	59.17	59.93	59.83

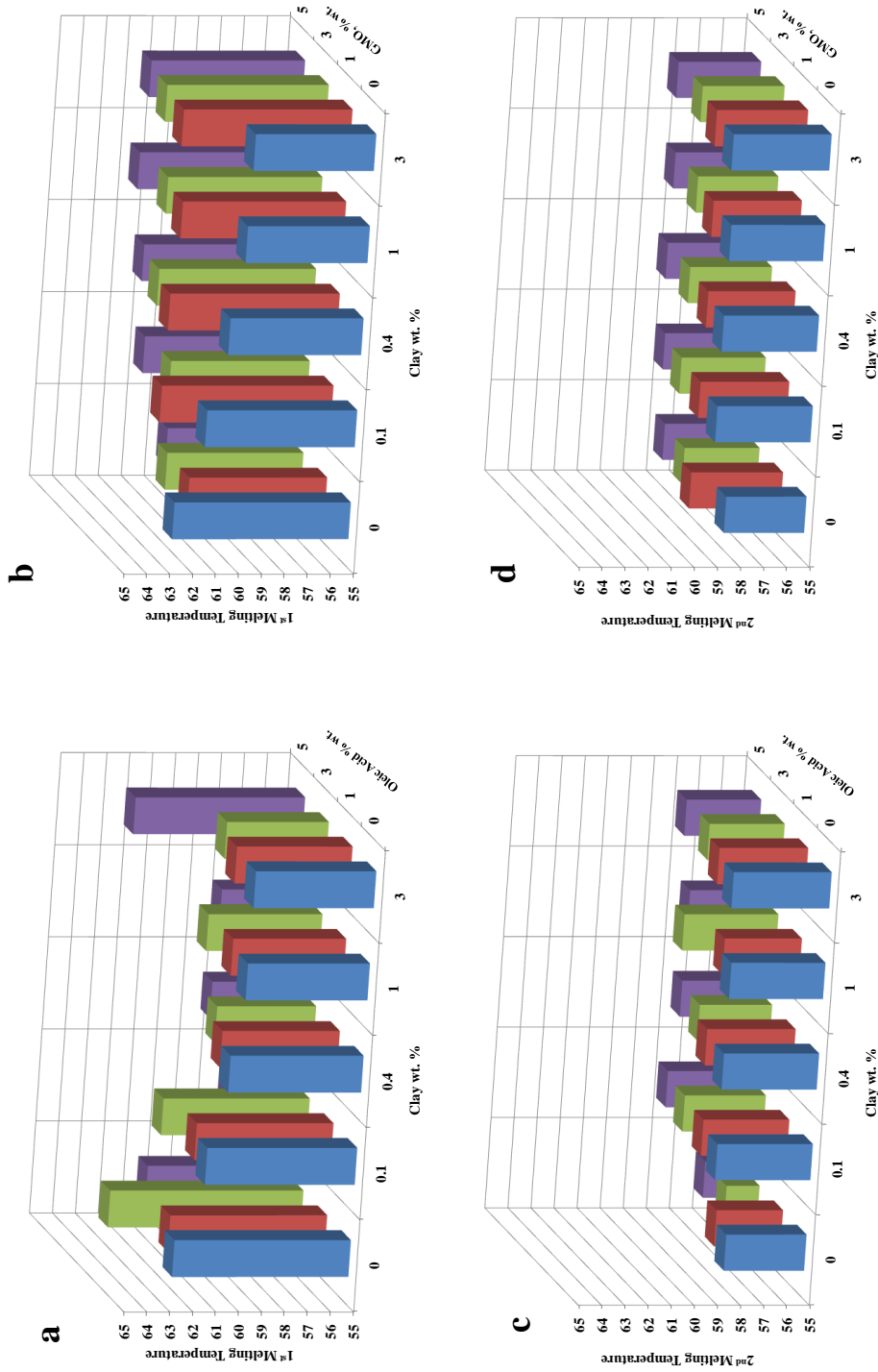


Figure 5.2 Variation of first and second melting points obtained from isothermal DSC analysis of PCL composite films depend on additive concentration; a and c-Clay & Oleic acid; b and d-Clay & GMO.

Table 5.2 The second melting temperatures of films which are melt crystallized by cooling at different rates.

Sample	Cooling rate, Φ , (°C/min)	2 nd Melting Temperature $T_{m,2}$ (°C)	Sample	Cooling rate, Φ , (°C/min)	2 nd Melting Temperature $T_{m,2}$ (°C)
PCL_IA0_OA0	2	56.62	PCL_C0.1_G3	2	59.90
	5	56.59		5	55.40
	10	56.33		10	56.17
	20	55.40		20	55.22
PCL_IA0_O3	2	56.40	PCL_C0.1_O5	2	54.81
	5	55.49		5	55.93
	10	55.55		10	53.27
	20	55.47		20	53.41
PCL_IA0_G3	2	55.10	PCL_C3_OA0	2	55.09
	5	54.80		5	55.32
	10	54.98		10	54.82
	20	54.85		20	55.14
PCL_C0.1_OA0	2	57.59	PCL_C3_O5	2	57.30
	5	54.90		5	56.68
	10	55.45		10	56.02
	20	55.61		20	55.11
PCL_C0.1_O3	2	54.95			
	5	54.98			
	10	55.36			
	20	55.09			

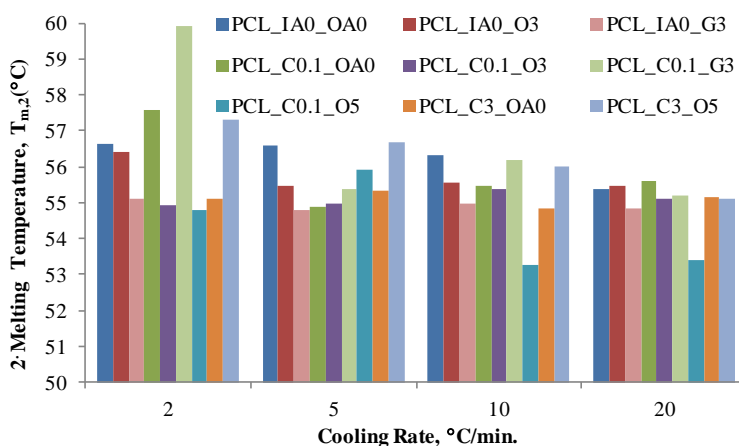


Figure 5.3 Variation of melting point temperatures of PCL composite films from nonisothermal DSC analysis.

5.1.2. Degree of crystallinity and statistical analysis

Degree of crystallinity values of PCL composite films from isothermal DSC analysis are given in Table 5.3 and selected PCL composite films for nonisothermal DSC analysis are given in Table 5.4. Degree of crystallinity values of composite films which calculated from first melting peak are higher than values calculated from second melting peak. This is because of different crystallization mechanisms due to melting from solution and melting from bulk of composite films.

Figure 5.4a-b shows the variation of degree of crystallinity of PCL composite films obtained from the first melting peak of isothermal DSC analysis depend on additive concentration, whereas Figure 5.4c-d shows the variation of degree of crystallinity of PCL composite films obtained from the second melting peak depend on additive concentration. Degree of crystallinity values from isothermal DSC analysis first melting peak (X_{c1}) and second melting peak (X_{c2}) changed between 43.37 (PCL_IA0_G5) – 64.49 (PCL_IA0_O3) and 34.33 (PCL_IA_G5) – 60.03 (PCL_C0.1_O1), respectively. When there is no inorganic additive, then degrees of crystallinities of composite films were increased with oleic acid and decreased with GMO addition. Also high amount of clay and oleic acid addition possibly cause defective crystal formation and low degree of crystallinity. The rest of the composite films show variation. The variation of degree of crystallinity and crystallization temperatures of selected PCL composite films obtained from the second melting peak of nonisothermal DSC analysis are given in Figure 5.6a-b. Degree of crystallinity values of selected PCL composite films from nonisothermal DSC analysis second melting peak (X_{c2}) changed between 35.66 (PCL_IA0_O3 with 20°C/min cooling rate) – 64.51 (PCL_C3_O5 with 2°C/min cooling rate), respectively. Crystallization temperatures of the composite films are given in Figure 5.6-b. Nonisothermal results show that crystallization temperature are increased with increasing cooling rate. Nevertheless degree of crystallinities also show similar tendency.

Isothermal DSC results of clay-oleic acid contained composite films are evaluated with statistical method and the central point results are given in Figure 5.5 and the model equations obtained are given in Table 5.6. As seen in Figure 5.7, 1st melting temperature is decreased with addition of oleic acid and clay separately, but, interaction of both additives are increased the temperature. At the same time, high load of organic and inorganic additives decreases 1st and 2nd degree of crystallinity value. 2nd degree of crystallinity values are increased with low amount of clay addition.

Table 5.3 Degree of crystallinity % values (DOC%) of PCL composite films obtained from isothermal DSC analysis.

Clay, % wt.	Organic Additive wt %	1 st Melting Peak		2 nd Melting Peak	
		DOC % by DSC		DOC % by DSC	
		O	GMO	O	GMO
0	0	57.81	57.81	42.85	42.85
	1	63.12	45.65	46.66	38.43
	3	64.49	46.00	47.31	36.60
	5	62.82	43.37	45.04	34.33
0.1	0	53.73	53.73	42.70	42.70
	1	64.09	60.06	60.03	42.18
	3	51.89	52.72	44.51	41.46
	5	52.13	57.57	42.77	40.68
0.4	0	51.09	51.09	42.75	42.75
	1	57.35	60.11	41.24	43.80
	3	56.62	64.25	43.00	46.04
	5	49.61	64.10	42.27	44.36
1	0	56.55	56.55	41.48	41.48
	1	58.73	55.93	40.19	41.32
	3	58.25	54.41	38.98	42.67
	5	52.53	51.16	37.02	37.69
3	0	53.82	53.82	40.31	40.31
	1	56.78	54.20	37.99	40.11
	3	55.88	51.54	35.87	39.22
	5	51.30	49.50	36.01	36.54

Table 5.4 Degree of crystallinity % values (DOC) and crystallization temperatures of PCL composite films obtained from nonisothermal DSC analysis at different cooling rates.

Sample	ϕ (°C/min)	2 nd Melting*	T_c (°C)	Sample	ϕ (°C/min)	2 nd Melting*	T_c (°C)
		DOC %				DOC %	
PCL_IA0_OA0	2	47.31	33.24	PCL_C0.1_G3	2	44.66	31.72
	5	38.21	28.69		5	43.09	30.18
	10	41.79	26.15		10	41.60	26.18
	20	41.22	21.00		20	45.33	21.62
PCL_IA0_O3	2	44.97	35.00	PCL_C0.1_O5	2	52.66	32.69
	5	43.19	30.98		5	45.90	29.66
	10	43.71	26.18		10	43.08	27.31
	20	35.66	21.57		20	40.58	21.68
PCL_IA0_G3	2	38.84	29.30	PCL_C3_OA0	2	45.70	34.23
	5	41.13	24.95		5	51.32	31.56
	10	38.76	21.16		10	42.09	28.97
	20	46.96	18.00		20	43.93	25.55
PCL_C0.1_OA0	2	45.00	29.81	PCL_C3_O5	2	64.51	36.40
	5	39.28	25.46		5	44.92	33.12
	10	40.66	20.58		10	43.37	30.43
	20	40.15	15.51		20	44.11	27.52
PCL_C0.1_O3	2	47.06	28.57				
	5	41.53	24.65				
	10	40.40	21.52				
	20	43.40	15.58				

* Melting of the films crystallized from the melt by cooling at different rates

Table 5.5 Central point samples for isothermal DSC results and levels for statistical evaluation.

Sample	$T_{m,1}$	$X_{c,1}$	$T_{m,2}$	$X_{c,2}$
PCL_C0.1_OA0	61.53	53.73	59.13	42.70
PCL_C0.1_O5	60.24	52.13	59.24	40.31
PCL_C3_OA0	57.49	53.82	58.23	42.77
PCL_C3_O5	62.39	51.30	58.23	36.01
PCL_C1.55_O2.5-1	60.22	51.11	58.42	43.37
PCL_C1.55_O2.5-2	60.07	50.41	58.62	43.60
PCL_C1.55_O2.5-3	60.05	50.46	58.29	43.88

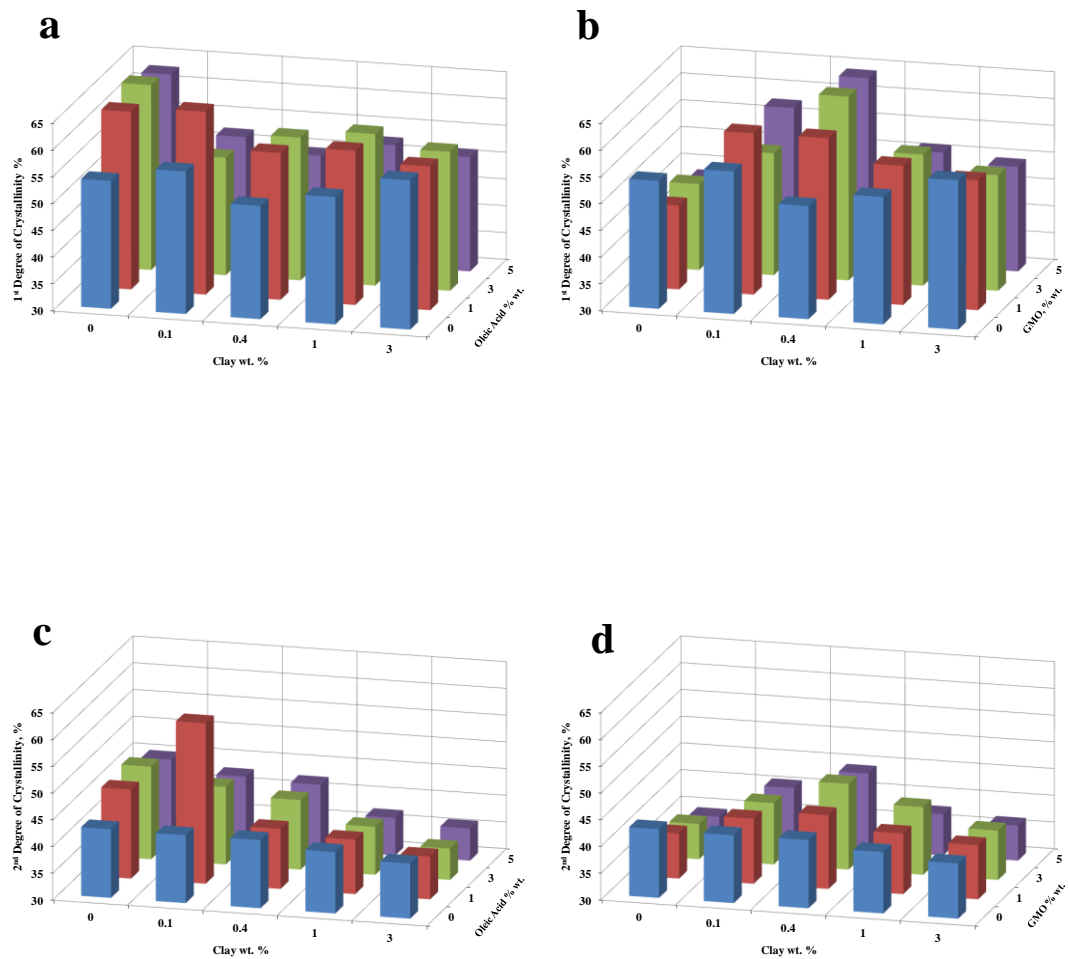


Figure 5.4 Variation of degree of crystallinity of PCL composite films obtained from isothermal DSC analysis depend on additive concentration; a- DOC from first melting peak for Clay-Oleic acid, b- DOC from first melting peak for Clay-GMO, c- DOC from second melting peak for Clay-Oleic acid, d- DOC from second melting peak for Clay-GMO.

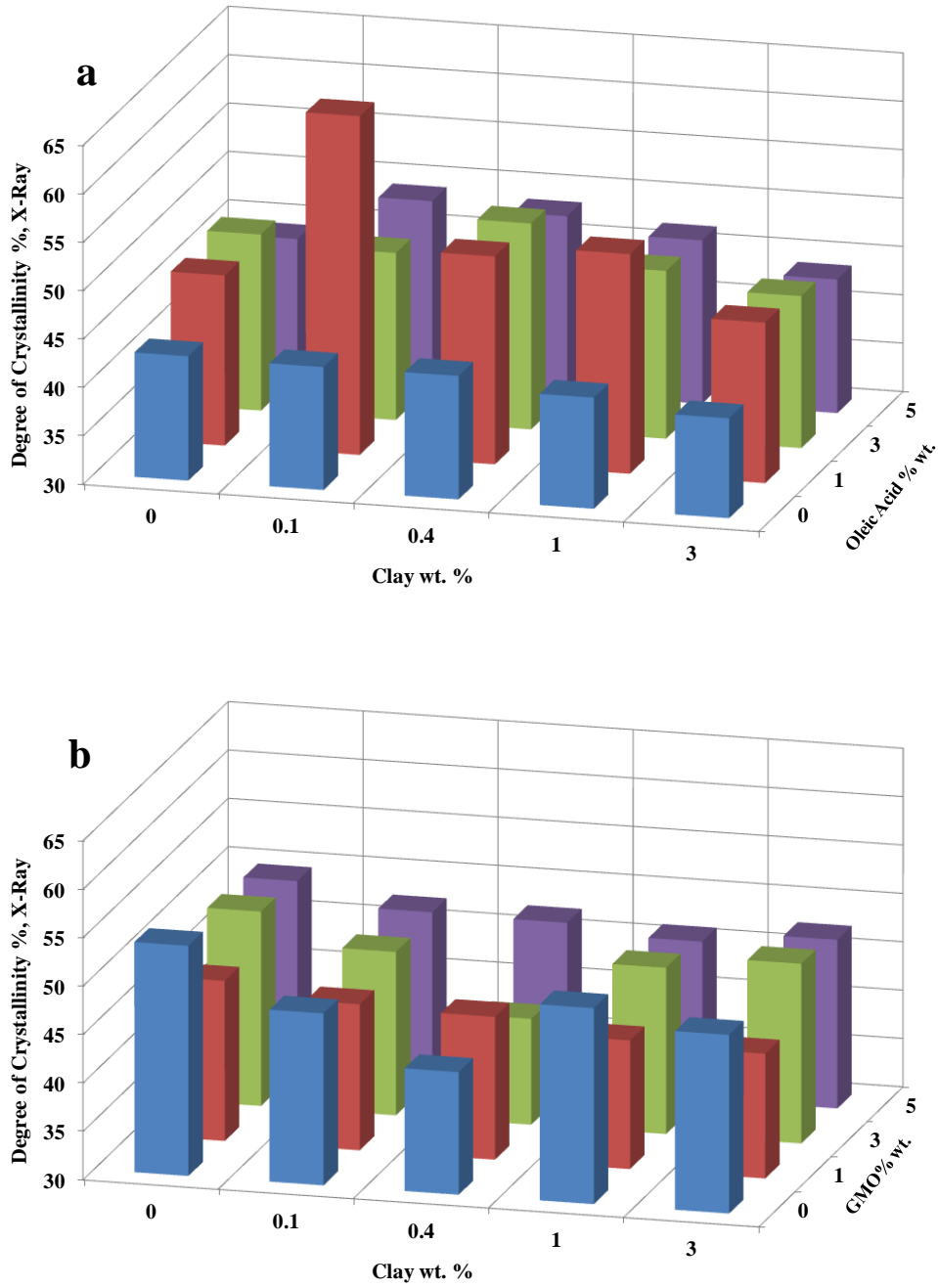


Figure 5.5 Variation of degree of crystallinity of PCL composite films obtained solvent casting from X-Ray analysis depend on additive concentration; a-Clay-Oleic acid, b-Clay-GMO.

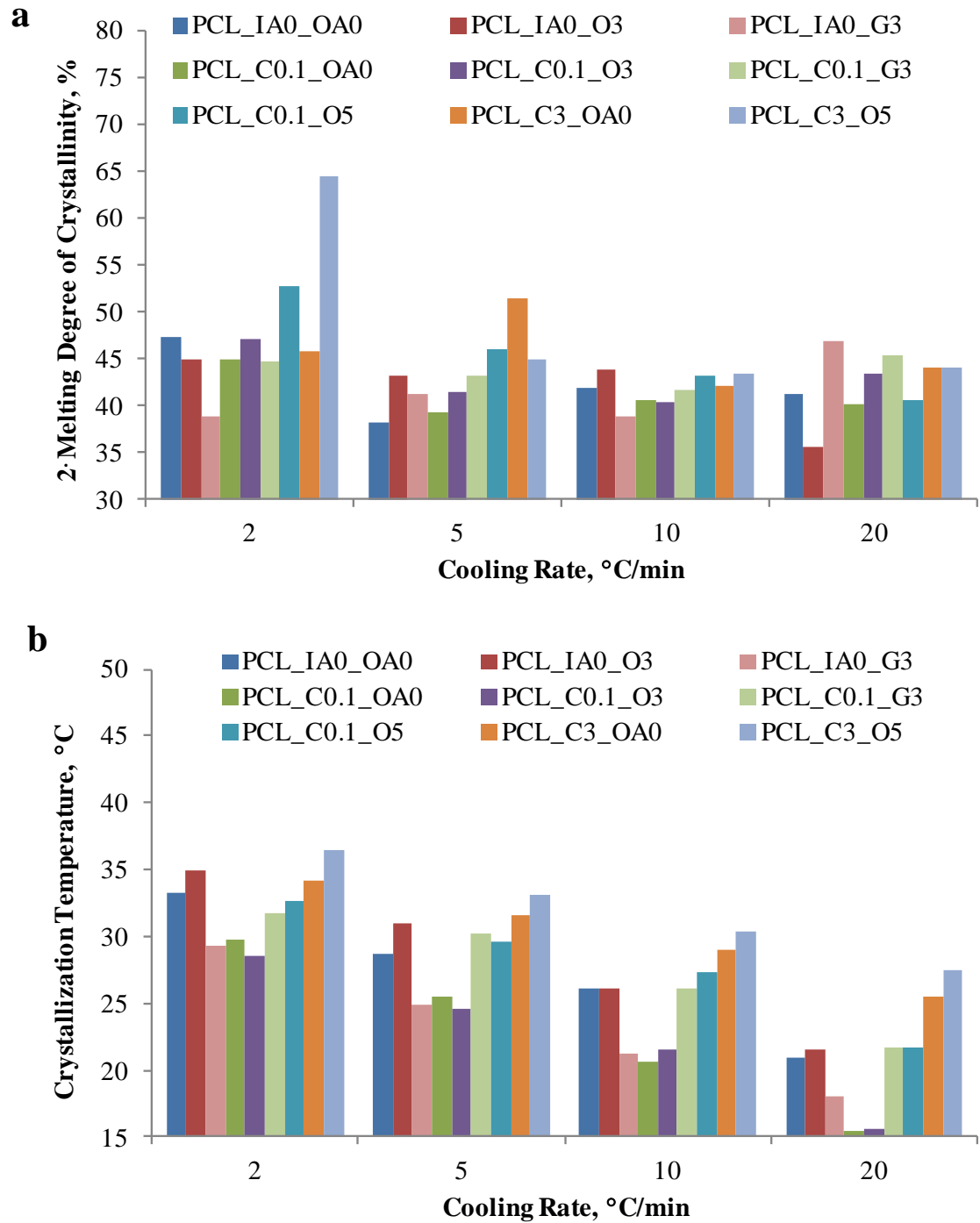


Figure 5.6 a. Variation of degree of crystallinity of PCL composite films obtained from nonisothermal DSC analysis of second melting peak at different cooling rates depend on additive concentration; b. Crystallization temperatures of composite films for each cooling rate.

Table 5.6 Model equations by statistical evaluation.

Parameter	Model Equation	R^2
$T_{m,1}$	$61.57-0.44 \times C-0.85 \times O+0.43 \times C \times O$	0.99
$X_{c,1}$	$53.72+0.032 \times C-0.31 \times O-0.06 \times C \times O$	0.94
$T_{m,2}$	$59.13+0.04 \times C-0.18 \times O-0.008 \times C \times O$	0.94
$X_{c,2}$	$42.77-0.82 \times C+0.045 \times O-0.302 \times C \times O$	0.99

C=Clay % wt.; O=Oleic Acid % wt.; C x O=Clay and Oleic Acid % wt. interaction

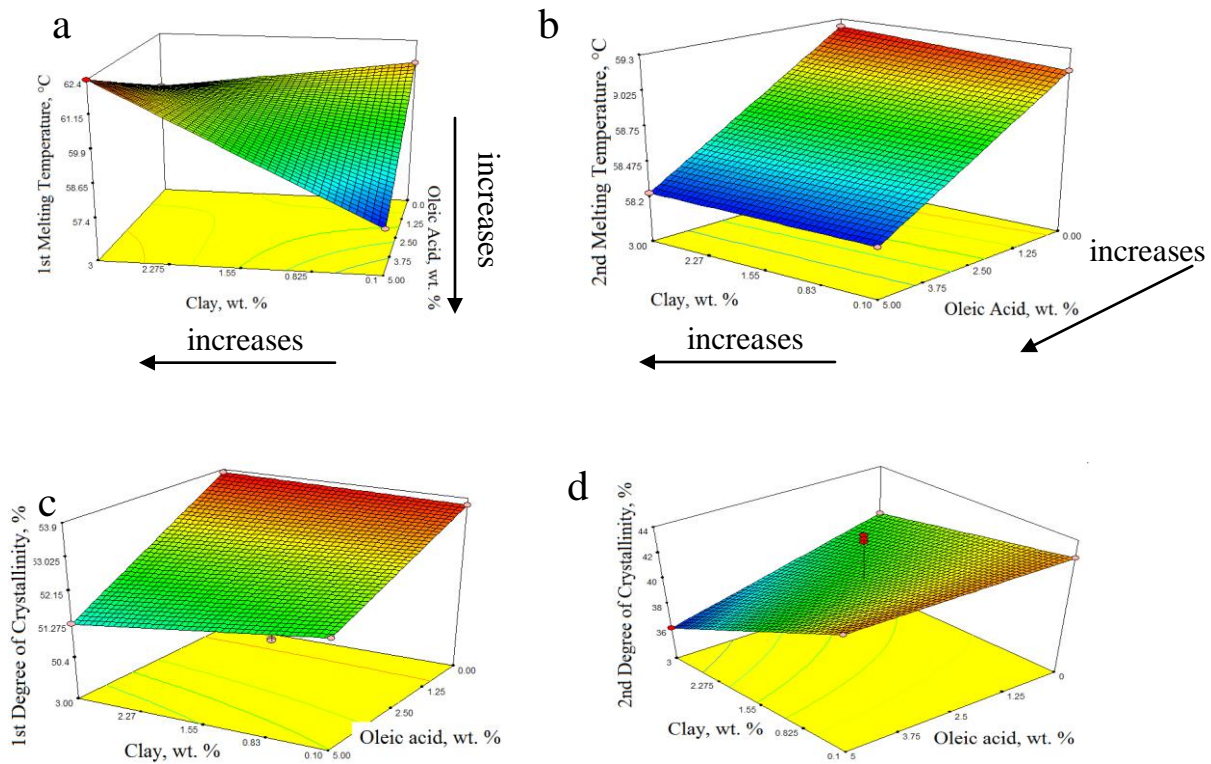


Figure 5.7 Statistical evaluation of isothermal DSC experiments for studying isothermal crystallization kinetics at 40 °C a. variation of 1st melting temperature; b. variation of 2nd melting temperature; c. Degree of crystallinity of solvent cast films; d. Degree of crystallinity of the melt crystallized films.

5.1.3. Crystallization kinetics

Results for the primary nucleation and secondary nucleation kinetics are given in this section.

5.1.3.1. Primary nucleation kinetics models

In this section, primary nucleation kinetics of isothermal and nonisothermal crystallization are investigated by several methods.

Avrami model for isothermal crystallization kinetics and statistical analysis

Avrami crystallization model (Eq. 3.19) is evaluated from isothermal DSC exotherm at 40 °C which is given in Figure 5.8. DSC exotherms of all composite films could be found in Appendix 1, Figure A1. From the exotherms, time dependent relative crystallinity is calculated and given in Figure 5.9 and Appendix A, Figure A2. All relative crystallinity (X_t) versus time curves have the same characteristic sigmoidal shape and crystallization half time, $t_{1/2}$, is defined from this curve. The curve consists both primary and secondary crystallization steps. Initial part of the S-shaped curves is generally considered as nucleation step of the crystallization process. Each curve showed a linear part considered as primary crystallization; subsequently, a second non-linear part deviated off slightly and considered to be due to secondary crystallization, which was caused by the spherulitic growth. Linear part of the curve is fitted by Avrami model and successfully applied for the PCL composite films. Avrami plot of %1 clay contained composite films with variation of oleic acid is given in Figure 5.10 and rest of the Avrami plots could be found in Appendix A, Figure A3. Avrami exponent, n , and growth rate constant, K , and crystallization half time, $t_{1/2}$, values are calculated from the Avrami plots and are given in Table 5.7 for central points and Table 5.8 for all composite films and are illustrated from Figure 5.11 to Figure 5.13.

Avrami exponent, n , decreased with oleic acid and accelerate crystallization process. GMO addition shows reverse effect. 1% and 3% oleic acid contained composite films show minimum n value which causes high velocity of polymer chain conformations during crystallization. Increasing n value shows reverse effect. Growth rate constant, K , is significantly increased with oleic acid addition and crystallization half time, $t_{1/2}$, proportionally decreased. Clay and GMO addition decreased the K values in comparison with neat PCL. Organic additives, oleic acid and glycerol mono

oleat have different effects on crystallization. Oleic acid accelerates but GMO slow down.

Statistical central point calculations were performed but selected composite films consist at least 0.1% clay, the single effect of oleic acid cannot be observed (Table 5.7). In Table 5.9, statistical results are given. The results show that clay addition is increased the Avrami exponent, n , and decreased the crystallization rate (Figure 5.14). Higher Avrami exponent values tend to decrease crystallization rate (Durmus et al., 2009). Finally, it could be emphasized that crystallization could be controlled with additives.

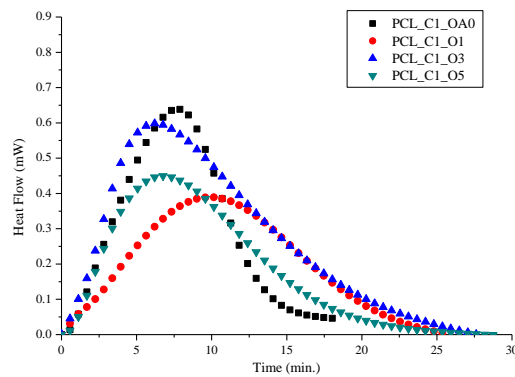


Figure 5.8 DSC exotherm of 1 wt% clay contained composite films with variation of oleic acid.

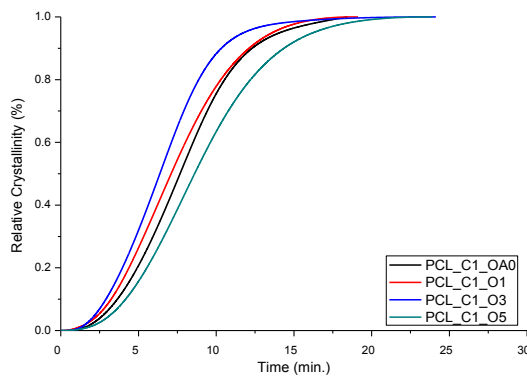


Figure 5.9 Time dependent relative crystallinity of 1 wt% clay contained composite films with variation of oleic acid.

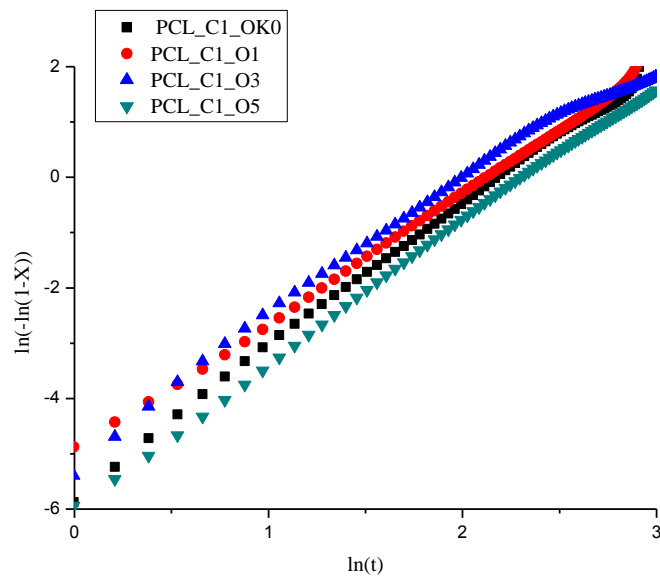


Figure 5.10 Avrami plot of 1 wt% clay contained composite films with variation of oleic acid.

Table 5.7 Central point samples for isothermal DSC results and levels for statistical evaluation.

Sample	n	$K \times 10^{-3}$	$t_{1/2}$ (min)
PCL_C0.1_OA0	2.21	5	8.67
PCL_C0.1_O5	2.33	3.9	8.39
PCL_C3_OA0	2.39	4.6	8.49
PCL_C3_O5	2.48	3.9	8.25
PCL_C1.55_O2.5-1	2.43	7.5	4.26
PCL_C1.55_O2.5-2	2.93	9.0	5.77
PCL_C1.55_O2.5-3	3.07	12.0	3.74

Table 5.8 Crystallization kinetics parameters of PCL composite films obtained by Avrami model.

Clay wt %	Organic Additive wt %	Avrami Exponent, n		$K_{\text{intercept}} \times 10^{-3}$		$t^{1/2}(\text{min})$	
		O	GMO	O	GMO	O	GMO
0	0	2.05		10.9		7.13	
	1	1.86	2.37	38.2	2.80	4.68	10.27
	3	1.86	2.05	17.5	5.30	6.83	10.63
	5	2.01	2.05	21.4	5.10	5.25	10.93
0.1	0	2.21		5.35		8.67	
	1	2.20	2.46	4.09	4.80	10.58	7.99
	3	2.13	2.26	5.80	2.55	8.85	12.48
	5	2.33	2.35	3.97	2.94	8.39	10.37
0.4	0	2.41		4.75		8.25	
	1	2.52	2.45	3.89	1.68	7.89	11.82
	3	2.59	2.40	4.12	4.36	7.58	8.06
	5	2.34	2.11	1.74	2.47	12.34	14.78
1	0	2.66		2.91		7.67	
	1	2.31	2.34	7.30	2.85	7.10	10.59
	3	2.58	2.53	5.61	3.88	6.37	7.97
	5	2.46	2.12	3.21	3.55	8.60	11.94
3	0	2.39		4.56		8.49	
	1	2.29	2.38	6.41	3.36	8.16	9.57
	3	2.45	2.13	5.09	4.80	7.41	10.80
	5	2.48	2.54	3.93	2.64	8.25	8.29

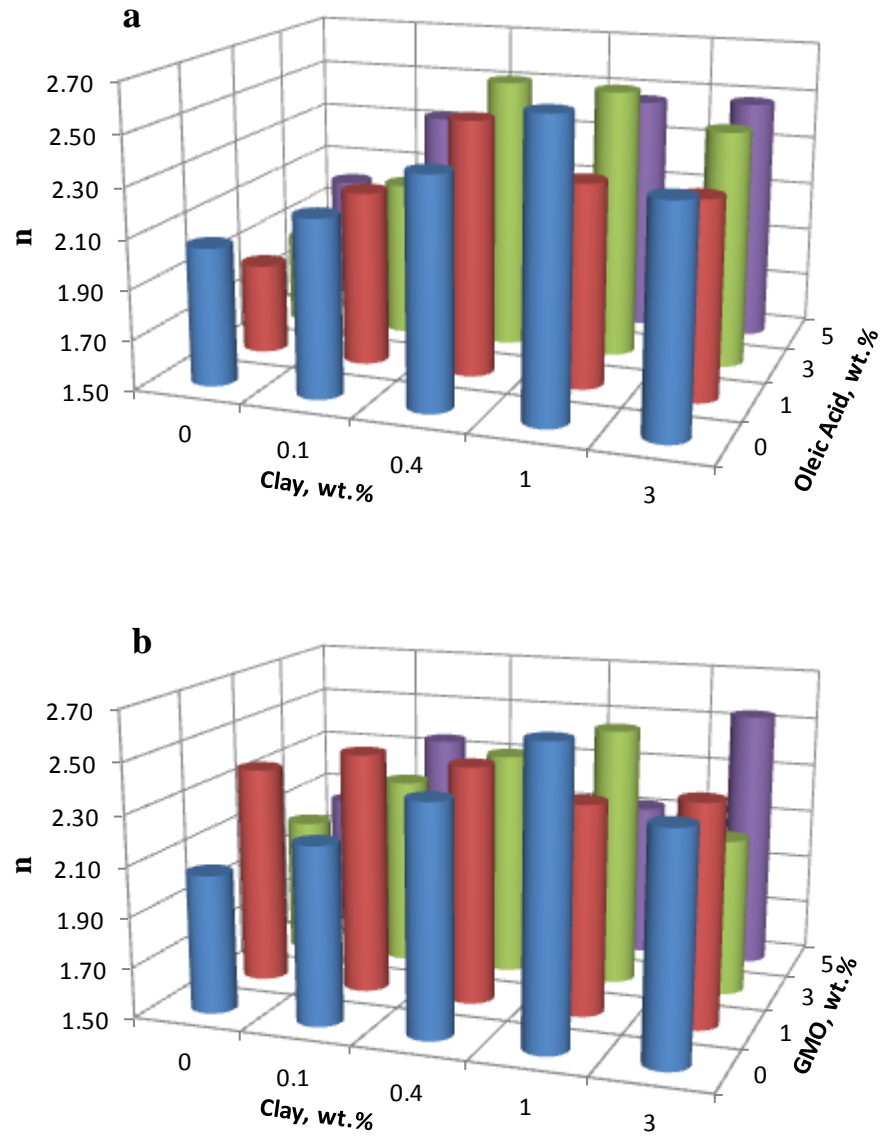


Figure 5.11 Variation of Avrami constant values of composite films a. Clay and Oleic Acid; b. Clay and GMO.

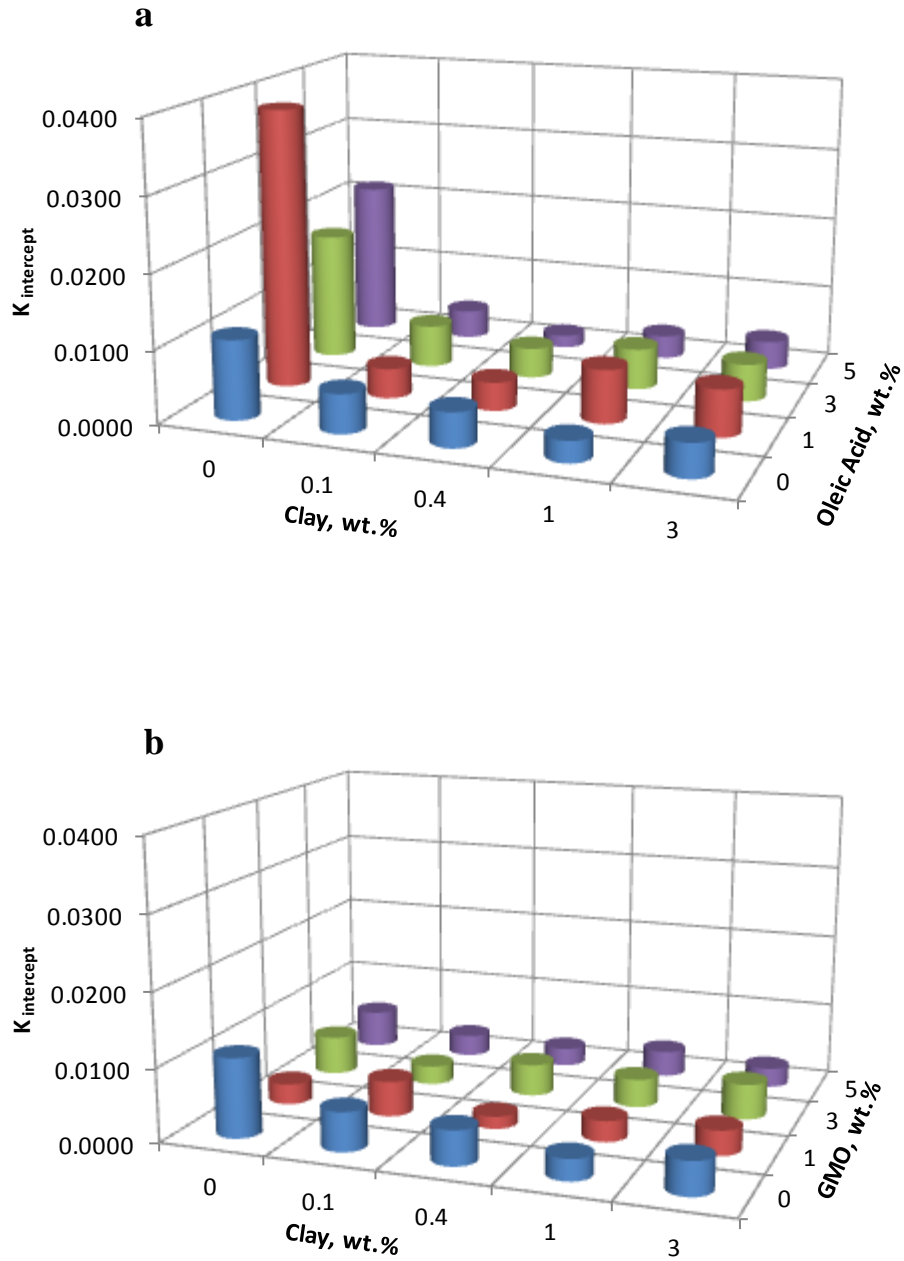


Figure 5.12 Variation of growth rate constant values of composite films a. Clay and Oleic Acid; b. Clay and GMO.

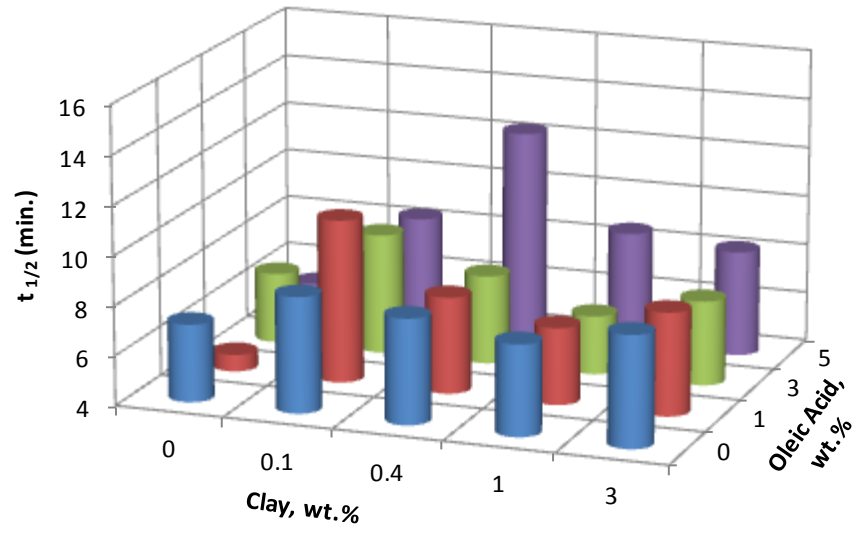
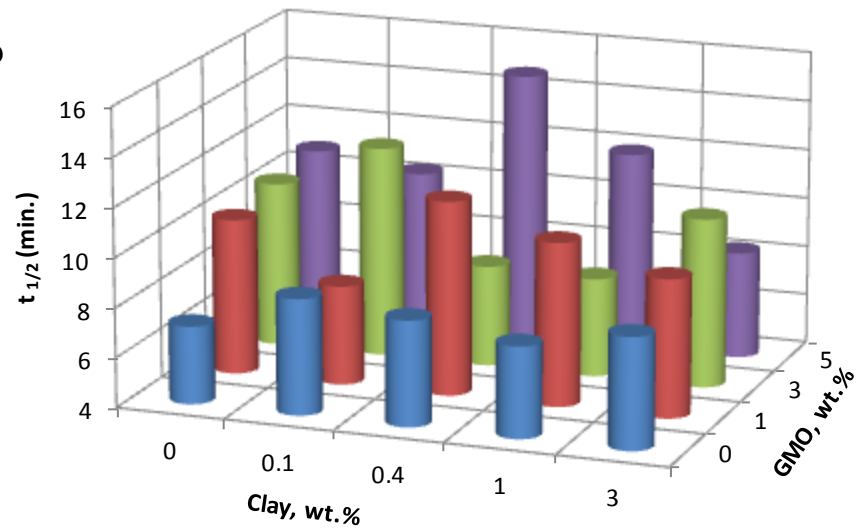
a**b**

Figure 5.13 Variation of crystallization half time values of composite films a. Clay and Oleic Acid; b. Clay and GMO.

Table 5.9 Model equations obtained by the statistical evaluation.

Örnek	Model Denklemi	R^2
n	$2.203+0.062x\mathbf{C}+0.024x\mathbf{O}+0.002x\mathbf{C}x\mathbf{O}$	0.95
K	$5.38-2.73x\mathbf{C}-2.83x\mathbf{O}+5.18x\mathbf{C}x\mathbf{O}$	0.98
t_{1/2}	$8.676+0.06x\mathbf{C}-0.056x\mathbf{O}+0.003x\mathbf{C}x\mathbf{O}$	0.99

C=Clay % wt.; O=Oleic Acid % wt.; CxO=Clay and Oleic Acid % wt. Interaction

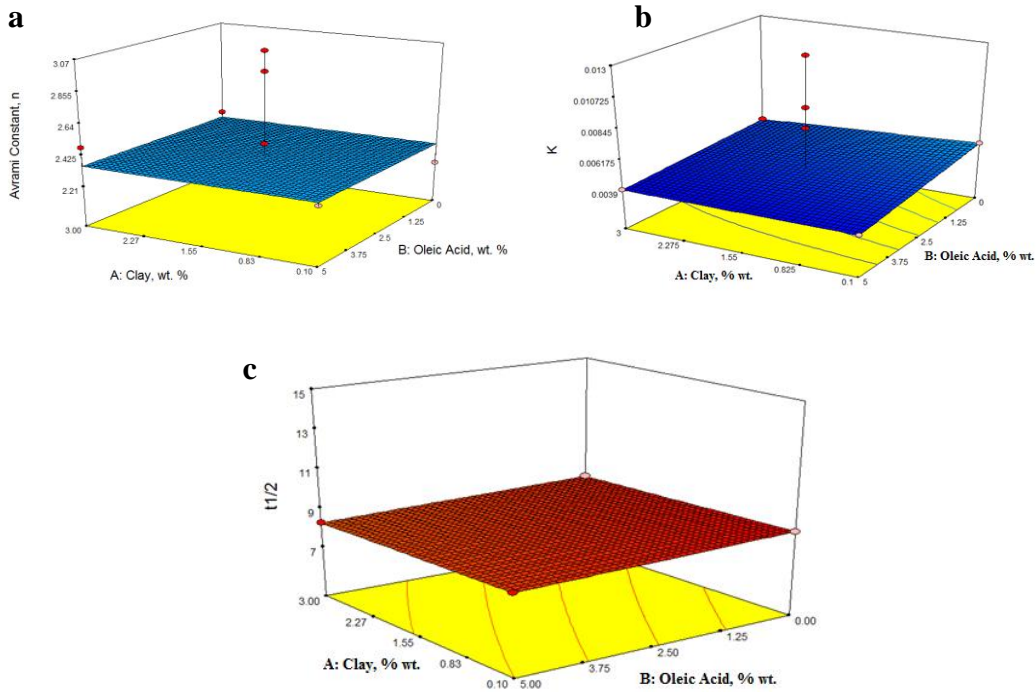


Figure 5.14 Statistical evaluation results of; a- Avrami exponent, n ; b- Growth rate constant, K ; c- Crystallization half time, $t_{1/2}$.

Avrami Jeziorny model for nonisothermal crystallization kinetics

The crystallization exotherms of neat PCL film at various cooling rates are illustrated in Figure 5.15 (Appendix B, Figure B1 includes nonisothermal exotherms of selected PCL composites). The relative crystallinity percent, X_t , as a function of crystallization time can be obtained from the crystallization exotherms of samples by partial integration of the crystallization exotherms. The X_t versus time plot of neat PCL is shown in Figure 5.16 and the others are given in Appendix C, Figure C1. All X_t versus time plots have the similar shape. In this case also, initial part of the S-shaped curves is generally considered as nucleation step of the crystallization process as in isothermal crystallization. The Avrami Jeziorny plot of the composite films are performed from time depended relative crystallinity percentage values and the plot of neat PCL film is shown in Figure 5.17. Avrami Jeziorny plot of the rest of the composite films are given in Appendix C, Figure C2. Each curve showed a linear part considered as primary crystallization; subsequently, a second nonlinear part considered as secondary crystallization, which was caused by the spherulitic growth.

End of the evaluations, Avrami-Jeziorny model is successfully fit the experimental data. The results are tabulated in Table 5.10. The exponent n varied from 3.05 to 4.14 for neat PCL, and from 2.61 to 6.45 for PCL/Clay composite films, respectively (Figure 5.18a). Although the range of exponent n in nonisothermal crystallization was more scattered than that obtained from isothermal crystallization, neat PCL and composite films had different n values for each cooling rate, indicating that the montmorillonite did act as a nucleating agent in the PCL matrix. As expected, the value of Z_c increased with increasing cooling rates for both PCL and composite films. Especially 3wt% clay + 5wt% oleic acid contained composite films have high n and Z_c values and the lowest crystallization half time 0,29 min is achieved for 3wt% clay added composite film without the organic additive for 20 °C/min cooling rate due to nucleating effect of clay in nonisothermal conditions (Figure 5.18b-c).

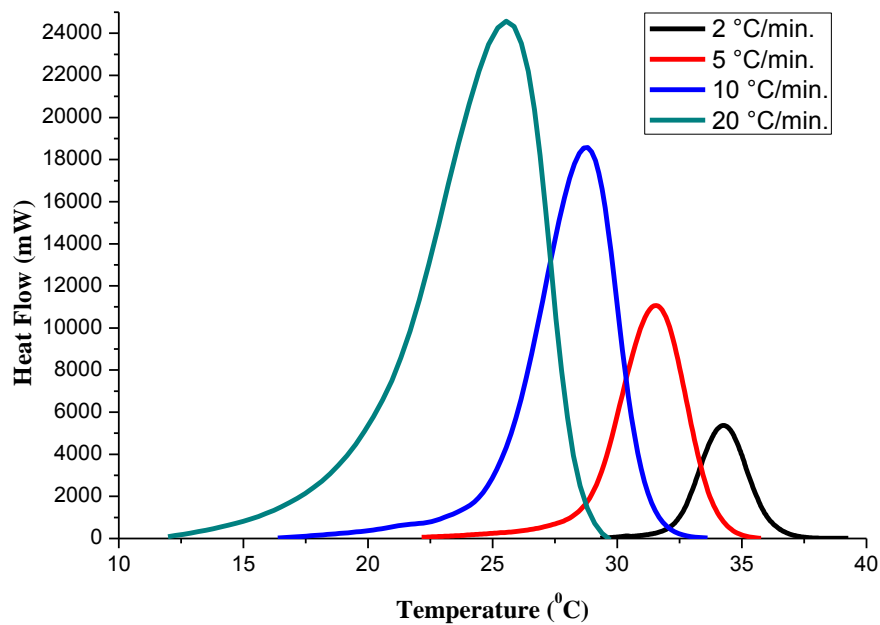


Figure 5.15 Temperature dependent nonisothermal crystallization exotherms of neat PCL with different cooling rates.

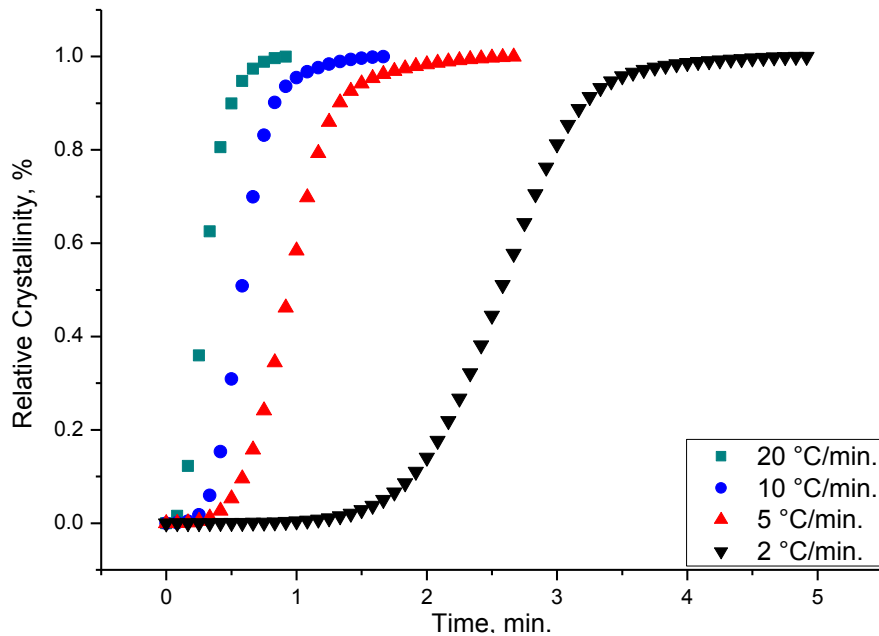


Figure 5.16 Time dependent relative crystallinity percent of neat PCL with different cooling rates.

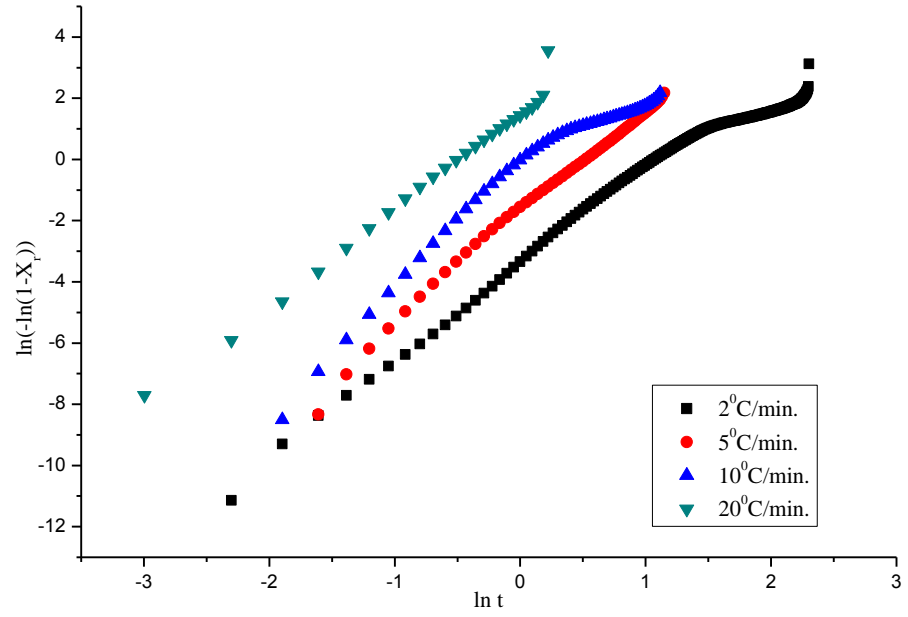


Figure 5.17 Avrami Jeziorny plot for neat PCL with different cooling rates.

Table 5.10 Nonisothermal crystallization kinetics parameters (n , Z_c) and crystallization half time ($t_{1/2}$) obtained by Avrami Jeziorny Model.

	ϕ (°C/min)	Avrami Jeziorny			R^2	ϕ (°C/min)	Avrami Jeziorny			R^2					
		n	Z_c (min ⁻¹)	$t_{1/2}$ (min)			n	Z_c (min ⁻¹)	$t_{1/2}$ (min)						
PCL_IA0_OA0	2	3.05	0.21	2.55	0.99	PCL_C0.1_G3	2	3.75	0.08	3.35	0.99				
	5	3.45	0.70	1.50			5	3.09	0.80	1.20					
	10	4.14	0.99	0.90			10	3.45	0.95	0.96					
	20	3.14	1.08	0.55			20	3.53	1.06	0.56					
PCL_IA0_O3	2	3.49	0.13	2.60		0.99	PCL_C0.1_O5	2	4.37	0.11		2.52	0.99		
	5	4.17	0.70	1.37				5	3.99	0.67		1.35			
	10	3.94	0.97	0.95				10	4.24	1.06		0.78			
	20	5.08	1.09	0.66				20	4.78	1.09		0.61			
PCL_IA0_G3	2	3.21	0.10	3.90			0.99	PCL_C3_OA0	2	4.68		0.08		2.57	0.99
	5	3.29	0.59	2.05					5	3.44		0.95		0.94	
	10	4.08	0.88	1.26					10	3.43		1.13		0.58	
	20	3.67	0.62	0.75					20	2.61		1.13		0.29	
PCL_C0.1_OA0	2	4.26	0.03	2.30	0.99			PCL_C3_O5	2	4.85	0.11	2.30		0.99	
	5	3.52	0.56	2.10					5	5.78	0.67	1.31			
	10	2.89	0.90	1.26					10	4.96	1.11	0.75			
	20	3.77	1.01	0.86					20	6.45	1.25	0.48			
PCL_C0.1_O3	2	3.35	0.08	4.45		0.99		PCL_C3_O5	2	4.85	0.11	2.30	0.99		
	5	2.70	0.63	2.05					5	5.78	0.67	1.31			
	10	3.78	0.88	1.26					10	4.96	1.11	0.75			
	20	3.35	1.01	0.81					20	6.45	1.25	0.48			

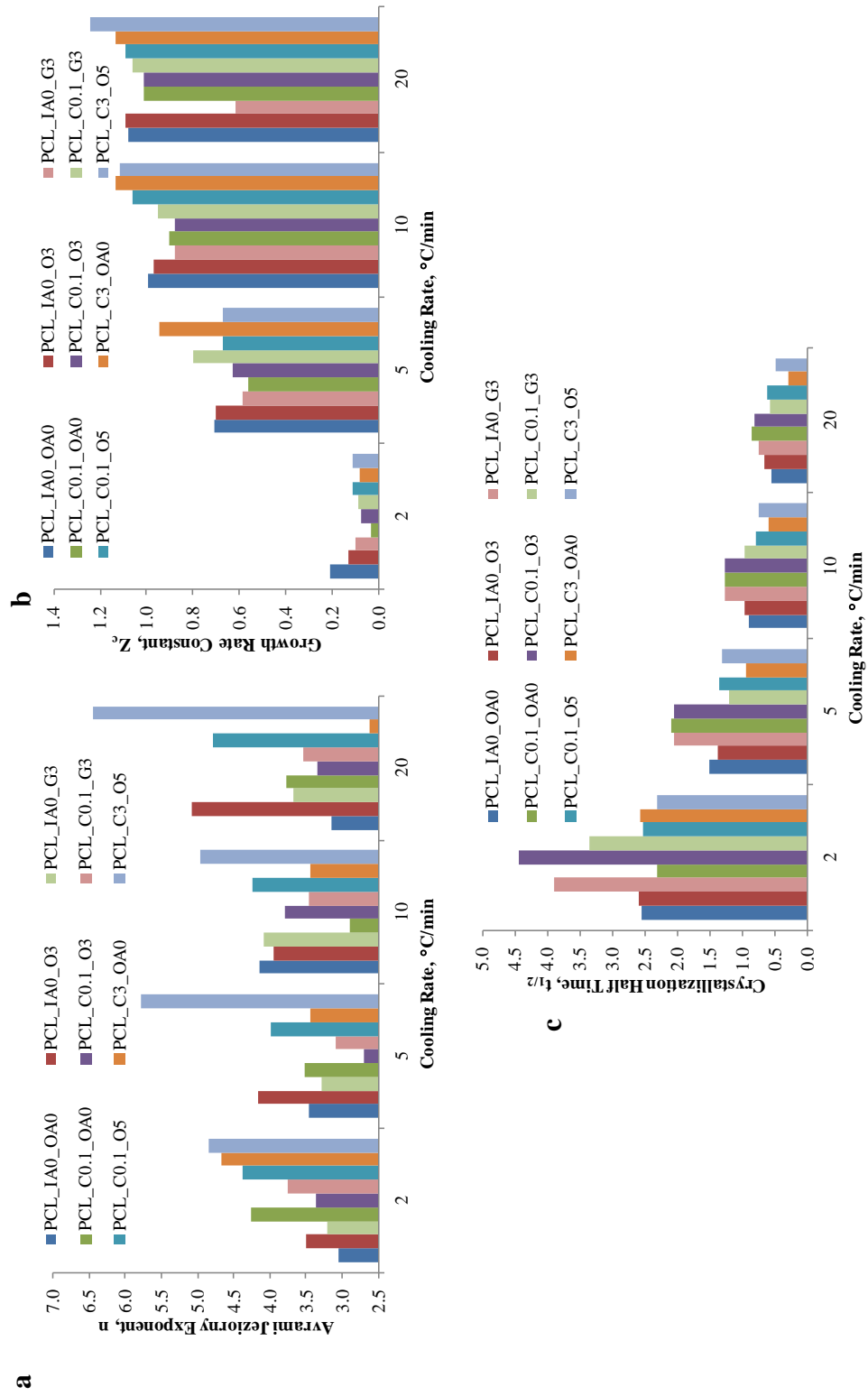


Figure 5.18 Variation of nonisothermal Avrami Jeziorny crystallization model results; a – Avrami Jeziorny exponent, n ; b – Growth rate constant, Z_c ; c – Crystallization half time, $t_{1/2}$.

Ozawa model for nonisothermal crystallization kinetics

The Ozawa model is applied and successfully fits the nonisothermal crystallization behavior of the samples.

The relative crystallinity percent, X_t , as a function of the crystallization temperature is obtained from the crystallization exotherms of samples by partial integration of the crystallization exotherms (Figure 5.19). X_t versus temperature plot of selected PCL composite films are given in Appendix D, Figure D1. All samples have same Z-shape graphics. Plotting $\ln[-\ln(1-X_t)]$ versus $\ln\phi$ at a given temperature, a straight line should be obtained.

Figure 5.20 shows the Ozawa plot of neat PCL at various temperatures. Ozawa plots of PCL composite films are given in Appendix D, Figure D2. Slopes of these straight lines give Ozawa constant m , and intercepts are $K(T)$. Nonisothermal crystallization kinetics parameters (m , $K(T)$) and regression coefficients values obtained by Ozawa Model are listed in Table 5.11. Figure 5.21 presents the variation of Ozawa constant m of selected PCL composite films depend on temperature. As the temperature and additive concentration increases, Ozawa constant m increases, but Ozawa rate constant decreases.

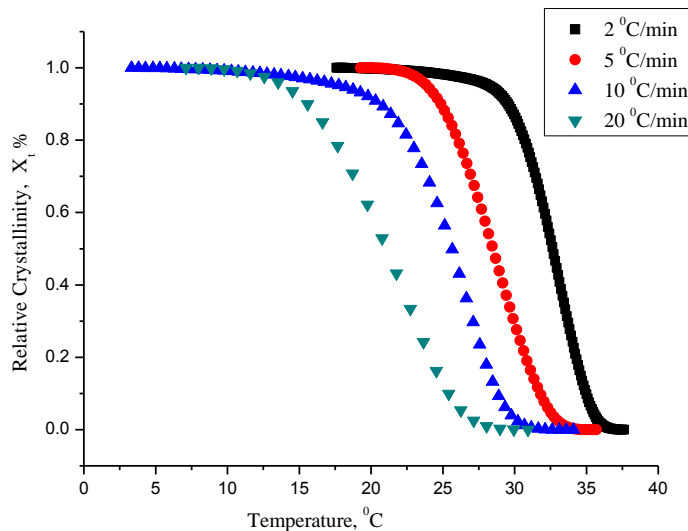


Figure 5.19 Relative crystallinity percent of neat PCL film, X_t , versus temperature at different cooling rates.

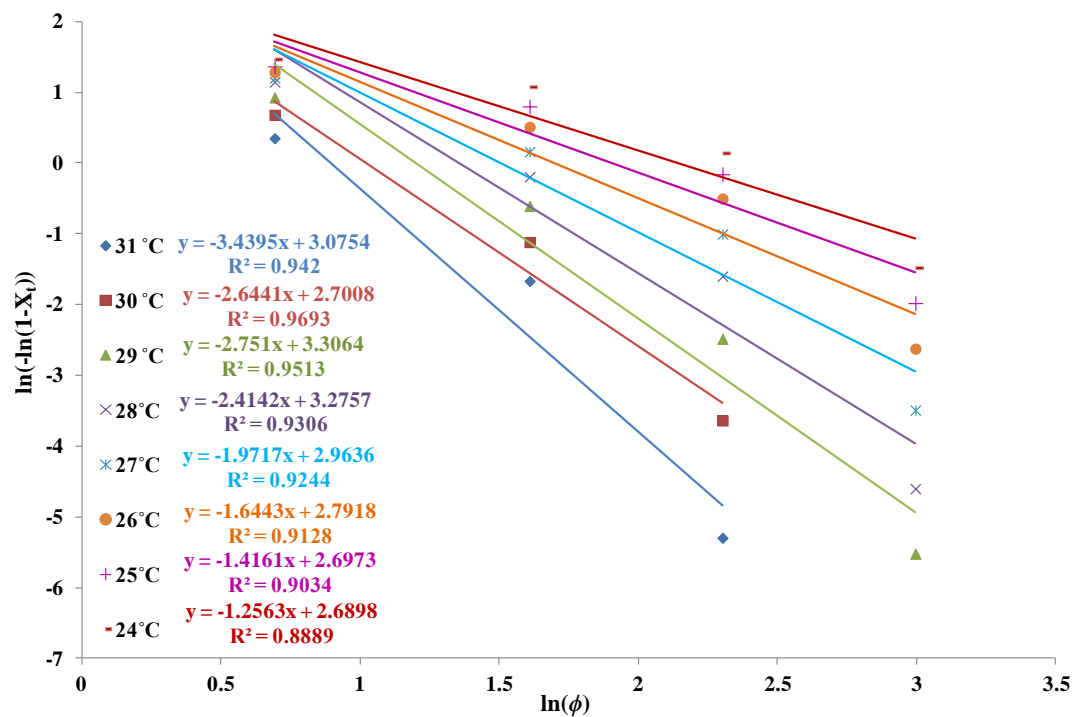


Figure 5.20 Ozawa plot of neat PCL.

Table 5.11 Nonisothermal crystallization kinetics parameters (m, K(T)) and regression coefficients values obtained by Ozawa Model.

	Sample	Temperature (°C)																	
		34	33	32	31	30	29	28	27	26	25	24	23	22	21	20	19		
Ozawa constant, m	PCL_IA0_OA0	-	-	-	3.44	2.64	2.75	2.41	1.97	1.64	1.42	1.26	-	-	-	-	-		
	PCL_IA0_O3	-	-	-	-	2.74	2.25	2.59	2.34	2.09	2.06	1.78	1.49	1.33	-	-	-		
	PLC_IA0_G3	-	-	-	-	-	-	2.5	2.33	2.19	2.02	1.86	1.76	1.64	1.83	1.61	1.41		
	PCL_C0.1_OA0	-	-	-	-	-	-	2.56	2.45	2.34	2.25	2.05	1.92	1.82	2.49	2.36	-		
	PCL_C0.1_O3	-	-	-	-	-	2.68	2.74	2.51	2.26	2.07	1.89	1.87	2.18	2.12	1.98	-		
	PCL_C0.1_G3	-	-	-	2.89	2.35	2.79	2.61	2.94	2.74	2.43	2.02	-	-	-	-	-		
	PCL_C0.1_O5	-	-	3.49	2.79	2.42	1.99	4.13	3.47	2.87	2.57	-	-	-	-	-	-		
	PCL_C3_OA0	-	-	4.59	3.1	2.14	5.21	3.42	2.26	1.67	-	-	-	-	-	-	-		
	PCL_C3_O5	3.29	2.45	1.97	2.65	2.89	2.17	1.45	1.05	-	-	-	-	-	-	-	-		
	PCL_IA0_OA0	-	-	-	3.08	2.7	3.31	3.28	2.96	2.79	2.7	2.69	-	-	-	-	-		
PCL_IA0_O3	-	-	-	-	3.27	3.09	3.78	3.7	4.34	4.29	3.93	3.54	3.25	-	-	-			
PLC_IA0_G3	-	-	-	-	-	-	2.27	2.46	2.69	2.8	2.88	2.97	3.06	3.91	3.74	3.55			
PCL_C0.1_OA0	-	-	-	-	-	-	2.55	2.83	2.99	3.16	3.11	3.24	3.29	5.31	5.3	-			
PCL_C0.1_O3	-	-	-	-	-	2.21	2.74	2.85	2.95	2.99	3.02	3.29	4.42	4.56	4.5	-			
PCL_C0.1_G3	-	-	-	2.41	2.4	3.43	3.7	3.69	5.37	5.06	4.5	-	-	-	-	-			
PCL_C0.1_O5	-	-	2.94	2.99	3.21	3.12	7.63	6.82	6.03	5.03	-	-	-	-	-	-			
PCL_C3_OA0	-	-	5.1	4.06	3.45	9.96	7.04	5.13	4.22	-	-	-	-	-	-	-			
PCL_C3_O5	3.48	3.2	2.97	4.17	5.92	4.82	3.71	3.11	-	-	-	-	-	-	-	-			
PCL_IA0_OA0	-	-	-	0.94	0.97	0.95	0.93	0.92	0.91	0.9	0.89	-	-	-	-	-			
PCL_IA0_O3	-	-	-	-	0.93	0.94	0.93	0.95	0.99	0.99	0.99	0.99	0.99	0.99	-	-			
PLC_IA0_G3	-	-	-	-	-	-	0.99	0.99	0.99	0.99	0.99	0.99	0.98	0.98	0.99	0.99			
PCL_C0.1_OA0	-	-	-	-	-	-	0.99	0.99	0.99	0.97	0.96	0.96	0.94	0.91	0.99	0.99			
PCL_C0.1_O3	-	-	-	-	-	0.97	0.96	0.98	0.98	0.98	0.97	0.97	0.96	0.97	0.97	-			
PCL_C0.1_G3	-	-	-	0.87	0.87	0.92	0.91	0.92	0.98	0.99	0.99	-	-	-	-	-			
PCL_C0.1_O5	-	-	0.98	0.99	0.99	0.99	0.9	0.89	0.89	0.89	-	-	-	-	-	-			
PCL_C3_OA0	-	-	0.88	0.89	0.91	0.9	0.91	0.93	0.94	-	-	-	-	-	-	-			
PCL_C3_O5	0.98	0.94	0.91	0.85	0.92	0.89	0.88	0.86	-	-	-	-	-	-	-	-			

 R^2

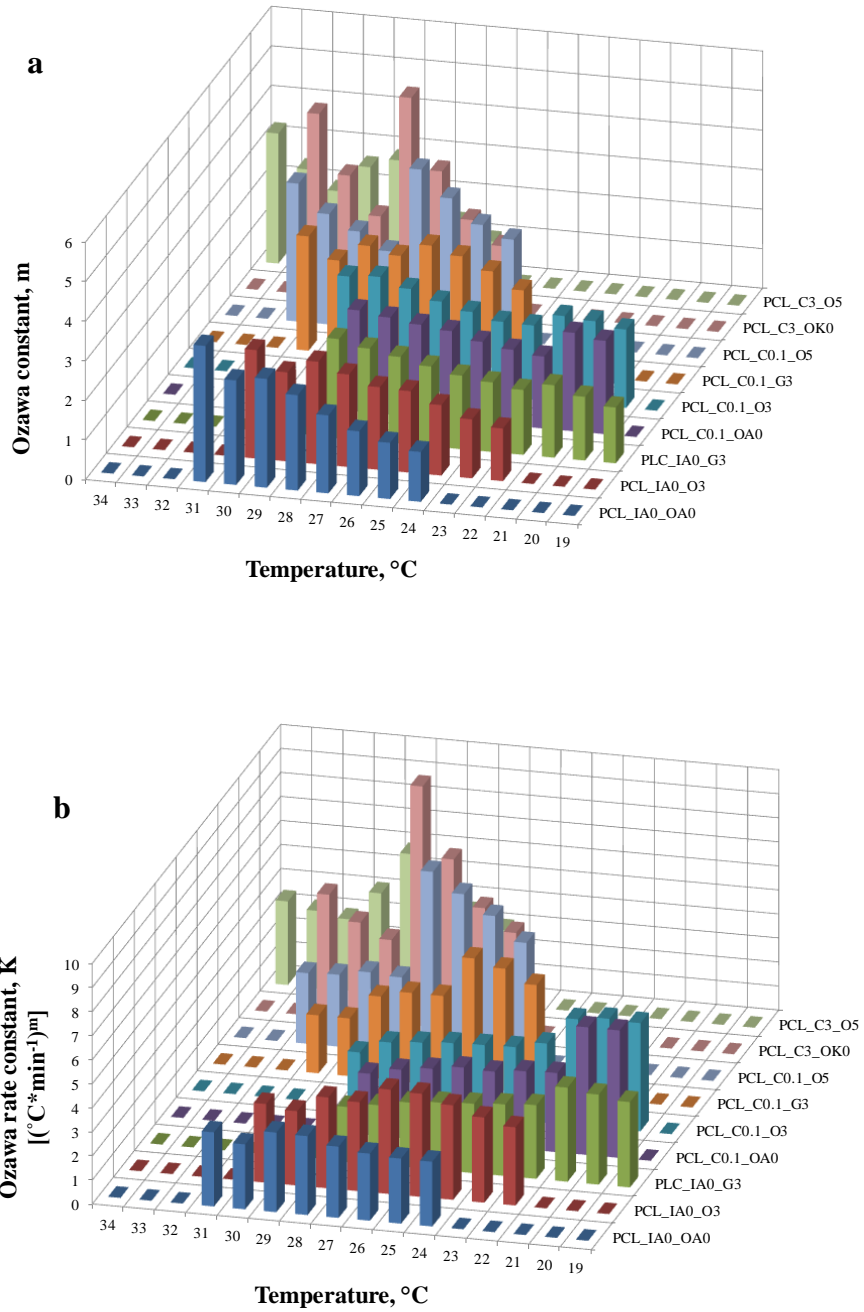


Figure 5.21 a- Variation of Ozawa exponent, b- rate constant $K(T)$ of selected PCL composite films at various temperatures.

Liu Mo model for comparison of isothermal and nonisothermal crystallization kinetics

Liu Mo crystallization model is successfully applied and fit the experimental data.

According to Liu model, plotting $\ln\phi$ versus $\ln t$, series of straight lines are obtained at a given value of relative crystallinity. Liu Mo plot of neat PCL film is given in Figure 5.22. Appendix E, Figure E1 includes Liu Mo plots of selected PCL composite films. The kinetic parameters, $F(T)$ and a , determined by intercept and slope of these lines, respectively. At a certain value of relative crystallinity, X_t , higher value of $F(T)$ means that high cooling rate is needed to reach this X_t in a unit time, which also indicates the difficulty in crystallization process. Liu–Mo model was applied to data at the relative crystallinity values of 20, 40, 60, and 80%. Table 5.12 summarizes the values of Liu–Mo parameters for the samples.

The parameter a was found between 0.99 and 1.63 at various relative crystallinities. Ratio variation of Avrami exponent under isothermal and nonisothermal conditions is shown in Figure 5.23a. Variation of $\ln F(T)$ values are shown in Figure 5.23b. 3% clay contained composite films show lower value which indicates ease of crystallization. 0.1% clay and organic additive load is increased the $\ln F(T)$ value and this causes difficulty in crystallization.

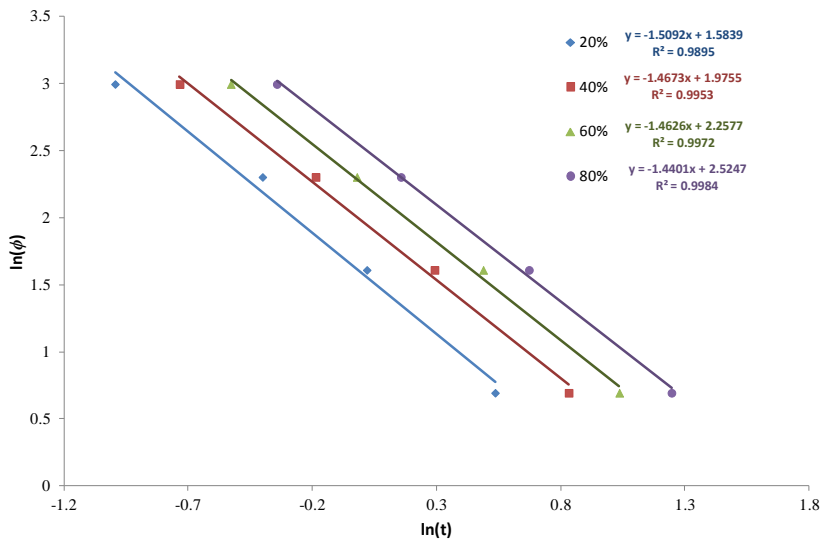


Figure 5.22 Liu Mo plot for neat PCL.

Table 5.12 Comparison of isothermal and nonisothermal crystallization kinetics parameter (α , $\ln F(T)$) and regression coefficient values obtained by Liu Mo Model.

Sample Code	Lui-Mo Model				Sample Code	Lui-Mo Model			
	Relative Crystallinity, %	α	$\ln F(T)$	R^2		Relative Crystallinity, %	α	$\ln F(T)$	R^2
PCL_IA0_OA0	20	1.51	1.58	0.99	PCL_C0.1_G3	20	1.34	1.72	0.99
	40	1.47	1.98	0.99		40	1.31	2.04	0.99
	60	1.46	2.26	0.99		60	1.31	2.29	0.99
	80	1.44	2.52	0.99		80	1.33	2.55	0.99
PCL_IA0_O3	20	1.74	1.71	0.99	PCL_C0.1_O5	20	1.55	1.67	0.97
	40	1.71	2.08	0.99		40	1.56	1.99	0.98
	60	1.63	2.37	0.99		60	1.56	2.20	0.98
	80	1.57	2.65	0.99		80	1.58	2.42	0.99
PLC_IA0_G3	20	1.48	2.22	0.99	PCL_C3_OA0	20	0.99	1.40	0.99
	40	1.43	2.52	0.99		40	1.04	1.58	0.99
	60	1.38	2.68	0.99		60	1.09	1.73	0.99
	80	1.39	2.88	0.99		80	1.18	1.92	0.99
PCL_C0.1_OA0	20	1.37	2.30	0.99	PCL_C3_O5	20	1.42	1.60	0.99
	40	1.36	2.59	0.99		40	1.41	1.82	0.99
	60	1.37	2.78	0.99		60	1.43	1.99	0.99
	80	1.39	2.98	0.99		80	1.45	2.17	0.99
PCL_C0.1_O3	20	1.51	2.25	0.99					
	40	1.40	2.58	0.99					
	60	1.36	2.77	0.99					
	80	1.37	2.95	0.99					

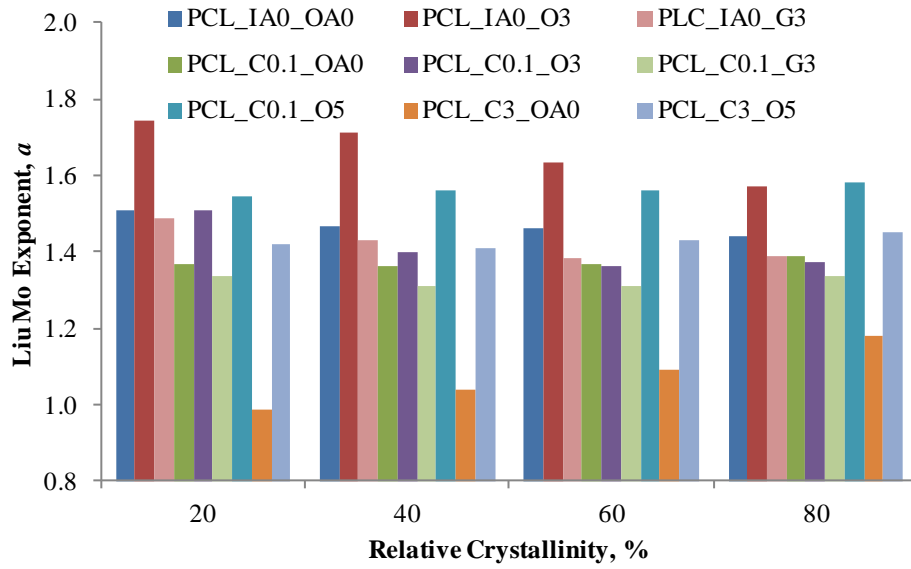
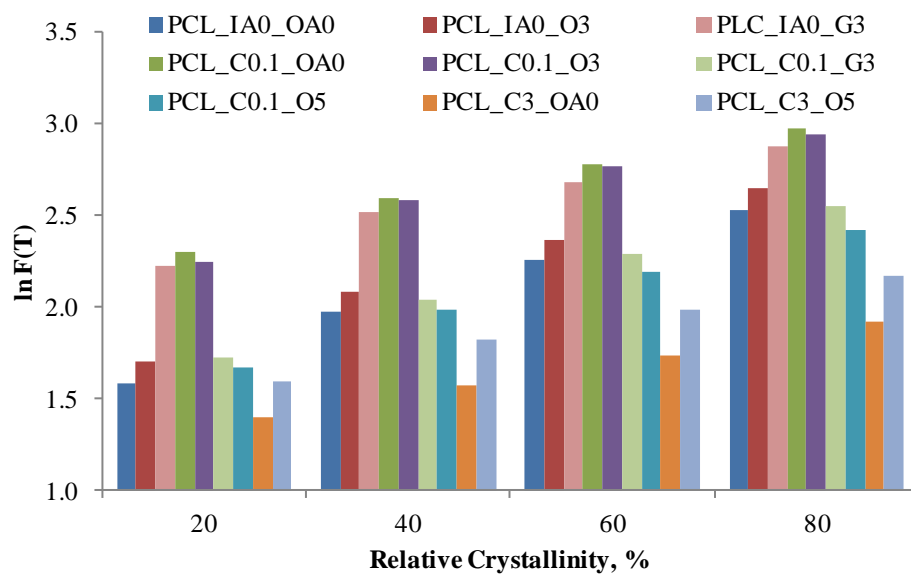
a**b**

Figure 5.23 Variation of Liu Mo parameters; a – Liu Mo constant, a ; b – Cooling rate value, $\ln F(T)$.

Secondary nucleation kinetics model: Lauritzen Hoffman

Lauritzen Hoffman (L-H) plot of nonisothermal crystallization of neat PCL film at different cooling rates is shown in

Figure 5.24. Appendix F, Figure F1 shows L-H plot of nonisothermal crystallization of selected PCL composite films at different cooling rates. It is revealed that with decreasing cooling rate, PCL composite films are shifted from Regime II to Regime III as seen in Figure 5.24 (see earlier Figure 3.20a).

It was reported that when the cooling rate increased, composite films passed through Regime III and nucleation rate and quality increased (Grozdanov et al., 2007). For PCL composite films obtained by solvent casting, when they slowly crystallize at room temperature, both crystallization and nucleation occurs in complexity on the surface as Regime II. Therefore crystals formed are imperfect and melting temperature decreases.

Variation of overall crystallization growth rate G_0 (Figure 5.25a-b), crystallization rate K_g (Figure 5.26a-b), growth crystal surface free energy σ_e (Figure 5.27a-b) of nonisothermally crystallized composite films obtained by Lauritzen Hoffman Model were calculated according to Regime II and to Regime III. Growth rate constants of Regime II is 10 times higher than the growth rate constant of Regime III. Solvent cast composite films show Regime II type crystallization at low cooling rates. In regime II, deposition of secondary nuclei (i) and the rate of lateral surface spreading (g) occurred at the same time and this caused formation of defective crystals. The melting temperatures of the solvent cast films show low melting temperatures due to the defective crystals. The ratio of regime rate constant is R ($K_{g,III}/K_{g,II}$) (Figure 5.28a) and regime transition temperature (Figure 5.28b) is $T_{III \rightarrow II}$ tabulated in Table 5.13 to Table 5.15. As increased cooling rate, overall crystallization growth rate G_0 , growth crystal surface free energy, and crystallization rate K_g also increased. Regime transition temperature $T_{II \rightarrow III}$ change is between 15.90°C (PCL_IK0_G3 with 20°C/min cooling rate) and 30.54 °C (PCL_C0.1_O3 with 2°C/min cooling rate). The results show that secondary crystallization also could be controlled under nonisothermal conditions.

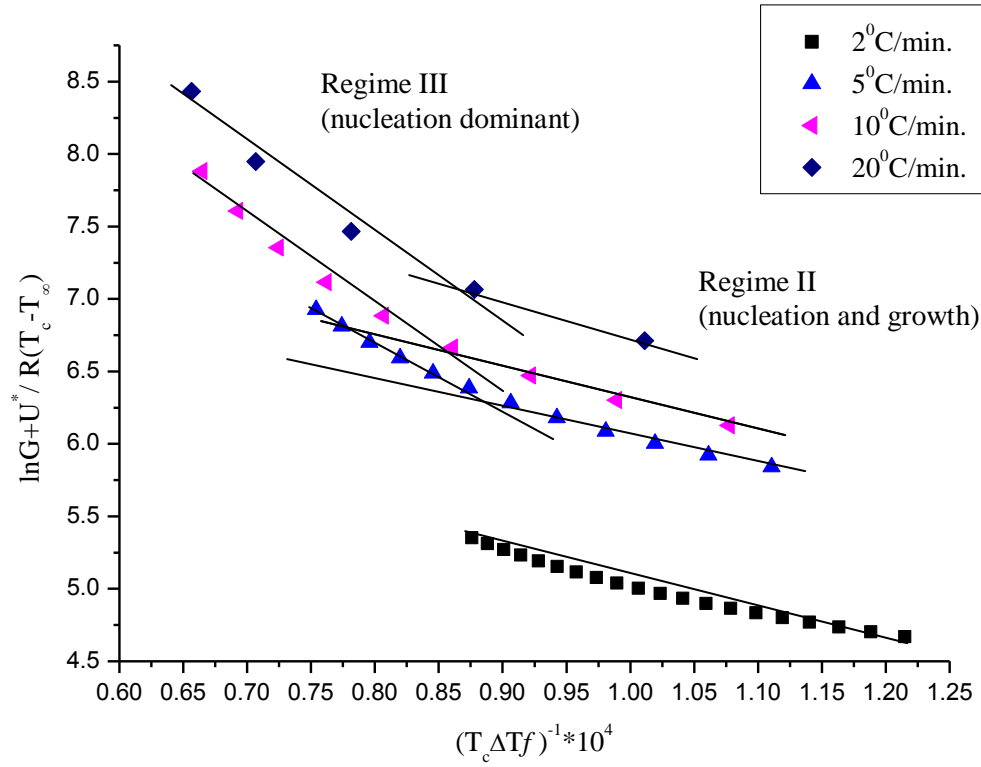


Figure 5.24 Lauritzen Hoffman plot of neat PCL.

Table 5.13 Variation of overall crystallization growth rate G_0 , crystallization rate K_g , growth crystal surface free energy σ_e of nonisothermal crystallized composite films obtained by Lauritzen Hoffman Model were calculated according to Regime IIb and to Regime III. The ratio of regime rate constant is R ($K_{g,III}/K_{g,II}$) and regime transition temperature is $T_{II \rightarrow III}$.

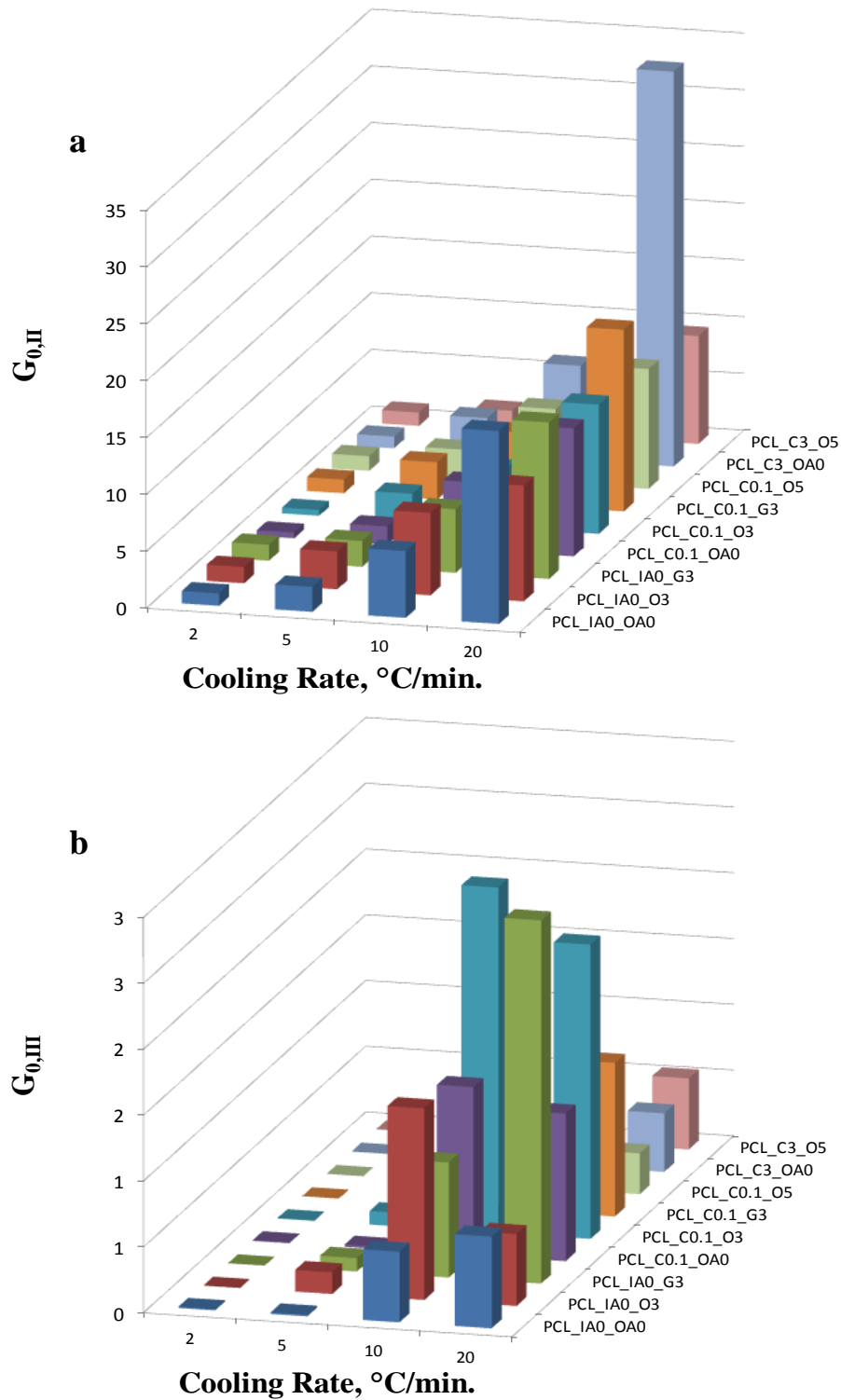
	Cooling rate, ϕ , ($^{\circ}\text{C}/\text{min}$)	Regime III			Regime II			R ($K_{g,III}/K_{g,II}$)	$T_{II \rightarrow III}$ ($^{\circ}\text{C}$)
		$G_0 \times 10^{-10}$	$K_{g,III} \times 10^{-4}$ (K^2)	$\sigma_e \times 10^2$ (J/m^2)	$G_0 \times 10^{-7}$	$K_{g,II} \times 10^{-4}$ (K^2)	$\sigma_e \times 10^2$ (J/m^2)		
PCL_IA0_OA0	2	0.01	3.94	2.04	1.09	1.71	1.77	2.30	28.50
	5	0.01	3.75	1.95	2.20	1.87	1.94	2.01	27.94
	10	0.54	7.95	4.13	5.88	2.36	2.45	3.37	20.50
	20	0.70	7.53	3.91	16.97	2.86	2.97	2.63	19.00
PCL_IA0_O3	2	-	-	-	1.44	1.96	2.03	-	-
	5	0.16	6.88	3.57	3.33	2.17	2.25	3.17	22.00
	10	1.45	9.42	4.89	7.26	2.60	2.70	3.62	18.00
	20	0.55	7.52	3.90	10.20	2.58	2.68	2.91	19.00
PCL_IA0_G3	2	-	-	-	1.41	2.35	2.44	-	-
	5	0.10	6.79	3.52	2.28	2.21	2.29	3.07	22.32
	10	0.87	9.11	4.73	5.60	2.63	2.73	3.46	18.51
	20	2.76	10.04	5.21	13.77	3.04	3.15	3.30	15.90

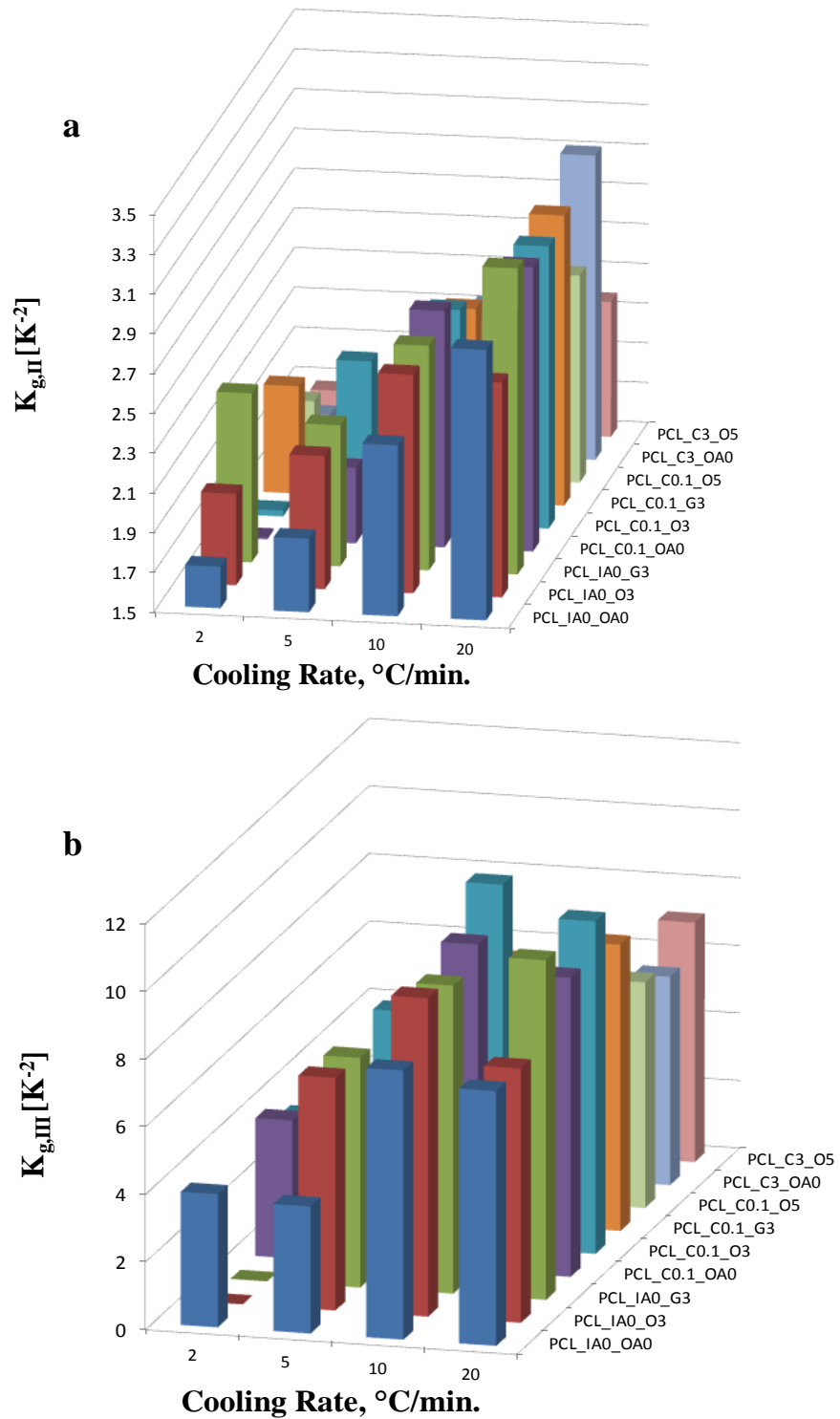
Table 5.14 Variation of overall crystallization growth rate G_0 , crystallization rate K_g , growth crystal surface free energy σ_e of nonisothermal crystallized composite films obtained by Lauritzen Hoffman Model were calculated according to Regime II and to Regime III. The ratio of regime rate constant is R ($K_{g,III}/K_{g,II}$) and regime transition temperature is $T_{II \rightarrow III}$.

	Cooling rate, ϕ , ($^{\circ}\text{C}/\text{min}$)	Regime III			Regime II			R ($K_{g,III}/K_{g,II}$)	$T_{II \rightarrow III}$ ($^{\circ}\text{C}$)
		$G_0 \times 10^{-10}$	$K_{g,III} \times 10^{-4}$ (K^2)	$\sigma_e \times 10^2$ (J/m^2)	$G_0 \times 10^{-7}$	$K_{g,III} \times 10^{-4}$ (K^2)	$\sigma_e \times 10^2$ (J/m^2)		
PCL_C0.1_OA0	2	0.01	4.08	2.12	0.50	1.51	1.57	2.70	26.60
	5	0.02	4.51	2.34	1.57	1.88	1.95	2.40	26.60
	10	1.28	9.65	5.01	5.94	2.69	2.79	3.59	17.95
	20	1.12	8.85	4.59	11.27	2.93	3.04	3.02	18.28
PCL_C0.1_O3	2	0.00	3.52	1.82	0.52	1.53	1.59	2.30	30.54
	5	0.10	6.80	3.53	2.47	2.30	2.39	2.96	21.78
	10	2.62	10.74	5.57	5.22	2.58	2.68	4.16	16.75
	20	2.24	9.84	5.10	11.38	2.92	3.03	3.37	17.45
PCL_C0.1_G3	2	-	-	-	1.20	2.04	2.12	-	-
	5	0.04	4.89	2.54	3.26	2.04	2.12	2.40	25.46
	10	0.46	7.80	4.05	6.37	2.47	2.56	3.16	20.49
	20	1.17	8.47	4.39	15.99	2.96	3.07	2.86	18.52

Table 5.15 Variation of overall crystallization growth rate G_0 , crystallization rate K_g , growth crystal surface free energy σ_e of nonisothermal crystallized composite films obtained by Lauritzen Hoffman Model were calculated according to Regime II and to Regime III. The ratio of regime rate constant is R ($K_{g,III}/K_{g,II}$) and regime transition temperature is $T_{II \rightarrow III}$.

	Cooling rate, ϕ , ($^{\circ}\text{C}/\text{min}$)	Regime III			Regime II			R ($K_{g,III}/K_{g,II}$)	$T_{III \rightarrow II}$ ($^{\circ}\text{C}$)
		$G_0 \times 10^{-10}$	$K_{g,III} \times 10^{-4}$ (K^2)	$\sigma_e \times 10^2$ (J/m^2)	$G_0 \times 10^{-7}$	$K_{g,III} \times 10^{-4}$ (K^2)	$\sigma_e \times 10^2$ (J/m^2)		
PCL_C0.1_O5	2	-	-	-	1.29	1.85	1.92	-	-
	5	0.01	3.76	1.95	2.40	1.87	1.93	2.02	28.25
	10	0.14	5.97	3.10	6.50	2.31	2.39	2.59	23.07
	20	0.31	6.68	3.46	10.56	2.54	2.64	2.63	21.35
PCL_C3_OA0	2	-	-	-	1.04	1.67	1.73	-	-
	5	0.01	3.31	1.72	3.19	1.80	1.87	1.84	29.50
	10	0.06	4.57	2.37	8.33	2.25	2.34	2.03	25.70
	20	0.44	6.16	3.20	34.79	3.03	3.15	2.03	20.90
PCL_C3_O5	2	-	-	-	1.18	1.67	1.73	-	-
	5	0.03	4.42	2.29	1.86	1.59	1.65	2.78	27.95
	10	0.02	3.63	1.88	3.79	1.73	1.79	2.10	28.93
	20	0.54	7.09	3.68	9.51	2.18	2.26	3.25	22.00





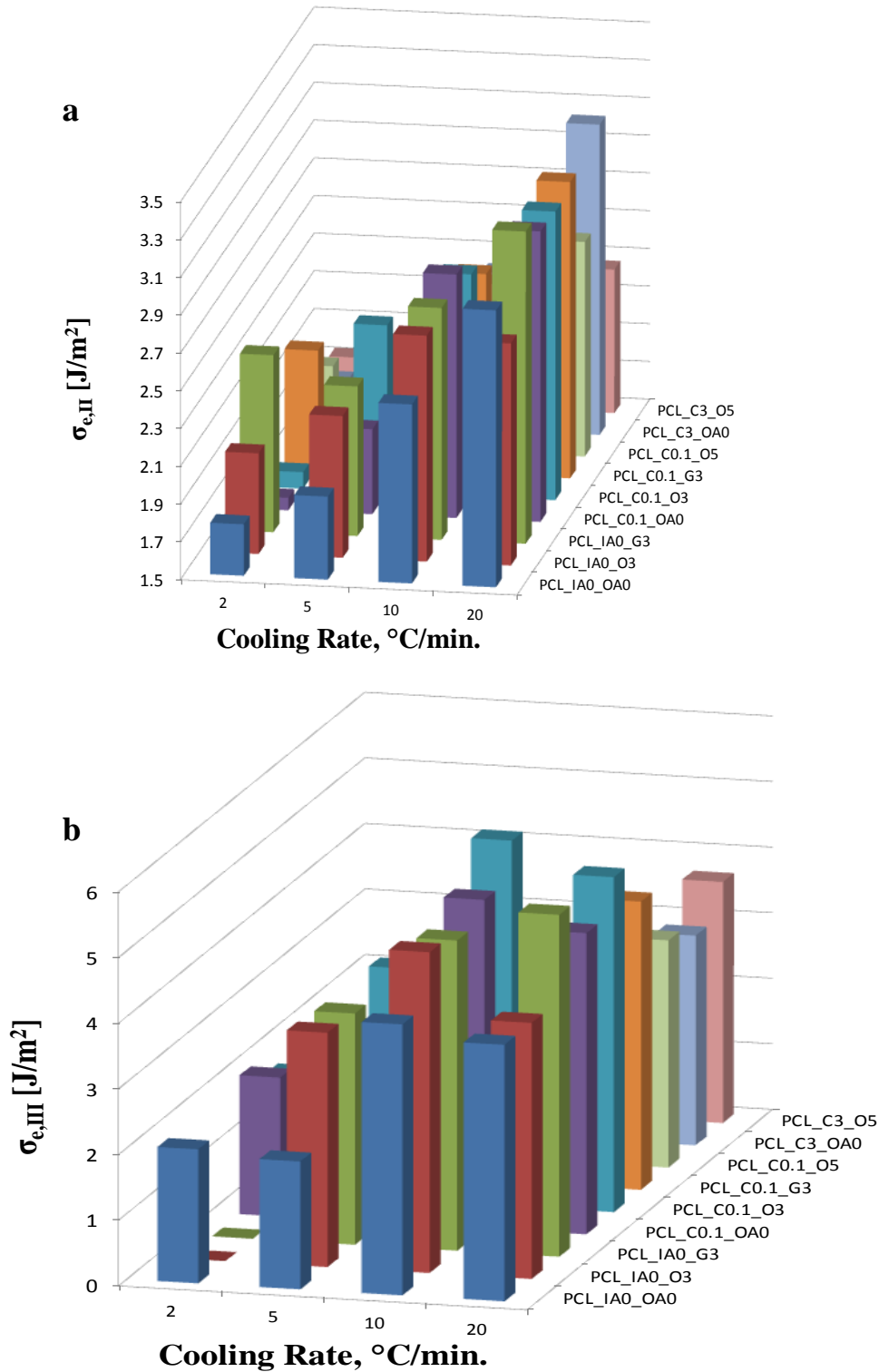


Figure 5.27 Variation of growth crystal surface free energy; a – Regime II; b – Regime III.

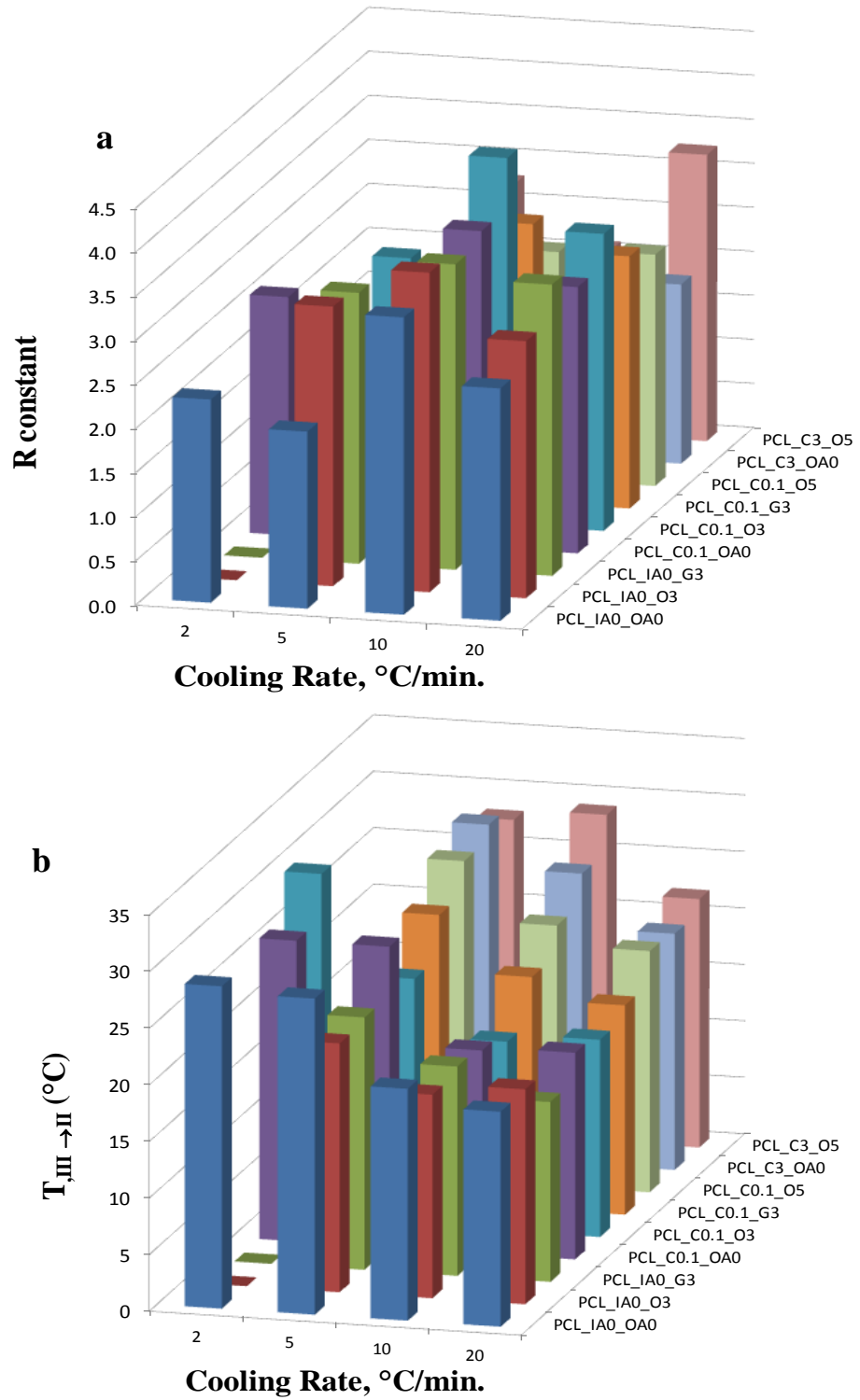


Figure 5.28 Variation of; a – R constant; b – Transition temperature from Regime III to II.

5.2. Crystallization Activation Energy

Kissinger and Augis–Bennett plots of the samples are given in Figure 5.29 and Figure 5.30, and the ΔE_A values are listed in Table 5.16. ΔE_A is negative because of exothermic nature of the transition from melt to crystalline state, and the negative activation energy values also imply that crystallization mechanisms are accelerated by decreasing the temperatures.

From the calculation based on the Kissinger approach, activation energies were found between -176.89 kJ/mol (PCL_C0.1_OA0) and -313.35 kJ/mol (PCL_C3_O5). From Augis–Bennett approach, activation energies were found between -144.72 kJ/mol (PCL_C0.1_OA0) and -271.58 kJ/mol (PCL_C3_OA0). 3% clay contained composite films have lower the activation energy values which shows that clay act as nucleating agent. Figure 5.31 shows comparison the results of both methods. There is a gap between results but the tendency is the same for both methods. Also the regression constants are above 90% for all calculations.

Table 5.16 Crystallization activation energy values obtained from Kissinger and Augis Bennet for nonisothermally crystallized selected PCL composite films.

Sample Code	Kissenger Slope	R ²	Augis–Bennett Slope	R ²	Kissenger Activation Energy, ΔE_A (kJ mol ⁻¹)	Augis–Bennett Activation Energy, ΔE_A (kJ mol ⁻¹)
PCL_IA0_OA0	26.612	0.98	22.223	0.97	-221.25	-184.76
PCL_IA0_O3	23.793	0.99	19.237	0.98	-197.82	-159.94
PCL_IA0_G3	27.184	0.99	23.204	0.99	-226.01	-192.92
PCL_C0.1_OA0	21.276	0.99	17.407	0.98	-176.89	-144.72
PCL_C0.1_O3	23.378	0.96	19.587	0.95	-194.36	-162.85
PCL_C0.1_G3	28.99	0.93	24.663	0.90	-241.02	-205.05
PCL_C0.1_O5	28.443	0.94	24.07	0.92	-236.48	-200.12
PCL_C3_OA0	37.436	0.98	32.665	0.97	-311.24	-271.58
PCL_C3_O5	37.689	0.98	32.57	0.99	-313.35	-270.79

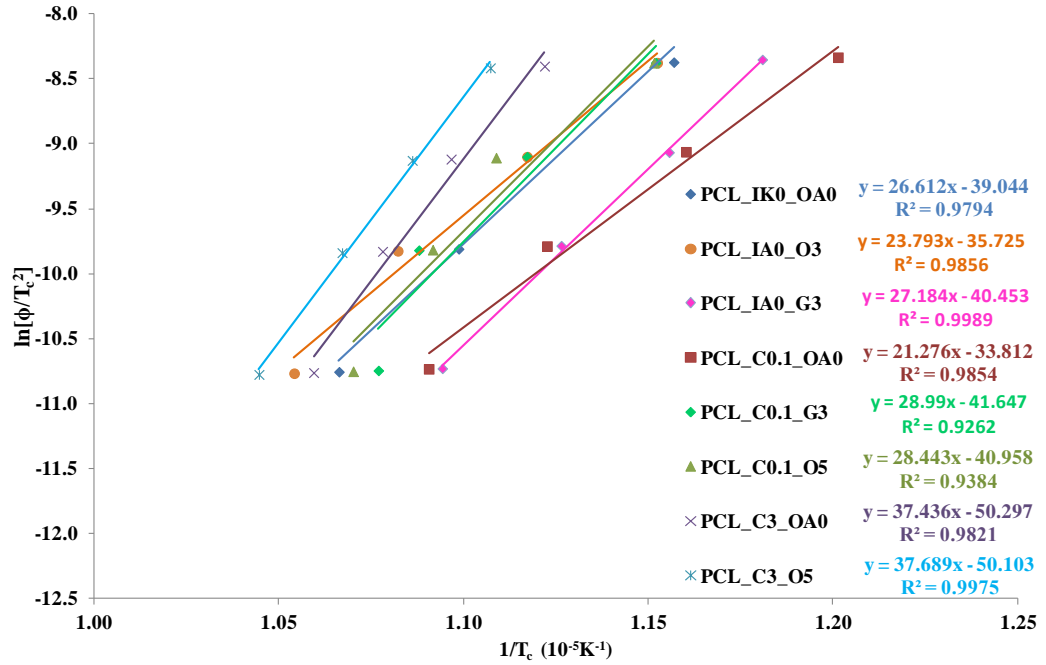


Figure 5.29 Kissinger plots of nonisothermally crystallized selected samples.

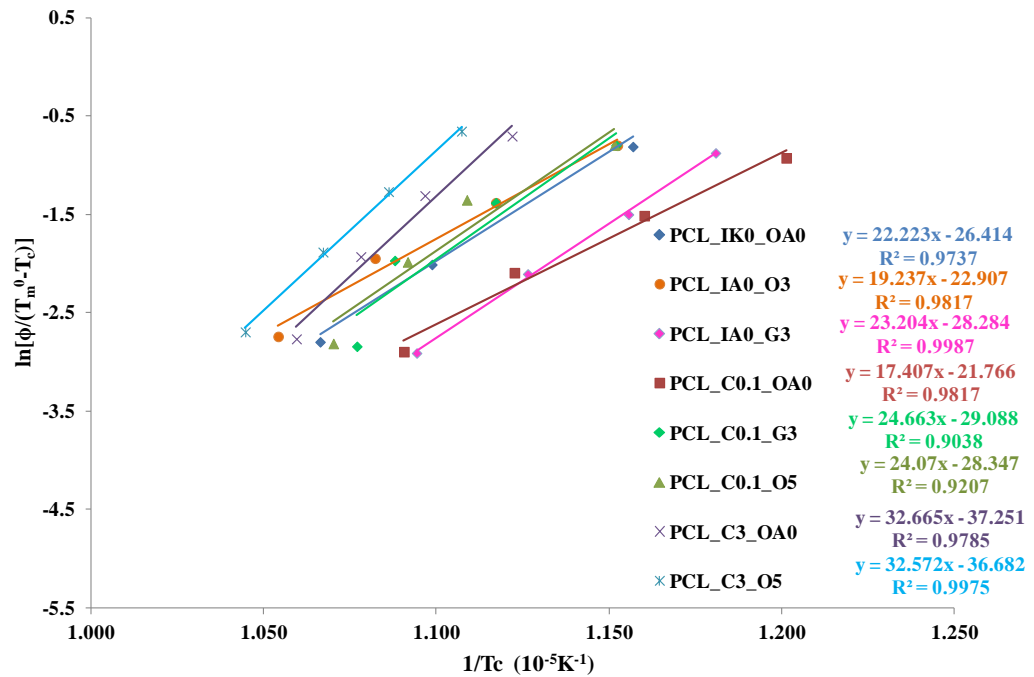


Figure 5.30 Augis-Bennett plots of nonisothermally crystallized selected samples.

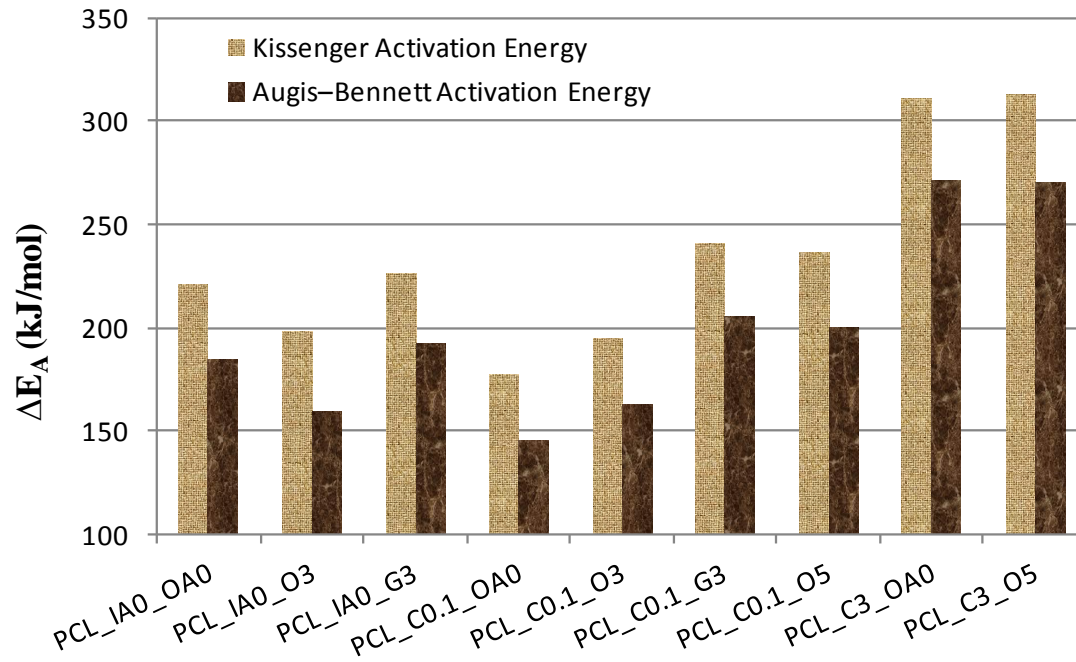


Figure 5.31 Comparison of crystallization activation energies calculated from different models.

5.3. Crystal Morphology and Growth Rate Kinetics

Figure 5.32 to Figure 5.34 show melting and crystallization of neat PCL, PCL_C0.1_O3 and PCL_C3_O5 with different cooling rates under nonisothermal conditions. POM picture of selected composite films are given in Appendix G, Figures G1 to G21. As seen from the pictures, porosity and amorph regions of the composite films are decreased after first melting which shows crystallization from solvent and melt have different mechanisms. The results are tabulated in Table 5.17. Beside melting start temperatures have scattering, there is increasing tendency with high amount of clay addition. However, the melting points from solvent cast films are higher than melting points which were obtained from DSC analysis. There is an inconsistency of the crystallization start temperature for PCL_C3_O5 film as 53.30 °C that is higher value than the 2 °C/min cooling rate. These deviations could be depended on temperature control devices. The film has been cooled by liquid nitrogen and heated on the hot plate. The temperature measurements have been taken from the films surface might have some deviations. As mentioned in nonisothermal crystallization, the crystallization temperature is decreased with increasing cooling rate. Especially oleic acid addition increased the crystallization temperature and crystallization half time is decreased. This shows that oleic acid is ease and accelerates the polymer chain conformation during the crystallization. 3% clay contained composite film shows reverse effect and causes defective crystals but addition of organic additives slightly accelerate the crystallization.

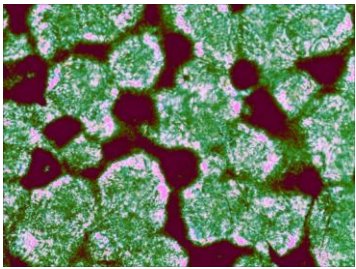
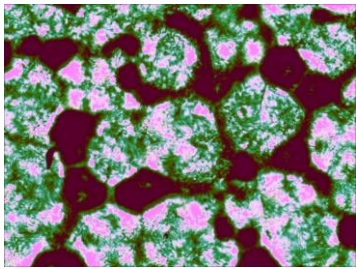
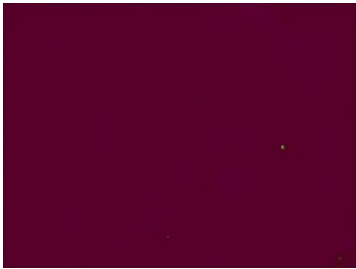
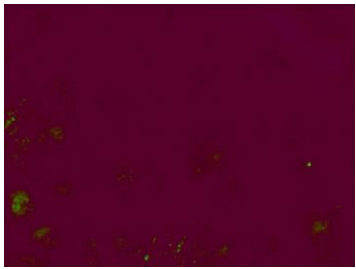
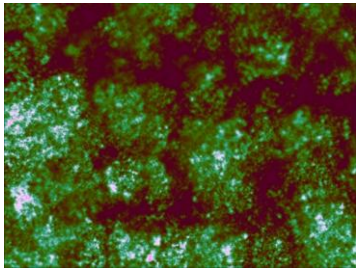
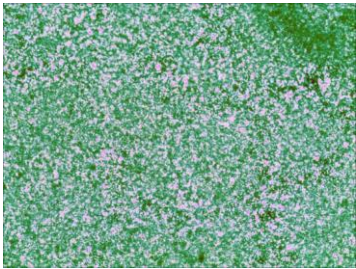
Neat PCL (2 °C/min)		
		
t = 0, T = 15.1 °C (crystal morphology of films by solvent casting)	t = 7 min 48 sec., T = 87.0 °C	t = 8 min 27 sec., T = 100.0 °C (fully melted)
		
t = 13 min 46 sec., T = 54.3 °C	t = 16 min 33 sec., T = 48.7 °C	t = 17 min 21 sec., T = 41.1 °C (crystals of films obtained by melt)

Figure 5.32 POM micro photos of neat PCL with 2 °C/min cooling rate.

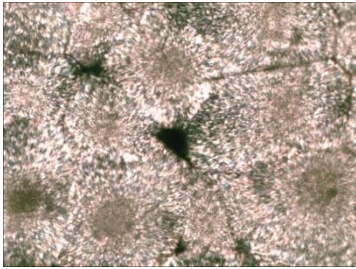
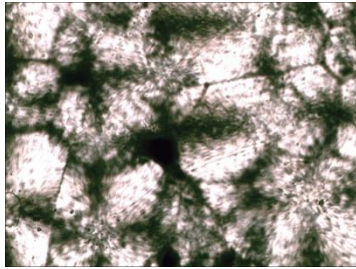
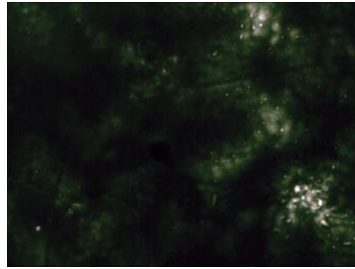
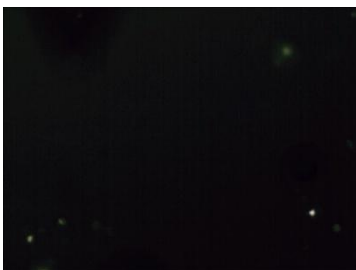
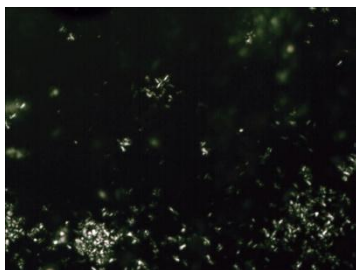
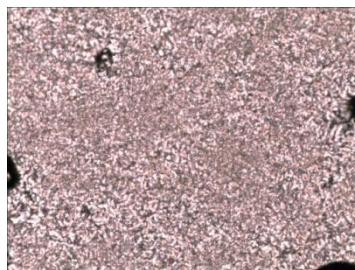
PCL_C0.1_O3 (2 °C/min)		
		
t = 0, T = 34.2 °C	t = 5 min 46 sec., T = 91.9 °C	t = 5 min 54 sec., T = 93.2 °C
		
t = 11 min 07 sec., T = 100.0 °C	t = 34 min 22 sec., T = 53.5 °C	t = 37 min 21 sec., T = 47.5 °C

Figure 5.33 POM micro photos of PCL_C0.1_O3 with 2 °C/min cooling rate.

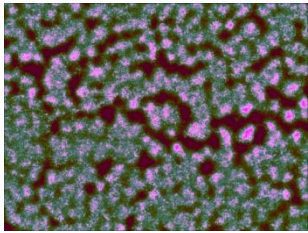
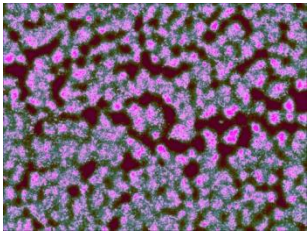
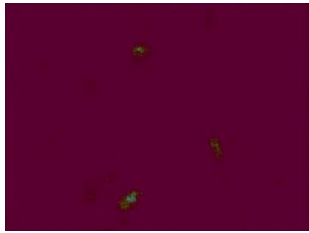
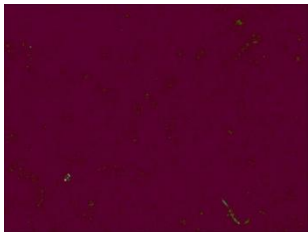
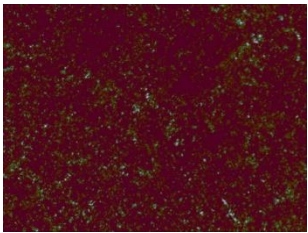
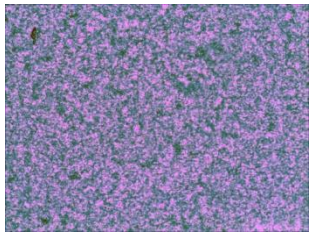
PCL_C3_O5 (20 °C/min)		
		
t = 0. T = 32.5 °C	t = 6 min 39 sec., T = 99.7 °C	t = 6 min 48 sec., T = 100.5 °C
		
t = 11 min 48 sec., T = 110.0 °C	t = 14 min 38 sec., T = 53.3 °C	t = 15 min 42 sec., T = 32.0 °C

Figure 5.34 POM micro photos of PCL_C3_O5 with 20 °C/min cooling rate.

Table 5.17 Melting and crystallization start temperatures of the films obtained by POM analysis.

Sample	ϕ , [°C/min]	Melting Start Temperature, T_m [°C]	Crystallization Start Temperature, T_s [°C]
Neat PCL	2	87.00	48.70
	5	72.50	49.30
	10	89.50	37.30
	20	83.50	31.30
PCL_C0.1_OA0	2	78.20	51.60
	20	86.40	28.70
PCL_C0.1_O3	2	91.90	53.50
	20	86.90	28.30
PCL_C0.1_G3	2	91.60	47.30
	20	77.40	27.30
PCL_C3_OA0	2	90.70	40.70
	5	93.40	33.70
	10	91.50	38.70
	20	91.70	33.70
PCL_C3_O5	2	90.20	49.70
	5	78.90	42.80
	10	86.80	36.80
	20	99.70	53.30
PCL_C3_G5	2	91.30	48.40
	5	93.70	56.58
	10	87.00	49.00
	20	91.40	40.00

5.4. Product Properties

5.4.1. Density

The geometrical, experimental and theoretical density values of prepared composite films are given in Table 5.18. Experimental density values of composite films were measured by Archimedes method which were close to theoretical density values, however, geometrical density values are lower than theoretical and experimental measurements due to porous structure of composite films. The variation of density values of composite films measured by Archimedes method depend on additive concentration is given in Figure 5.35. The minimum density value measured for 3 wt % oleic acid doped films (PCL_IA0_O3) is 0.97 g/cm^3 , the maximum density value is obtained for %1 clay added film (PCL_C1_OA0) as 1.2 g/cm^3 . Experimental density of films measured with clay additions as expected. Clay addition causes a slight increase in experimental densities for 0.1, 0.4 and 1 wt%, but for 3 wt% causes the density decrease. Because the small amount of clay acts as a nucleating agent and increases the degree of crystallinity of the films and the density increases. But 3 wt% clay cause imperfect crystals. The effect of organic additives are negligible.

Table 5.18 Density values of composite films.

Clay, wt. %	Organic Additive wt %	$\rho_{\text{geometrical}}$ g/cm ³		$\rho_{\text{theoretical}}$ g/cm ³		$\rho_{\text{experimental}}$ g/cm ³	
		O	GMO	O	GMO	O	GMO
0	0	0.740		1.145		1.030	
	1	0.850	1.250	1.142	1.143	1.010	1.110
	3	0.930	1.190	1.136	1.139	0.970	1.090
	5	0.840	1.430	1.130	1.135	1.080	1.080
0.1	0	1.006		1.145		1.159	
	1	1.061	1.136	1.146	1.147	1.110	1.115
	3	1.052	1.059	1.139	1.143	1.181	1.160
	5	1.052	1.028	1.134	1.139	1.129	1.144
0.4	0	1.320		1.146		1.170	
	1	1.298	1.032	1.143	1.144	1.153	1.148
	3	1.410	1.036	1.137	1.140	1.139	1.127
	5	1.483	1.097	1.131	1.137	1.182	1.149
1	0	1.299		1.149		1.200	
	1	1.230	1.019	1.146	1.147	1.163	1.147
	3	1.217	1.052	1.139	1.143	1.073	1.136
	5	1.361	1.049	1.134	1.139	1.169	1.150
3	0	1.175		1.156		1.162	
	1	1.169	0.996	1.153	1.154	1.151	1.166
	3	1.400	0.992	1.147	1.150	1.143	1.155
	5	1.266	1.110	1.141	1.146	1.171	1.155

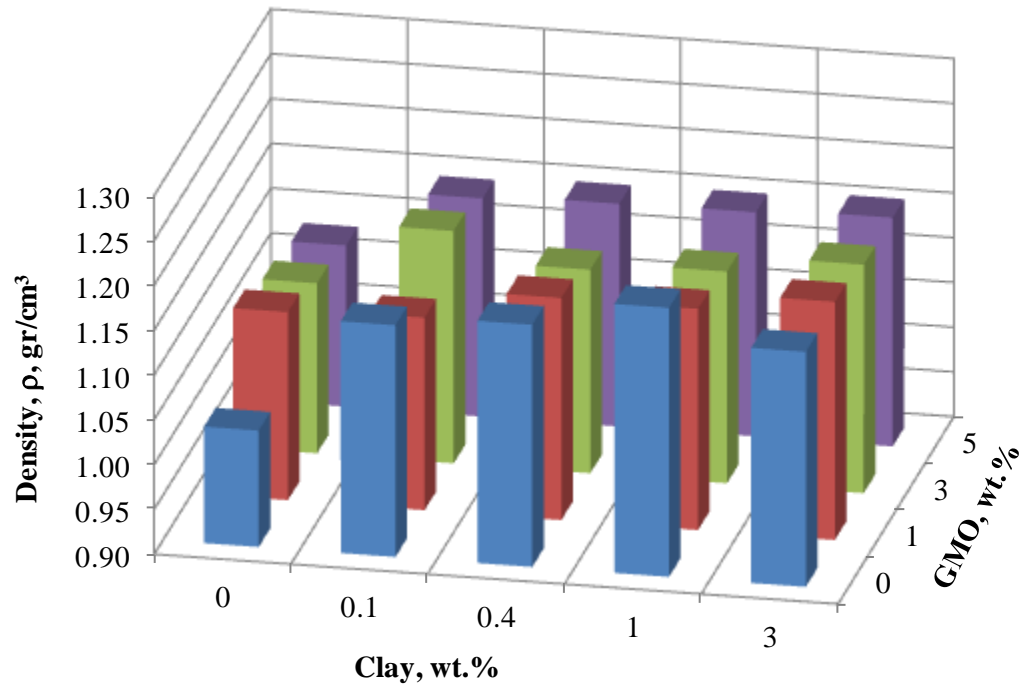
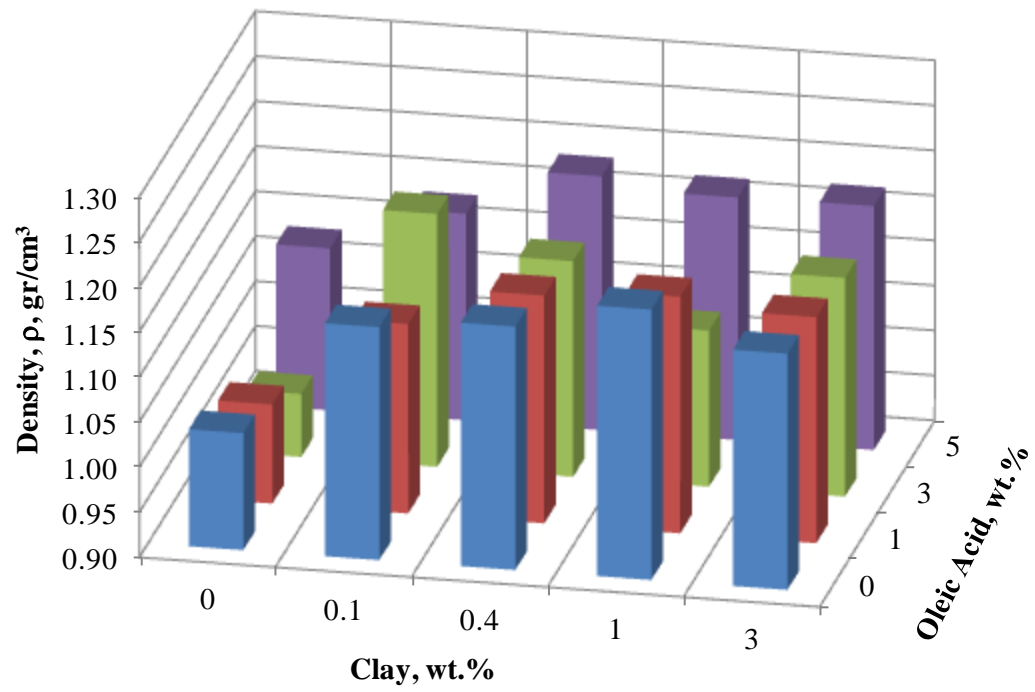


Figure 5.35 The variation of density values of composite films measured by Archimedes method depend on additive concentration.

Table 5.19 shows the measured contact angle and obtained surface tension values of composite films. The measured contact angle values changed between 61.6° and 83.4° for sample PCL_C3_G5 and PCL_C0.4_G3 respectively. Figure 5.36 shows the variation of measured contact angle values of PCL composite films depend on additive concentration. Clay and oleic acid addition have no significant effect, but the GMO decreased the contact angle value. It can be concluded that the composite films are gained higher wettability properties by addition of GMO. The composite films can be used in different packaging applications by adjusting properties with additives. Surface tension of the neat PCL was found as 255.25 mN/m. Surface tension of the PCL composite films change between 35.9 (PCL_C1_G5) and 327.9 mN/m (PCL_C0.1_OA0). Figure 5.37 illustrates the variation of obtained surface tension values of PCL composite films depend on additive concentration. The surface tension values are especially decreased with GMO addition. Hydrophobic property of neat PCL is especially decreased with GMO additive.

Table 5.19 Contact angle and surface tension value of composite films.

Clay, wt. %	Organic Additive, wt %	$\theta_{\text{average}} (^{\circ})$		Std. dev.		$\gamma_{\text{average}} \text{ (mN/m)}$		Std. dev.	
		O	GMO	O	GMO	O	GMO	O	GMO
0	0	79.9		-		255.3		-	
	1	70.4	79.9	-	-	243.1	152.6	-	-
	3	74.1	77.4	-	-	140.4	207.2	-	-
	5	69.9	70.4	-	-	241.2	139.2	-	-
0.1	0	78.5		0.8		327.9		18.3	
	1	72.0	66.6	0.3	0.4	140.5	94.8	4.1	15.1
	3	70.6	63.0	1.2	3.1	138.0	97.9	11.2	22.6
	5	74.0	73.5	1.1	7.9	120.6	80.3	13.9	15.9
0.4	0	77.9		1.5		141.8		12.3	
	1	71.0	70.9	0.5	3.1	148.4	98.0	20.0	23.2
	3	71.9	83.4	0.3	1.5	166.6	75.7	7.5	0.8
	5	72.6	75.6	0.3	0.9	145.4	118.5	10.1	15.3
1	0	79.3		0.3		179.8		7.4	
	1	75.8	71.7	0.4	0.4	241.2	105.3	29.3	1.6
	3	81.4	68.6	0.2	0.3	96.7	105.6	19.5	2.7
	5	72.0	68.2	0.5	0.4	176.6	35.9	19.1	3.5
3	0	79.5		0.4		164.3		11.4	
	1	77.8	65.6	0.6	0.4	131.6	59.4	5.9	10.1
	3	73.0	72.6	0.4	0.5	142.1	43.5	4.4	7.8
	5	76.3	61.6	0.4	0.3	148.3	62.0	9.0	5.5

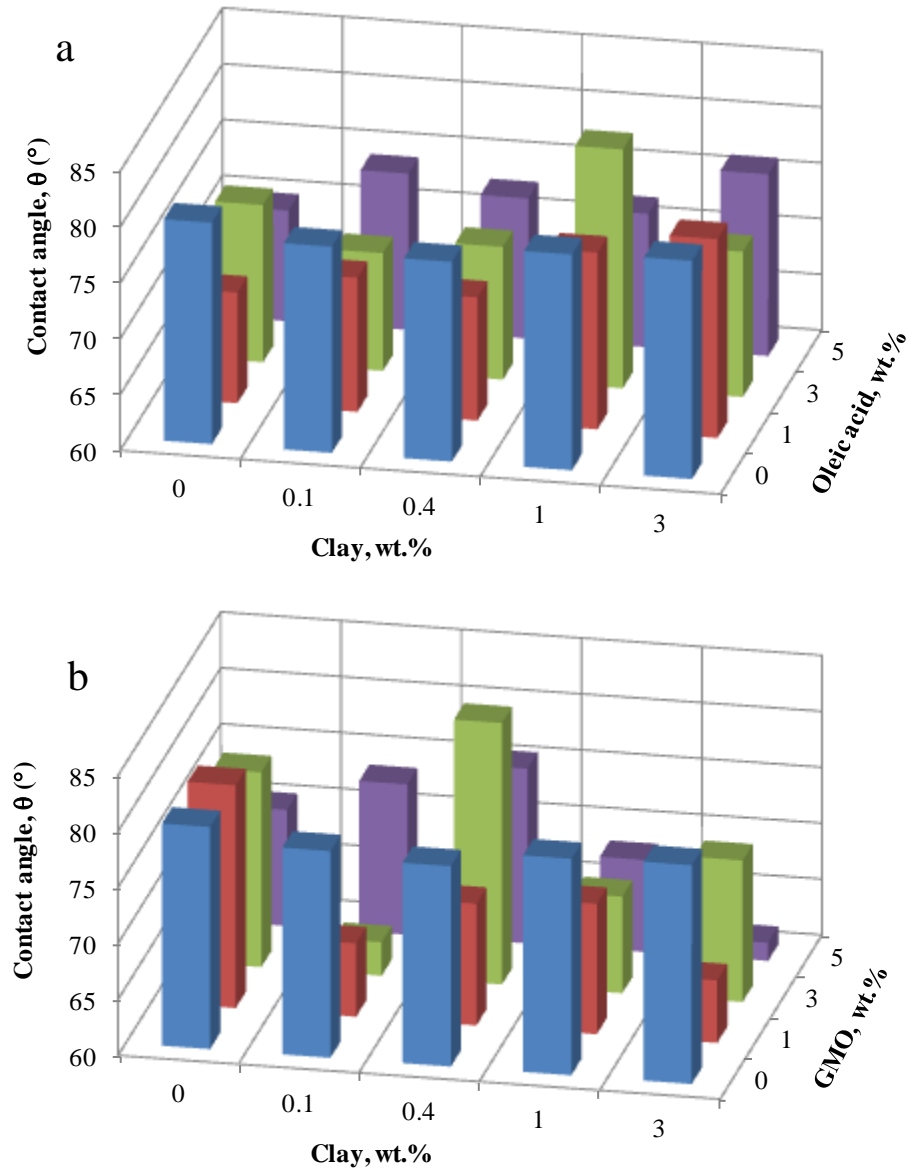


Figure 5.36 Variation of measured contact angle of composite films depend a-Clay-Oleic acid; b-Clay-GMO concentration.

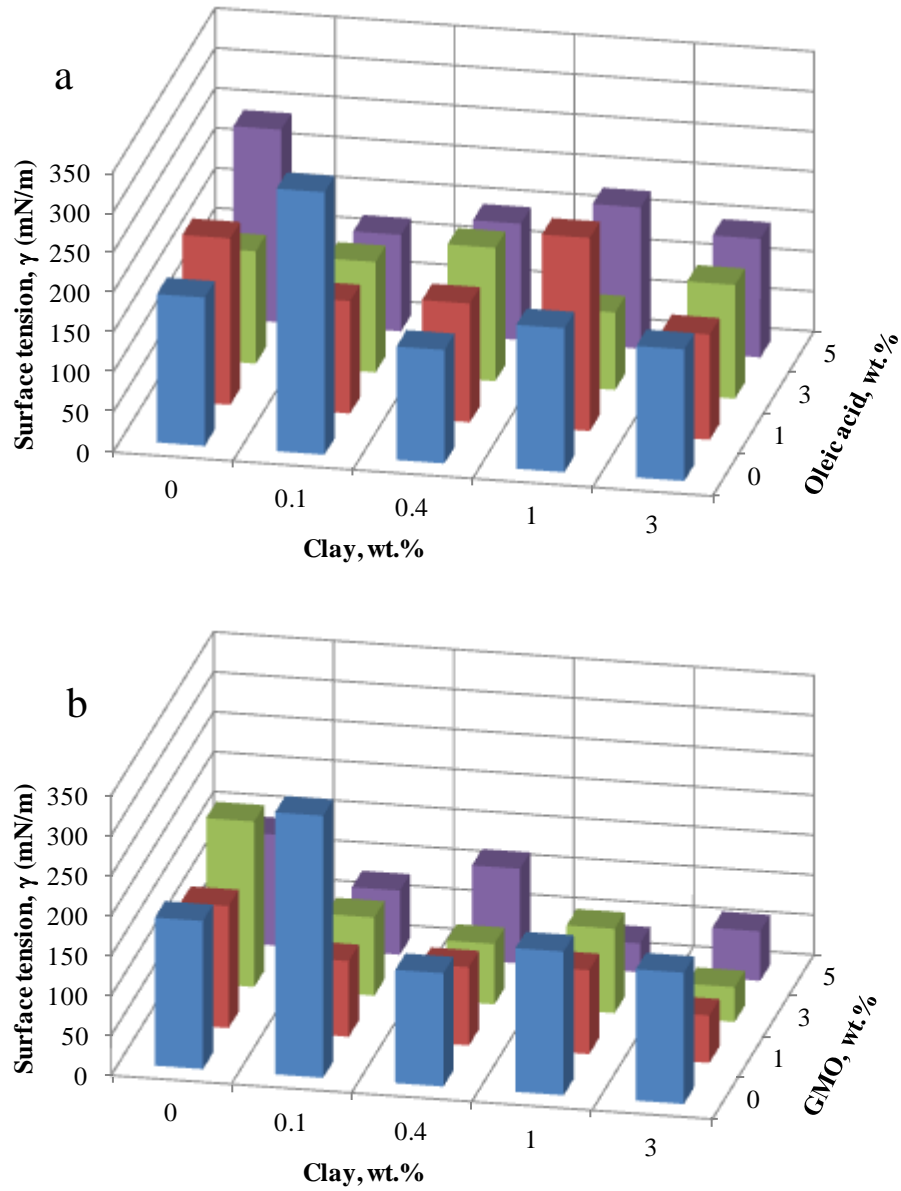


Figure 5.37 Variation of measured surface tension of composite films depend a-Clay–Oleic acid; b-Clay–GMO concentration.

5.4.2. Structural properties

Structural properties were considered by FTIR analysis, SEM observation, XRD and isothermal and nonisothermal DSC analysis.

Figure 5.38 illustrates FTIR spectra of organoclay.

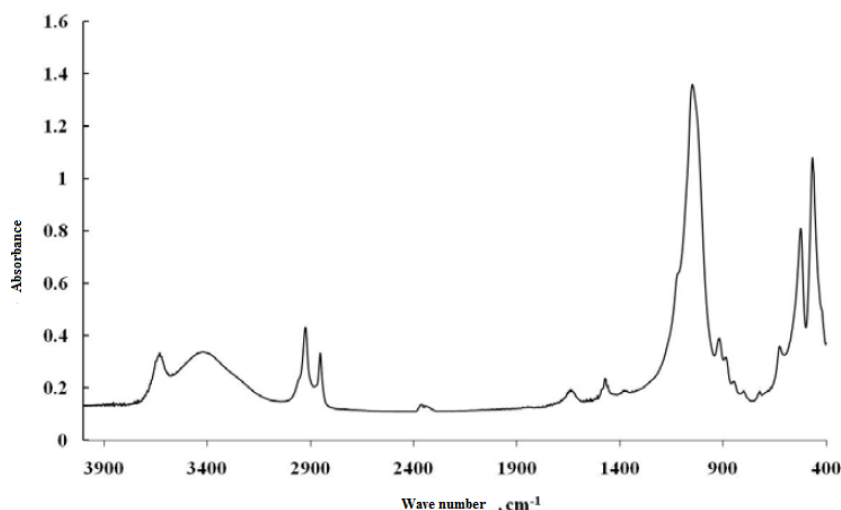


Figure 5.38 FTIR spectra of organoclay.

Figure 5.39 illustrates FTIR spectra of the neat PCL and clay contained composite films. The characteristic infrared bands of PCL were given in Table 5.20 (Elzein et al., 2004). FTIR spectra of prepared PCL composite films are given in Appendix H, Figure H1. The bands in Figures (Appendix H, Figure H1) are consistent with literature. Strong bands are observed such as carbonyl stretching mode around 1727 cm^{-1} for all the samples. It is revealed that the band at 1293 cm^{-1} the backbone C–C and C–O stretching modes in the crystalline PCL. The Si–O–Si bending vibrations show the clay existence at 470 cm^{-1} . The absorbance value of the band is proportionally increased with clay addition. However the Si–O stretching vibrations give several well resolved strong bands in the $1120\text{--}1000\text{ cm}^{-1}$ region but it is compensated by functional group bands of PCL.

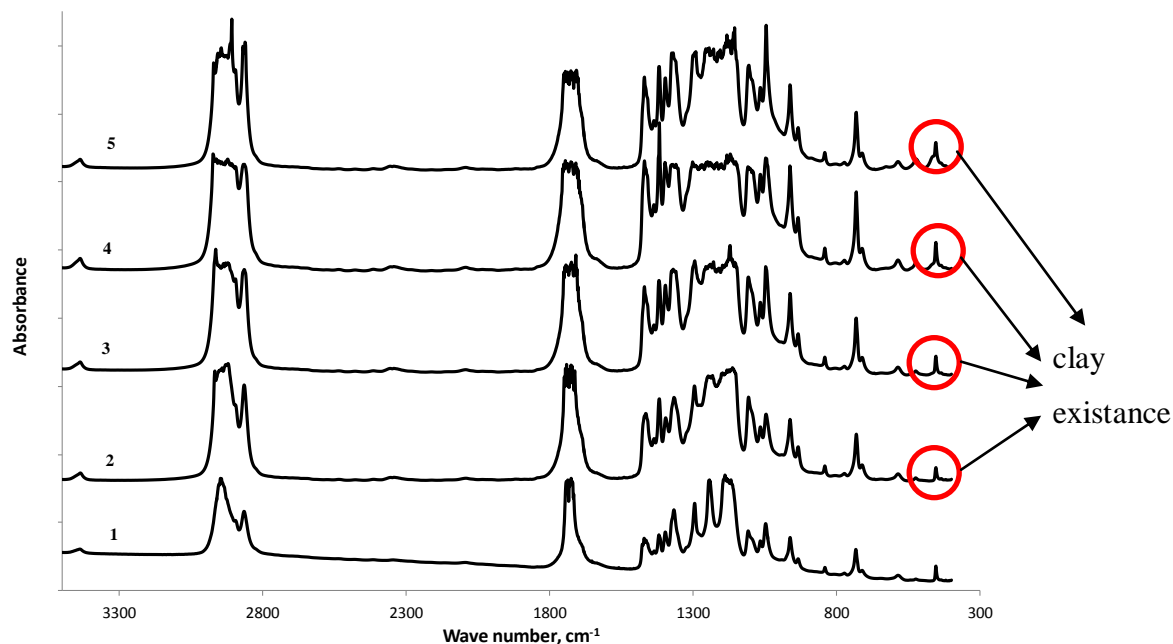


Figure 5.39 FTIR spectra of the composite films; 1-Neat PCL; 2- 0.1 wt% clay; 3- 0.4 wt% clay; 4- 1 wt% clay; 5- 3 wt% clay.

Table 5.20 Characteristic FTIR infrared bands for neat PCL.

Position [cm ⁻¹]	Vibrator	Position [cm ⁻¹]	Vibrator
2949	Asymmetric CH ₂ stretching	1240	Asymmetric COC stretching
2865	Symmetric CH ₂ stretching	1190	CC-O stretching
1727	Carbonyl stretching	1170	Symmetric COC stretching
1293	C-O and C-C stretching in crystalline phase	1157	C-O and C-C stretching in amorphous phase

Surface morphology of the PCL composite films was investigated by SEM and results are given in Figure 5.40 for the film without clay and in Figure 5.41 for the film with 1 wt% clay addition by increasing organic additives. The other results for the remaining films can be seen in Appendix I, Figures I1-33. It can be seen that composite films have porous structure which is also observed in density measurements. It is observed that addition of oleic acid increased porosity and the pore diameter, clay and GMO addition shows vice versa effect. Especially GMO contained composite films show smooth surface.

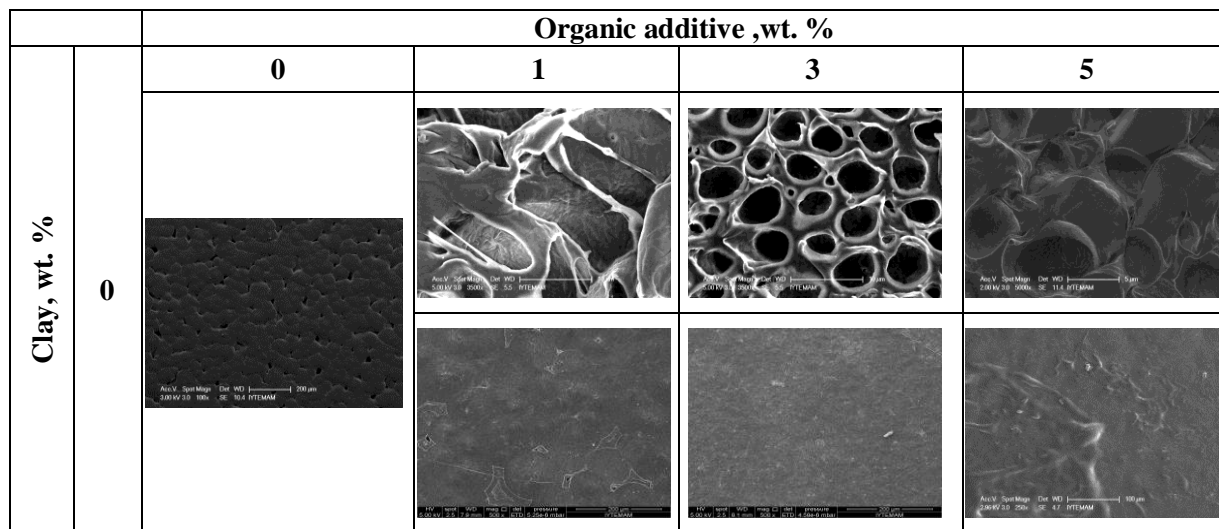


Figure 5.40 Effects of increasing different organic additives (top row: Oleic acid, bottom row: GMO) concentration on surface morphologies of PCL composite films by SEM analysis.

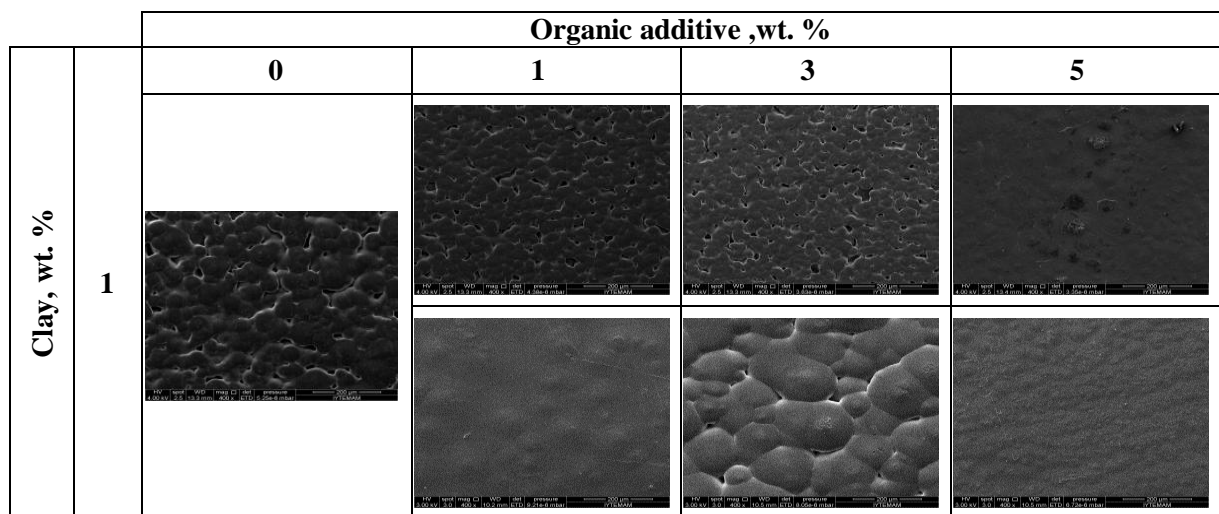


Figure 5.41 Effects of 1 wt% clay contained PCL composite films with increasing different organic additives (top row: Oleic acid, bottom row: GMO) concentration on surface morphologies by SEM analysis.

Crystal structure of all PCL composite films obtained by solvent casting are identified by XRD analysis. In Figure 5.42, the XRD analysis of neat PCL, clay and 3% clay contained composite films could be seen. Clay has a peak around 2θ degrees of 5. In the clay contained composite films, the peak was compensated due to exfoliated structure is given in Appendix J and Figure J1. According to the patterns, the maximum peak was observed at 2θ degrees of 21.8 and 24.08 for all composite

films. In Figure 5.43 from the SEM picture of the ruptured composite film PCL_C3_OA0 after tensile test XRD results of all composite films are proved the homogeneity of the clay distribution can be observed (Pavlidou and Papaspyrides, 2008).

The degree of crystallinity percent and the crystal thickness values calculated are given in Table 5.21. Degree of crystallinity percent of the samples were calculated from the ratio of the area of crystal peak to the total area of the peak of the XRD pattern by Gaussian function. Crystal thickness values are calculated by means of Scherrer equation (Eq. 4.3). Degrees of crystallinity percent of the samples are illustrated as depend on additive concentration in Figure 5.44. Crystal thickness of the films depend on additive concentration is given in Figure 5.45. The highest crystallinity is obtained for PCL_C0.1_O1 composite film. For all other composites, the crystallinity is lower than the neat PCL's. In general, the addition of clay slightly decreased crystallinity, the addition of organic additives also decreased, which acted as the plastifier. The maximum relative crystallinity value was obtained for the sample of PCL_C0.1_O1. Crystal thickness of the PCL composite films changed between 8.77 (PCL_IA0_O1) and 119.72nm (PCL_C0.1_O3). The small amount of clay addition (until 1 wt% clay) causes an increase in crystall thickness, but the effect is reversed for 3 wt% clay. Oleic acid has an increasing effect but the effect of GMO is insignificant. Similar observations were found by various researchers who worked with clay contained composite films (Di Maio et al., 2004; Lepoittevin et al., 2002).

XRD results are also obtained for central points and examined by central point statistical model and shown in Figure 5.46. The obtained model equation is:

$$\text{XRD - DOC, \%} = 47.74 - 0.237 \times \text{C} - 0.29 \times \text{O} - 0.41 \times \text{C} \times \text{O} \text{ with } R^2 = 0.76$$

Interaction effect of additives are also obtained on the results. The results show that high load of organic and inorganic additives decreases the degree of crystallinity which obtained from solvent casted films. The degree of crytsallinity values increased with low amount of clay addition and the results are match with calculated degree of crystallinity values from DSC 1st melting peak.

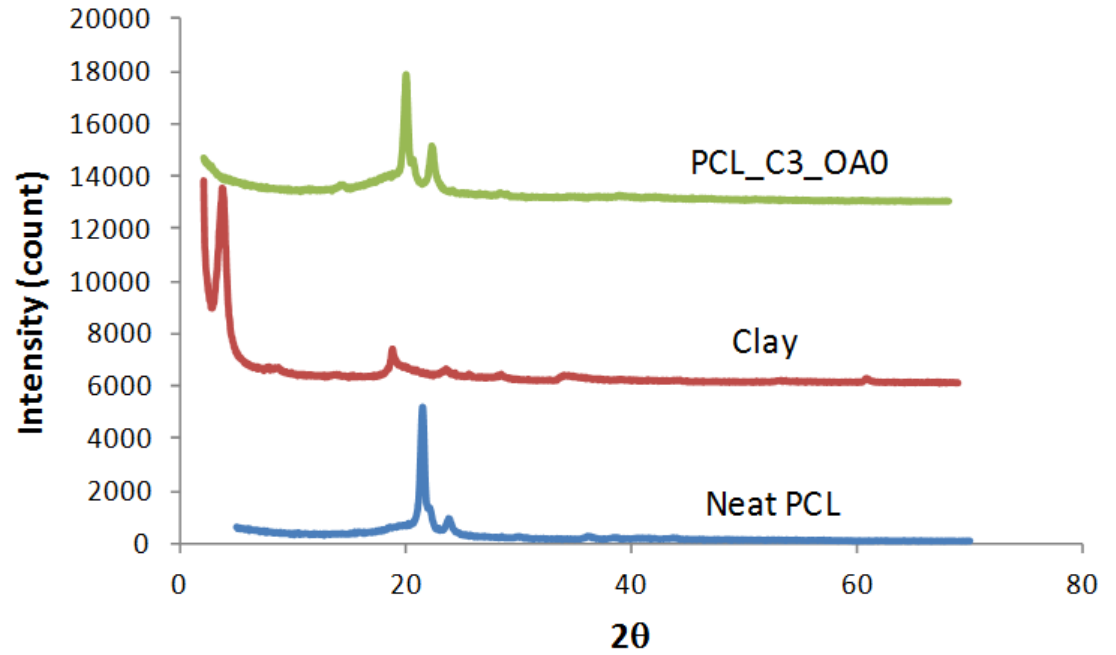


Figure 5.42 XRD analysis of neat PCL, clay, 3 wt% clay contained composite films.

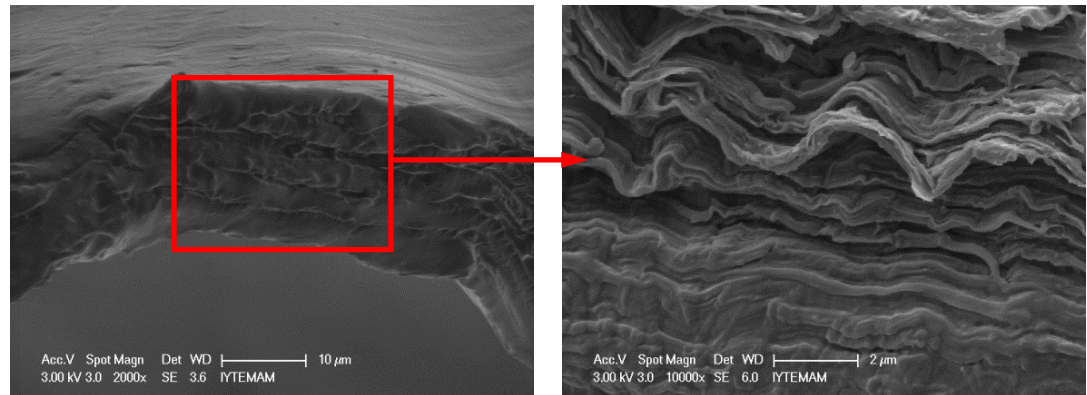


Figure 5.43 SEM picture of ruptured PCL_C3_OA0 from tensile test.

Table 5.21 XRD analysis results of PCL composite films.

Clay wt %	Organic Additive wt %	Degree of Crystallinity, % (X-Ray)		Crystal Thickness, nm	
		O	GMO	O	GMO
0	0	53.77		15.91	
	1	47.58	46.54	8.77	29.00
	3	48.20	50.09	24.71	22.87
	5	44.12	49.63	26.61	21.53
0.1	0	47.76		41.65	
	1	81.90	45.09	69.78	20.23
	3	47.26	46.89	119.72	35.10
	5	49.01	47.38	30.50	30.51
0.4	0	42.66		41.57	
	1	51.48	44.76	22.06	30.49
	3	51.28	40.94	41.60	27.01
	5	48.41	47.25	35.12	35.10
1	0	50.24		41.56	
	1	52.69	43.29	41.59	27.02
	3	47.34	47.18	30.49	34.17
	5	46.89	46.27	30.51	27.01
3	0	48.45		27.02	
	1	46.58	42.89	35.09	35.11
	3	45.71	48.56	27.01	30.50
	5	43.81	47.43	69.72	30.50

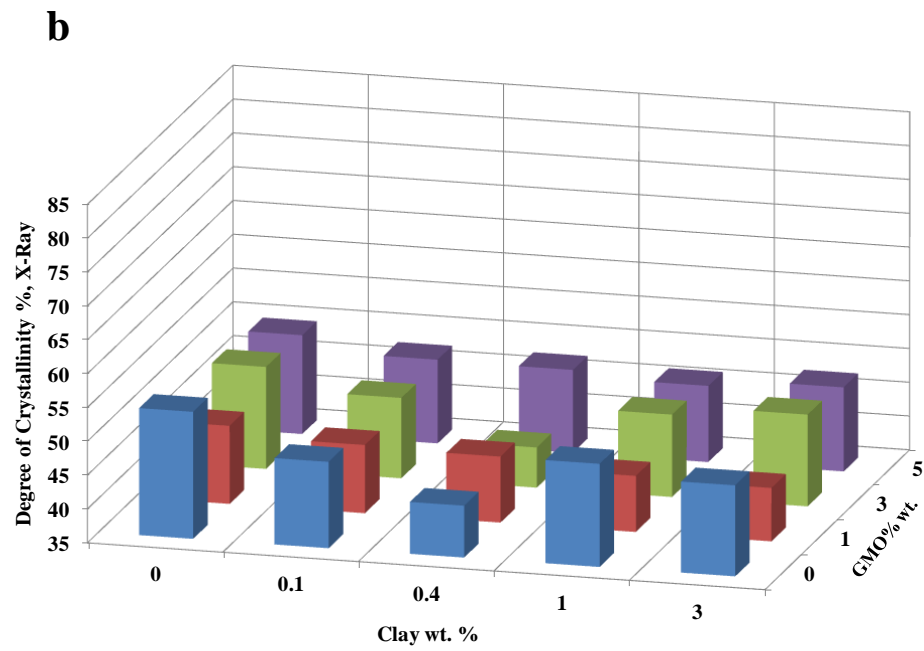
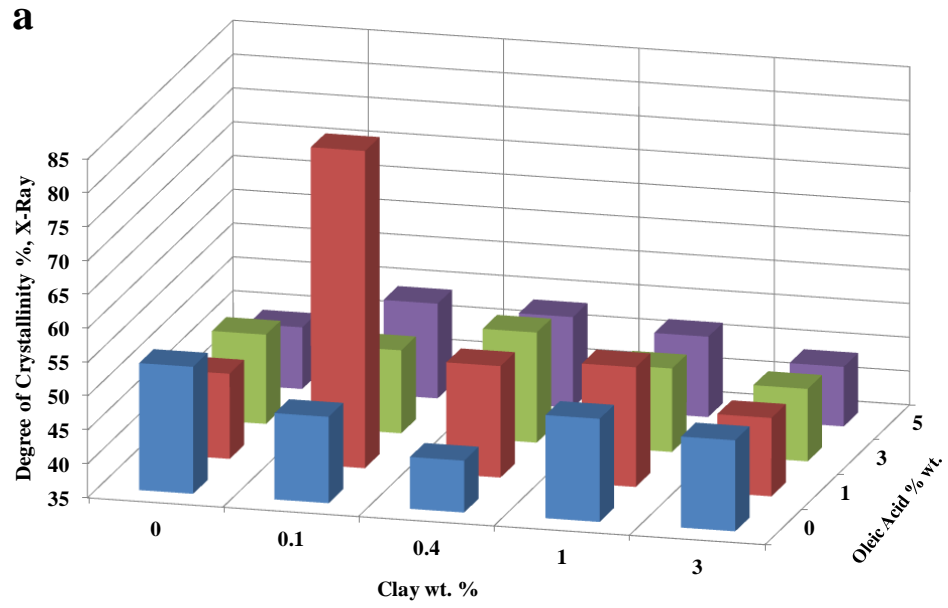


Figure 5.44 Variation of degree of crystallinity values of composite; a-Clay-Oleic acid; b-Clay-GMO.

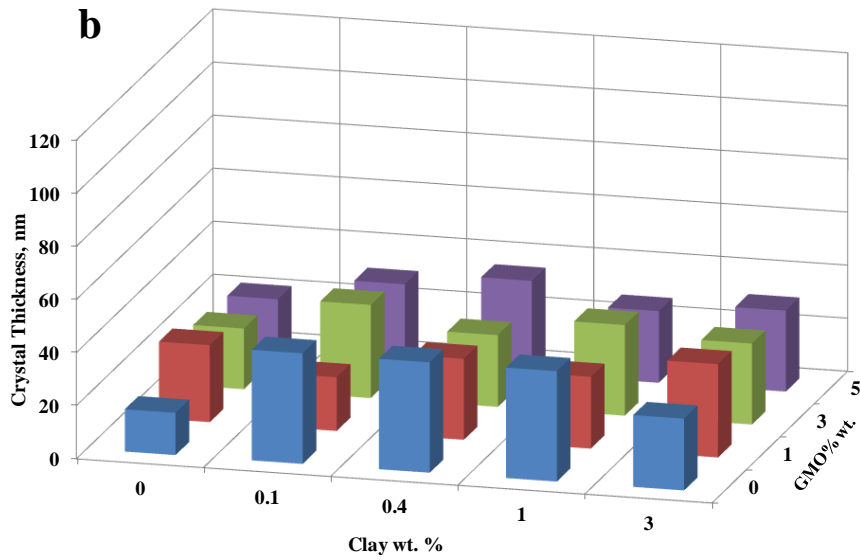
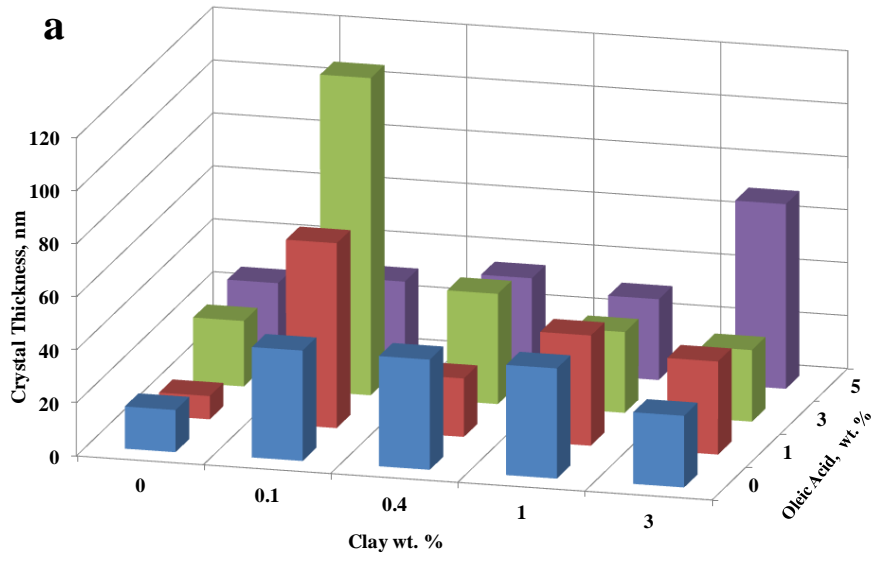


Figure 5.45 Variation of crystal thickness values of composite; a-Clay-Oleic acid; b-Clay-GMO.

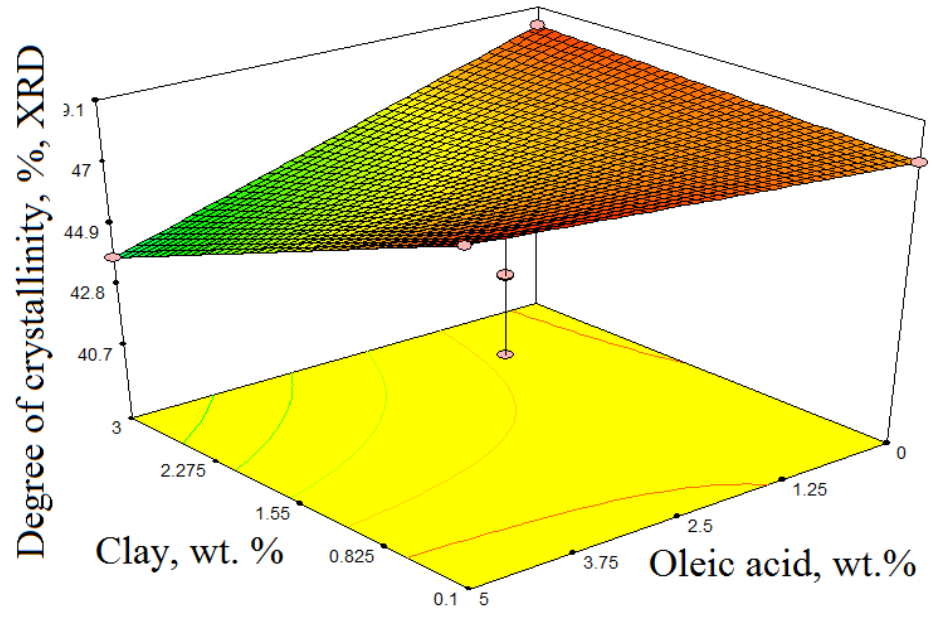


Figure 5.46 Variation of degree of crystallinity by central point statistical model.

5.4.3. Mechanical properties

The stress – strain diagram of neat PCL is given in Figure 5.47. Rest of the diagrams is given in Appendix K, Figure K1 and K2. PCL is ductile material which could be elongated around 600%. The mechanical evaluation parameters are given in Table 5.22. The Young's modulus values were obtained between 157.0 (PCL_C3_G1) and 95.9 (PCL_IA0_O5) and standard deviations change between 23.0 - 6.5. The yield point values were obtained between 10.7 (PCL_IA0_G1) and 5.2 (PCL_IA0_O5) and standard deviations change between 2.6 – 0.2. The tensile stress values were obtained between 17.8 (PCL_IA0_G1) and 6.7 (PCL_C0.4_OA0) and standard deviations change between 3.5 – 0.4. The elongation at break values were obtained between 730.9 (PCL_IA0_G1) and 85.7 (PCL_C0.1_G5) and standard deviations change between 124.7 – 5.1. The Young's modulus values are given in Figure 5.48. GMO contained composite films show slightly higher values than oleic acid. Clay additions first decrease, and then slightly increase the Young's modulus value and stiffer material is obtained. The yield points and tensile stress values of the composite films are given in Figure 5.49 and Figure 5.50. The same effects can also be observed in the tensile properties. The elongation values are given in Figure 5.51. Elongation values are especially increased with high load of clay and organic additives. This type of flexible films could be used in axially oriented film application for packaging. To observe compatibility between the filler particles and polymer matrix, Pukanszky model is used. The results are given in Figure 5.52. The negative values show poor interactions and the worst interaction (-70.6) is obtained for 0.1 wt% clay dopped composite without organic additives. The addition of organic additives improves the polymer matrix – inorganic additive compatibility. GMO shows better results than oleic acid as compatibilizer. It could be said that organic additives are good compatibilizer between polymer matrix and filler particles.

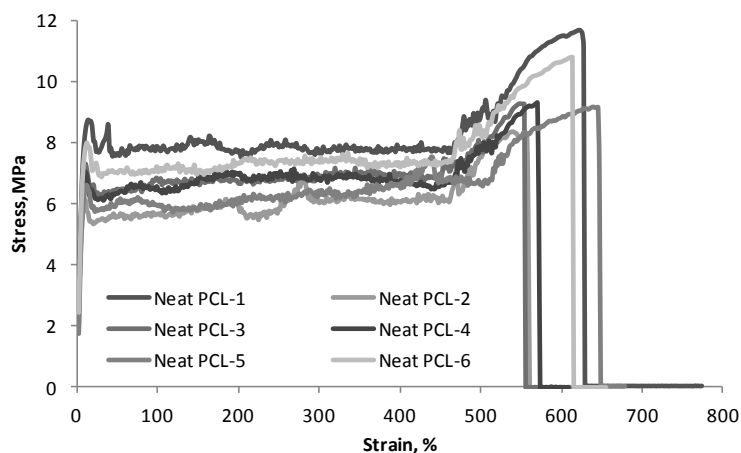


Figure 5.47 Strain - stress diagram of neat PCL film.

Table 5.22 Mechanical properties and polymer additive interaction parameter *B* values calculated from Pukanszky Model of PCL films.

Clay wt %	Organic Additives, wt. %	Young's Modulus (MPa)		Std. Dev.		Yield Point (MPa)		Std. Dev.		Tensile Stress (MPa)		Std. Dev.		Elongation at Break (%)		Std. Dev.		Pukanszky constant, B		
		O	GMO	O	GMO	O	GMO	O	GMO	O	GMO	O	GMO	O	GMO	O	GMO	O	GMO	O
0	0	116.9		13.4		7.3		0.9		9.7		1.2		592.7		39.2				
	1	96.4	158.7	11.1	16.8	6.4	10.7	0.5	0.4	8.6	17.8	0.7	0.4	559.1	730.9	43.4	5.1			
	3	134.0	116.0	10.8	13.2	8.5	7.2	0.5	0.5	13.0	11.9	0.8	1.1	703.2	668.2	45.7	71.4			
	5	95.9	129.3	11.8	15.4	5.2	9.0	0.8	0.8	9.4	14.3	1.5	1.5	699.2	705.9	60.6	60.9			
	0	113.4		9.8		7.0		0.4		9.3		0.6		584.7		8.7				-70.6
0.1	1	107.7	101.3	12.7	10.1	7.2	7.3	0.6	0.7	10.0	11.0	0.8	1.6	628.9	641.8	48.0	79.8	0.8	1.0	
	3	107.1	117.4	8.7	18.2	7.8	8.2	0.5	1.2	11.0	11.7	1.3	2.2	651.7	609.9	63.4	94.0	1.5	1.7	
	5	96.9	114.9	6.5	10.3	6.9	7.8	0.5	1.2	8.7	6.8	1.6	1.2	582.9	85.7	88.0	20.4	0.4	2.3	
	0	105.7		10.7		6.7		1.0		6.7		0.5		455.7		97.9				-32.1
	1	113.3	111.4	9.3	11.8	7.8	8.1	0.2	0.8	10.1	12.3	1.2	2.6	683.7	665.8	96.6	75.7	6.5	41.2	
0.4	3	118.4	103.7	10.9	9.1	7.8	7.8	0.5	0.9	9.7	11.1	1.5	1.5	626.3	626.3	74.3	43.1	3.0	6.2	
	5	105.2	111.1	7.5	13.8	6.9	6.9	0.4	1.0	8.1	8.8	1.2	0.8	474.8	506.3	124.7	24.4	0.5	-0.2	
	0	129.4		11.9		7.7		1.3		9.8		0.7		604.9		58.1				9.1
	1	109.2	109.0	13.6	9.7	6.4	7.0	0.3	0.4	9.6	12.5	0.8	1.0	659.4	729.7	66.6	7.8	-5.5	0.7	
	3	106.5	111.5	19.4	7.9	7.0	7.5	1.2	0.6	9.5	10.4	1.7	0.9	662.1	589.8	110.8	47.2	0.2	1.8	
1	5	105.8	120.2	8.1	12.6	7.7	7.7	0.2	0.7	11.1	12.0	1.1	1.4	689.3	624.7	91.9	81.3	2.0	2.1	
	0	128.3		16.7		7.5		0.6		9.1		1.1		511.6		108.9				2.8
	1	111.4	157.0	14.4	23.0	7.3	7.2	0.3	2.6	10.1	10.3	1.2	3.5	672.2	581.2	112.0	63.1	1.5	1.0	
	3	101.8	133.2	15.7	15.8	7.0	8.7	0.6	0.7	10.7	11.8	1.4	0.7	707.0	615.3	80.4	50.9	0.5	4.4	
	5	120.7	139.8	13.5	6.6	7.8	8.9	0.9	0.8	11.7	11.2	1.6	1.6	707.7	519.8	63.6	50.0	2.1	3.8	

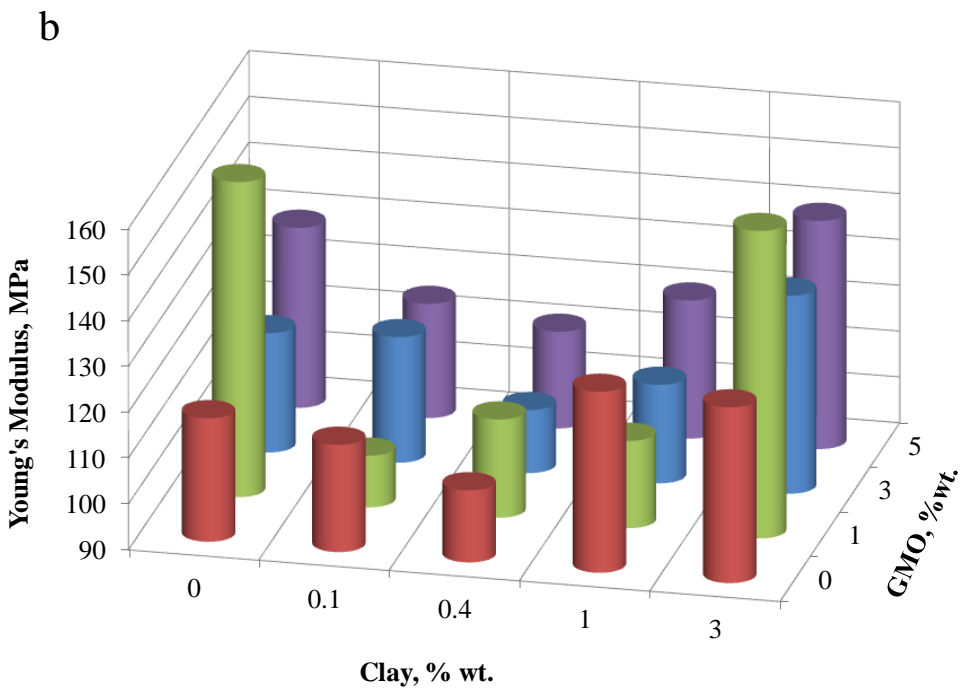
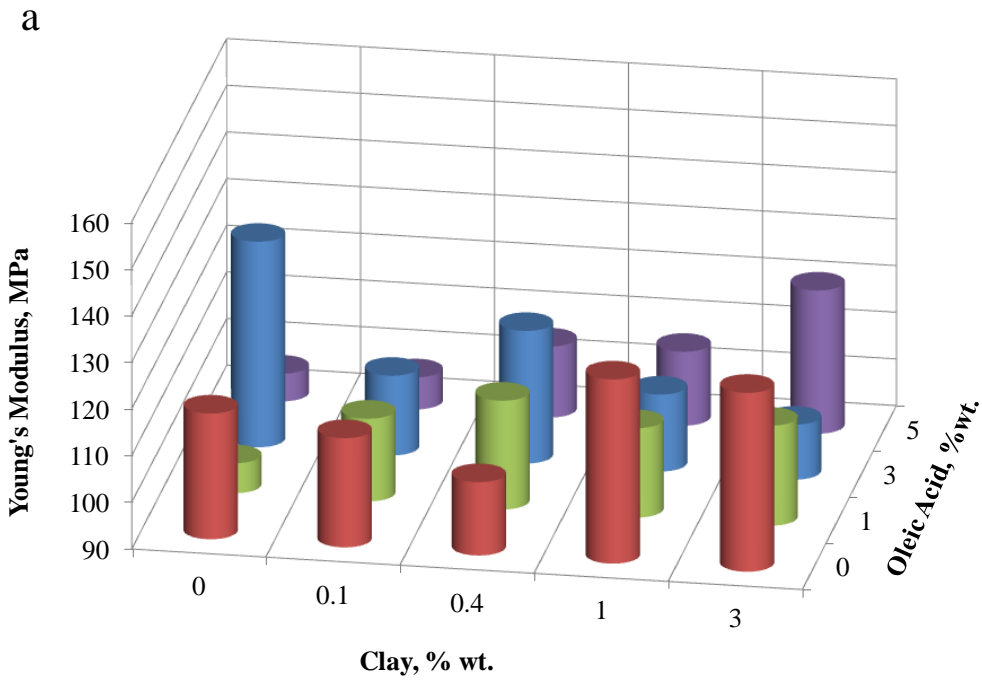


Figure 5.48 Variation of Young Modulus of PCL composite films with additive concentration; a-Clay-Oleic acid; b-Clay-GMO.

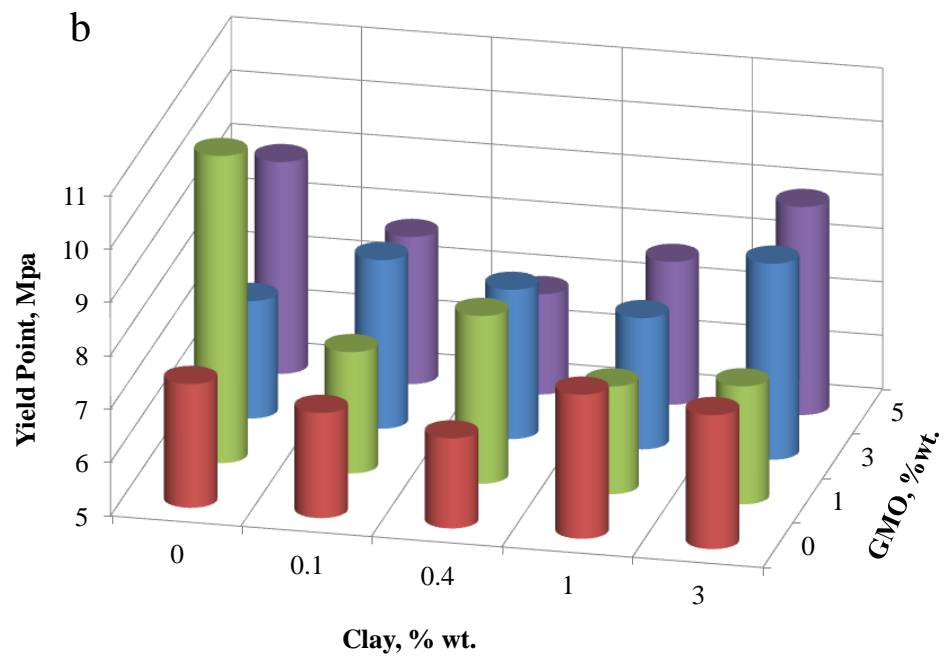
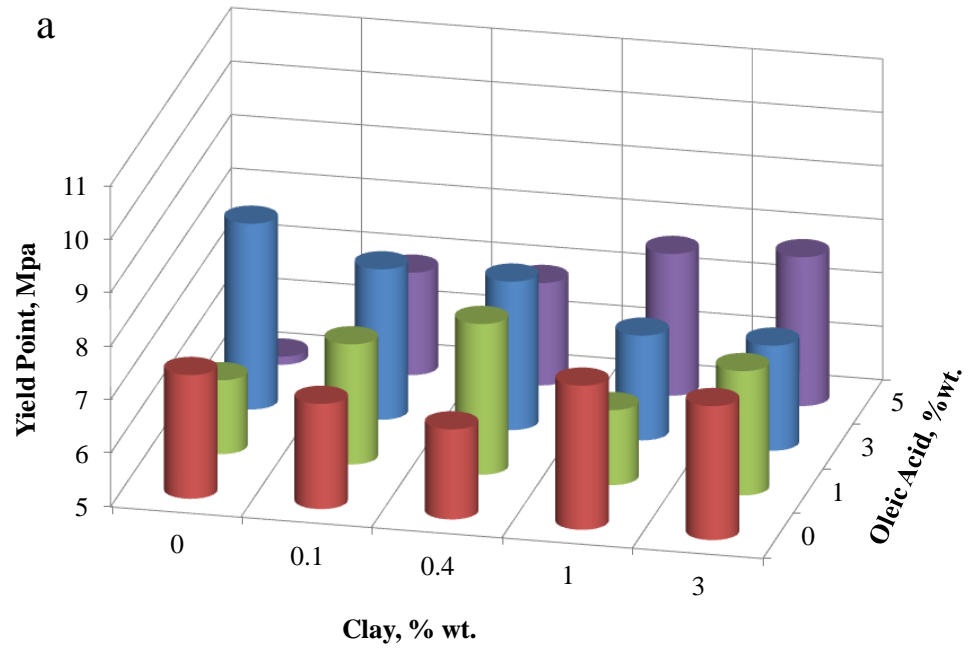


Figure 5.49 Variation of Yield Points of PCL composite films with additive concentration; a-Clay-Oleic acid; b-Clay-GMO.

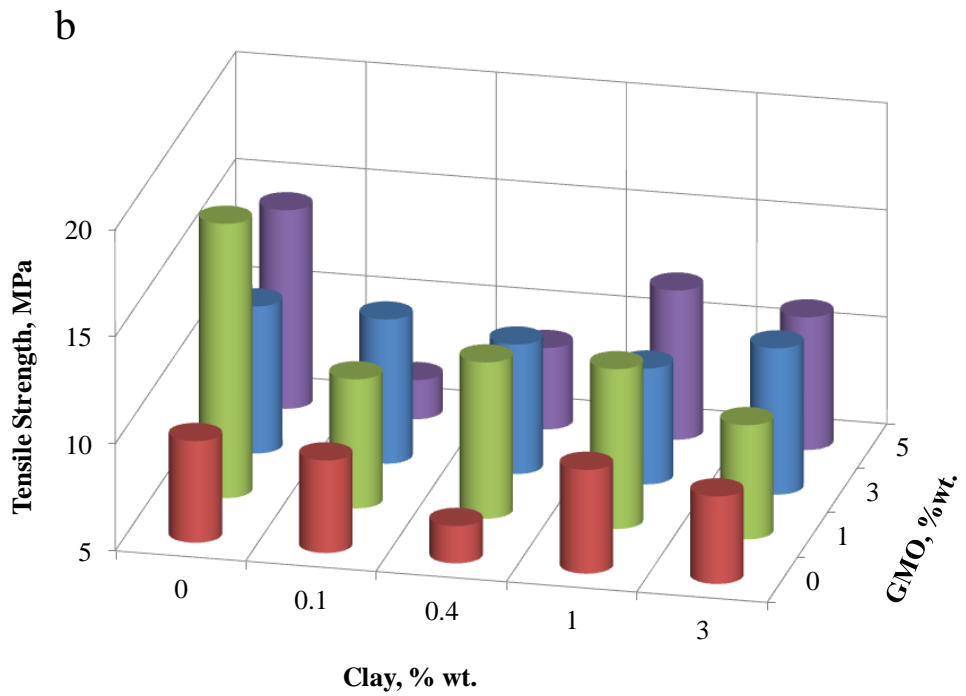
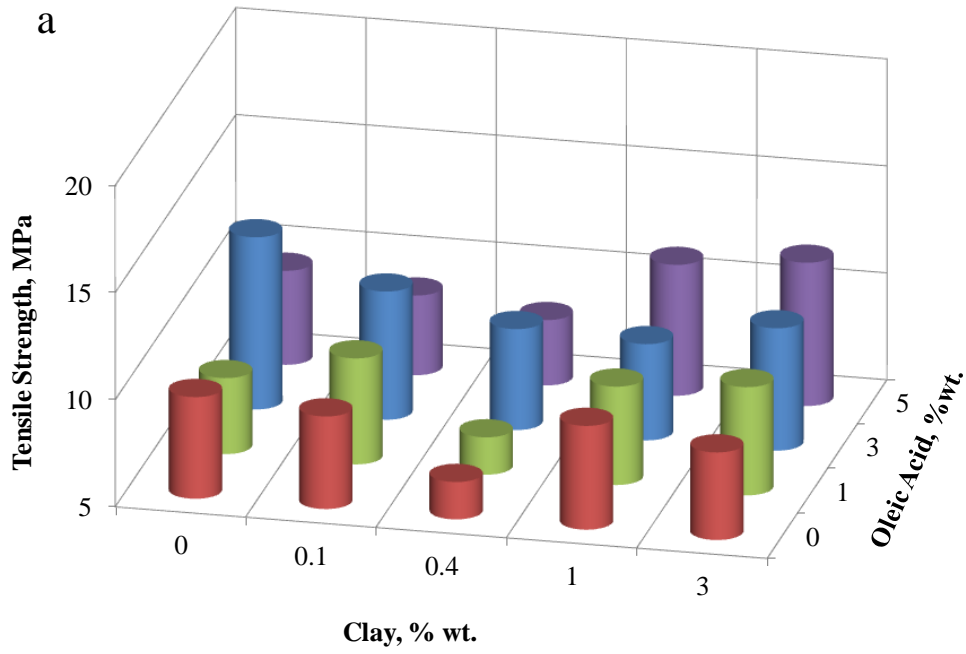


Figure 5.50 Variation of Tensile Strength of PCL composite films with additive concentration; a-Clay-Oleic acid; b-Clay-GMO.

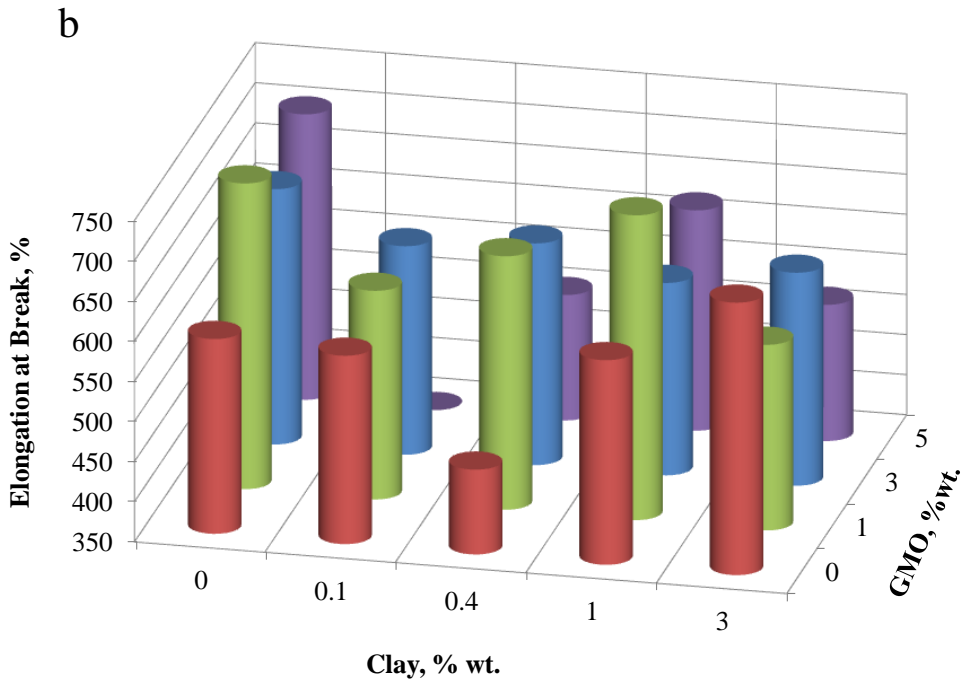
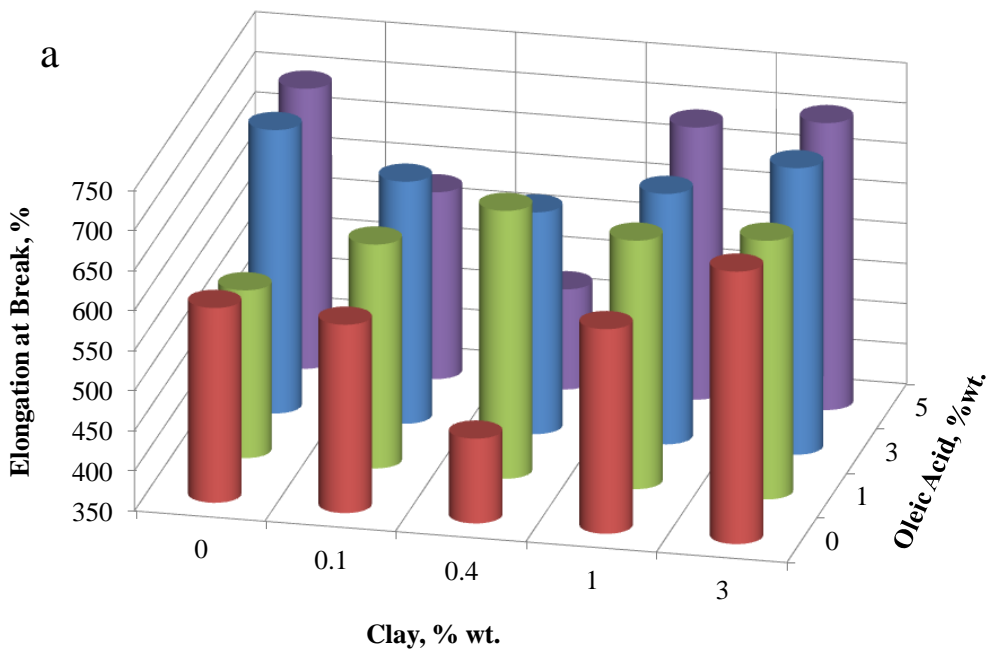


Figure 5.51 Variation of Elongation values of PCL composite films with additive concentration; a-Clay-Oleic acid; b-Clay-GMO.

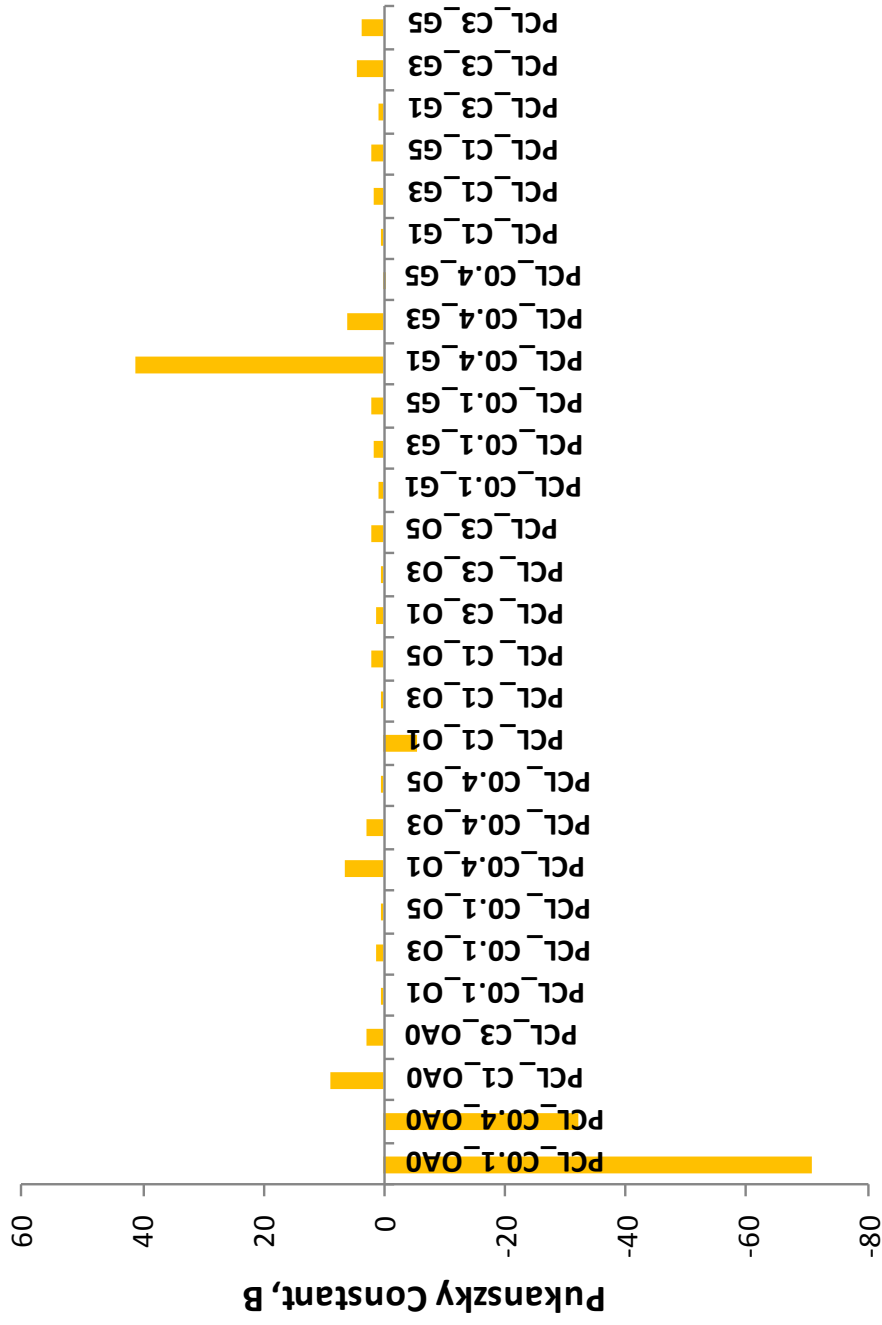


Figure 5.52. Variation of Pukanszky constant values of PCL composite films depend on additive concentration.

5.4.4. Degradation results

Thermal and biological degradation of composite films were examined.

5.4.4.1. Thermal degradation

Thermal degradation behavior of composite films is analyzed from TGA thermograms which are given in Appendix L, Figure L1. TGA thermogram of organoclay is given in Figure 5.53. First decrease of the profile reflect the water vaporization, then organic functional groups degrade between 250°C and 450°C.

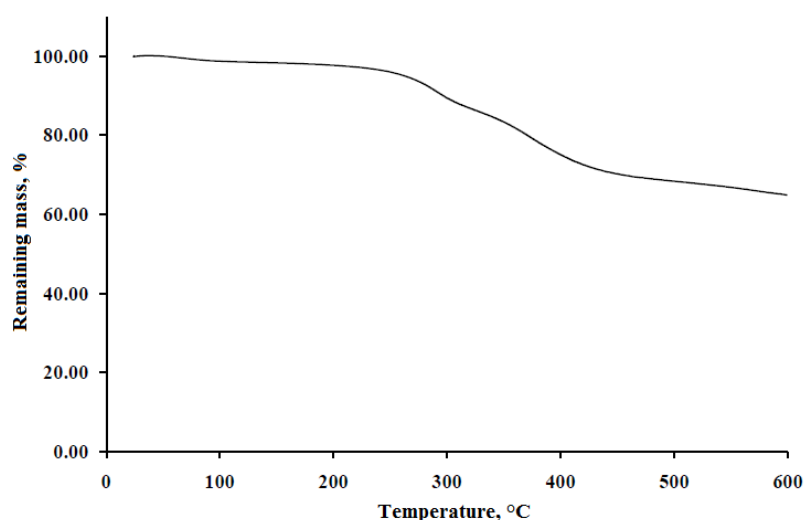


Figure 5.53 TGA thermogram of organoclay.

Degradation onset temperature values are given in Table 5.23 and Figure Figure 5.54. The values change between 373.1 (PCL_C3_OA0) and 222 (PCL_IA0_O5). Clay addition is increased the degradation temperature meanwhile oleic acid and GMO addition is decreased when they are used alone. The amount of remaining ash values are given in Table 5.23 and Figure 5.55. The values change between 9.31 (PCL_C0.1_O1) and 0.08 (PCL_IA0_O3). Clay contained composite films have higher ash amount due to non degraded clay particles. It can be concluded that clay addition is improved the thermal degradation properties of PCL.

The degradation activation energy values are calculated by Brodio's method. The results are given in Table 5.23 and

Figure 5.56. The results change between 62.77 kJ/mol (PCL_C3_O3) and 293.52 kJ/mol (PCL_IA0_O1). The decrease of the activation energy means the accelerarating

affect of the additive on thermal degradation. The values show slight increase by oleic acid addition. Meanwhile clay and GMO addition is sharply decreased the activation energy but 5 wt% GMO addition increased again. Clay and GMO contained composite films show higher values in comparison with clay and oleic acid contained composite films and that means clay-GMO contained composite films are less easily degraded than clay-oleic acid contained films with regard to degradation activation energy.

Table 5.23 Thermal degradation results of PCL composite films.

Clay, wt %	Organic Additive, %wt	Degradation onset Temperature, T _d (°C)		Amount of Ash at 600°C, %		Brodio's Degradation Activation Energy, kJ/mol	
		O	GMO	O	GMO	O	GMO
0	0	339.8		1.21		277.14	
	1	268.3	270.3	0.51	0.8	293.52	78.57
	3	233.3	265.8	0.08	1.3	238.15	65.50
	5	222	252.7	0.243	1.54	212.04	215.80
0.1	0	347.2		0.22		98.86	
	1	353.8	345.9	9.31	2.18	87.81	157.54
	3	360.5	350.6	1.05	3.33	78.51	182.75
	5	330.6	329.9	1.19	1.21	72.91	93.37
0.4	0	351.9		0.54		89.21	
	1	343.8	330.1	1.25	1.133	98.45	135.77
	3	338.6	319.6	1.67	0.303	81.29	130.91
	5	312.1	346.3	0.16	3.273	80.22	178.52
1	0	343.3		2.3		78.63	
	1	344.3	350.3	0.83	5.45	66.98	134.14
	3	336.9	346.8	0.17	4.81	88.41	128.49
	5	330.5	329.1	2.24	3.13	74.74	96.15
3	0	373.1		3.8		96.64	
	1	346.6	338.7	3.32	4.64	85.48	133.17
	3	350.8	326.6	1.23	3.41	62.77	113.61
	5	348.9	337.6	2.35	6.17	74.00	134.81

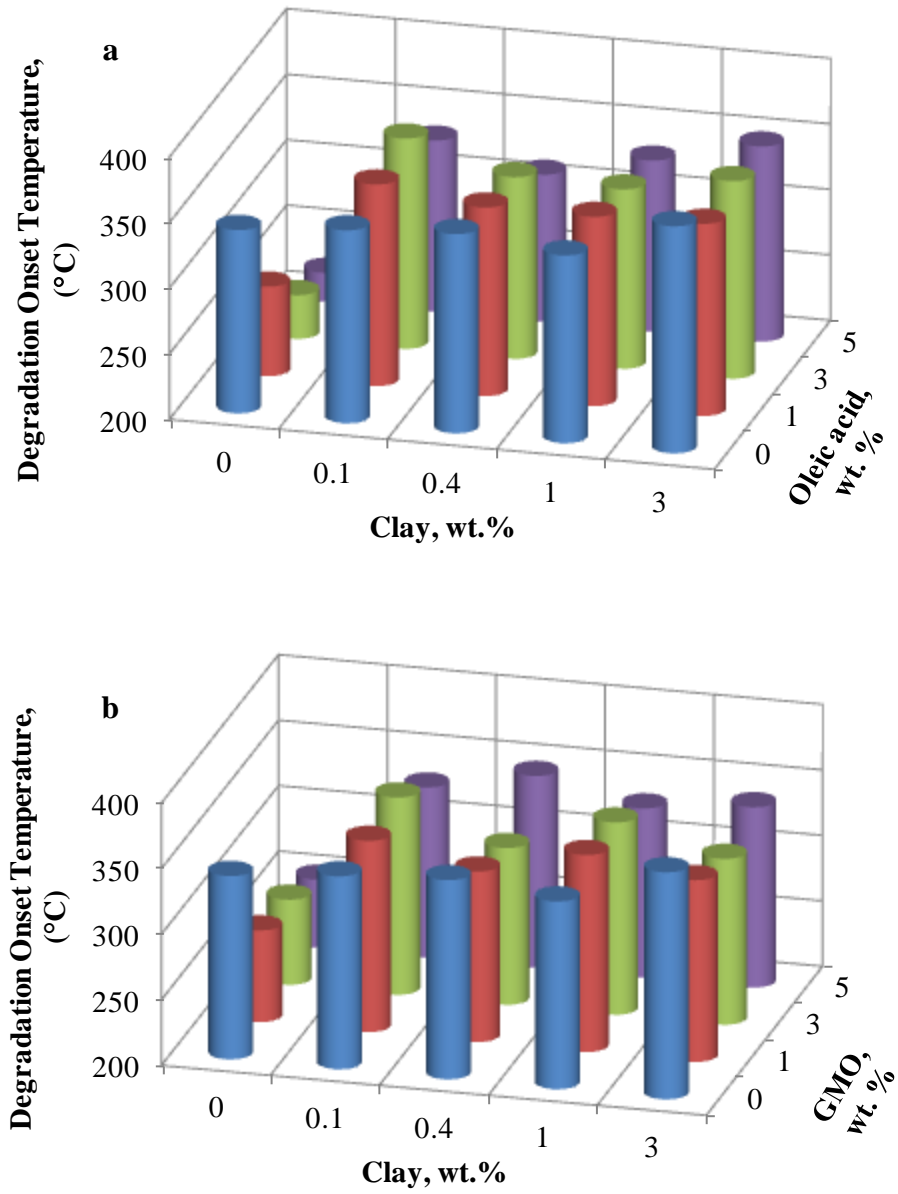


Figure 5.54 Variation of degradation beginning temperature of composite films; a- Clay-Oleic Acid; b – Clay-GMO.

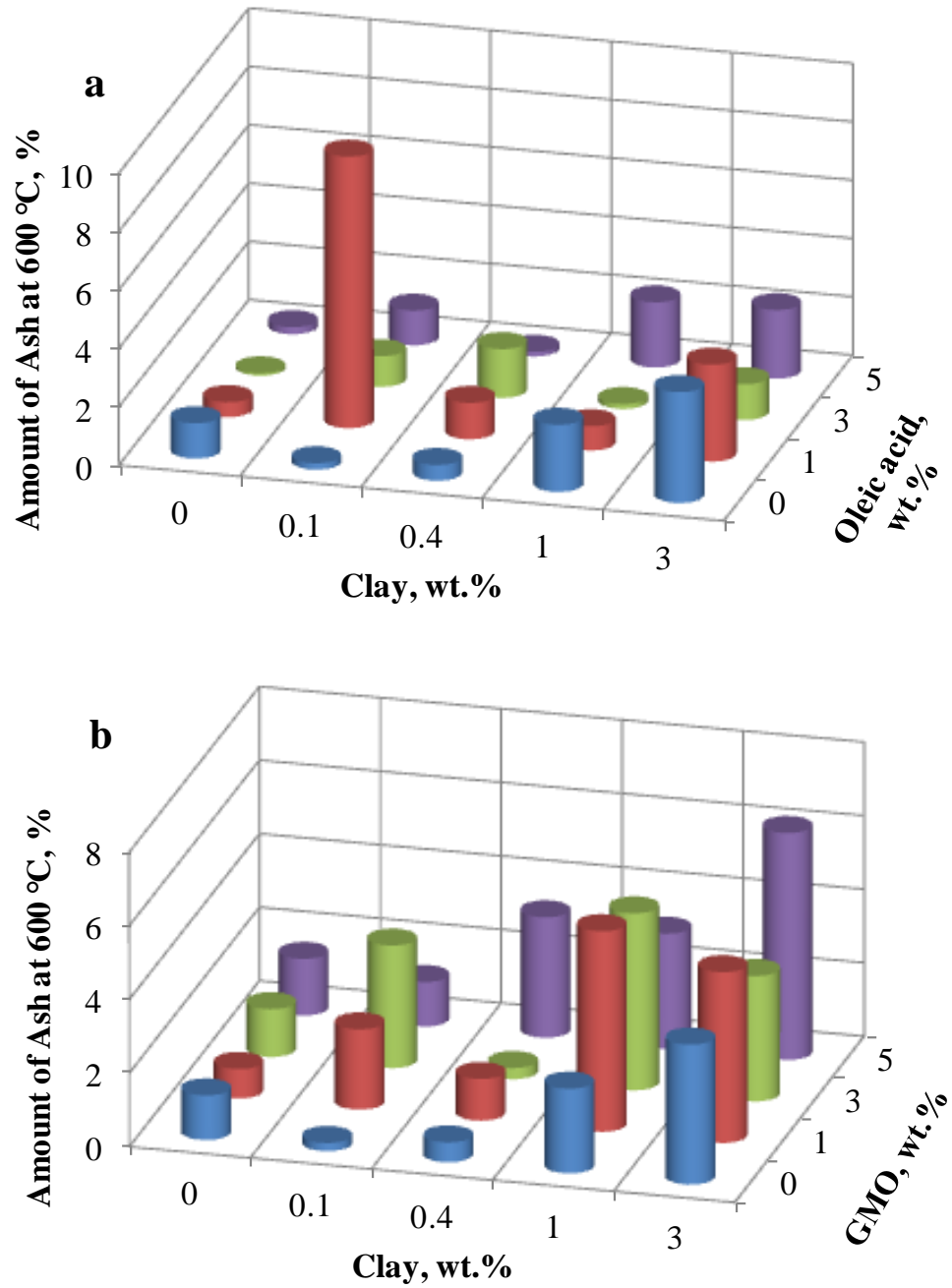


Figure 5.55 Variation of remaining ash amount of composite films; a- Clay-Oleic Acid; b – Clay-GMO.

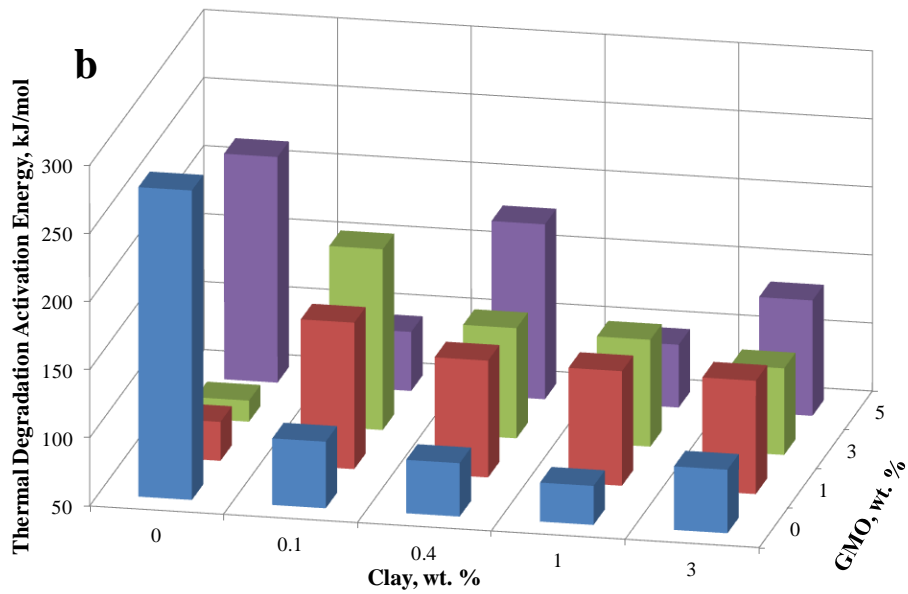
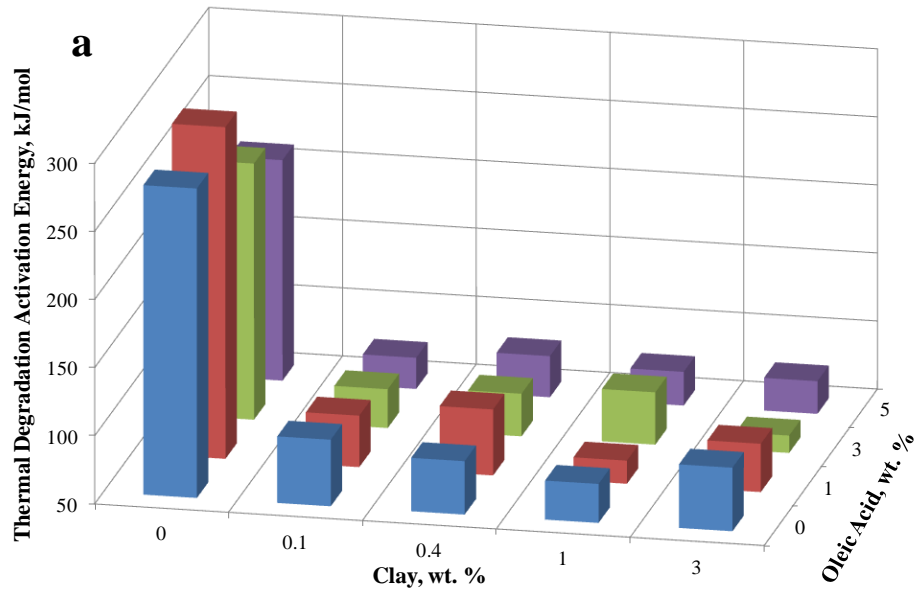


Figure 5.56 Degradation activation energy obtained from Broido Model of composite films depend on additive concentration; a-Clay - Oleic acid, b- Clay – GMO.

5.4.2.2. Biodegradation in Soil

From soil burial tests, weight loss values of PCL composite films were calculated. The results were tabulated in Table 5.24 and Figure 5.57 to Figure 5.59. It was clearly seen that neat PCL had no weight loss and 0.1, 0.4% clay with oleic acid and GMO contained composite films had low weight loss % because of the high degree of crystallinity. But, 1 and 3% clay with oleic acid and GMO contained composite films had higher weight loss % and the films are totally degraded end of 9 months. Degradation was much higher for the films with defective crystal structure (3 wt% clay dopped).

According to literature (Zhao et al., 2008), it has been reported that the biodegradation of PCL proceeds by a rapid weight loss through surface erosion with minor reduction of the molecular weight. In contrast the abiotic hydrolysis of PCL proceeds by a reduction in molecular weight combined with minor weight loss. Considering this study, it has seen that less weight losses were obtained, some of them showed no change at all. These results showed the effect of abiotic hydrolysis of PCL by minor weight loss. If viscosity measurements would have been performed, the reduction of molecular weight would be observed.

The thickness of the composite films are measured for 9 months at regular intervals and given in Table 5.25 and Figure 5.60. Most of the composite films have decreasing thickness value but some films show reverse behavior. The increase in the film thickness might be caused by the water adsorption from the soil. Especially the films with GMO, the colour change was observed during experiments.

FTIR analysis of the composite films is performed for each months and FTIR graphs are given in Appendix M, Figure M1 to M5. C-O and C-C stretching in amorphous and crystalline phase peaks are at 1157 cm^{-1} and 1293 cm^{-1} . The FTIR peak area ratios of $A_{\text{amorphous}}/A_{\text{crystalline}}$ (1157/1293) of PCL composite films before and after soil burial test were calculated by Simpson Rule and these values are given in Table 5.26 and shown in Figure 5.61. According to these values, ratios before soil burial test are higher than the ratios after soil burial test. This result indicates that first, amorphous regions of the films were digested by bacteria.

Amorphous and crystalline peaks obtained from the FTIR graphs were plotted separately and given in Appendix N, Figures N1 – N10. Photographs of the composite films taken during degradation experiments are given in Figure 5.62 to Figure 5.66.

Table 5.24 Weight loss values of composite films followed by 9 months.

Clay wt %	Organic Additive wt %	Weight loss, wt. %					
		after 3 months		after 5 months		after 9 months	
		O	GMO	O	GMO	O	GMO
0	0	0		0		0	
	1	6.98	6.06	3.13	6.06	5.41	5.56
	3	3.23	3.57	13.33	0.00	5.88	4.88
	5	3.70	8.70	5.88	6.98	6.67	6.45
0.1	0	6.06		5.56		3.57	
	1	3.33	5.00	3.13	2.78	9.38	6.06
	3	3.13	6.67	4.17	5.26	3.45	11.54
	5	8.57	8.57	5.26	7.32	6.98	7.89
0.4	0	6.67		3.85		0	
	1	5.71	6.06	4.88	6.06	3.57	6.06
	3	3.57	0	3.45	5.00	6.67	5.56
	5	3.03	10.00	7.69	36.67	7.69	degraded
1	0	0		46.15		degraded	
	1	3.33	0	13.79	23.33	degraded	degraded
	3	6.45	6.67	19.35	30.00	degraded	degraded
	5	8.33	12.12	18.75	14.71	degraded	degraded
3	0	0		5.88		degraded	
	1	2.86	3.45	8.11	26.32	degraded	degraded
	3	6.67	6.67	20.69	35.29	degraded	degraded
	5	3.45	5.88	9.76	35.29	degraded	degraded

Table 5.25 Thickness of the composite films measured for 9 months.

Clay wt %	Organic Additive wt %	Thickness, μm							
		before degradation		after 3 months		after 5 months		after 9 months	
		O	GMO	O	GMO	O	GMO	O	GMO
0	0	79.1		81.4		82.6		73.8	
	1	77.7	77.7	91.8	73.6	72.2	68.4	91.6	74.0
	3	69.6	69.6	71.0	71.0	64.0	100.6	75.0	92.6
	5	67.1	67.1	61.4	99.4	75.4	95.6	69.8	79.8
0.1	0	77.0		74.2		82.0		67.6	
	1	73.9	73.9	73.0	83.4	75.2	79.0	75.0	74.2
	3	74.5	74.5	77.6	73.4	66.2	86.6	66.4	58.8
	5	98.1	98.1	102.0	78.4	101.0	97.6	106.2	85.4
0.4	0	67.0		69.4		65.0		58.6	
	1	87.4	87.4	87.2	72.8	111.4	86.0	64.0	75.4
	3	72.6	72.6	70.8	99.6	82.6	111.8	66.2	94.2
	5	88.3	88.3	82.6	74.4	104.0	84.0	91.0	d*
1	0	70.9		76.2		81.6			
	1	72.0	72.0	64.2	72.2	87.0	79.4	d*	d*
	3	78.1	78.1	74.4	68.8	81.8	62.2	d*	d*
	5	76.4	76.4	80.8	74.4	84.4	77.8	d*	d*
3	0	80.3		87.2		78.6		d*	
	1	73.2	73.2	74.6	71.6	77.6	72.6	d*	d*
	3	70.1	70.1	66.4	72.8	59.6	d*	d*	d*
	5	82.0	82.0	68.8	80.4	82.4	79.6	d*	d*

d* = degraded

Table 5.26 $A_{\text{amorphous}}/A_{\text{crystalline}}$ ratio of the composite films for 9 months.

Clay wt %	Organic Additive wt %	$A_{\text{amorphous}}/A_{\text{crystalline}}$							
		before degradation		after 3 months		after 5 months		after 9 months	
		O	GMO	O	GMO	O	GMO	O	GMO
0	0	6.56		6.25		6.33		6.57	
	1	6.87	7.05	7.25	7.12	6.51	6.63	6.92	6.77
	3	6.89	7.05	6.97	7.14	6.6	6.49	6.89	6.91
	5	6.69	7.22	6.8	7.71	6.5	7.05	6.77	7.1
0.1	0	6.74		6.65		6.19		6.28	
	1	7.05	6.31	7	6.38	6.5	5.68	6.69	5.93
	3	6.6	6.69	6.7	6.58	5.87	6.07	6.25	6.08
	5	7.04	7.19	7.05	7.1	6.54	6.58	6.88	6.9
0.4	0	6.68		6.74		6.15		6.45	
	1	6.89	7.16	6.76	7.01	6.47	6.61	6.19	6.88
	3	6.82	6.92	6.5	6.65	6.15	6.32	6.34	6.58
	5	6.73	6.86	6.73	6.62	6.2	5.76	6.45	degraded
1	0	6.64		6.74		5.63		degraded	degraded
	1	6.82	6.88	7.02	6.88	5.53	5.75	degraded	degraded
	3	6.93	6.78	7.08	6.9	5.78	5.67	degraded	degraded
	5	6.64	6.84	6.83	6.89	5.72	6.28	degraded	degraded
3	0	6.7		6.78		6.11		degraded	degraded
	1	6.84	6.69	8.44	6.5	6.13	5.71	degraded	degraded
	3	6.6	6.85	6.57	6.6	5.62	5.58	degraded	degraded
	5	6.73	6.41	6.66	6.49	6.19	5.7	degraded	degraded

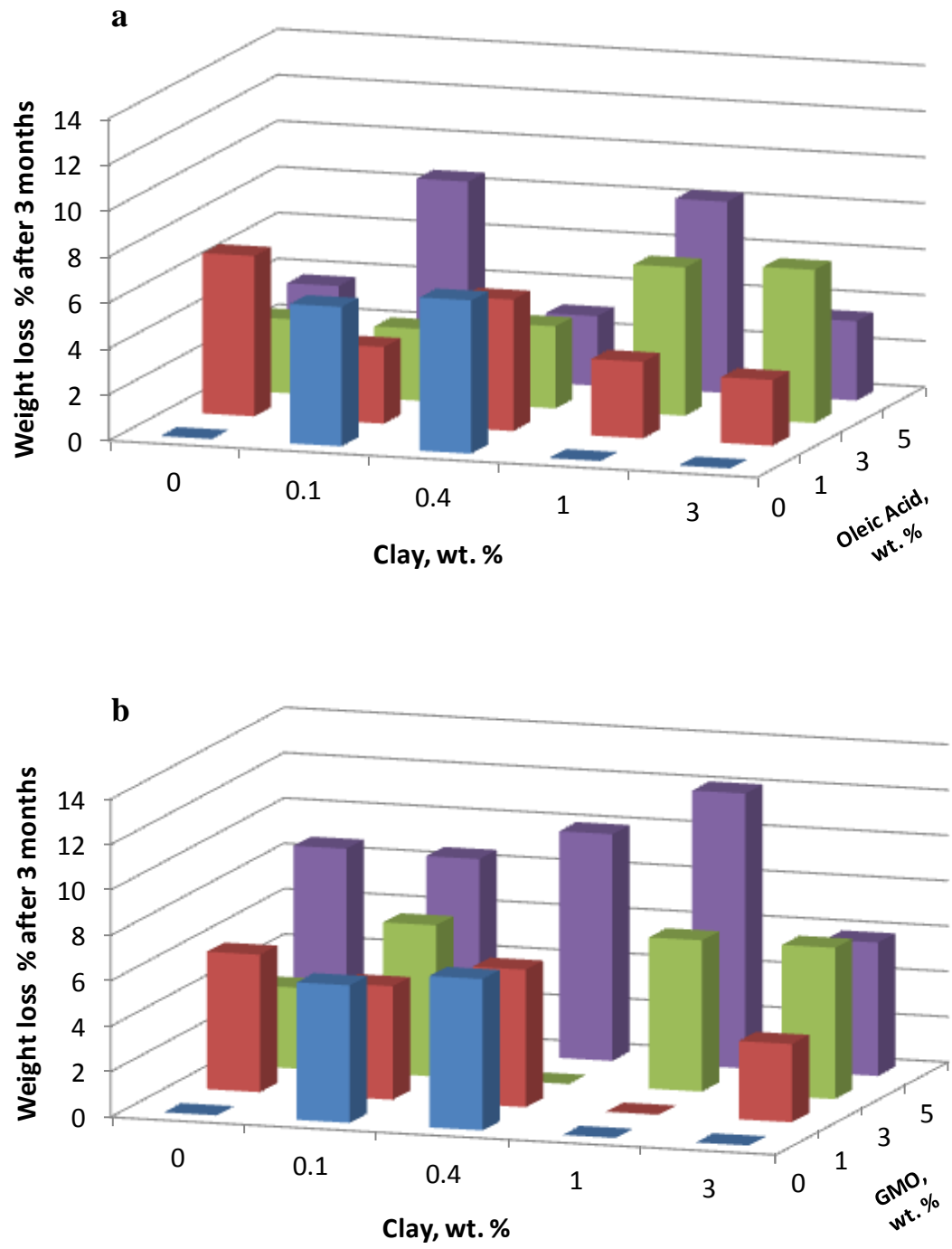


Figure 5.57 Variation of weight loss values after 3 months; a-Clay-Oleic acid; b-Clay-GMO.

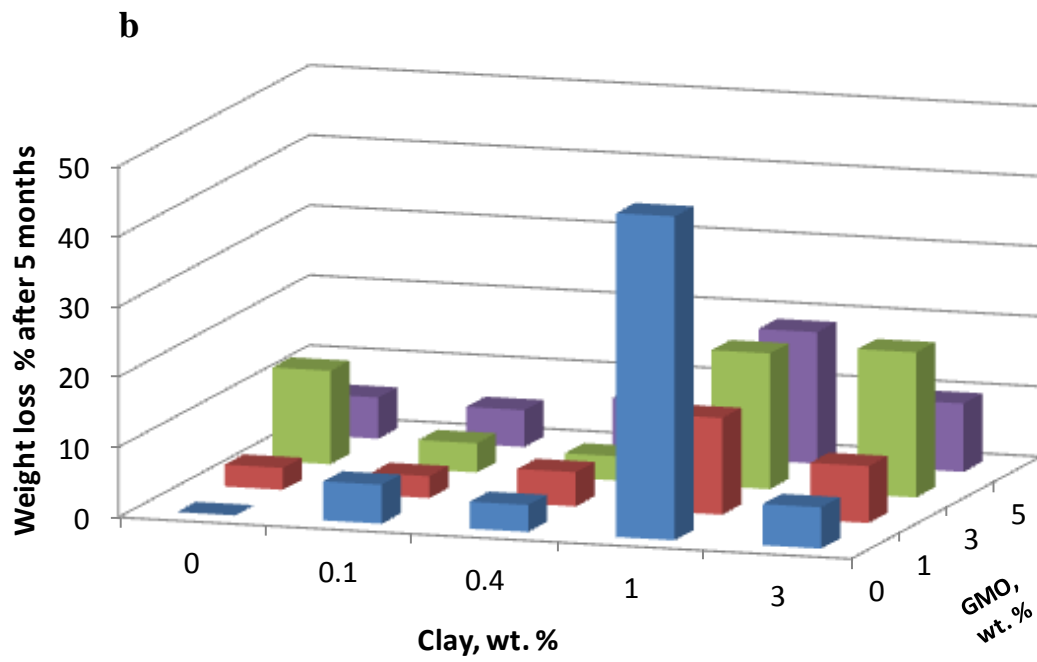
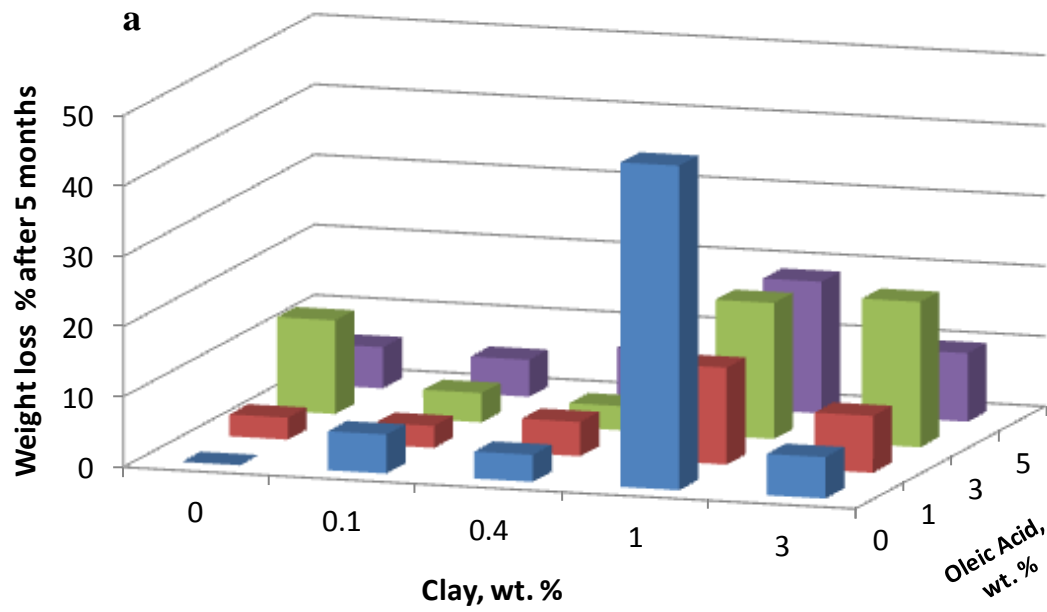


Figure 5.58 Variation of weight loss values after 5 months; a-Clay-Oleic acid; b-Clay-GMO.

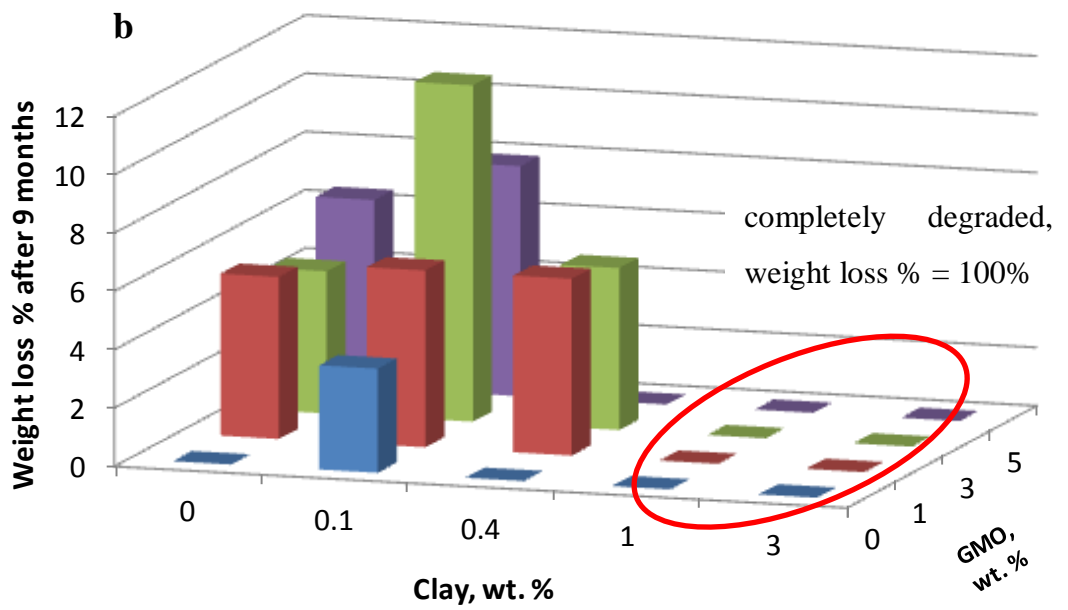
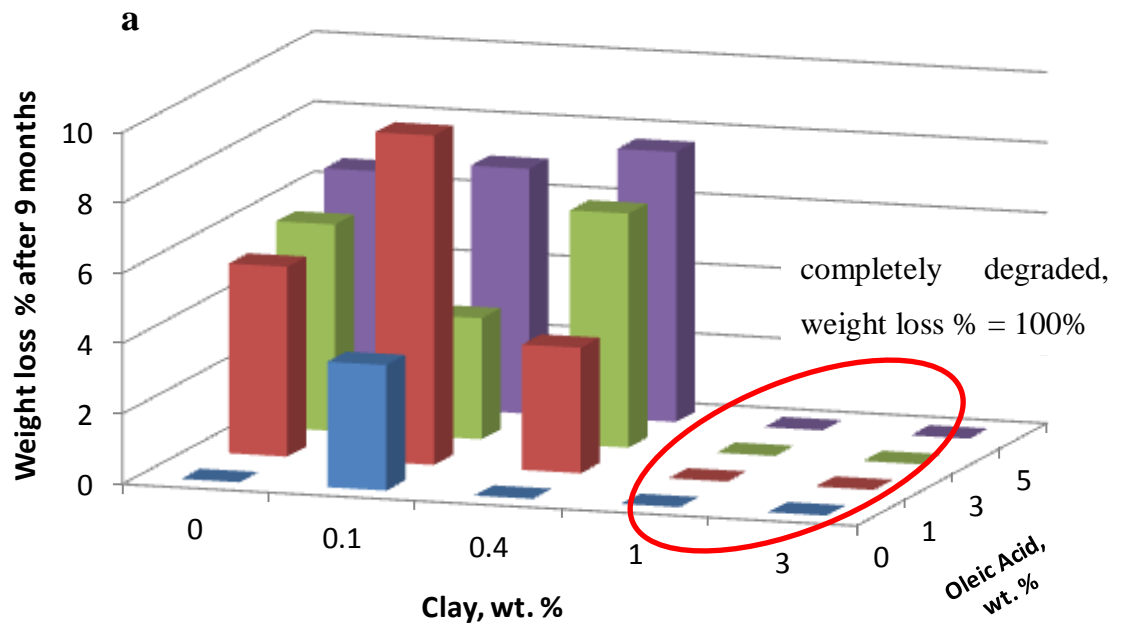


Figure 5.59 Variation of weight loss values after 9 months; a-Clay-Oleic acid; b-Clay-GMO.

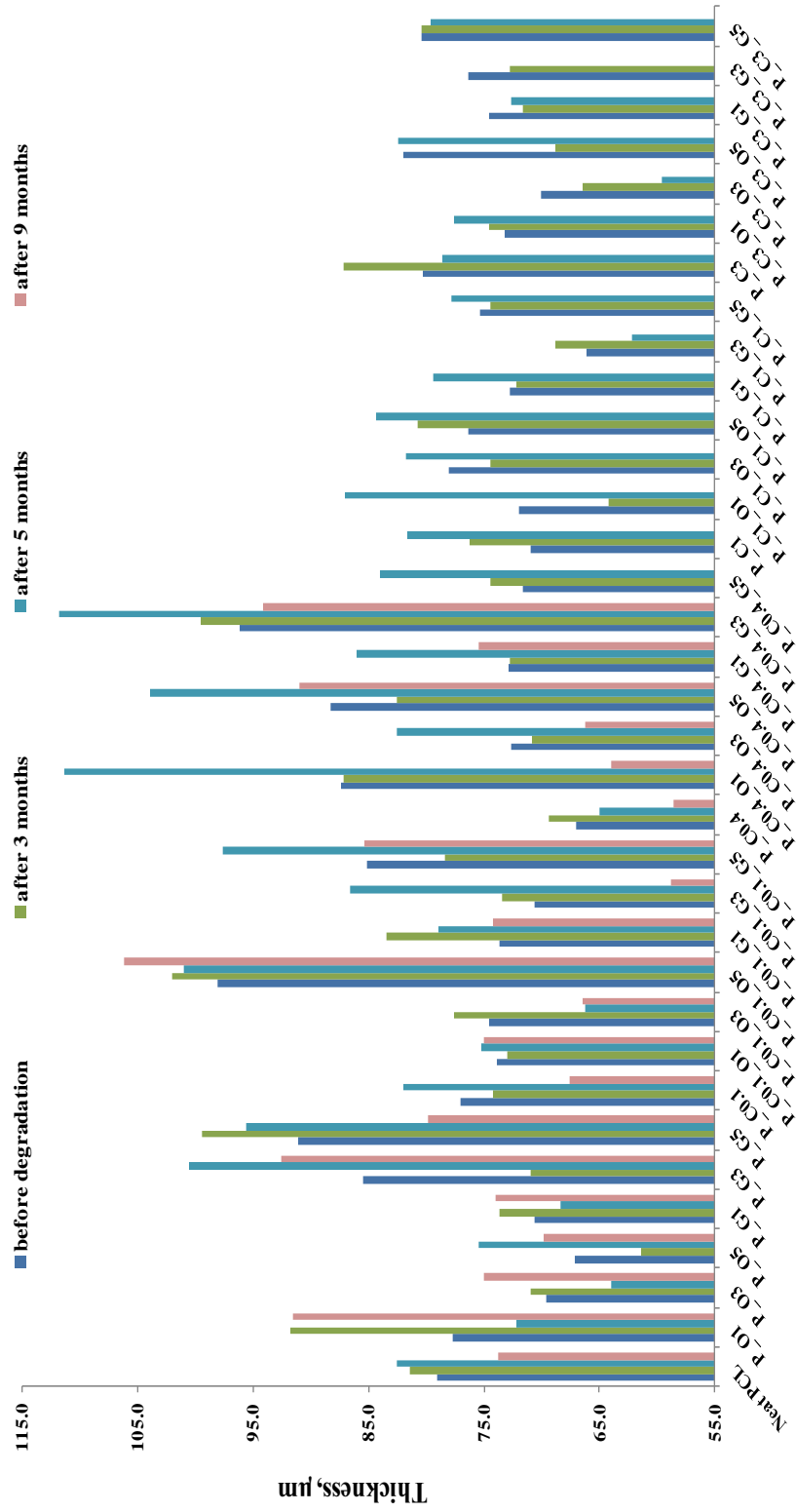


Figure 5.60 Variation of thickness of the composite films for before soil burial and after 3, 5 and 9 months of soil burial.

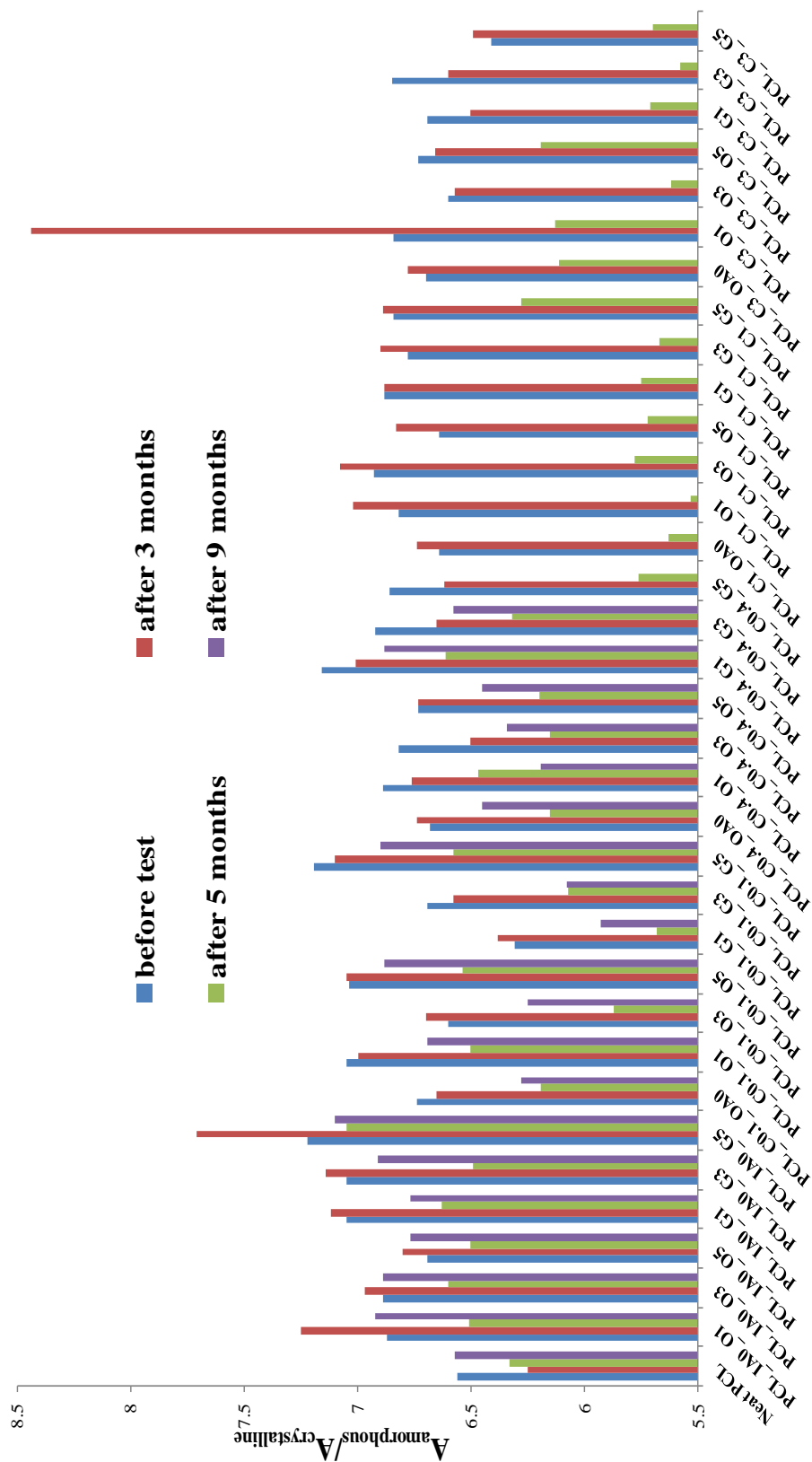


Figure 5.61 Variation of $A_{\text{amorphous}}/A_{\text{crystalline}}$ ratio of the composite films for before soil burial and after 3, 5 and 9 months of soil burial.

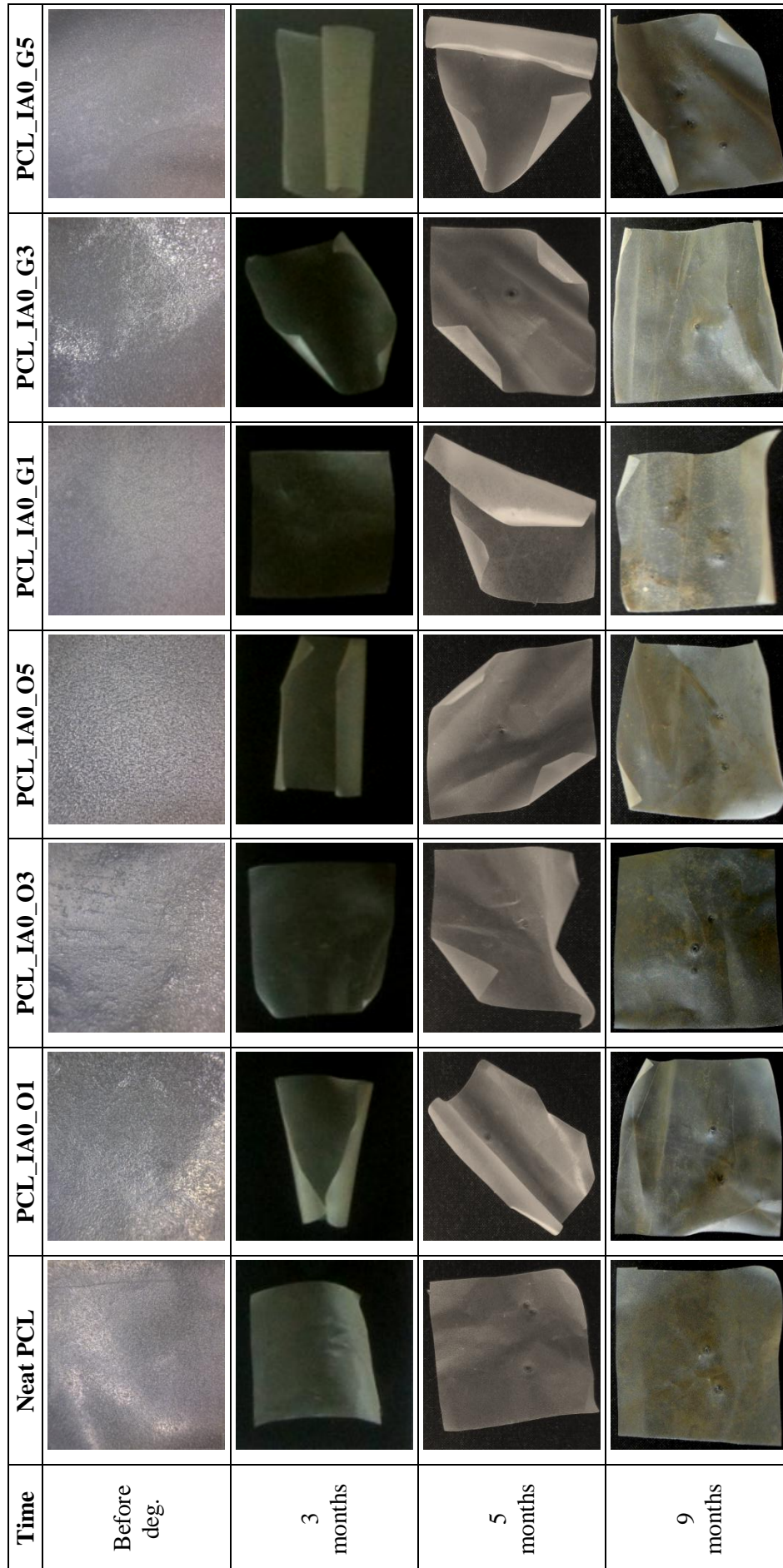


Figure 5.62 Photographs of degradation progress of neat PCL with increasing organic addition before soil burial and after 3, 5 and 9 months of soil burial.






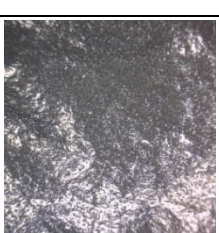

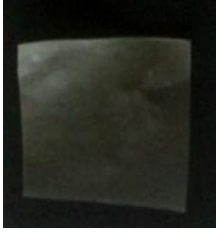

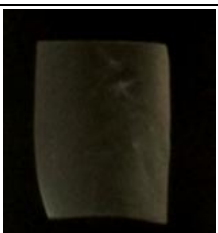

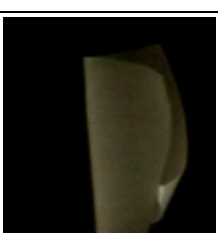


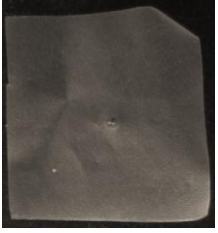
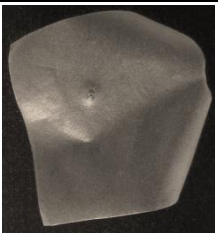
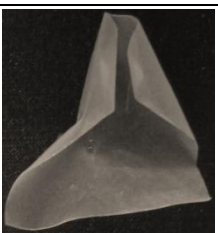
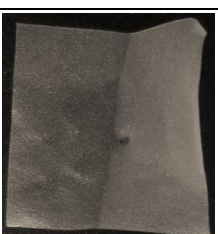
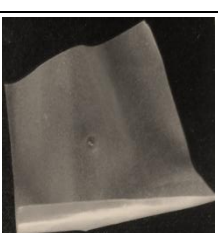
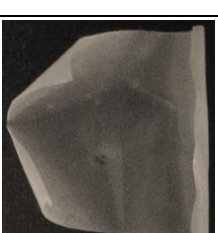
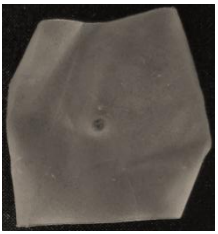
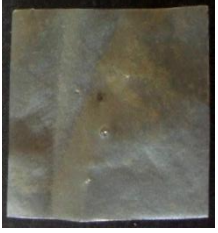

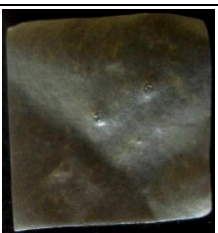
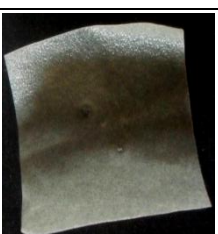


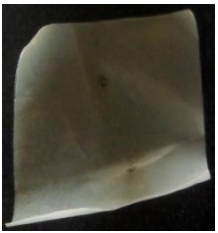
Time	PCL_C0.1_IA0	PCL_C0.1_O1	PCL_C0.1_O3	PCL_C0.1_O5	PCL_C0.1_G1	PCL_C0.1_G3	PCL_C0.1_G5
Before deg.							
3 months							
5 months							
9 months							

Figure 5.63 Photographs of degradation progress of 0.1% clay contained PCL films with increasing organic addition before soil burial and after 3, 5 and 9 months of soil burial.






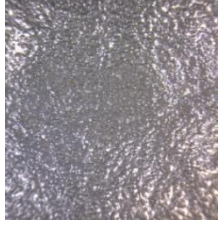





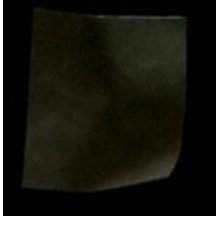
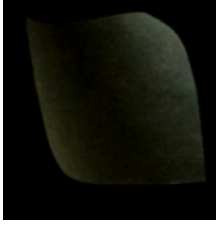

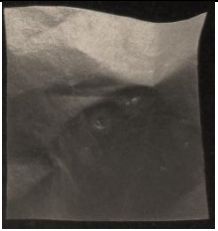
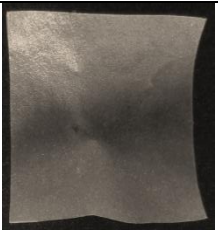
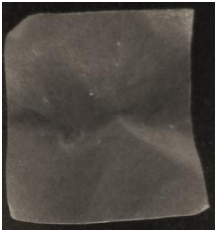
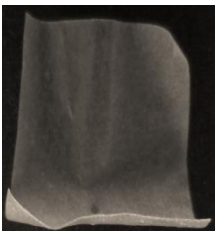
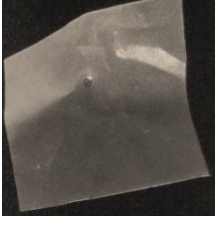
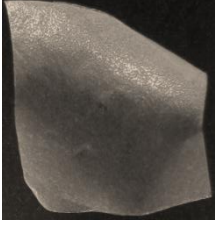


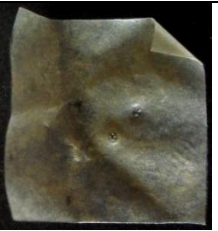
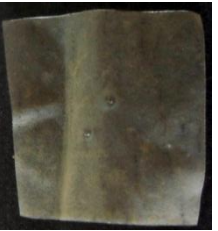


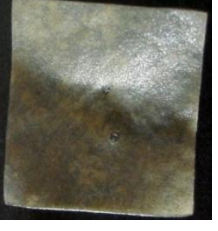
Time	PCL_C0.4_OA0	PCL_C0.4_O1	PCL_C0.4_O3	PCL_C0.4_O5	PCL_C0.4_G1	PCL_C0.4_G3	PCL_C0.4_G5
Before deg.							
3 months							
5 months							
9 months							degraded

Figure 5.64 Photographs of degradation progress of 0.4% clay contained PCL films with increasing organic addition before soil burial and after 3, 5 and 9 months of soil burial.









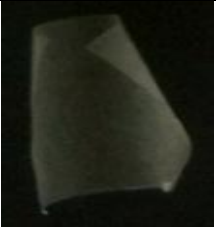
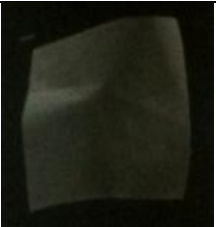


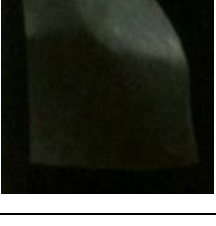
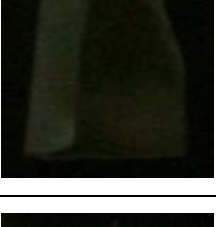
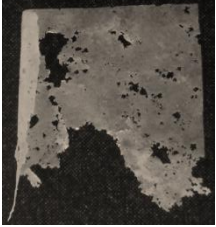
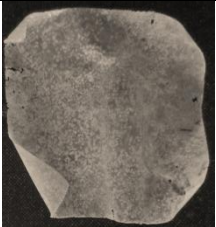
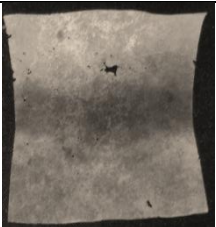

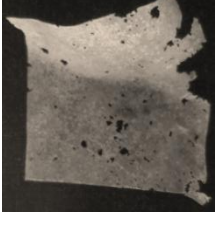

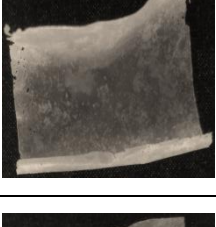
Time	PCL_C1_OA0	PCL_C1_O1	PCL_C1_O3	PCL_C1_O5	PCL_C1_G1	PCL_C1_G3	PCL_C1_G5
Before deg.							
3 months							
5 months							
9 months	completely degraded						

Figure 5.65 Photographs of degradation progress of 1% clay contained PCL films with increasing organic addition before soil burial and after 3 and 5 months of soil burial, they are completely degraded in 9 months.






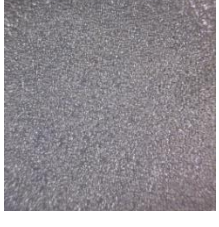





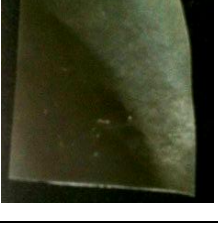
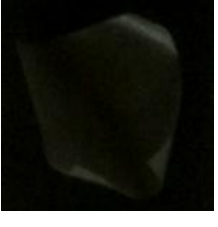
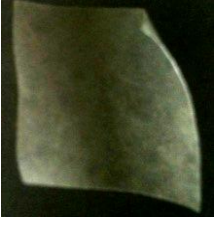
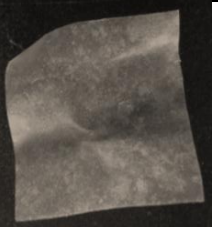
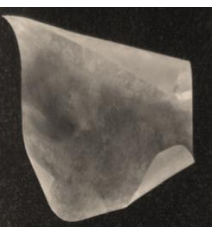
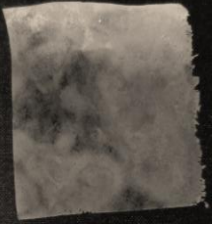

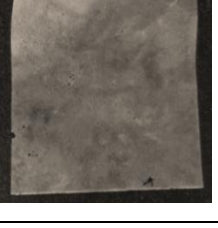
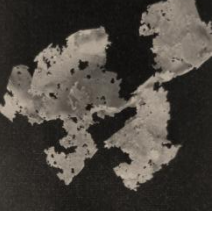

Time	PCL_C3_OA0	PCL_C3_O1	PCL_C3_O3	PCL_C3_O5	PCL_C3_G1	PCL_C3_G3	PCL_C3_G5
Before deg.							
3 months							
5 months							
9 months	completely degraded						

Figure 5.66 Photographs of degradation progress of 3% clay contained PCL films with increasing organic addition before soil burial and after 3 and 5 months of soil burial, they are completely degraded in 9 months.

6. CONCLUSION

Biodegradable and non-toxic materials have many application in packaging, medical, tissue engineering and drug delivery applications. PCL has been approved by the Food and Drug Administration (FDA) in specific applications used in the human body as (for example) a drug delivery device, suture (sold under the brand name Monocryl or generically), or adhesion barrier. Due to wide range applications, PCL composites prepared with inorganic and organic additives can be promising new materials in this area.

The 1st melting temperatures are obtained from melting of the crystals which occurred from solvent casting at room temperature. The mean values of 1st melting temperatures calculated from average of isothermal and nonisothermal DSC results. 2nd melting temperatures are obtained from melting of crystals which obtained from isothermal and nonisothermal crystallization. 1st melting temperatures are higher than 2nd melting temperatures due to forming of crystals at different conditions from solvent casting and from melt. The first melting temperatures of solvent casted composites decrease with increasing clay addition, but the organic additives slightly increase. The second melting temperatures which correspond the industrial extrusion process are lower than the first melting temperatures. The effects of clay and organic additives are not very dominant. From the nonisothermal crystallization, the melting temperature decreases with increasing cooling rate. In isothermal conditions, high amount of clay and organic additives caused low degree of crystallinity due to defective crystal formation and reverse effect obtained in nonisothermal conditions. From the 1st melting peak, DOC% values increases with oleic acid and decreased with GMO in the absence of clay. From the 2nd isothermal melting peak, oleic acid addition is slightly increases and GMO addition decreased the DOC%. Low amount of clay and oleic acid addition also increased the DOC%. From the 2nd nonisothermal melting peaks, high amount of clay and oleic acid contained films showed maximum values of DOC%. This shows that crystallization could be controlled with additives and temperatures.

Avrami exponent, n , values change between 1.86-2.66 which show 2 dimensional crystal growth. Also growth rate constant values, K , show that oleic acid significantly accelerate the crystallization under isothermal conditions (Kahraman et al., 2011). Avrami model insufficient by itself even in isothermal conditions because of secondary nucleation. Crystallinity properties of polymers varies according to the cooling rates, therefore from the nonisothermal crystallization, crystallinity behavior of composite films was obtained for various temperatures and for various cooling rates.

Under nonisothermal conditions, crystallization is significantly accelerated by increasing cooling rates. Crystal growth rate constant values are calculated by Avrami Jeziorny and GMO addition increased the crystal growth of clay contained composite films. Crystal growth kinetics was observed by Ozawa model at each temperature, while crystallization was occurring. The growth rate increased with decreasing temperature for all composite films. The Liu-Mo model was applied to observe the difficulty level of crystal occurrence and to compare Avrami and Ozawa exponents. 3% clay contained composite films show lower value which indicates ease of crystallization. 0.1% clay and organic additive load is increased the $\ln F(T)$ value and this causes difficulty in crystallization. Ozawa exponents are nearly 1.5 times of Avrami exponents. The crystallization activation energy of the crystallization process was determined by Kissinger and Augis–Bennett models. The crystallization activation energy calculations show decrease with 3% clay addition and this proves the nucleating agent effect (Kahraman et al., 2011). The result matches with result of the Liu-Mo model examinations. Secondary nucleation effects are evaluated by Lauritzen Hoffman model. The results showed that nucleation rate is higher at higher cooling rates. Growth rate constants of Regime II is 10 times higher than the growth rate constant of Regime III. Solvent cast composite films show Regime II type crystallization at low cooling rates. In regime II, deposition of secondary nuclei (i) and the rate of lateral surface spreading (g) occurred at the same time and this caused formation of defective crystals. The melting temperatures of the solvent cast films show low melting temperatures due to the defective crystals. $T_{II \rightarrow III}$ change between 15.90°C and 29.50°C. As the cooling rate was increased, regime transition temperature decreased.

Experimental density of films measured with clay additions as expected. Clay addition causes a slight increase in experimental densities for 0.1, 0.4 and 1 wt%, but for 3 wt% causes the density decrease. Because the small amount of clay acts as a nucleating agent and increases the degree of crystallinity of the films and the density increases. But 3 wt% clay cause imperfect crystals. The effect of organic additives are negligible. However, there is a gap between the experimental and theoretical densities due to porous structure of the solvent casted films. SEM pictures also confirmed the porous structure of the composite films. Smooth surface structure is obtained from GMO contained composite films. Contact angle measurements show no significant difference but organic additive addition increases the contact angle and the films have higher wettability properties. Tensile testing was performed for all composite films. From stress-strain diagram of the PCL film, it could be said that the composite films are ductile and quite strong via elongation curve and observation during the test. Neat PCL has already flexible surface and values of the elongation at break is 597.69 %. High load of clay and organic additives especially increased elongation and tensile

stress values. Degree of crystallinity, X_{c1} , Young's Modulus, tensile strength and percentage elongation at break of PCL composite films were determined and interaction parameter B (according to Pukanzky Model) were calculated. Parameter B in the model characterises the interaction between PCL and Clay, and the higher the B values (positive) indicate the better interaction. The absence of oleic acid and GMO, clay particles were not dispersed homogenously in PCL matrix. Organic additives were provided well dispersion of clay in PCL matrix. (Kahraman et al., 2012).

Thermal and biological degradation properties are examined. The results showed that thermal degradation start temperature of the composite films are increased with clay addition and improved the thermal properties. The degradation activation energies calculated for all films. Clay and GMO contained composite films show higher values in comparison with clay and oleic acid contained composite films and that means clay-GMO contained composite films are less easily degraded than clay-oleic acid contained films with regard to degradation activation energy.

The soil degradation tests have been performed for 9 months up to now. Neat PCL, 0.1% and 0.4% clay contained composite films show slight degradation but biodegradation of 1% and 3% clay contained composite films was accelerated and after 6 months, they are degraded. This could be explained with the crystal structure of the composite films. From XRD patterns of before and after soil burial of samples, it was observed that the degree of crystallinity percent highly increased after soil burial. That means, first amorphous regions of the films were digested by bacteria. From FTIR spectrum of before and after soil buried PCL composite films, although the spectra of films are qualitatively similar, they are quantitatively different. Before and after soil burial test of the ratio of A/A (1157/1293) of FTIR peak ratios of PCL composite films were calculated. The amorph/crystal peak areas ratio of A/A (1157/1293) before soil burial test higher than the ratio of A/A (1157/1293) after soil burial test. This result also indicated that first amorphous regions of the films was digested by bacteria. Low amount of clay contained composite films have higher amount of perfect crystals and high load of clay particles lowered the perfect crystal occurrence and ease the biodegradation in the soil burial. Also, GMO addition into 1% and 3% clay contained composite films accelerates the biodegradation.

7. RECOMMENDATIONS

As future study, isothermal crystallization could be performed at least two more crystallization temperatures in order to obtain secondary nucleation kinetics parameters for isothermal conditions by Lauritzen-Hoffman model.

For the packaging applications, barrier properties (oxygen, vapour, air, etc.) should be analyzed. Because the composite films are obtained by solvent casting method in this study, the films have porous structure and the barrier properties could be measured for the films obtained by extrusion process.

Composite films could be produced with extrusion process and crystallization and product properties can be compared with the obtained results for solvent casting method.

The intercalated structure of clay in the composite films could be visualized in detail by TEM (Transmission Electron Microscope) photos.

Further statistical evaluations could be carried out to define the relations between crystallization and product properties of the composite films.

REFERENCES

- Acar I., Durmuş A. and Özgümüş S.**, 2007, Nonisothermal crystallization kinetics and morphology of poly(ethylene terephthalate) modified with poly(lactic acid), *Journal of Applied Polymer Science*, 106, 4180-4191p.
- Acierno S., Maio E., Iannace S. and Grizzuti N.**, 2005, Structure development during crystallization of polycaprolactone, *Rheologica Acta*, 45, 387-392p.
- Alexandre M. and Dubois P.**, 2000, Polymer-layered silicate nanocomposites: preparation, properties and uses of a new class of materials, *Mater Sci Eng R*, 28, 1-63.p.
- Aloisi G. G., Elisei F., Nocchetti M., Camino G., Frache A., Costantino U. and Latterini L.**, 2010, Clay based polymeric composites: Preparation and quality characterization, *Materials Chemistry and Physics*, 123, 372-377p.
- Avella M., Bondioli F., Cannillo V., Pace E., Errico M. and Ferrari A.**, 2006, Poly(ϵ -caprolactone)-based nanocomposites: Influence of compatibilization on properties of poly(ϵ -caprolactone)-silica nanocomposites, *Composites Science and Technology*, 66, 886-894p.
- Balazs A., Singh C., Zhulina E. and Lyatskaya Y.**, 1999, Modeling the phase behavior of polymer/clay nanocomposites, *Acc Chem Res*, 32, 651-657p.
- Becker O., Varley R. and Simon G.**, 2004, Thermal stability and water uptake of high performance epoxy layered silicate nanocomposites, *Eur Polym J*, 40, 187-195p.
- Bharadwaj R., Murga M. and Chavira A.**, 2002, Structure-property relationships in cross-linked polyester-clay nanocomposites, *Polymer* 43, 3699-3705p.
- Bittiger H. and Marchessault R.**, 1923, Crystal Structure of Poly- ϵ -caprolactone, *Acta Cryst.*, B26, 112-119p.
- Blaga A.**, 1973, Properties and Behaviour of Plastics, *Canadian Building Digest*, Report No:CBD-157, pp. 4p.
- Chen H., Li L.-J., Ou-Yang W.-C., Hwang J. C. and Wong W.-Y.**, 1997, Spherulitic Crystallization Behavior of Polycaprolactone with a Wide Range of Molecular Weight, *Macromolecules*, 30, 1718-1722p.
- Davis G. and Song J.**, 2006, Biodegradable packaging based on raw materials from crops and their impact on waste management, *Industrial crops and products*, 23, 147-161p.
- Di Maio E., Iannace S., Sorrentino L. and Nicolais L.**, 2004, Isothermal crystallization in PCL/clay nanocomposites investigated with thermal and rheometric methods, *Polymer*, 45, 8893-8900p.
- Durmuş A., Ercan N., Soyubol G., Deligöz H. and Kaşgöz A.**, 2009, Nonisothermal crystallization kinetics of poly(ethylene terephthalate)/clay nanocomposites prepared by melt processing, *Polymer Composites*, NA-NAp.

REFERENCES (continued)

- Durmus A. and Yalçinyuva T.**, 2008, Effects of additives on non-isothermal crystallization kinetics and morphology of isotactic polypropylene, *Journal of Polymer Research*, 16, 489-498p.
- Elzein T., Nasser-Eddine M., Delaite C., Bistac S. and Dumas P.**, 2004, FTIR study of polycaprolactone chain organization at interfaces, *Journal of Colloid and Interface Science*, 273, 381-387p.
- Fischer H.**, 2003, Polymer nanocomposites: from fundamental research to specific applications, *Mater Sci Eng*, 23, 763-772p.
- Flory J.**, 1962, Polymer Crystallization, *Amer. Chem. Soc.*, 84, 2857p.
- Flory P.**, 1985, Thermodynamics of high polymer solutions, *J. Chern. Phys*, 10, 51-61p.
- Fornes D. and Paul R.**, 2004, Structure and Properties of Nanocomposites Based on Nylon-11 and -12 Compared with Those Based on Nylon-6, *Macromolecules*, 37, 7698-7709p.
- Fukushima K., Abbate C., Tabuani D., Gennari M., Rizzarelli P. and Camino G.**, 2010, Biodegradation trend of poly(ϵ -caprolactone) and nanocomposites, *Materials Science and Engineering: C*, 30, 566-574p.
- Gan Z., Zhang J. and Jiang B.**, 1997, Non-isothermal crystallization of a phase-separated PCL/PEO diblock copolymer, *J Appl Polym Sci* 63,
- Gedde U.**, 1995, *Polymer Physics*, Chapman&Hall, 312p.
- Geil P.**, 1963, *Polymer Single Crystals*, John Wiley & Sons, 9,
- Giannelis P.**, 1996, Polymer layered silicate nanocomposites, *Advance Materials*, 8, 29-35p.
- Ginzburg V., Singh C. and Balazs A.**, 2000, Theoretical phase diagrams of polymer/clay composites: the role of grafted organic modifiers, *Macromolecules* 33, 1089–1099p.
- Gopakumar T. G., Lee J. A., Kontopoulou M. and Parent J. S.**, 2002, Influence of clay exfoliation on the physical properties of montmorillonite/polyethylene composites, *Polymer*, 43, 5483–5491p.
- Gorrasi G., Tortora M., Vittoria V., Galli G. and Chiellini E.**, 2002, Transport and mechanical properties of blends of polycaprolactone and modified montmorillonite–polycaprolactone nanocomposite, *Journal of Polymer Science*, 40, 1118-1124p.
- Grozdánov A., Buzarovska A., Bogoeva-Gaceva G., Avella M., Errico M. E. and Gentile G.**, 2007, Nonisothermal crystallization kinetics of kenaf fiber/polypropylene composites, *Polymer Engineering & Science*, 47, 745-749p.

REFERENCES (continued)

- Hiemenz P. C.**, 1984, *Polymer Chemistry: The Basic Concepts*, Marcel Dekker Press, New York,
- Hoffman J. and Lauritzen J.**, 1961, *Theory of Crystallization*, Research NBS 65A, 297p.
- Hoidy W. H., Al-Mulla E. A. J. and Al-Janabi K. W.**, 2010, Mechanical and Thermal Properties of PLLA/PCL Modified Clay Nanocomposites, *Journal of Polymers and the Environment*, 18, 608-616p.
- Homminga D., Goderis B., Dolbnya I. and Groeninckx G.**, 2006, Crystallization behavior of polymer/montmorillonite nanocomposites. Part II. Intercalated poly(ϵ -caprolactone)/montmorillonite nanocomposites, *Polymer*, 47, 1620-1629p.
- Huang Y., Liu H., He P., Yuan L., Xiong H., Xu Y. and Yu Y.**, 2010, Nonisothermal crystallization kinetics of modified bamboo fiber/PCL composites, *Journal of Applied Polymer Science*, NA-NAP.
- Jana R. N. and Cho J. W.**, 2010, Non-isothermal crystallization of poly(ϵ -caprolactone)-grafted multi-walled carbon nanotubes, *Composites Part A: Applied Science and Manufacturing*, 41, 1524-1530p.
- Janeschitz H.**, 2010, *Crystallization Modalities in Polymer Melt Processing*, Springer-Verlag/Wien, 228p.
- Kahraman T., Cesur S. and Balkose D.**, 2011, Crystallization Kinetics Of Polycaprolactone-Clay-Oleic Acid Composite Films By Primary And Secondary Nucleation Models, 18th International Symposium on Industrial Crystallization, ISIC18, 18, 235-237p.
- Kahraman T., Cesur S. and Balkose D.**, 2012, Oleik Asit/ Gmo ve Kil Katkılı Pcl Kompozit Filmlerin Ürün Özellikleri, *UKMK-10*, 10, 350-358p.
- Kahraman T., Cesur S. and Balkose D.**, 2011, PCL-Organokil ve Oleik asit katkılı kompozit filmlerin kristalizasyonu ve Son Ürün Özelliklerinin Karakterizasyonu, 1st National Composite Materials Symposium (KOMPEGE), 1, 175-178p.
- Ke Z. and Yongping B.**, 2005, Improve gas barrier property of PET film with montmorillonite by in situ interlayer polymerization, *Mater Lett*, 59, 3348–3351p.
- Kim S. H., Ahn S. H. and Lee S. G.**, 2004, Surface-modified silica nanoparticle-reinforced poly(ethylene 2,6-naphthalate), *Journal of Applied Polymer Science*, 94, 812-818p.
- Krishnamoorti R. and Giannelis E.**, 1997, Rheology of end-tethered polymer layered silicate nanocomposites, *Macromolecules*, 30, 4097–4102p.

REFERENCES (continued)

- Labidi S., Azema N., Perrin D. and Lopez-Cuesta J.-M.**, 2010, Organo-modified montmorillonite/poly(ϵ -caprolactone) nanocomposites prepared by melt intercalation in a twin-screw extruder, *Polymer Degradation and Stability*, 95, 382-388p.
- Lagaly G.**, 1999, Introduction: from clay mineral-polymer interactions to clay mineral-polymer nanocomposites, *Appl Clay Sci*, 15, 1-9p.
- LeBaron P., Wang Z. and Pinnavaia T.**, 1999, Polymer-layered silicate nanocomposites: an overview, *J. Appl Clay Sci*, 15, 11-29p.
- Lee Y. and Park T. G.**, 2011, Facile Fabrication of Branched Gold Nanoparticles by Reductive Hydroxyphenol Derivatives, *Nanobiometaterials*, 27, 2965-2971p.
- Lepoittevin B., Devalckenaere M., Pantoustier N. and Alexandre M.**, 2002, Polycaprolactone/clay nanocomposites prepared by melt intercalation: mechanical, thermal, rheological properties, *Polymer*, 43, 4017-4023p.
- Lincoln D., Vaia R., Wang Z. and Hsiao B.**, 2001, Secondary structure and elevated temperature crystallite morphology of nylon 6/layered silicate nanocomposites, *Polymer* 42, 1621-1631p.
- Liu H., Huang Y. and Yuan L.**, 2010, Isothermal crystallization kinetics of modified bamboo cellulose/PCL composites, *Carbohydrate Polymers*, 79, 513-519p.
- Lovera D., Márquez L., Balsamo V., Taddei A., Castelli C. and Müller A. J.**, 2007, Crystallization, Morphology, and Enzymatic Degradation of Polyhydroxybutyrate/Polycaprolactone (PHB/PCL) Blends, *Macromolecular Chemistry and Physics*, 208, 924-937p.
- Luduená L., Alvarez V. and Vazquez A.**, 2007, Processing and microstructure of PCL/clay nanocomposites, *Materials Science and Engineering: A*, 460-461, 121-129p.
- Ludueña L. N., Vazquez A. and Alvarez V. A.**, 2008, Crystallization of polycaprolactone-clay nanocomposites, *Journal of Applied Polymer Science*, 109, 3148-3156p.
- Maiti P., Nam P., Okamoto M., Kotaka T., Hasegawa N. and Usuki A.**, 2002, Influence of crystallization on intercalation, morphology, and mechanical properties of propylene/clay nanocomposites, *Macromolecules*, 35, 2042-2049p.
- Maiti P., Nam P. H. and Okamoto M.**, 2002, Influence of Crystallization on Intercalation, Morphology, and Mechanical Properties of Polypropylene/Clay Nanocomposites, *Macromolecules*, 35, 2042-2049p.
- Mandelkern L.**, 1964, *Crystallization of Polymers*, McGraw-Hill, England, 442p.

REFERENCES (continued)

- Manias E.**, 2001, Origins of the materials properties enhancements in polymer/clay nanocomposites, *Nanotechnology*, 25, 1145-1149p.
- Mareaua V.**, 2005, Prud'homme, R.E. *Polymer*, 46, 7255p.
- Mark J.**, 2007, *Physical Properties of Polymers Handbook*, Springer-Verlag/Wien, 2,215-230p.
- Mersmann A.**, 2001, *Crystallization Technology Handbook*, Marcel Dekker, 846p.
- Metin D., Tihminlioglu F., Balkose D. and Ulku S.**, 2003, The effect of interfacial interactions on the mechanical properties of polypropylene/natural zeolite composites, *Elsevier Composite*, 35, 23 - 32p.
- Mitchell C. A. and Krishnamoorti R.**, 2005, Non-isothermal crystallization of in situ polymerized poly(ϵ -caprolactone) functionalized-SWNT nanocomposites, *Polymer*, 46, 8796-8804p.
- Mochizuki M. and Hayashi T.**, 1999, Studies on Biodegradable Poly(Hexano-6-Lactone) Fibers, *Pure Appl. Chem.*, 71, 2177 - 2188p.
- Montgomery D. C.**, 1997, *Design and Analysis of Experiments*, John Wiley & Sons, 5, 284p.
- Nam J. Y. and Ray S. S.**, 2003, Crystallization behavior and morphology of biodegradable polylactide/layered silicate nanocomposite, *Macromolecules*, 36, 7126-7131p.
- Okada A. and Usuki A.**, 2006, Twenty Year of Polymer-Clay Nanocomposites, *Macromolecular Materials Engineering*, 291, 1449-1476p.
- Osman M., Mittal V. and Lusti H.**, 2004, The aspect ratio and gas permeation in polymer-layered silicate nanocomposites, *Macromol Rapid Commun*, 25, 1145-1149p.
- Pantoustier N., Lepoittevin B., Alexandre M., Kubies D., Calberg C. and Jerome R.**, 2002, Biodegradable polyester layered silicate nanocomposites based on polycaprolactone, *Polym Eng Sci*, 42, 1928-1937p.
- Papageorgiou G. Z., Achilias D. S., Bikiaris D. N. and Karayannidis G. P.**, 2005, Crystallization kinetics and nucleation activity of filler in polypropylene/surface-treated SiO₂ nanocomposites, *Thermochimica Acta*, 427, 117-128p.
- Pashaei S. and Syed A.**, 2011, Thermal degradation kinetics of Nylon6/crysnano nanoclay nanocomposites by TGA, *Chemical Industry & Chemical Engineering Quarterly*, 2, 141-151p.
- Pavlidou S. and Papaspyrides C. D.**, 2008, A review on polymer-layered silicate nanocomposites, *Progress in Polymer Science*, 33, 1119-1198p.
- Pennings A.**, 1967, *Crystal Growth*, Pergamon Oxford, England, 332p.

REFERENCES (continued)

- Perez C. J. and Alvarez V. A.**, 2009, Overall crystallization behavior of polypropylene-clay nanocomposites; Effect of clay content and polymer/clay compatibility on the bulk crystallization and spherulitic growth, *Journal of Applied Polymer Science*, 114, 3248-3260p.
- Prarthana U. and Vikrant V.**, 2011, Review: Crystallization of Biodegradable Polymers, *Polymer-Plastics Technology and Engineering*, 50, 1289–1304p.
- Rattaa V., Ayambemb A., Younga R., McGrathb J. and Wilkesa G.**, 2000, Thermal stability, crystallization kinetics and morphology of a new semicrystalline polyimide Polymer, 41, 8121-8138p.
- Ray S. and Okamoto M.**, 2003, Polymer-layered silicate nanocomposite: a review from preparation to processing, *Prog Polym Sci*, 28, 1539–1641p.
- Rodriguez F.**, 1987, *Principles of Polymer Systems*, McGraww Hill Book Company, 3rd printing, 110-125p.
- Rosa D. S., Guedes C. G. F. and Casarin F.**, 2005, Mechanical Behavior and Biodegradation of Poly(ϵ -caprolactone)/Starch Blends with and without Expansor, *Polymer Bulletin*, 54, 321-333p.
- Seretoudi G., Bikiaris D. and Panayiotou C.**, 2002, Synthesis, characterization and biodegradability of poly(ethylene succinate)/poly(ϵ -caprolactone) block copolymers, *Polymer*, 43 5405-5415p.
- She H., Xiao X. and Liu R.**, 2007, Preparation and characterization of polycaprolactone-chitosan composites for tissue engineering applications, *Journal of Materials Science*, 42, 8113-8119p.
- Skoglund P. and Fransson A.**, 1996, Continuous Cooling and Isothermal Crystallization of Polycaprolactone, *Journal of Applied Polymer Science*, 61, 2455-2465p.
- Stejny K., Dlugosz J. and Keller J.**, 1979, Crystallization of Polymers, *A.J. Mater. Sci.* , 14, 1291p.
- Tetto J. and Steeves D.**, 1999, Biodegradable polycaprolactone/clay nanocomposites, *Ann Tech Conf Soc Plast Eng*, 24, 1628–1632p.
- Vaia R. and Wagner H.**, 2004, Framework for nanocomposites, *Mater Today*, 7, 32-37p.
- Varlot K., Reynaud E., Kloppfer M. and Vigier G.**, 2001, Clay-reinforced polyamide: preferential orientation of the montmorillonite sheets and the polyamide crystalline lamellae, *Journal of Polymer Science*, 39, 1360-1370p.
- Vassiliou A. A., Papageorgiou G. Z., Achilias D. S. and Bikiaris D. N.**, 2007, Non-Isothermal Crystallisation Kinetics of In Situ Prepared Poly(ϵ -caprolactone)/Surface-Treated SiO₂ Nanocomposites, *Macromolecular Chemistry and Physics*, 208, 364-376p.

REFERENCES (continued)

- Vyazovkin S. and Dranca I.**, 2006, Isoconversional Analysis of Combined Melt and Glass Crystallization Data, *Macromol. Chem. Phys.*, 207, 20–25p.
- Vyazovkin S., Dranka I., Fan X. and Advincula R.**, 2004, Kinetics of the thermal and thermo-oxidative degradation of a polystyrene–clay nanocomposite, *Macromol Rapid Commun*, 25, 498–503p.
- Vyazovkin S., Stone J. and Sbirrazzuoli N.**, 2005, Hoffman–Lauritzen Parameters for Non-Isothermal Crystallization of Poly(Ethylene Terephthalate) and Poly(Ethylene Oxide) Melts, *Journal of Thermal Analysis and Calorimetry*, 80, 177–180p.
- Wang J.-L. and Dong C.-M.**, 2006, Physical properties, crystallization kinetics, and spherulitic growth of well-defined poly(ϵ -caprolactone)s with different arms, *Polymer*, 47, 3218-3228p.
- Wang X.-L., Huang F.-Y., Zhou Y. and Wang Y.-Z.**, 2009, Nonisothermal Crystallization Kinetics of Poly(ϵ -Caprolactone)/Montmorillonite Nanocomposites, *Journal of Macromolecular Science, Part B*, 48, 710-722p.
- Wegner G.**, 1979, *Farad. Discuss. , Roy. Soc. Chem.*, 68, 494p.
- Wong S.-C. and Baji A.**, 2007, Fracture strength and adhesive strength of hydroxyapatite-filled polycaprolactone, *Journal of Materials Science: Materials in Medicine*, 19, 929-936p.
- Woodruff M. A. and Hutmacher D. W.**, 2010, The return of a forgotten polymer—Polycaprolactone in the 21st century, *Progress in Polymer Science*, 35, 1217-1256p.
- Wu D., Wu L., Wu L., Xu B., Zhang Y. and Zhang M.**, 2007, Nonisothermal cold crystallization behavior and kinetics of polylactide/clay nanocomposites, *Journal of Polymer Science Part B: Polymer Physics*, 45, 1100-1113p.
- Wu T.-M., Hsu S.-F., Chien C.-F. and Wu J.-Y.**, 2004, Isothermal and nonisothermal crystallization kinetics of syndiotactic polystyrene/clay nanocomposites, *Polymer Engineering and Science*, 44, 2288-2297p.
- Wu T., Xie T. and Yang G.**, 2009, Preparation and characterization of poly(ϵ -caprolactone)/Na⁺-MMT nanocomposites, *Applied Clay Science*, 45, 105-110p.
- Yingwei D., Salvatore I. and Nicholas L.**, 2005, Barrier and Mechanical Properties of Polycaprolactone /Organoclay Nanocomposites, *Macromolecules*, 228, 115-124p.
- Zhao J., Guo L., Yang X. and Weng J.**, 2008, Preparation of bioactive porous HA/PCL composite scaffolds, *Applied Surface Science*, 255, 2942-2946p.

CURRICULUM VITAE

Tansel KAHRAMAN



Yenigun Mah. Oncü Sit. N Blok D:6 Yenişehir-BURSA

Mobile Phone: 0090-506-957-96-64

E-mail:kahramantansel@gmail.com

PERSONAL INFORMATION

TR Identity No	26233447450
Birth Date & Place	08.09.1987 / Bursa
Marital Status	Single
Driving Licence	Class B-2006
Languages	English (Advance), Italian (Upper Intermediate), German (Beginner)

EDUCATIONAL BACKGROUND

2012-present	Robert Bosch A.Ş., Bursa Plant (Product Development Engineer)
2010-2013	MS in Chemical Engineering, Ege University
2008-2010	BS in Chemical Engineering, Ege University
2007-2008	BS in Chemical Engineering, La Sapienza, Italy, (Through Erasmus Student Exchange Program)
2006-2007	BS in Chemical Engineering, Ege University (Transfer from Ataturk University)
2005-2006	BS in Chemical Engineering, Ataturk University, Erzurum, Turkey (Third place in department)

EXPERIENCE

- Polarized Optical Microscope with heating/cooling control (POM),
- Isothermal and Nonisothermal Differential Scanning Calorimetry (DSC),
- Contact Angle,
- Scanning Electron Microscopy (SEM),
- Gas Permeability Tests,
- Mechanical Testing,
- Biodegradation tests with simulated soil testing systems were used in Master Thesis.

- 04/2010 – 11/2010 Secreteriat and Organizing committee –
Chamber of Chemical Engineers
**(“International Polymeric Composites Symposium-
Exhibition and Brokerage Event”)**
- 2007-2008 LA SAPIENZA” University of Roma, Roma/ITALY
**(“Organic Matter Reduction an Olive Vegetation Waste
Water by Photocatalysis with Titanium Dioxide
Nanoparticles”)**
- 2006–2007 Anadolu Glass Factory (Şişecam), Bursa/TURKEY

RESEARCH PROJECTS & PRESENTATIONS

- 2010-2012 TUBITAK (110M157) (The Scientific and Technological
Research Council of Turkey) Project - “Modelling of
Crystallization Kinetics and Investigation of Affecting
Parameters on Desired Product Properties in PCL Composites
with Inorganic and Organic Additives”
- 2011 -2013 Ege University, BAP (11MUH041) Project - “İnorganik ve
Organik Katkılı PCL Kompozitlerde Kristalizasyon Sürecinin
Modellenmesi ve İstenen Ürün Özelliklerine Etki Eden
Parametrelerin İncelenmesi”
- 2012 Cesur, S., D. Balköse, B. Alp, T. Kahraman, Y. Küçükgöksel,
“Crystallization Kinetics and Affecting Parameters on PCL
Composites with Inorganic and Organic Additives”,
POLYSOLVAT-9, 9th International IUPAC Conference on
Polymer-Solvent Complexes & Intercalates, 11-14 September
2012, Kiev, Ukraine, Oral Presentation, Abstract in CD.

- 2011 Kahraman, T., S. Cesur, D. Balköse, "Oleik asit ve kil katkı polikaprolakton kompozit filmlerinin karakterizasyonu ve kristalliğinin kontrolü" KOMPEGE 2011, I. Ulusal Ege Kompozit Malzemeler Sempozyumuna, 17-19 Kasım 2011 Kuşadası, İZMİR
- 2011 Kahraman T., Cesur S., Balkose D., (Reference # 167) "Crystallization Kinetics Of Polycaprolactone-Clay-Oleic Acid Composite Films By Primary And Secondary Nucleation Models",18th International Symposium on Industrial Crystallization (18. Uluslararası Endüstriyel Kristalizasyon Sempozyumu), ISIC18, 12-17 Eylül 2011, Zürih, İsviçre, Poster Bildiri
- 2011 Polymer Chemistry – Research Project (Oral Presentation)
"Investigation of Crystallization Kinetics of Heated and Non-Heated Al - Biaxially Oriented Polypropylene (BOPP) Films"
- 2010 PETKIM Petrochemical Holding A.S.
"Aspen Simulation of the Aromatics plant"
- 2010 ICAST 2010 (Poster presentation)
"Evaluation of Sugar Industry by Process Integration"
- 2010 Kahraman, T., ve S. Cesur, "Şeker Endüstrisinde Enerji Kullanımı Açısından Süreç İyileştirme Uygulamaları", UKMK-9, 9. Ulusal Kimya Mühendisliği Kongresi, Bildiri Numarası: 7-553, sözlü sunum, CD içinde Tam Makale, Ankara, 22-25 Haziran 2010
- 2008 Design Report about Production of Formalin
- 2008 Diploma Project on "Thermal integration in Sugar Industry"
- 2007 Project Report for OMY 160 Technical English Course on Autoglass

ADDITIONAL TRAINING

Computer	Windows Office Programs (Word, Excel, Power Point), Visual Basic, Intellicad, Matlab, UNIFAC, Aspen Plus, Aspen Pinch, Minitab, Endnote, OriginPro
2012	Moderation Skills, Robert Bosch
2012	Lean Administration, Robert Bosch
2010/2011	ISO9001 – OHSAS Seminar Participation
2008/2009	Total Quality Management, Ege University, İzmir
2008/2009	KAIZEN, Ege University, İzmir
2007/2008	Italian Language Course, Leonardo Da Vinci, Rome, Italy
2006/2007	Hazard Analysis and Critical Control Point, Ege University, İzmir

PROFESSIONAL MEMBERSHIPS

Member of Management Committee of ESN-Izmir (Erasmus Student Network)

Member of ESN-Rome

Member of Chemical Engineering Society

REFERENCE**Associate Professor Serap CESUR**

Ege University - Faculty of Engineering **Tel:** +90(232) 311 40 45 – 4045

e-mail: cesur.serap@gmail.com

Prof. Dr. Devrim BALKÖSE

İzmir Technology University - Faculty of Engineering **Tel:** +90(232) 750 66 52

e-mail: devrimbalkose@iyte.edu.tr

Assistant Professor Ali DURMUŞ

Istanbul University - Faculty of Engineering **Tel:** +90 (212) 473 70 70

e-mail: durmus@istanbul.edu.tr

APPENDICES

APPENDIX A. Isothermal Exotherms, Relative Crystallinity Percentage as Function of Time Plots and Isothermal Avrami Plots

APPENDIX B. Nonisothermal DSC Exotherms of Composite Films

APPENDIX C. Avrami Jeziorny Plots

APPENDIX D. Ozawa Plots

APPENDIX E. Liu Mo Plots

APPENDIX F. Lauritzen Hoffman Plots

APPENDIX G. Polarized Optical Microphotos

APPENDIX H. FTIR Analysis

APPENDIX I. SEM Microphotos

APPENDIX J. XRD Patterns of Composite Films

APPENDIX K. Mechanical Analysis

APPENDIX L. Thermal Degradation Plots

APPENDIX M. Biodegradation Plots

APPENDIX A. Isothermal Exotherms, Relative Crystallinity Percentage as Function of Time Plots and Isothermal Avrami Plots

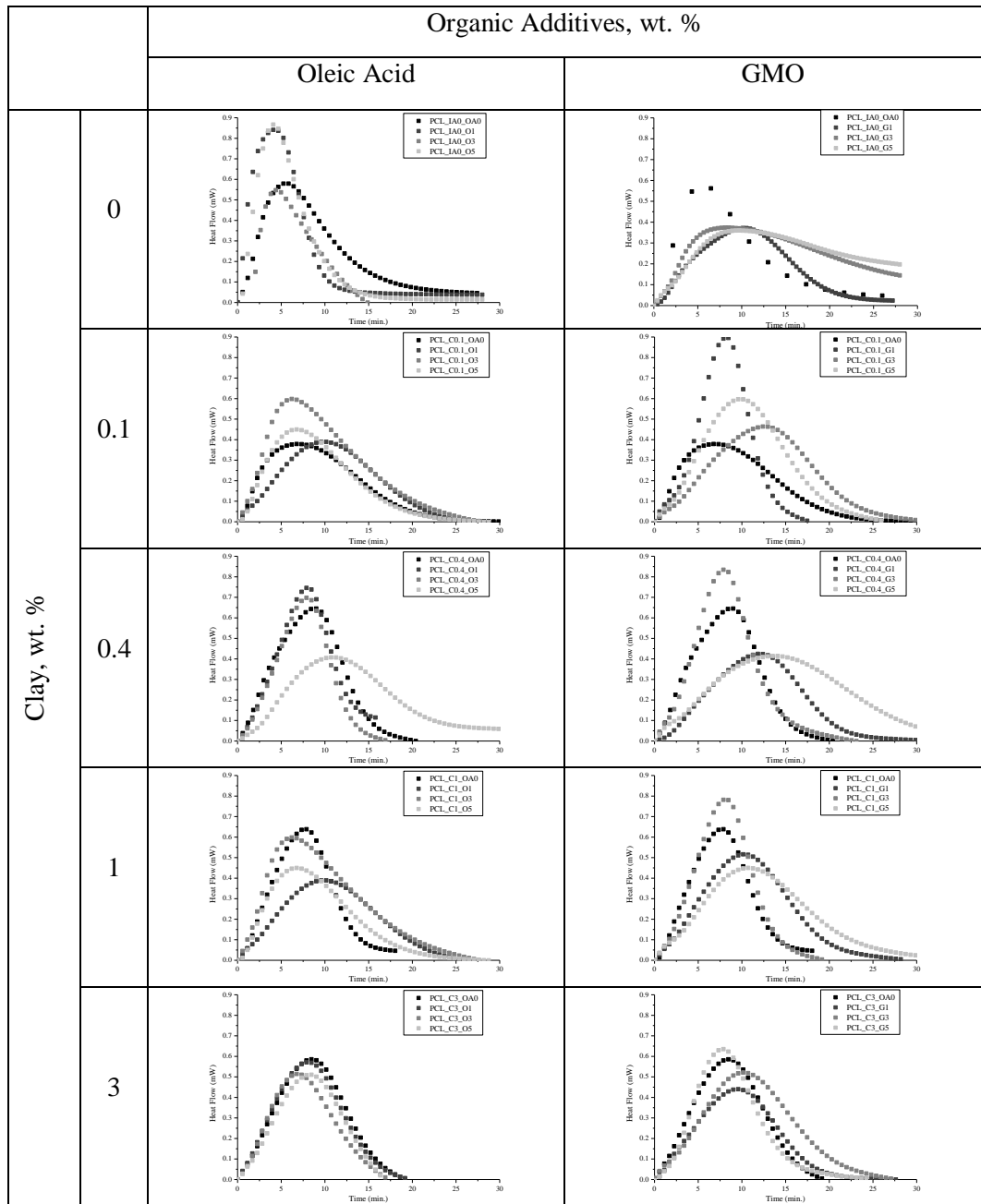


Figure A1. DSC exotherms of PCL composite films with inorganic additive by increasing organic additive concentrations.

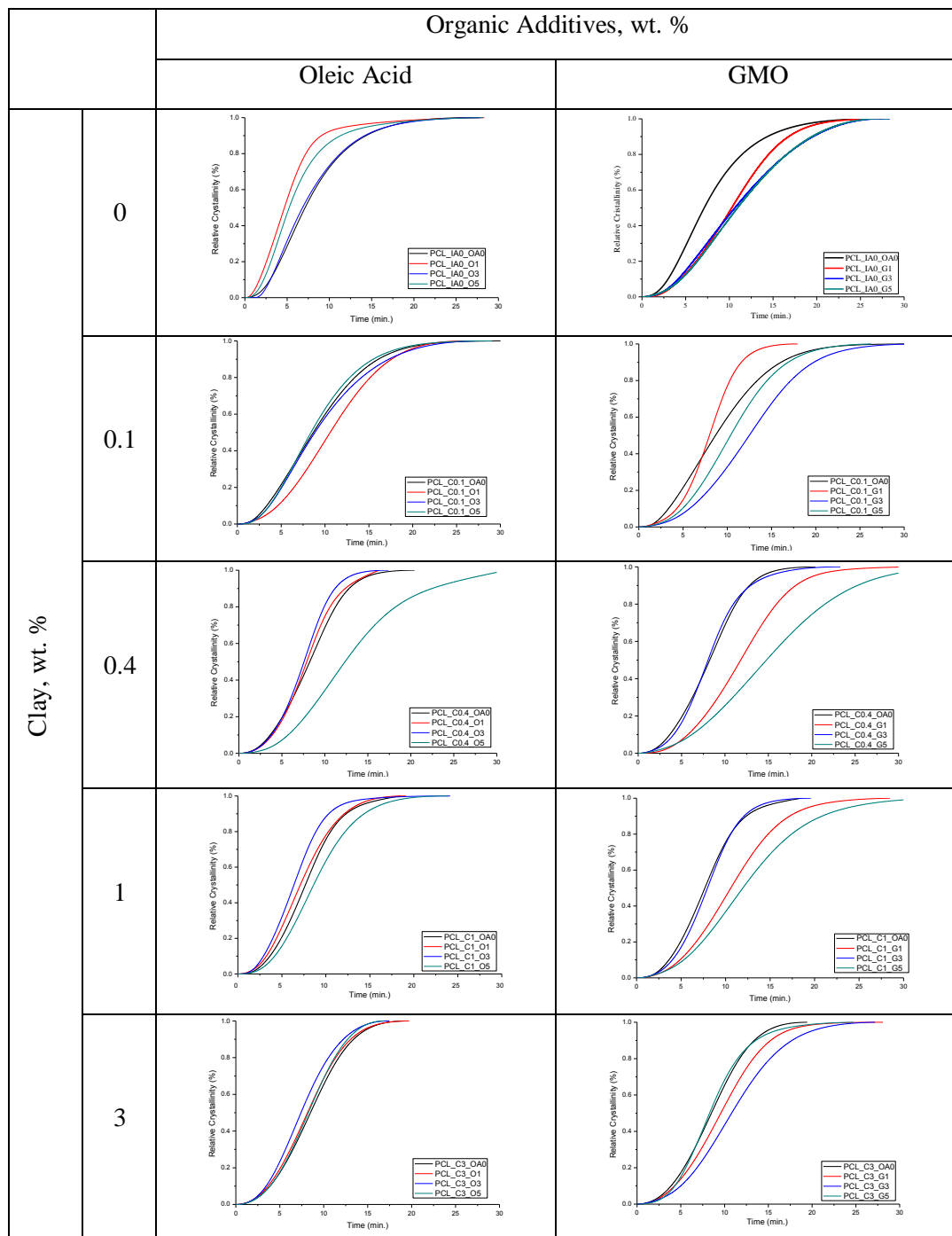


Figure A2. Relative degree of crystallinity % change of PCL based composite films by increasing organic additive concentration with respect to time.

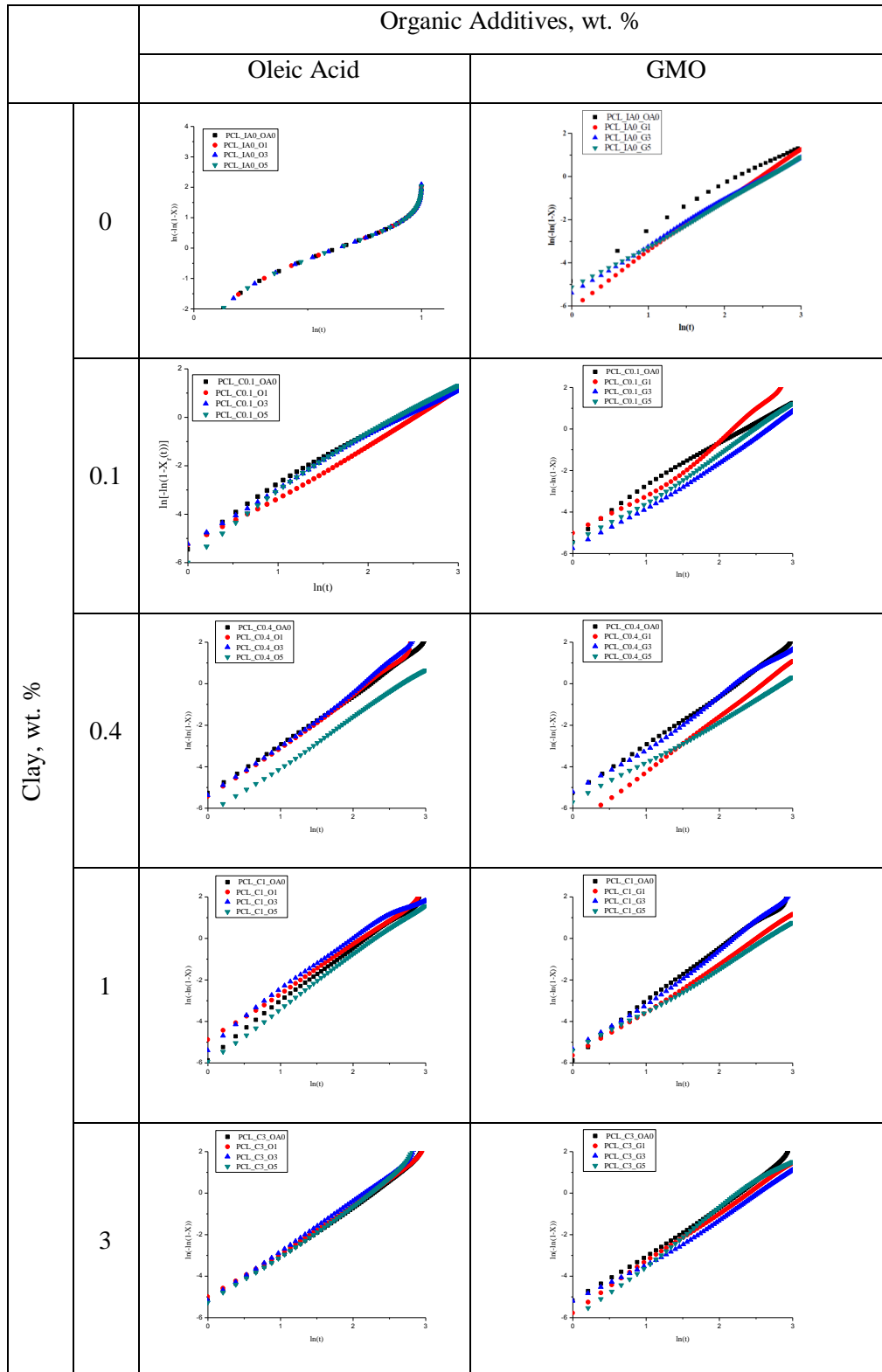


Figure A3. Avrami plots of PCL composite films.

APPENDIX B. Nonisothermal DSC Exotherms of Composite Films

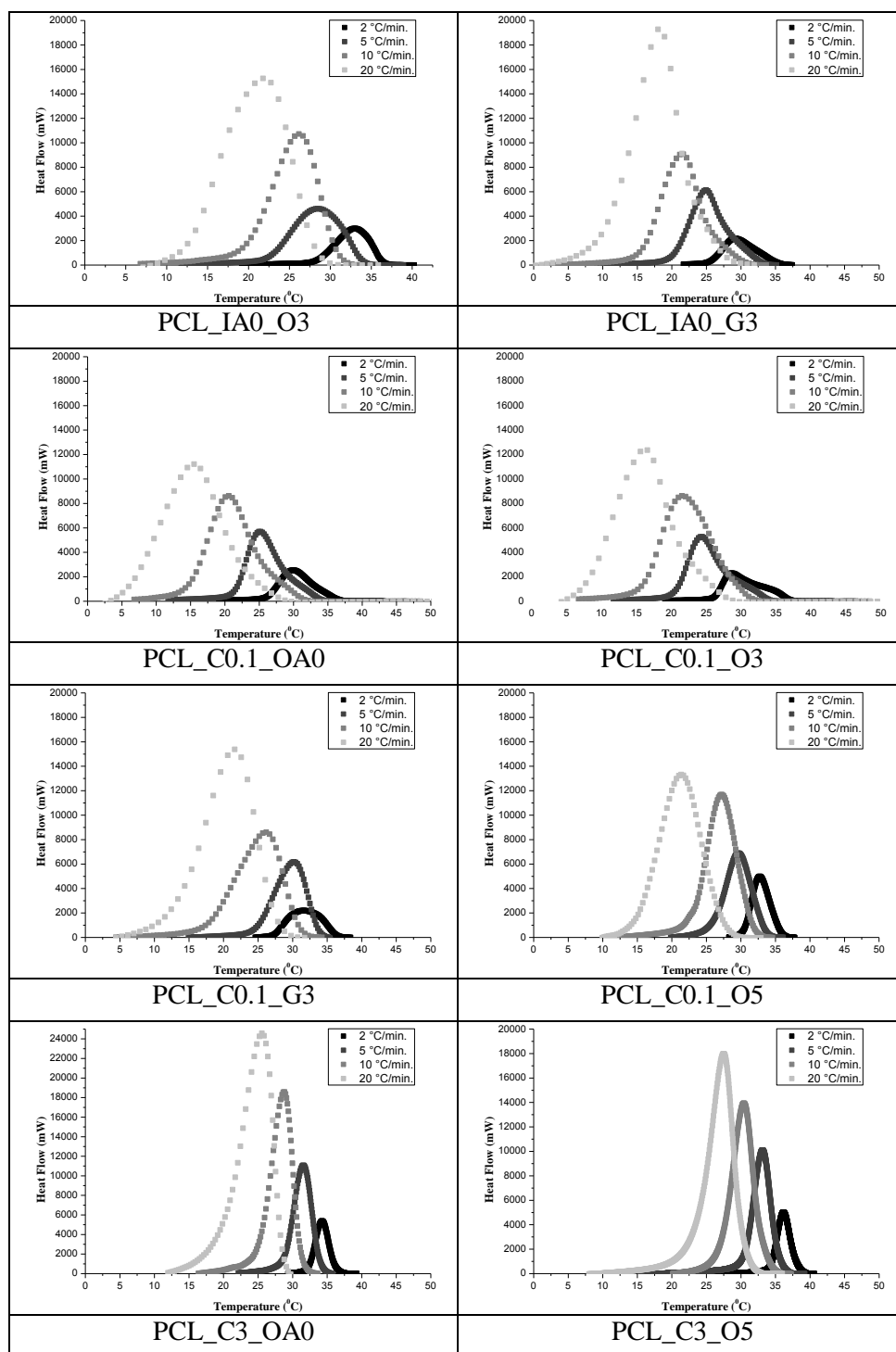


Figure B1. Nonisothermal crystallization exotherms of selected composite films.

APPENDIX C. Avrami Jeziorny Plots

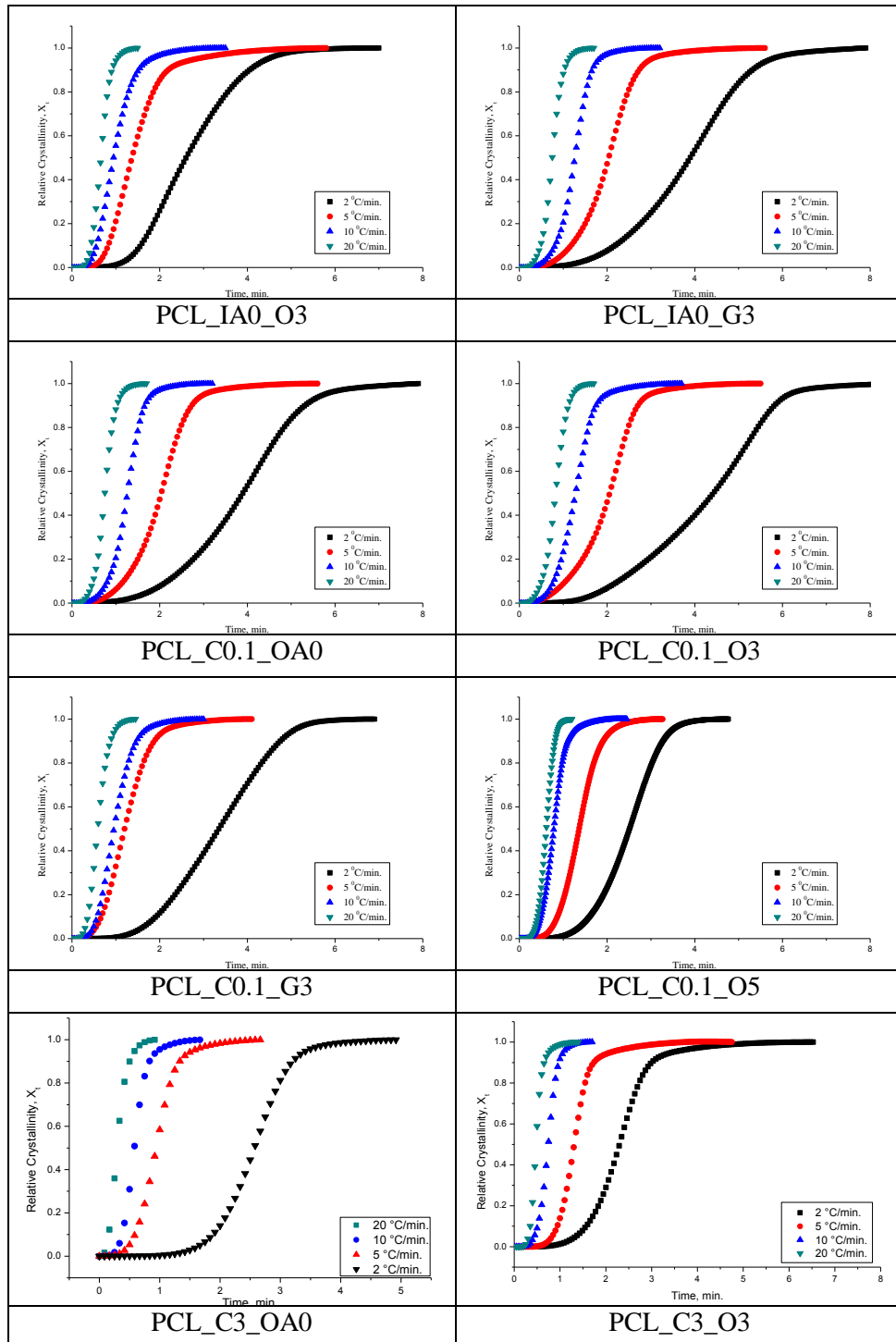


Figure C1. Variation of relative degree of crystallinity versus time plot for nonisothermal crystallization for selected PCL composite films.

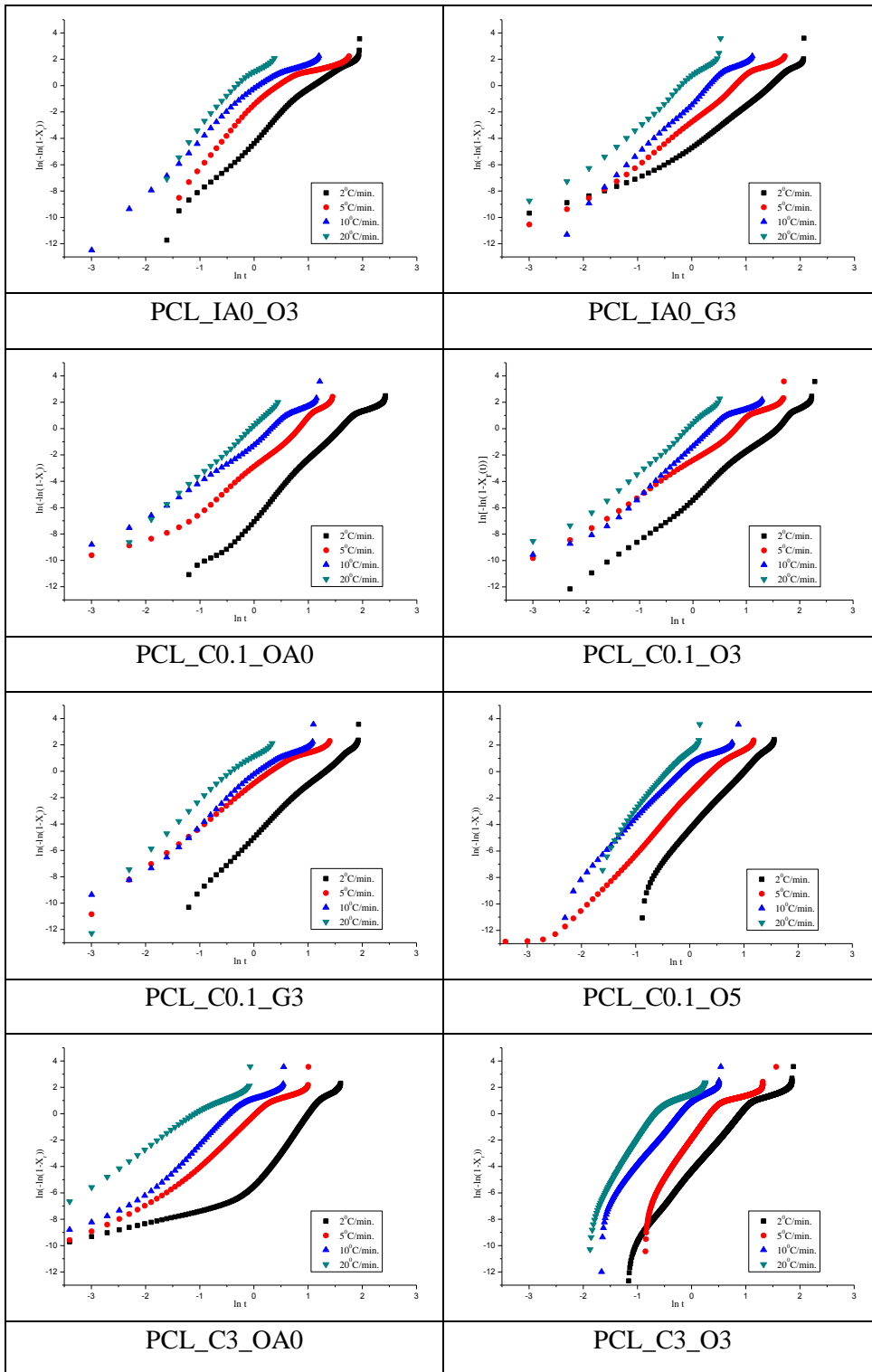


Figure C2. Avrami Jeziorny plots of the composite films.

APPENDIX D. Ozawa Plots

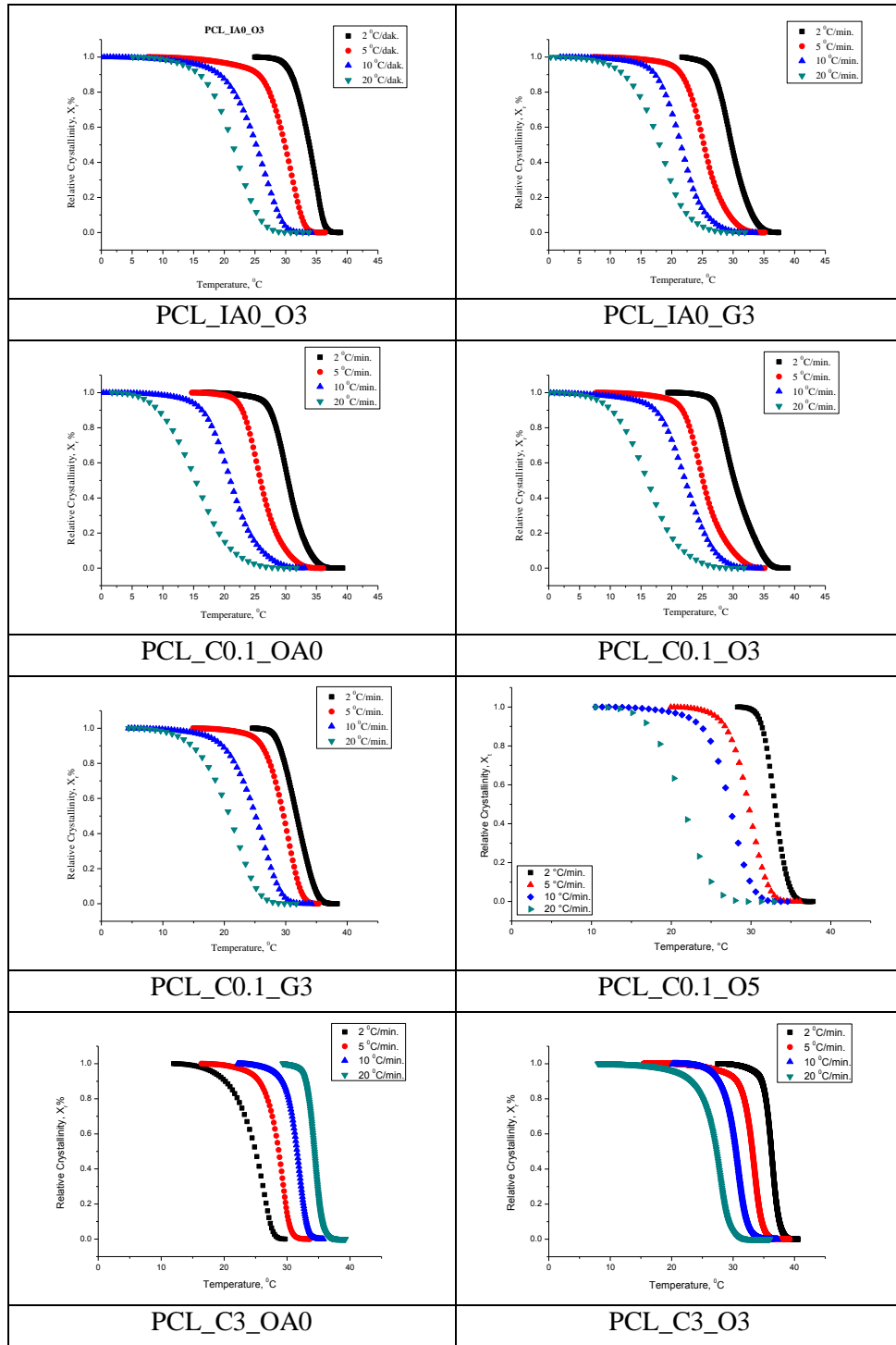


Figure D1. Variation of relative degree of crystallinity percent versus temperature plots for nonisothermal crystallization of selected PCL composite films.

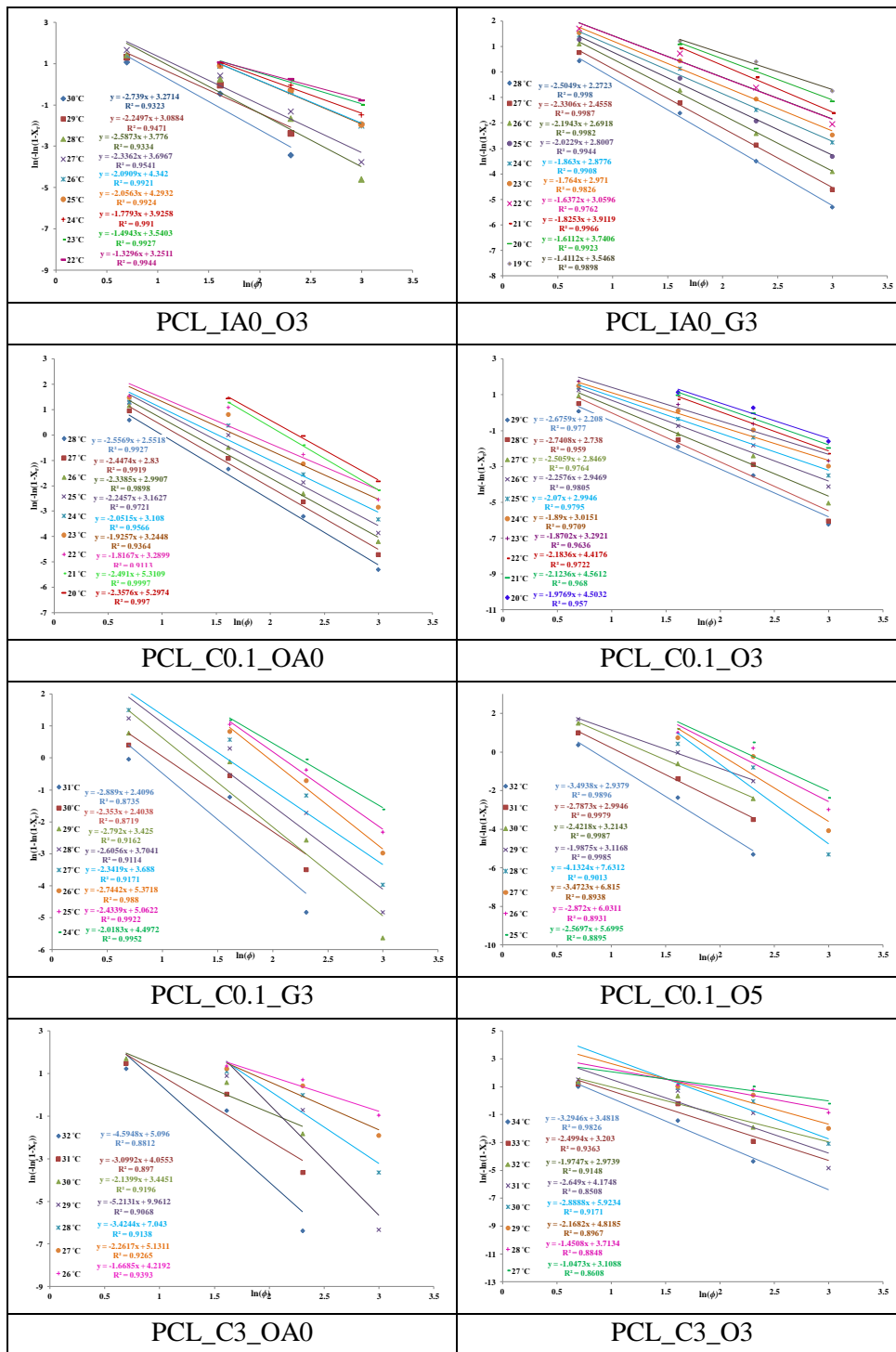


Figure D2. Ozawa plots for nonisothermal crystallization of selected PCL composite films.

APPENDIX E. Liu Mo Plots

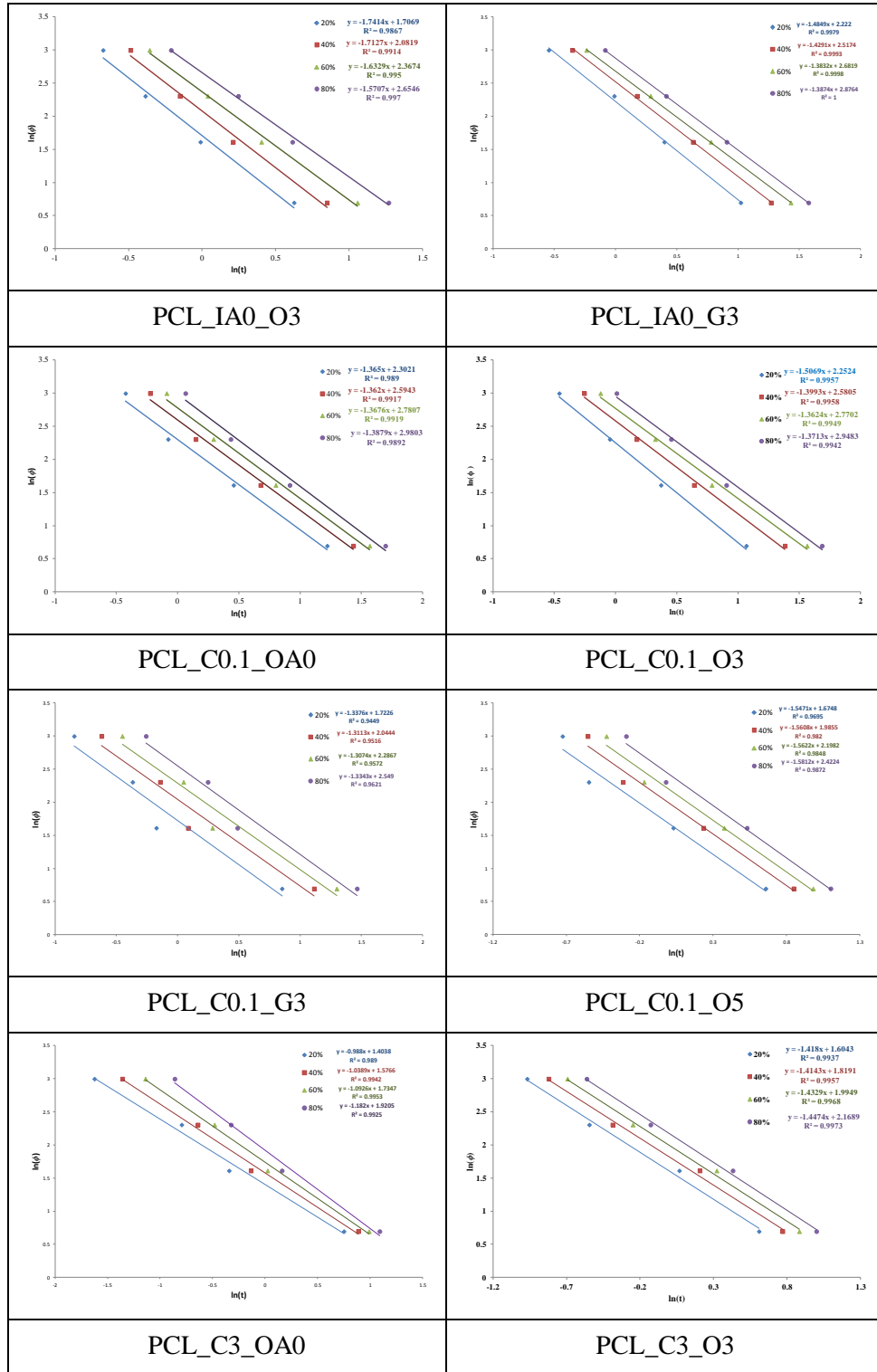


Figure E1. Liu Mo plots for nonisothermal crystallization of selected PCL composite films.

APPENDIX F. Lauritzen Hoffman Plots

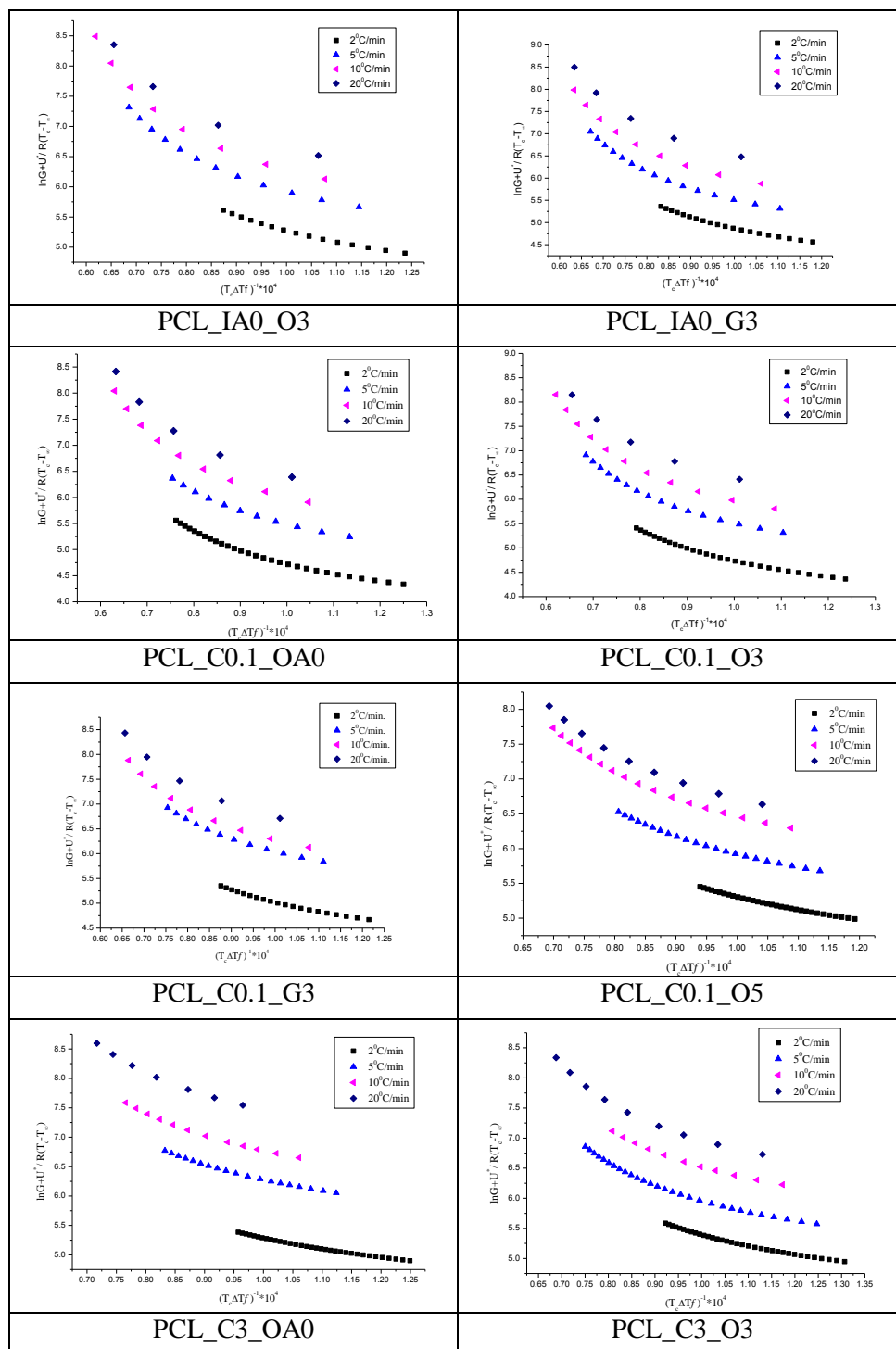


Figure F1. Lauritzen Hoffman plots for nonisothermal crystallization of selected PCL composite films.

APPENDIX G. Polarized Optical Microphotos

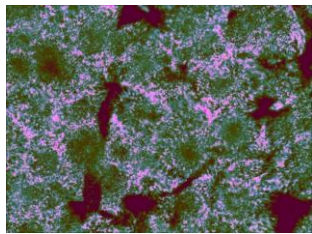
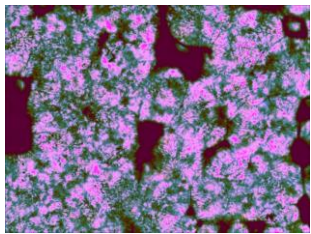
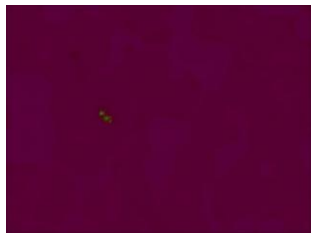
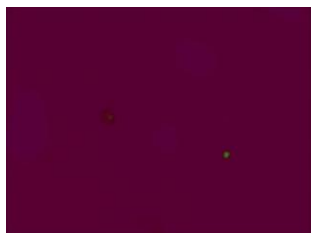
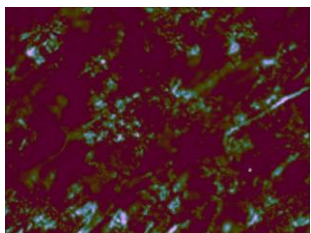
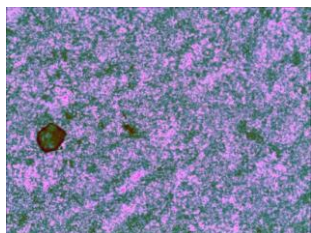
Neat PCL, (5 °C/min)		
		
t = 0. T = 35.2 °C	t = 3 min 45 sec., T = 72.5 °C	t = 4 min 37 sec., T = 81.2 °C
		
t = 12 min 46 sec., T = 90.0°C	t = 16 min 06 sec., T = 49.3°C	t = 21 min 27 sec., T = 28.4°C

Figure G1. POM micro photos of neat PCL with 5 °C/min cooling rate.

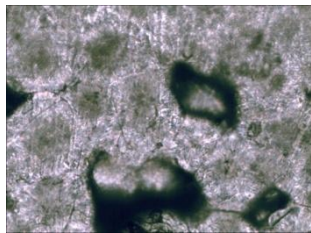
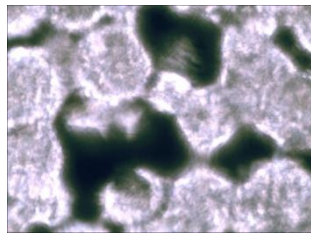
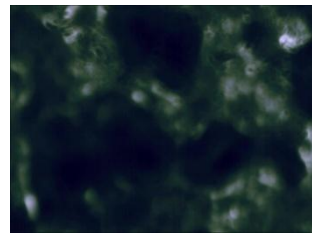

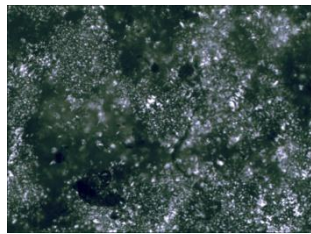
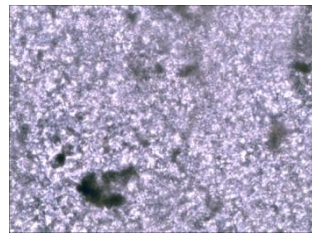
Neat PCL, (10 °C/min)		
		
t = 0. T = 35.8 °C	t = 4 min 27 sec., T = 89.5 °C	t = 5 min 6 sec., T = 96.0 °C
		
t = 10 min 15 sec., T = 100.0°C	t = 16 min 16 sec., T = 37.3°C	t = 17 min 37 sec., T = 24.7°C

Figure G2. POM micro photos of neat PCL with 10 °C/min cooling rate.

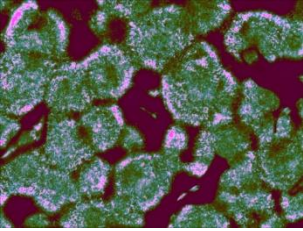
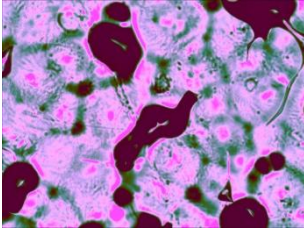
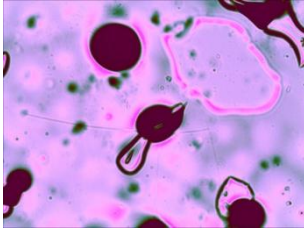
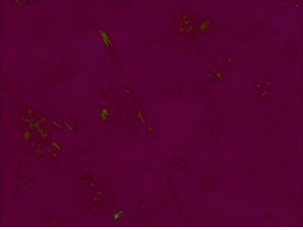
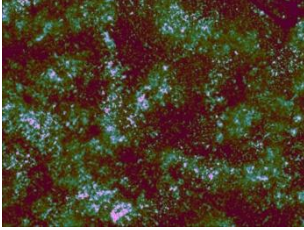
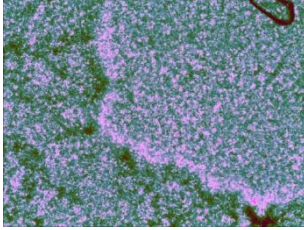
Neat PCL, (20 °C/min)		
		
t = 0. T = 35.0 °C	t = 4 min 53 sec., T = 83.8 °C	t = 5 min 23 sec., T = 83.8 °C
		
t = 10 min 28 sec., T = 100.0 °C	t = 13 min 26 sec., T = 31.3 °C	t = 14 min 17 sec., T = 14.7 °C

Figure G3. POM micro photos of neat PCL with 20 °C/min cooling rate.

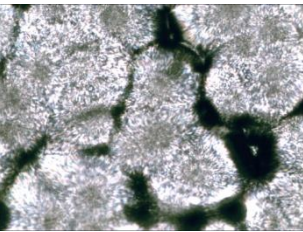
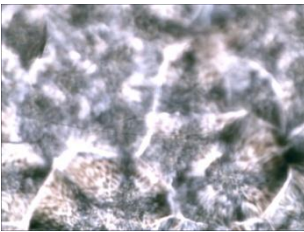


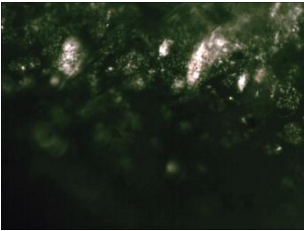
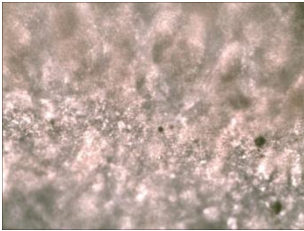
PCL_C0.1_OA0 (2 °C/min)		
		
t = 0. T = 30.0 °C	t = 4 min 49 sec., T = 78.2 °C	t = 4 min 58 sec., T = 83.8 °C
		
t = 9 min 59 sec., T = 100.0 °C	t = 23 min 46 sec., T = 51.6 °C	t = 25 min 17 sec., T = 47.9 °C

Figure G4. POM micro photos of PCL_C0.1_OA0 with 2 °C/min cooling rate.

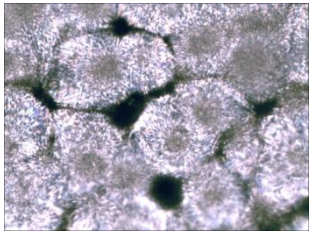



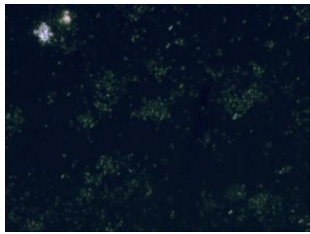
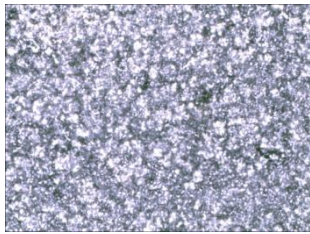
PCL_C0.1_OA0 (20 °C/min)		
		
t = 0. T = 20.0 °C	t = 6 min 38 sec., T = 86.4 °C	t = 6 min 51 sec., T = 85.5 °C
		
t = 11 min 59 sec., T = 100.0°C	t = 15 min 13 sec., T = 28.7°C	t = 15 min 40 sec., T = 22.0°C

Figure G5. POM micro photos of PCL_C0.1_OA0 with 20 °C/min cooling rate.

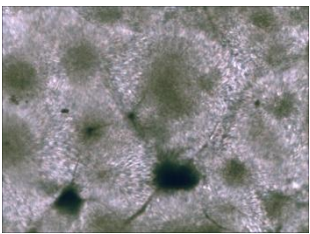
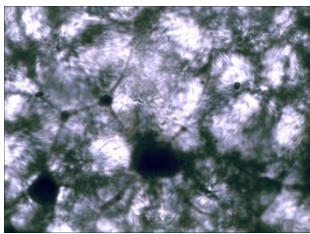
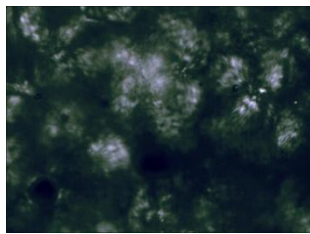
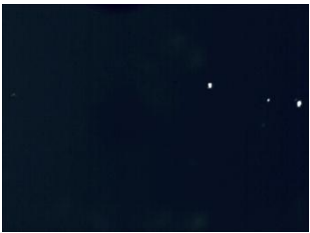
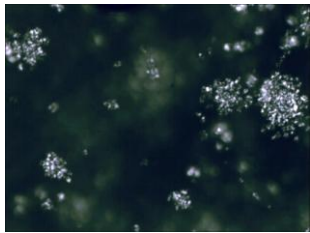
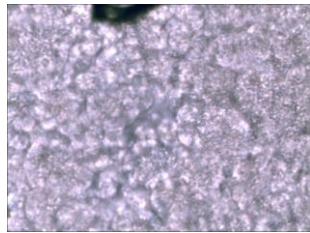
PCL_C0.1_O3 (20°C/min)		
		
t = 0. T = 18.9 °C	t = 6 min 48 sec., T = 86.9 °C	t = 6 min 56 sec., T = 88.2 °C
		
t = 12 min 07 sec., T = 100.0°C	t = 15 min 42 sec., T = 28.3°C	t = 16 min 36 sec., T = 10.3°C

Figure G6. POM micro photos of PCL_C0.1_O3 with 20 °C/min cooling rate.

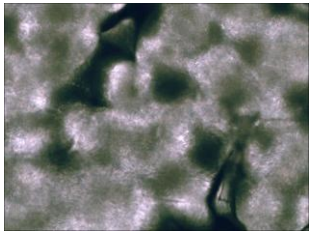
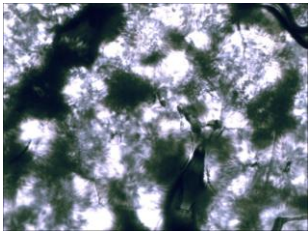
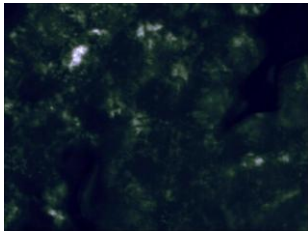

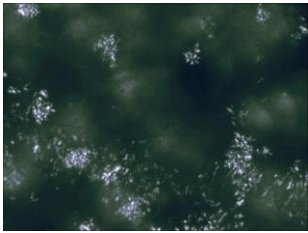
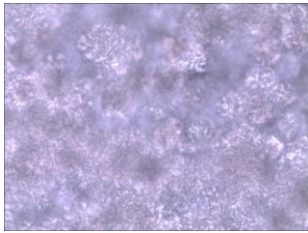
PCL_C0.1_G3 (2 °C/min)		
		
t = 0. T = 32.3 °C	t = 5 min 56 sec., T = 91.6 °C	t = 6 min 06 sec., T = 93.3 °C
		
t = 11 min 07 sec., T = 100.0 °C	t = 27 min 27 sec., T = 47.3 °C	t = 30 min 01 sec., T = 42.2 °C

Figure G7. POM micro photos of PCL_C0.1_G3 with 2 °C/min cooling rate.

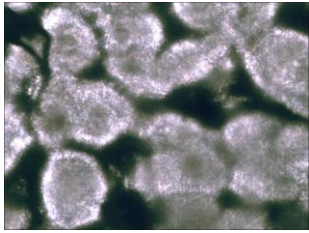
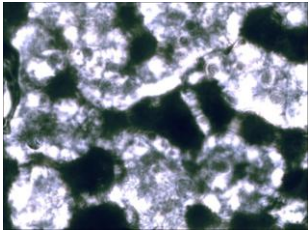
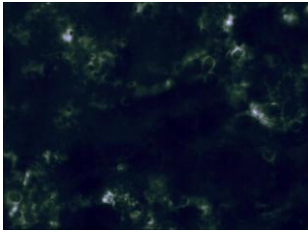

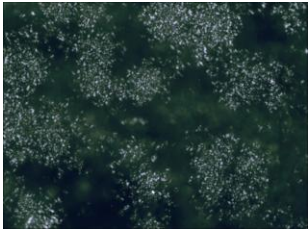
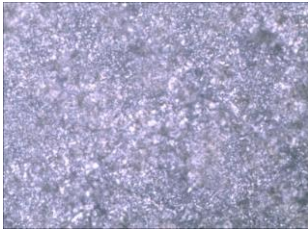
PCL_C0.1_G3 (20 °C/min)		
		
t = 0. T = 18.9 °C	t = 5 min 51 sec., T = 77.4 °C	t = 6 min 03 sec., T = 79.4 °C
		
t = 11 min 05 sec., T = 100.0 °C	t = 14 min 44 sec., T = 27.3 °C	t = 15 min 05 sec., T = 20.3 °C

Figure G8. POM micro photos of PCL_C0.1_G3 with 20 °C/min cooling rate.

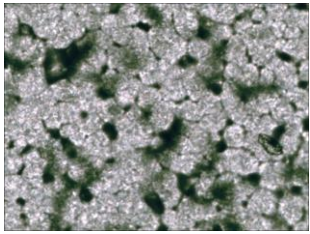
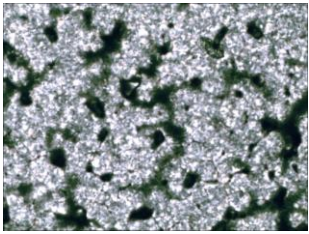

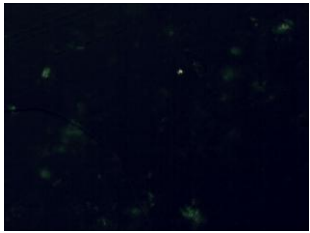
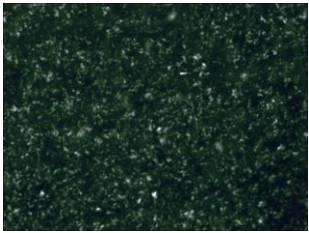
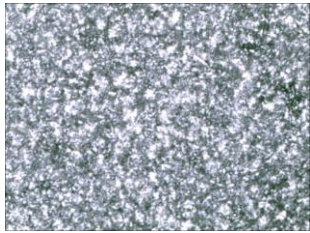
PCL_C3_OA0 (2 °C/min)		
		
t = 0. T = 29.4 °C	t = 6 min 08 sec., T = 90.7 °C	t = 6 min 35 sec., T = 95.2 °C
		
t = 11 min 50 sec., T = 100.0 °C	t = 41 min 29 sec., T = 40.7 °C	t = 42 min 42 sec., T = 38.3 °C

Figure G9. POM micro photos of PCL_C3_OA0 with 2 °C/min cooling rate.

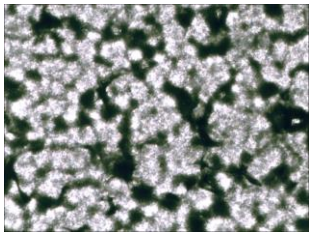
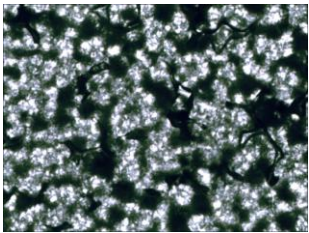
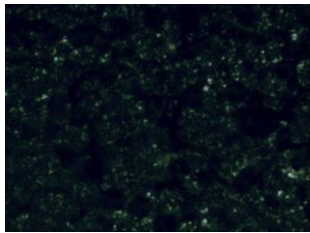
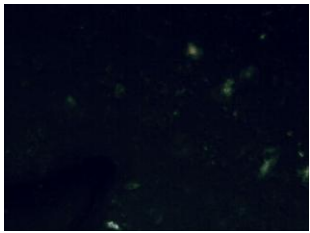
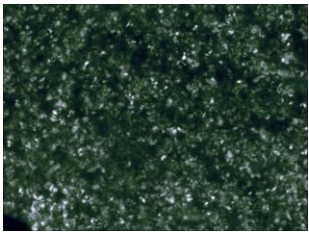
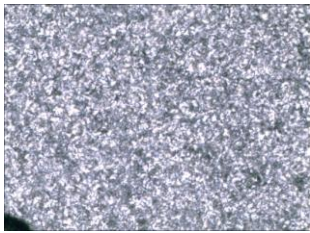
PCL_C3_OA0 (5 °C/min)		
		
t = 0. T = 38.6 °C	t = 5 min 29 sec., T = 93.4 °C	t = 5 min 45 sec., T = 96.1 °C
		
t = 10 min 11 sec., T = 100.0 °C	t = 23 min 27 sec., T = 33.7 °C	t = 24 min 10 sec., T = 30.1 °C

Figure G10. POM micro photos of PCL_C3_OA0 with 5 °C/min cooling rate.

PCL_C3_OA0 (10 °C/min)		
t = 0. T = 21.7 °C	t = 6 min 59 sec., T = 91.5 °C	t = 7 min 14 sec., T = 94.0 °C
t = 12 min 15 sec., T = 100.0 °C	t = 18 min 23 sec., T = 38.7 °C	t = 19 min 51 sec., T = 24.0 °C

Figure G11. POM micro photos of PCL_C3_OA0 with 10 °C/min cooling rate.

PCL_C3_OA0 (20 °C/min)		
t = 0. T = 28.0 °C	t = 6 min 22 sec., T = 91.7 °C	t = 6 min 29 sec., T = 92.8 °C
t = 11 min 05 sec., T = 100.0 °C	t = 14 min 24 sec., T = 33.7 °C	t = 15 min 10 sec., T = 18.3 °C

Figure G12. POM micro photos of PCL_C3_OA0 with 20 °C/min cooling rate.

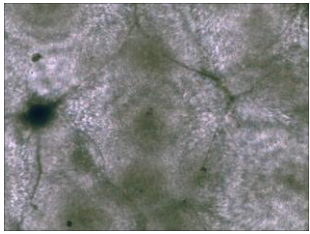
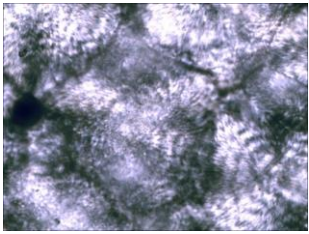
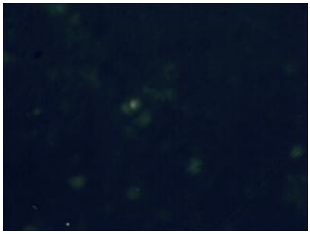
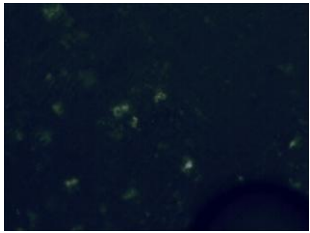
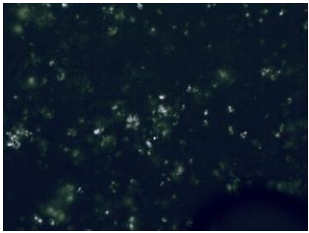
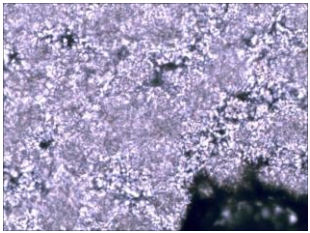
PCL_C3_O5 (2 °C/min)		
		
t = 0. T = 31.2 °C	t = 5 min 54 sec., T = 90.2 °C	t = 6 min 09 sec., T = 92.7 °C
		
t = 11 min 10 sec., T = 110.0 °C	t = 41 min 12 sec., T = 49.7 °C	t = 43 min 56 sec., T = 46.3 °C

Figure G13. POM micro photos of PCL_C3_O5 with 2 °C/min cooling rate.

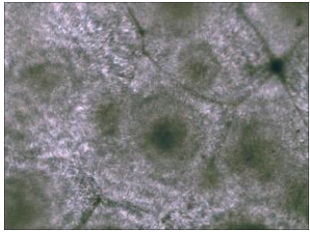
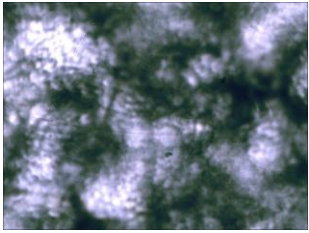

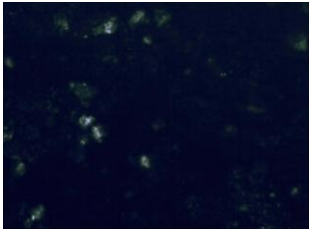
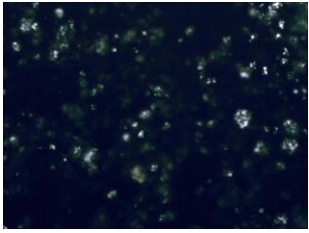
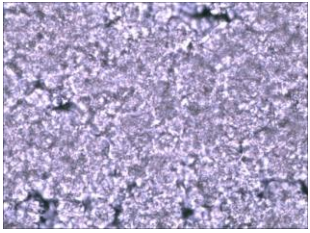
PCL_C3_O5 (5 °C/min)		
		
t = 0. T = 20.1 °C	t = 5 min 53 sec., T = 78.9 °C	t = 6 min 01 sec., T = 78.9 °C
		
t = 11 min 03 sec., T = 110.0 °C	t = 24 min 30 sec., T = 42.8 °C	t = 25 min 52 sec., T = 35.9 °C

Figure G14. POM micro photos of PCL_C3_O5 with 5 °C/min cooling rate.

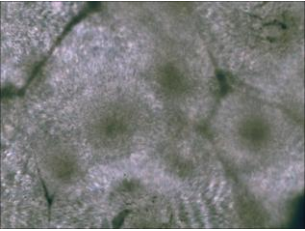
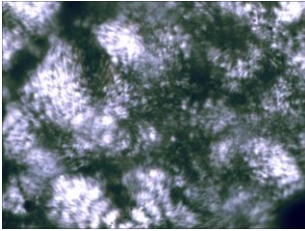
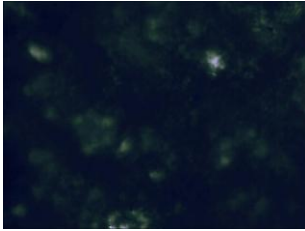
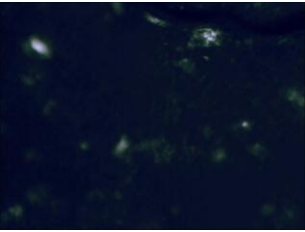
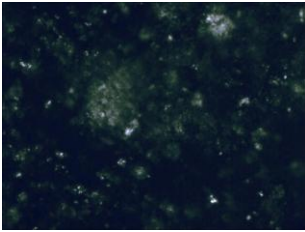
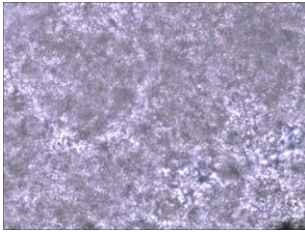
PCL_C3_O5 (10 °C/min)		
		
t = 0. T = 31.5 °C	t = 5 min 32 sec., T = 86.8 °C	t = 5 min 38 sec., T = 87.8 °C
		
t = 10 min 38 sec., T = 110.0 °C	t = 17 min 57 sec., T = 36.8 °C	t = 18 min 55 sec., T = 27.2 °C

Figure G15. POM micro photos of PCL_C3_O5 with 10 °C/min cooling rate.

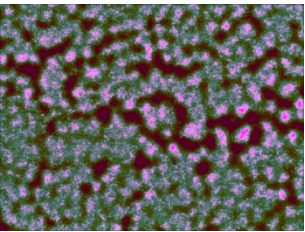
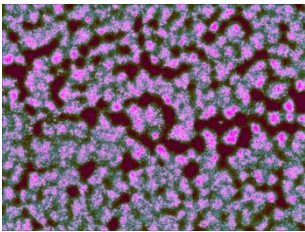
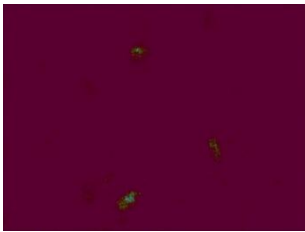
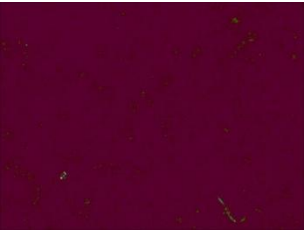
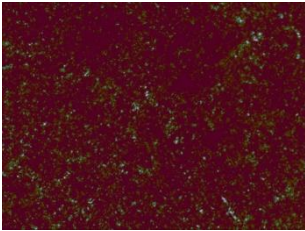
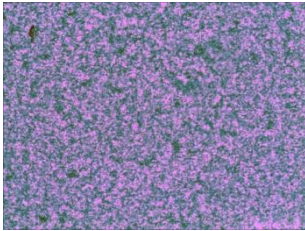
PCL_C3_O5 (20 °C/min)		
		
t = 0. T = 32.5 °C	t = 6 min 39 sec., T = 99.7 °C	t = 6 min 48 sec., T = 100.5 °C
		
t = 11 min 48 sec., T = 110.0 °C	t = 14 min 38 sec., T = 53.3 °C	t = 15 min 42 sec., T = 32.0 °C

Figure G16. POM micro photos of PCL_C3_O5 with 20 °C/min cooling rate.

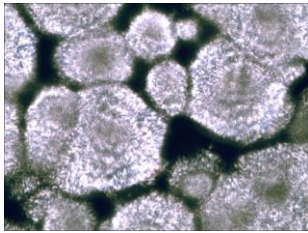
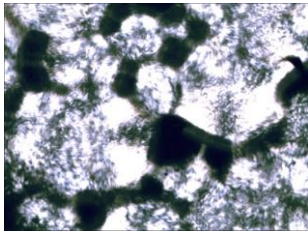
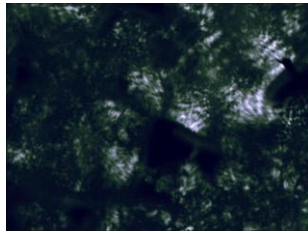

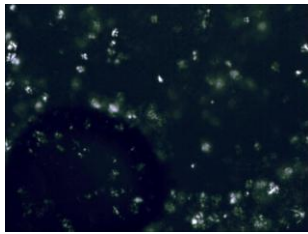
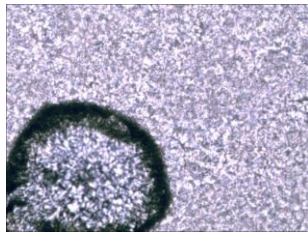
PCL_C3_G5 (2 °C/min)		
		
t = 0. T = 30.2 °C	t = 6 min 05 sec., T = 91.3 °C	t = 6 min 18 sec., T = 93.2 °C
		
t = 11 min 18 sec., T = 110.0°C	t = 42 min 06 sec., T = 48.4°C	t = 46 min 10 sec., T = 40.2°C

Figure G17. POM micro photos of PCL_C3_G5 with 2 °C/min cooling rate.

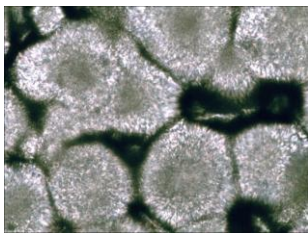
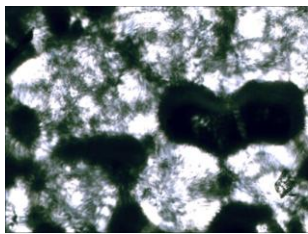
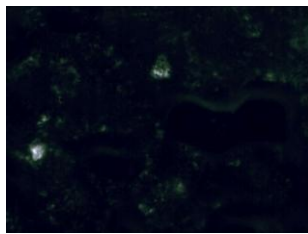
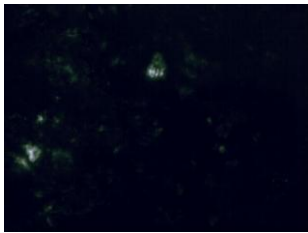
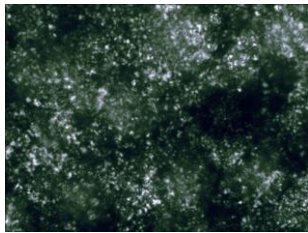

PCL_C3_G5 (5 °C/min)		
		
t = 0. T = 30.2 °C	t = 6 min 21 sec., T = 93.7 °C	t = 6 min 49 sec., T = 97.4 °C
		
t = 11 min 49 sec., T = 110.0°C	t = 22 min 30 sec., T = 56.58°C	t = 25 min 29 sec., T = 41.7°C

Figure G18. POM micro photos of PCL_C3_G5 with 5 °C/min cooling rate.

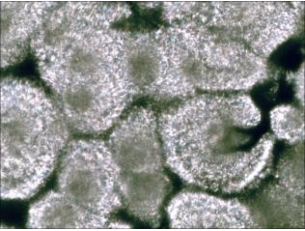
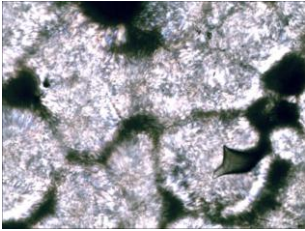
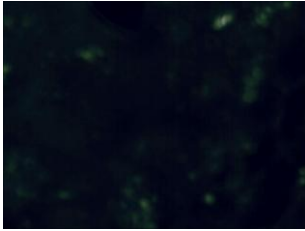
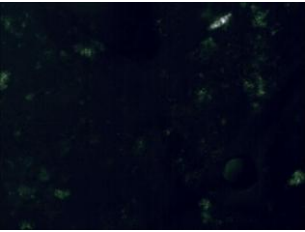
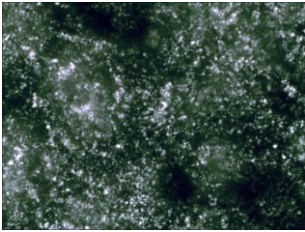
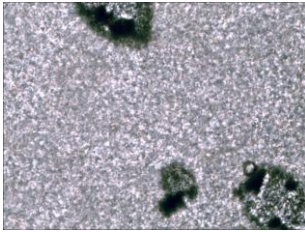
PCL_C3_G5 (10 °C/min)		
		
t = 0. T = 27.2 °C	t = 5 min 59 sec., T = 87.0 °C	t = 6 min 39 sec., T = 93.7 °C
		
t = 11 min 39 sec., T = 110.0 °C	t = 17 min 45 sec., T = 49.0 °C	t = 1- min 35 sec., T = 30.7 °C

Figure G19. POM micro photos of PCL_C3_G5 with 10 °C/min cooling rate.

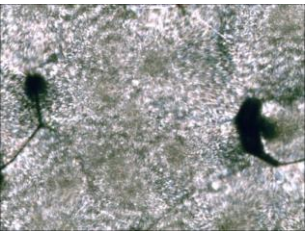
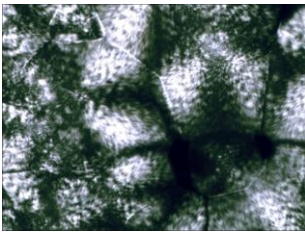
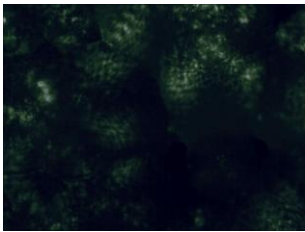
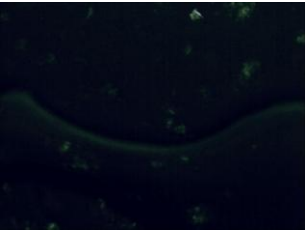
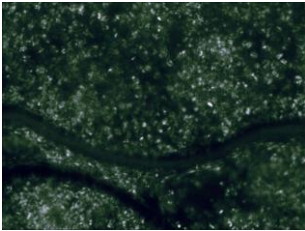
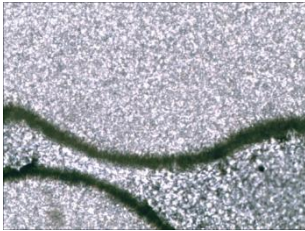
PCL_C3_G5 (20 °C/min)		
		
t = 0. T = 22.2 °C	t = 6 min 55 sec., T = 91.4 °C	t = 7 min 02 sec., T = 92.5 °C
		
t = 12 min 02 sec., T = 110.0 °C	t = 15 min 32 sec., T = 40.0 °C	t = 16 min 13 sec., T = 26.3 °C

Figure G20. POM micro photos of PCL_C3_G5 with 20 °C/min cooling rate.

APPENDIX H. FTIR Analysis

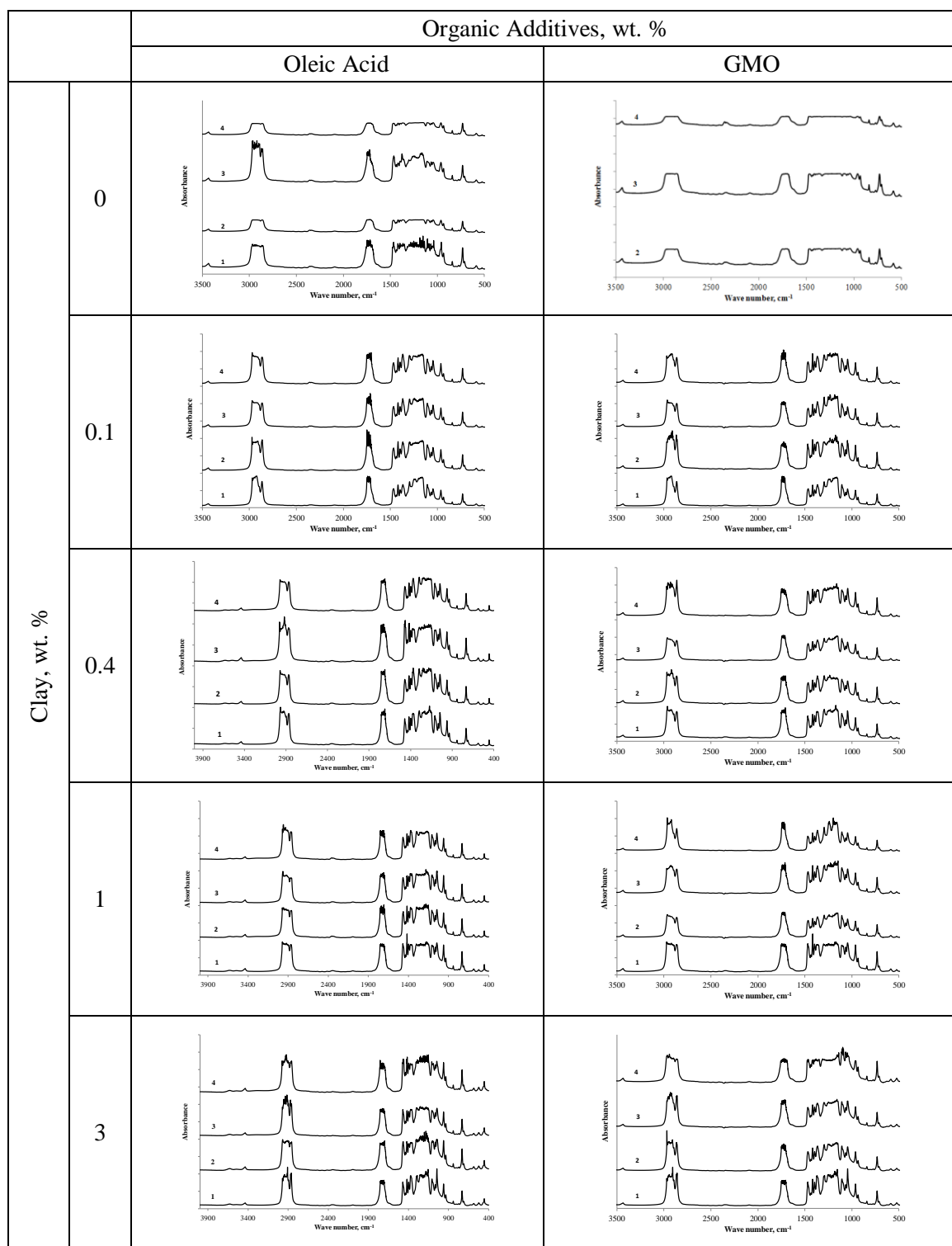


Figure H1. FTIR spectra of PCL composite films by increasing organic additive concentration; 1 – no organic additive, 2 – 1 wt% OA, 3 – 3 wt. OA, 4 – 5 wt% OA.

APPENDIX I. SEM Microphotos

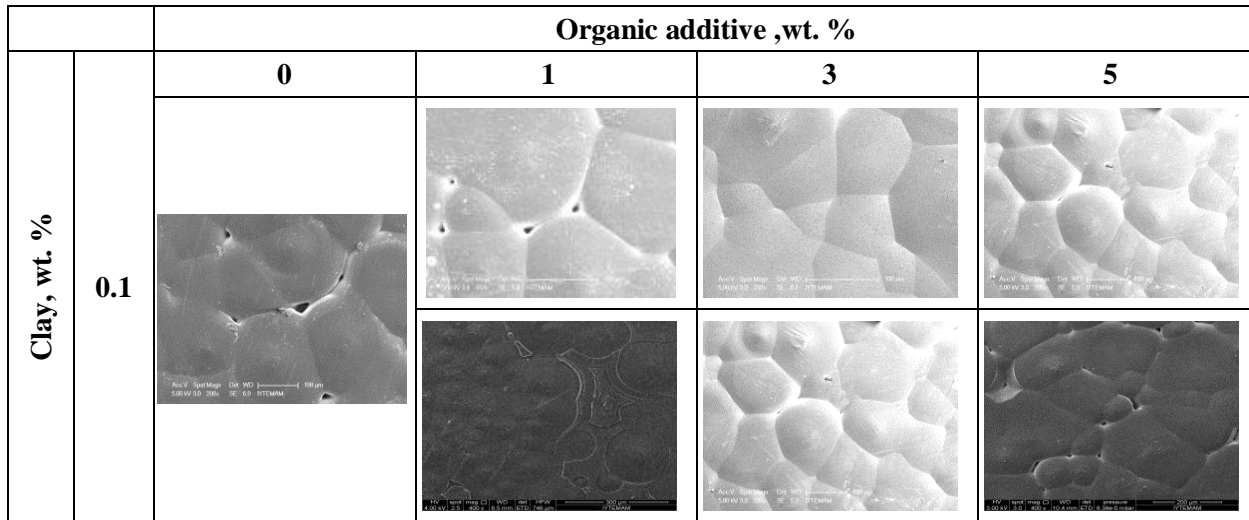


Figure I1. Effects of 0.1 wt% clay contained PCL composite films with increasing different organic additives (top row: Oleic acid, bottom row: GMO) concentration on surface morphologies by SEM analysis.

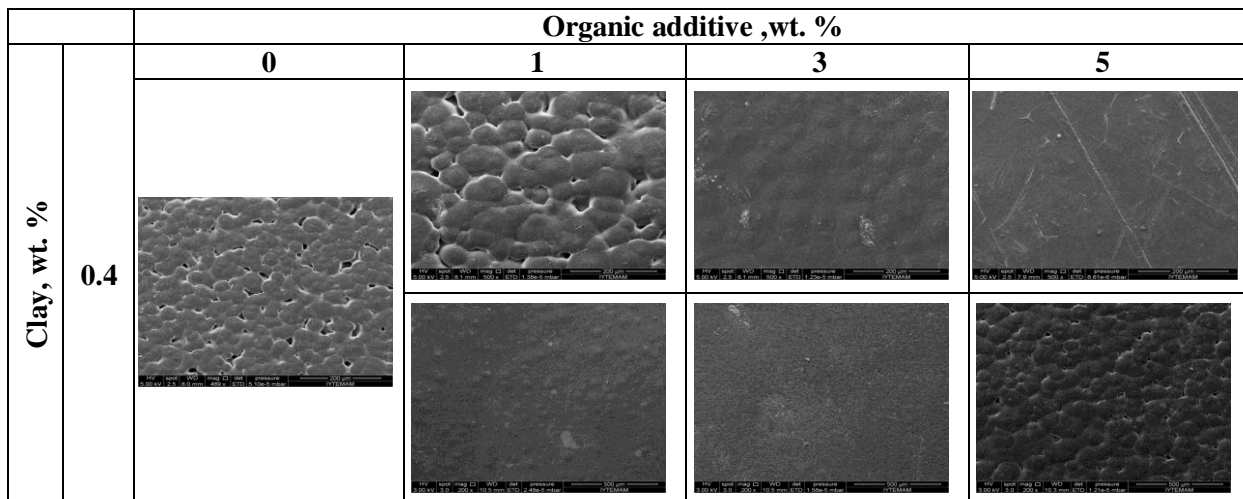


Figure I2. Effects of 0.4 wt% clay contained PCL composite films with increasing different organic additives (top row: Oleic acid, bottom row: GMO) concentration on surface morphologies by SEM analysis.

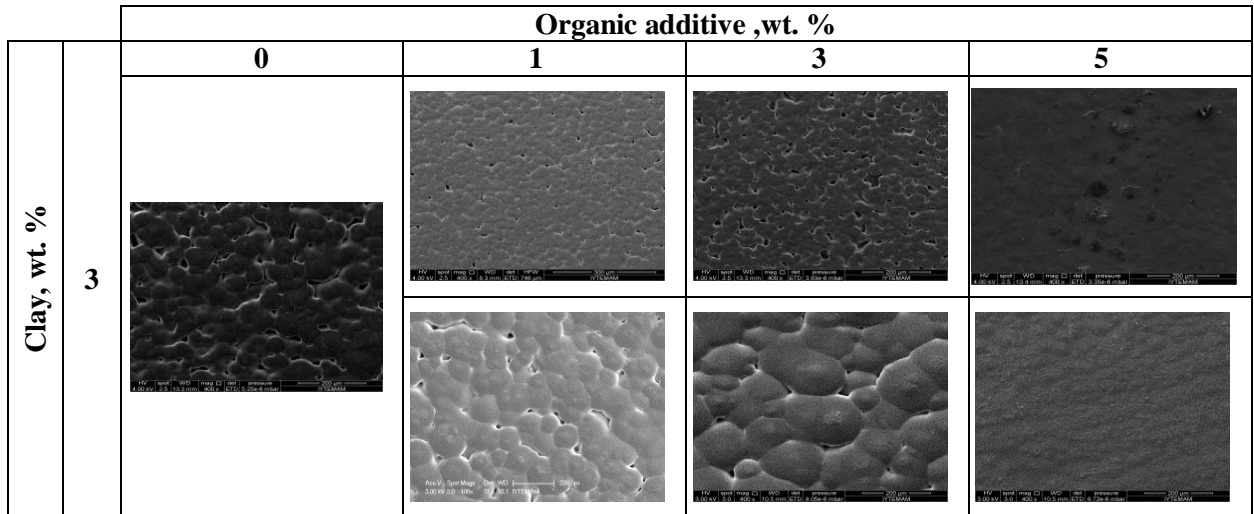


Figure I2. Effects of 3 wt% clay contained PCL composite films with increasing different organic additives (top row: Oleic acid, bottom row: GMO) concentration on surface morphologies by SEM analysis.

APPENDIX J. XRD Patterns of Composite Films

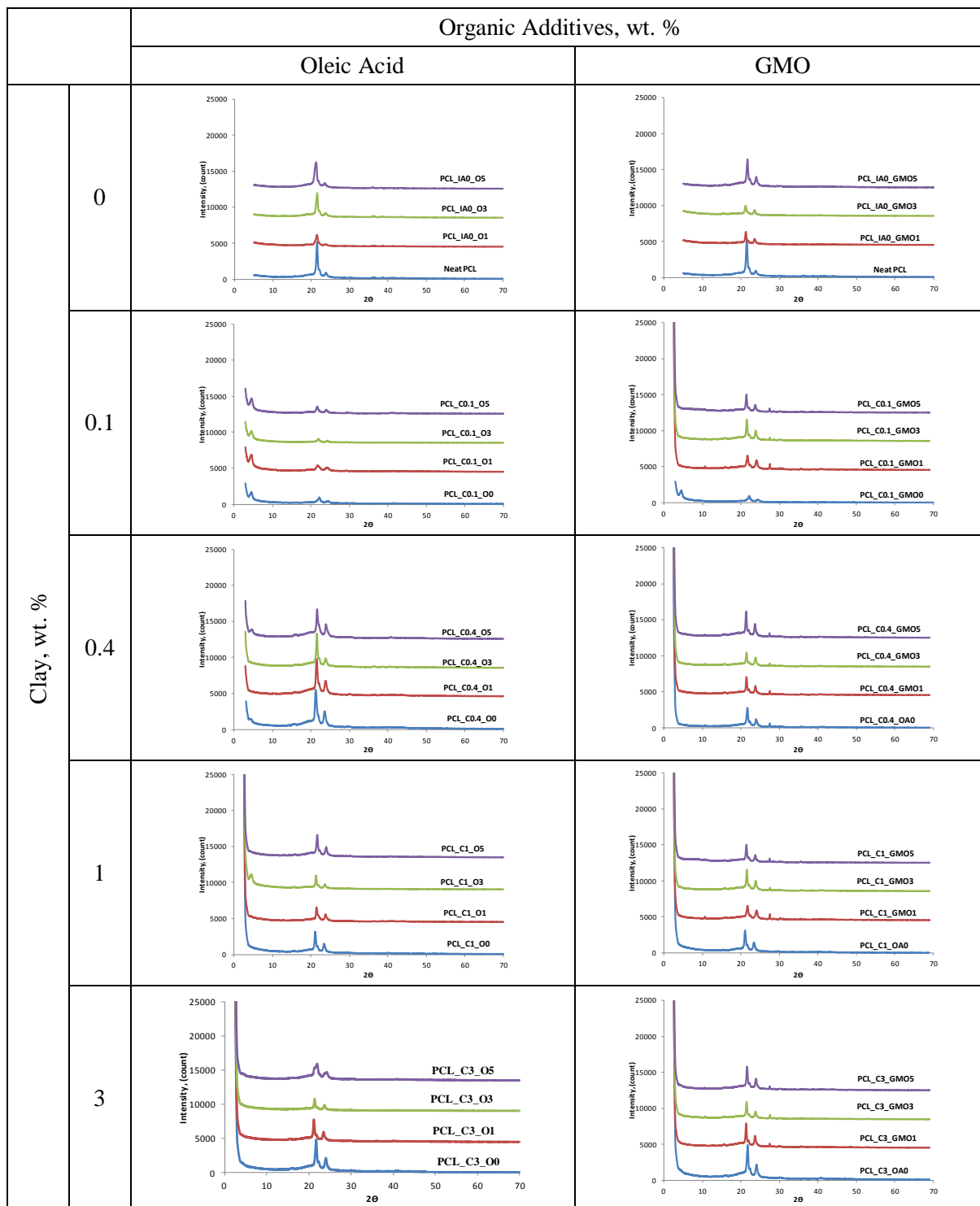


Figure J1. XRD patterns of PCL composite film by increasing organic additive concentration.

APPENDIX K. Mechanical Analysis

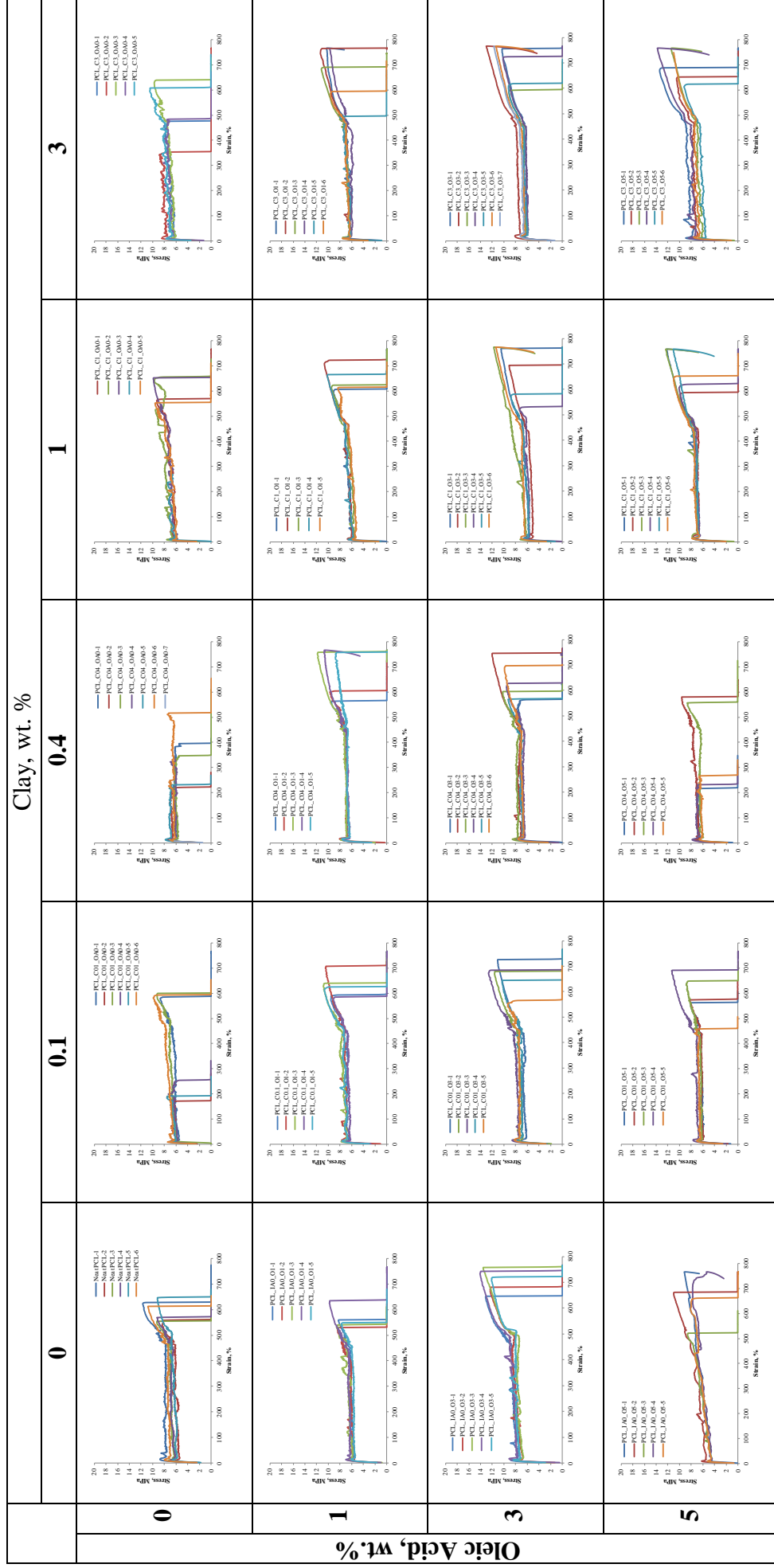


Figure K1. Stress - Strain diagrams of the clay and oleic acid contained PCL composite films.

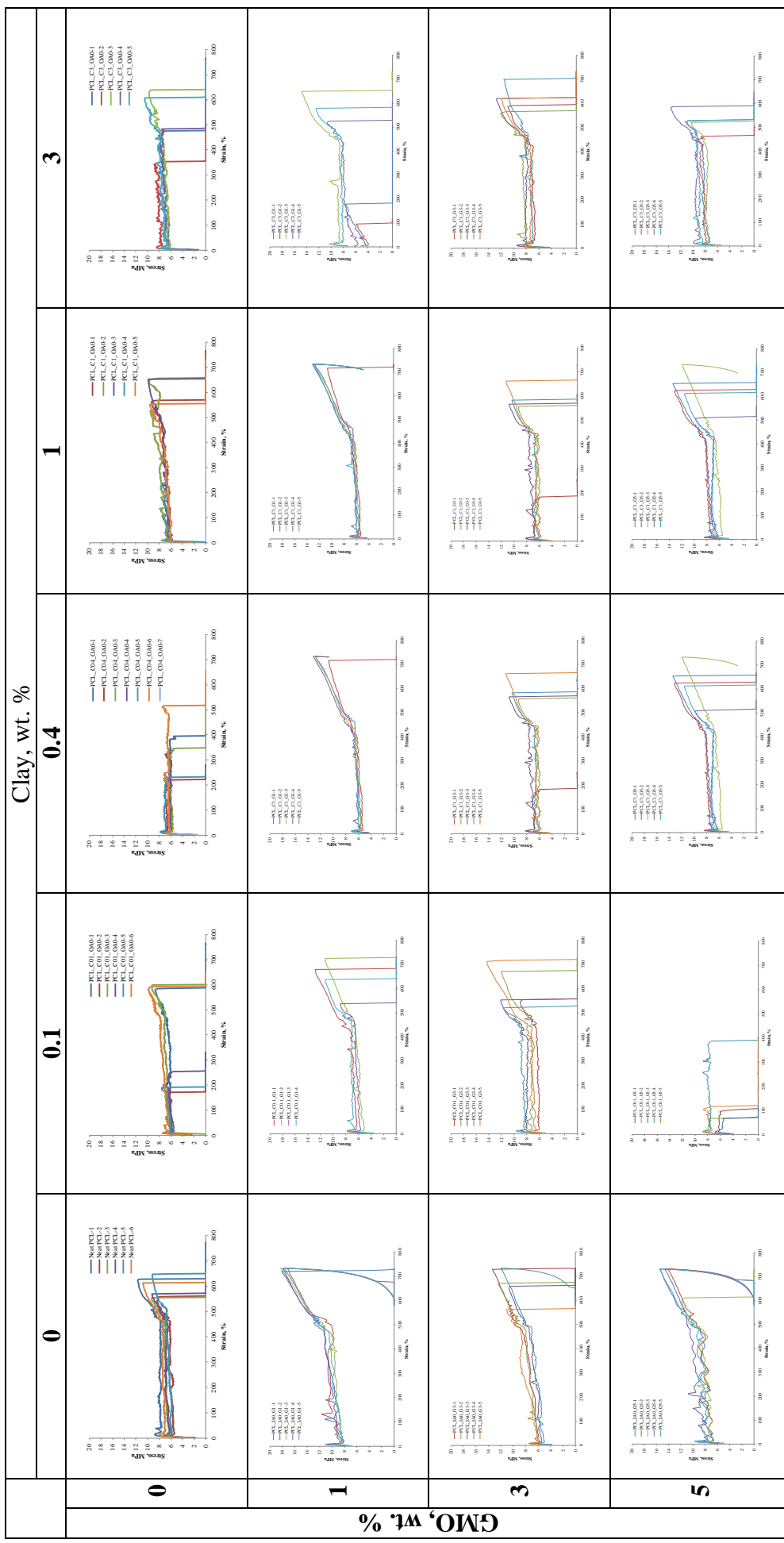


Figure K2. Stress - Strain diagrams of the clay and GMO contained PCL composite films.

APPENDIX L. Thermal Degradation Plots

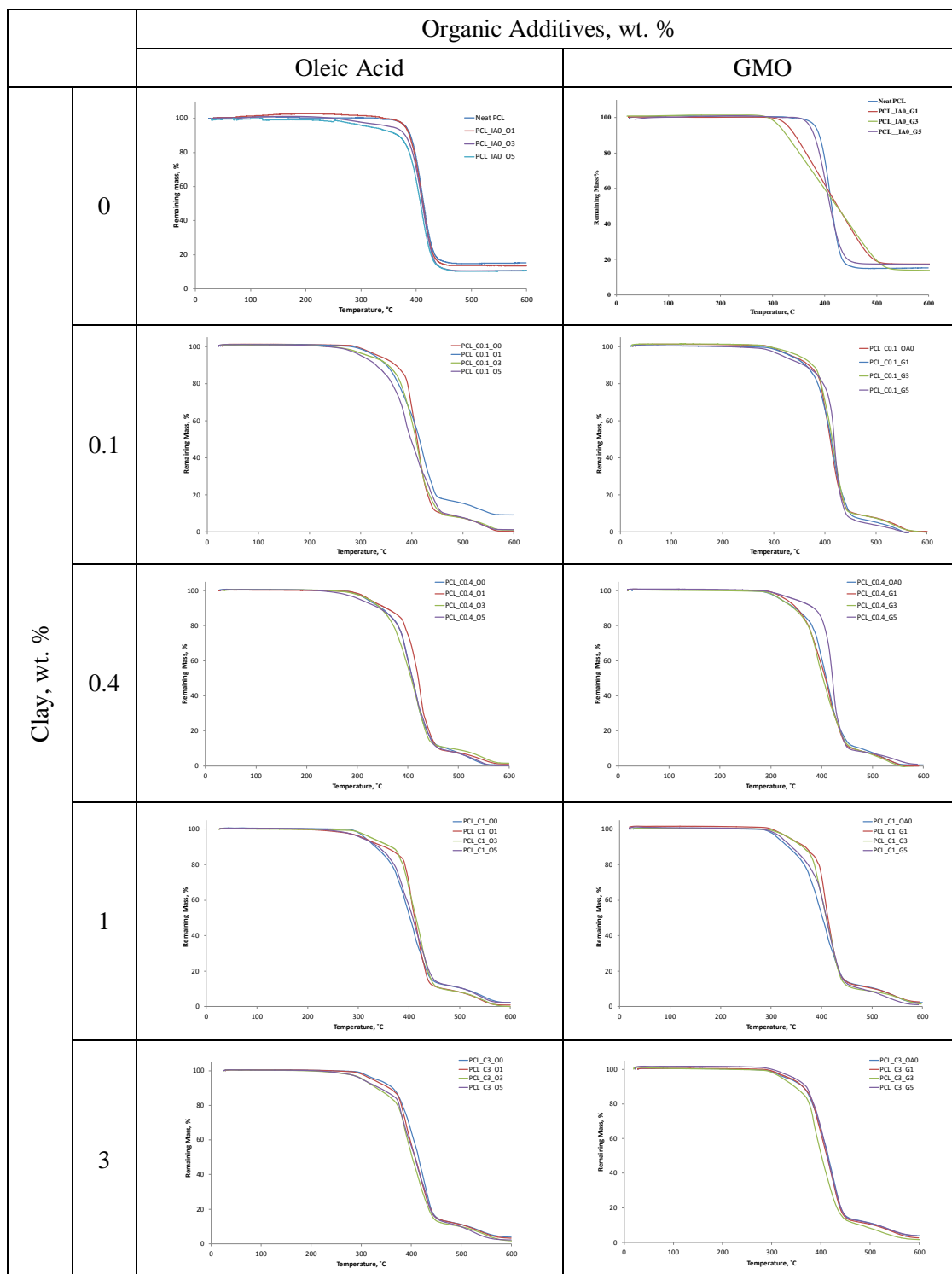


Figure L1. Thermograms of PCL composite films by increasing organic additive concentration.

APPENDIX M. Biodegradation Plots

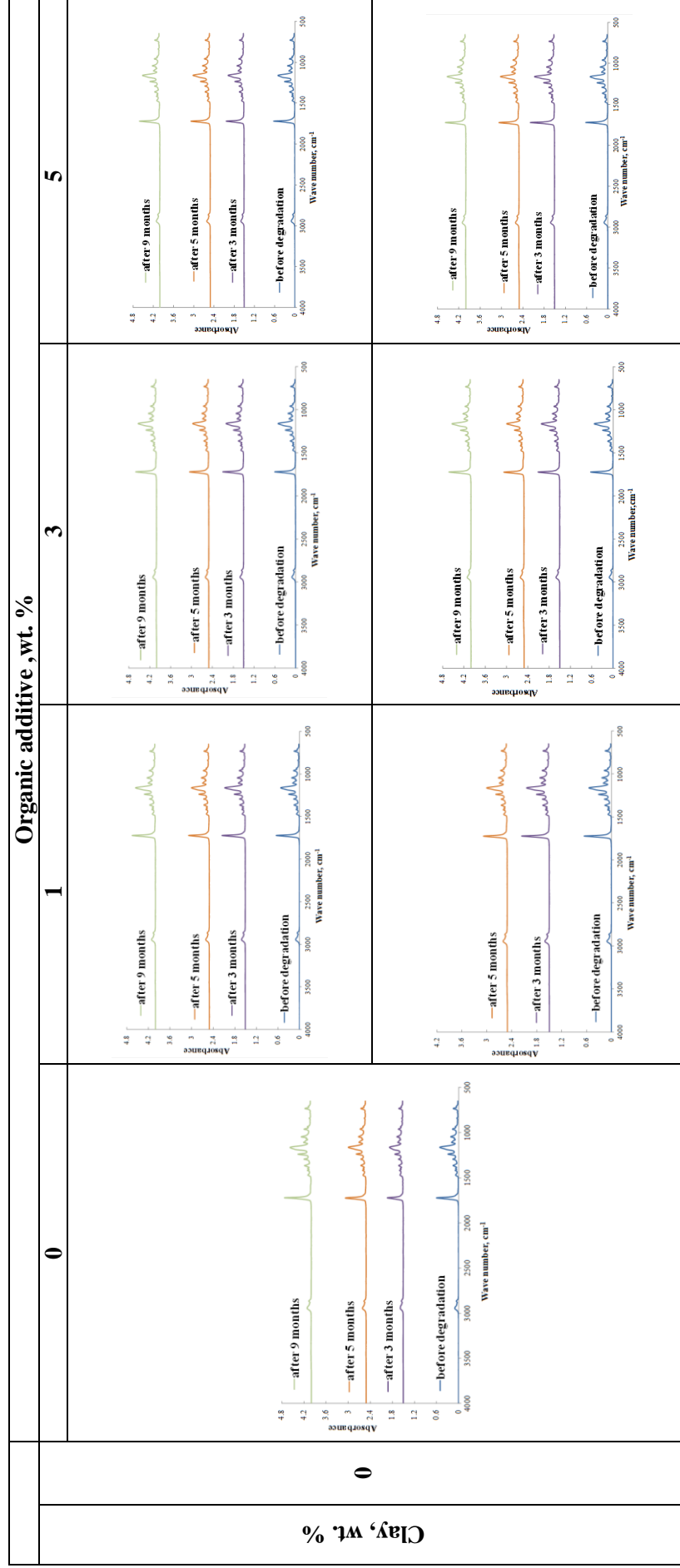


Figure M.1 FTIR plots of before and after soil buried PCL composite films by increasing organic additive concentration
(Top row: Oleic acid, Bottom row: GMO).

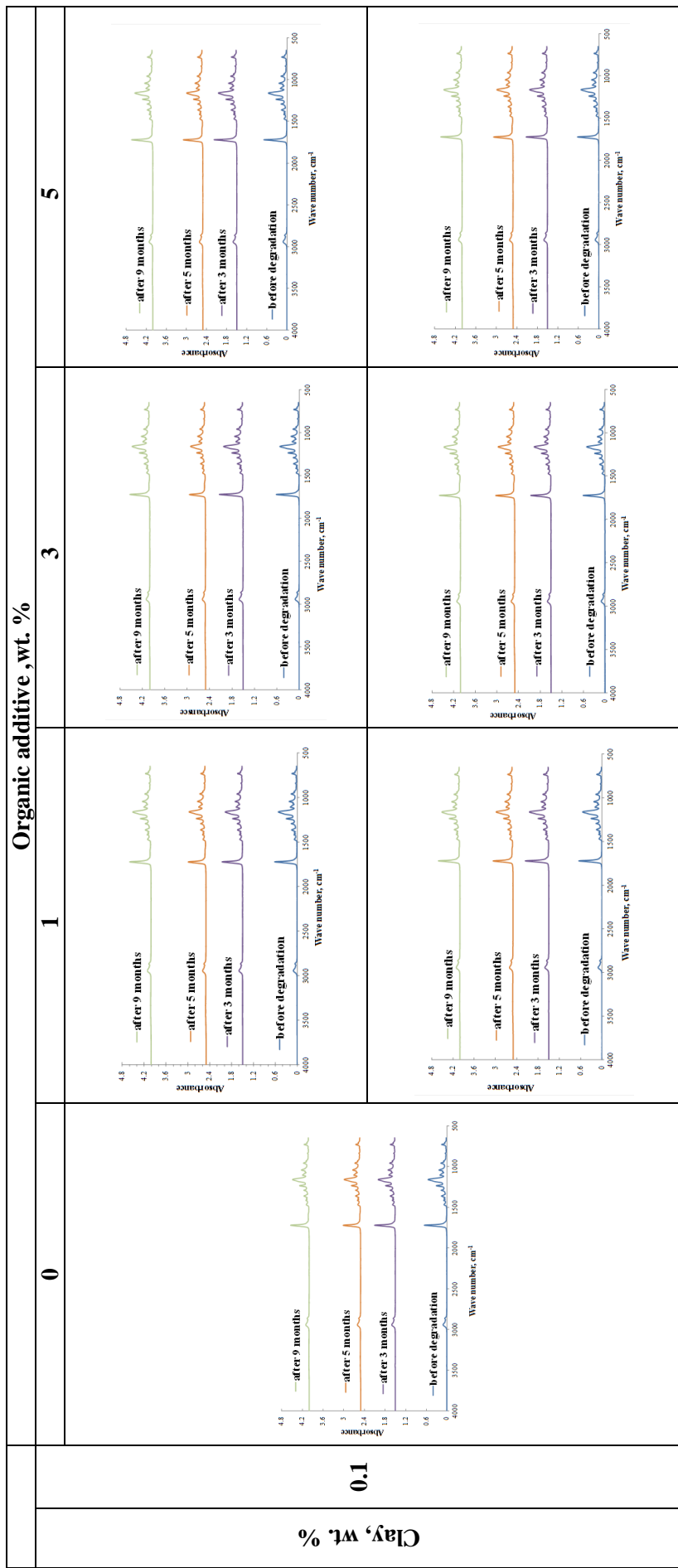


Figure M.2 FTIR plots of before and after soil buried PCL composite films by increasing organic additive concentration (Top row: Oleic acid, Bottom row: GMO).

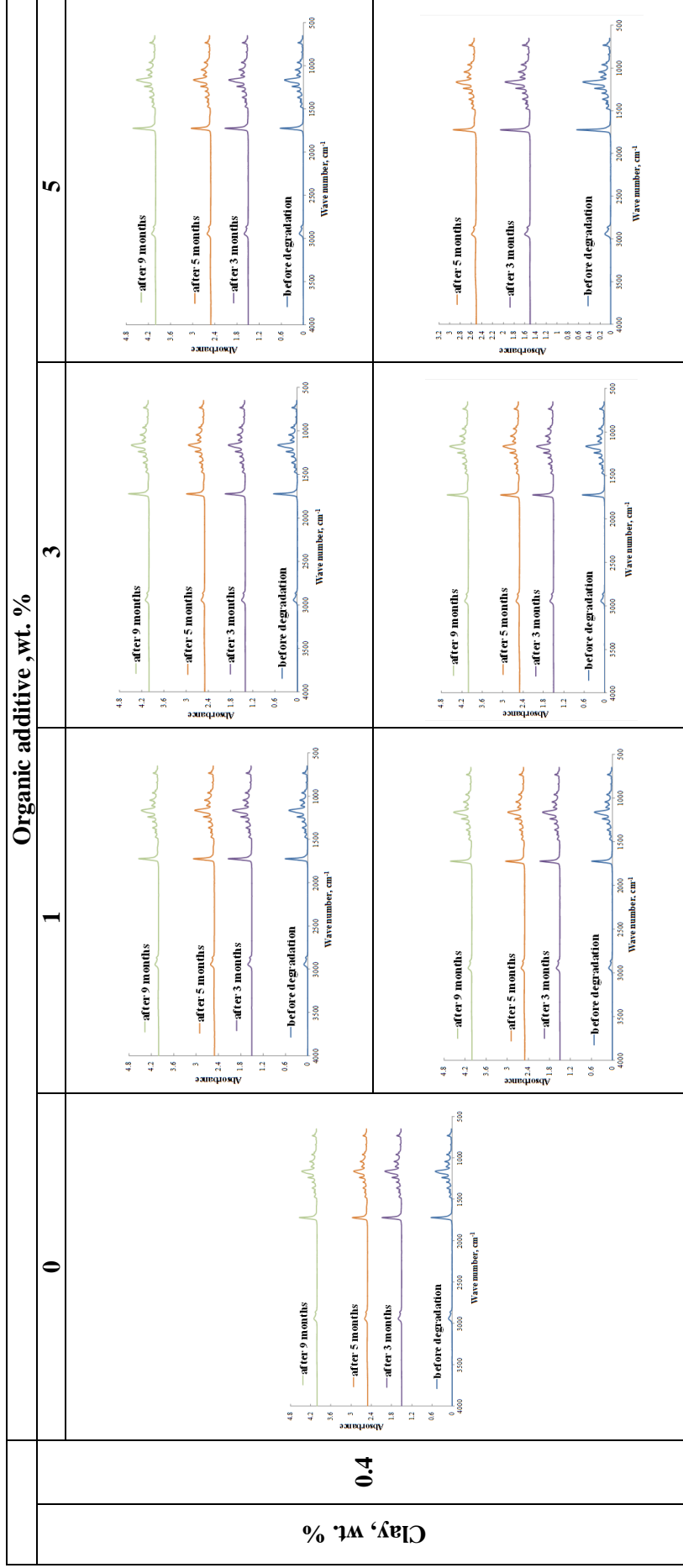


Figure M.3 FTIR plots of before and after soil buried PCL composite films by increasing organic additive concentration (Top row: Oleic acid, Bottom row: GMO).

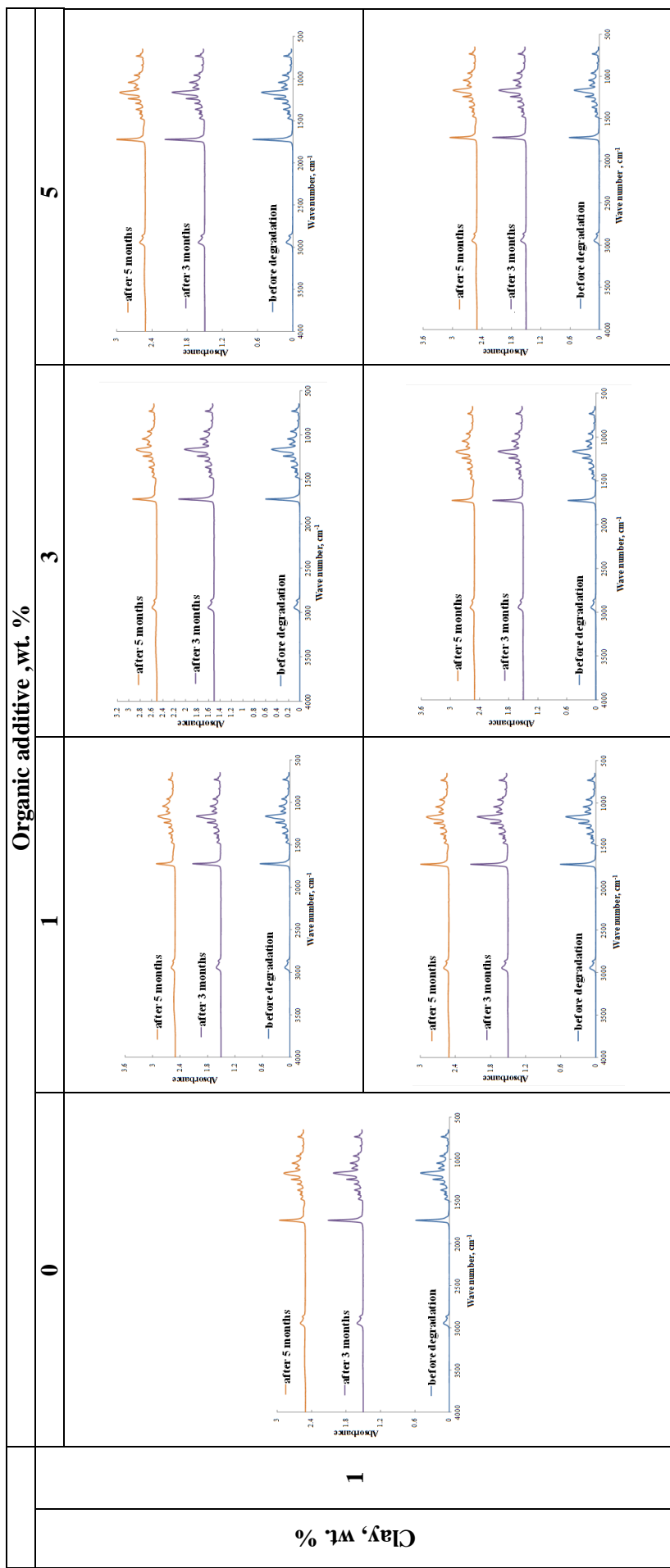


Figure M.4 FTIR plots of before and after soil buried PCL composite films by increasing organic additive concentration (Top row: Oleic acid, Bottom row: GMO).

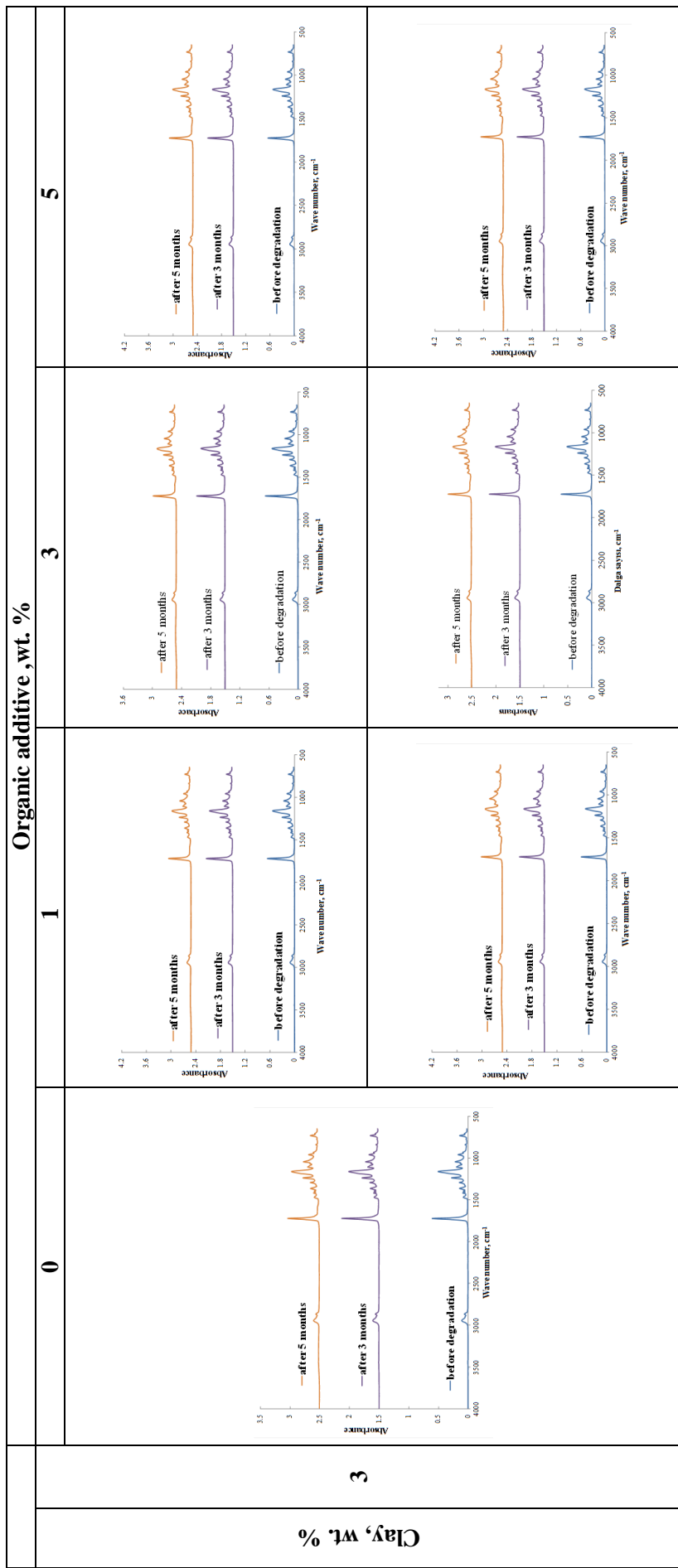


Figure M.5 FTIR plots of before and after soil buried PCL composite films by increasing organic additive concentration (Top row: Oleic acid, Bottom row: GMO).

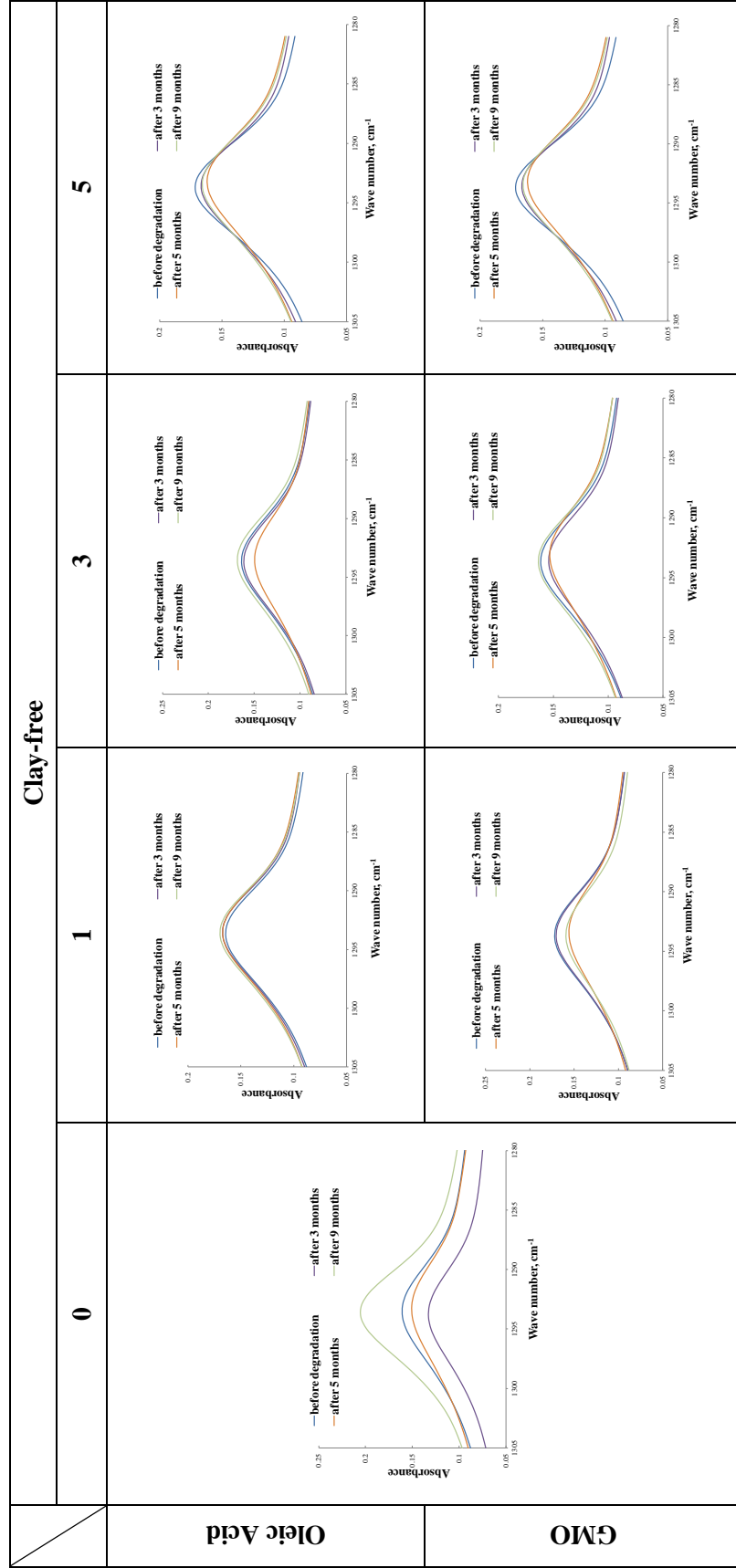


Figure M.6 Crystal peaks of films which are clay-free with respect to increasing organic additive before soil burial degradation, after 3, 6 and 9 months.

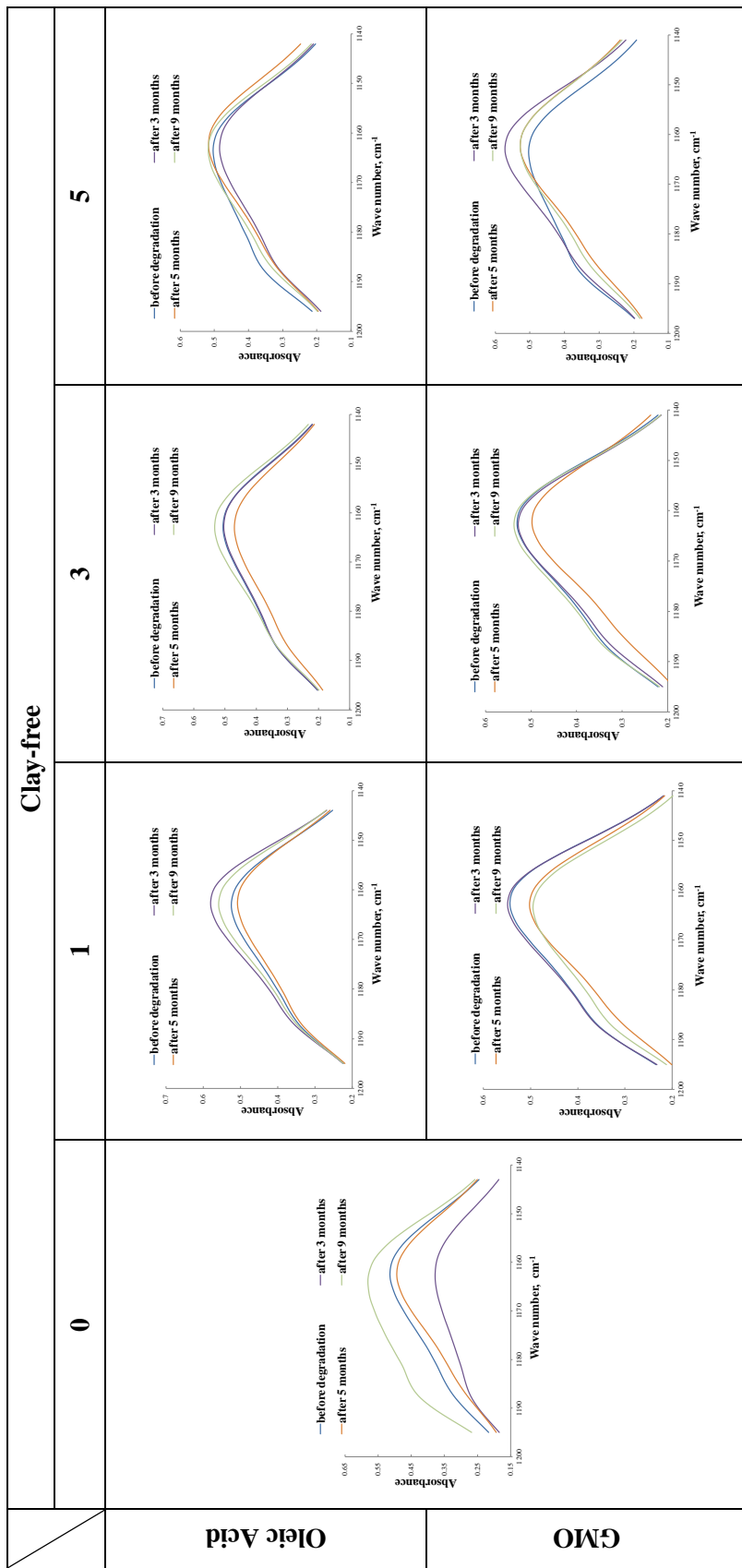


Figure M.7 Amorphous peaks of films which are clay-free with respect to increasing organic additive before soil burial degradation, after 3, 6 and 9 months.

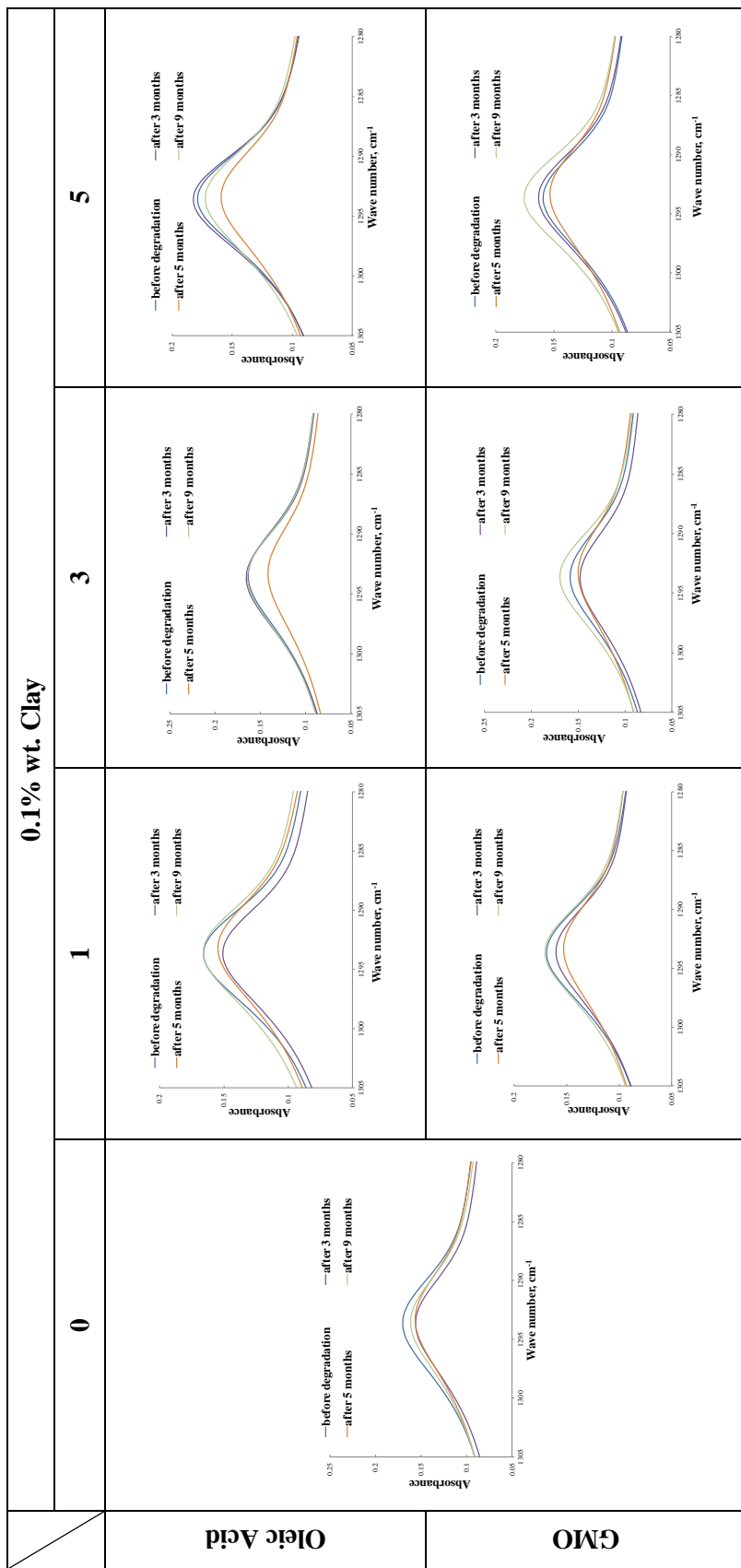


Figure M.7 Crystal peaks of films which have 0.1 % clay with respect to increasing organic additive before soil burial degradation, after 3, 6 and 9 months.

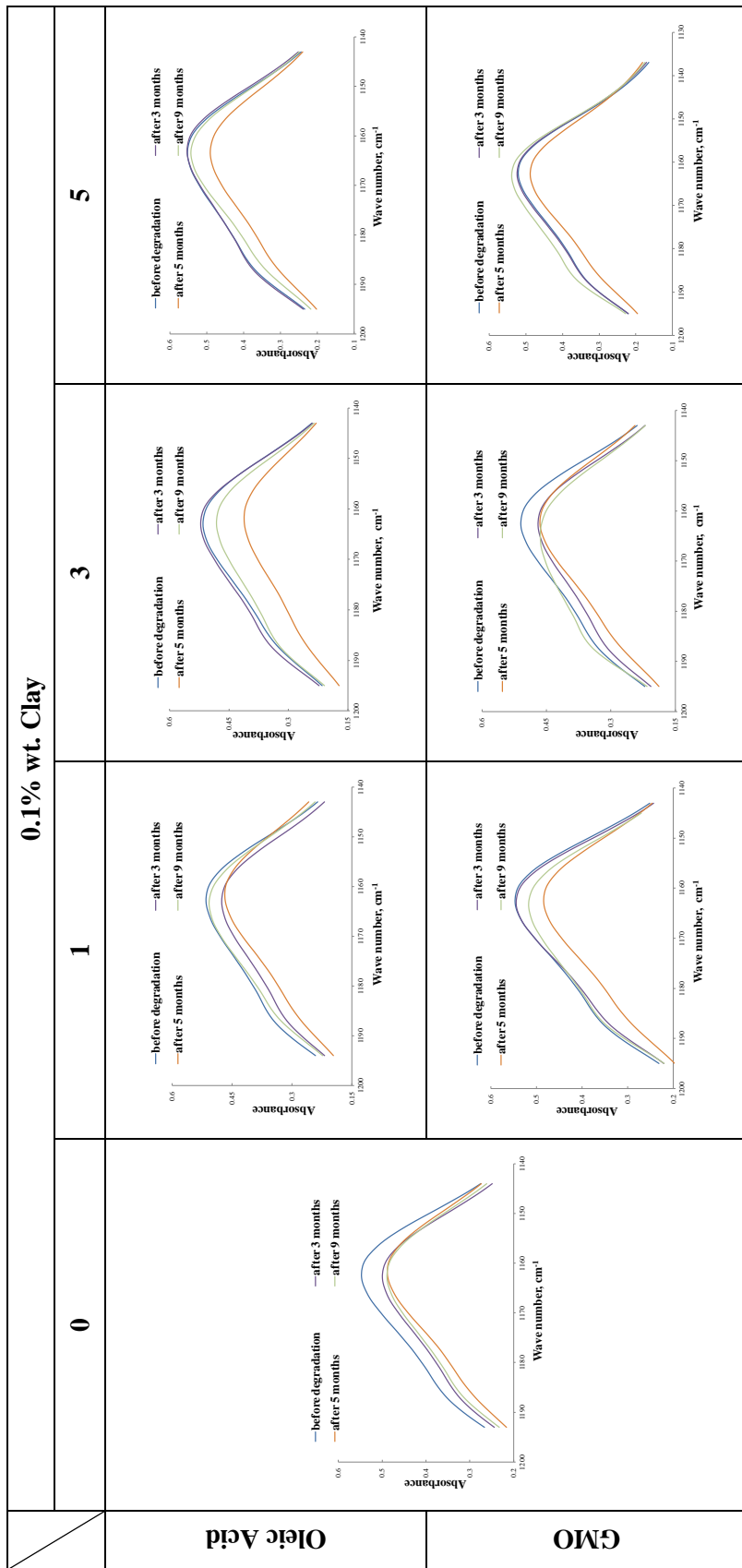


Figure M.8 Amorphous peaks of films which have 0.1 % clay with respect to increasing organic additive before soil burial degradation, after 3, 6 and 9 months.

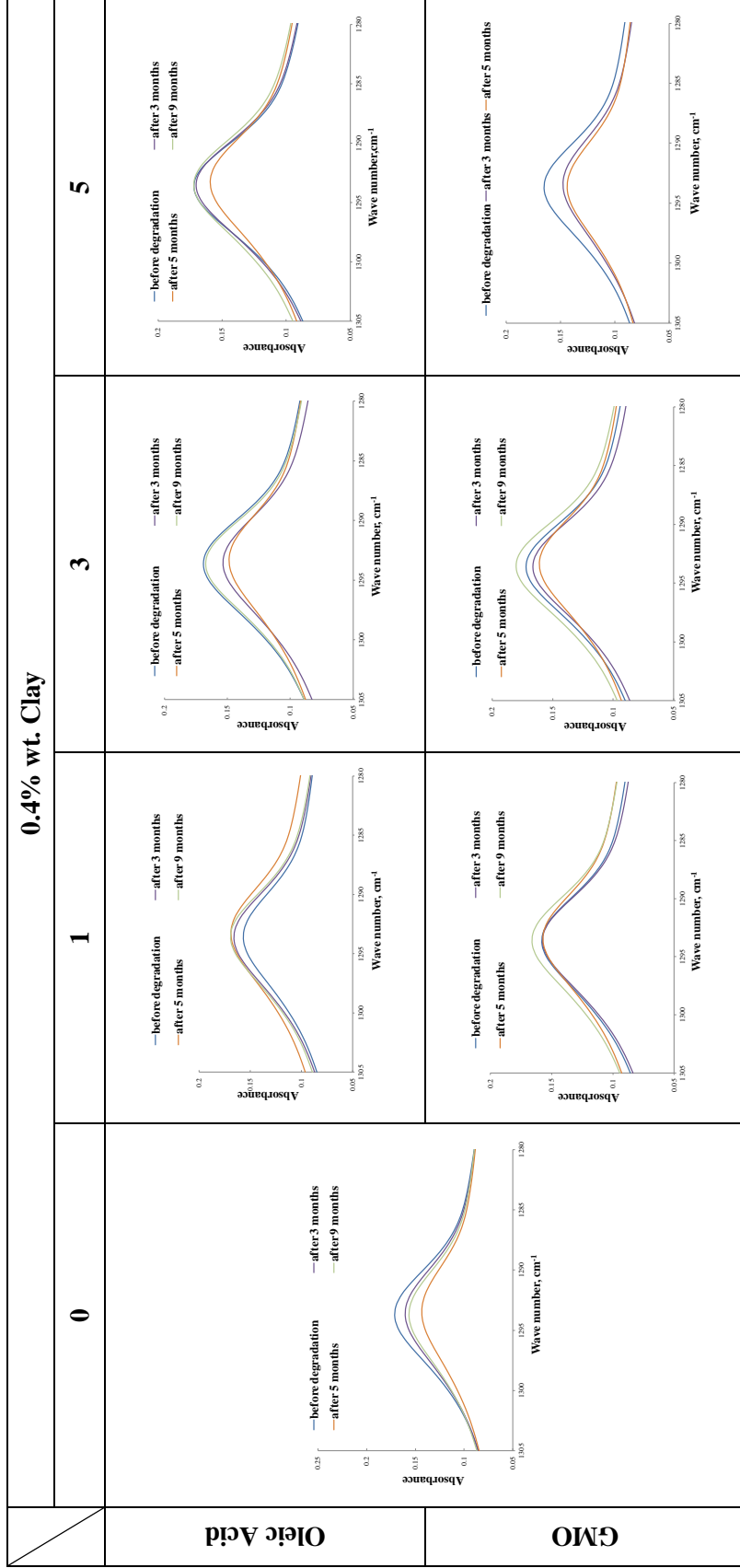


Figure M.9 Crystal peaks of films which have 0.4 % clay with respect to increasing organic additive before soil burial degradation, after 3, 6 and 9 months.

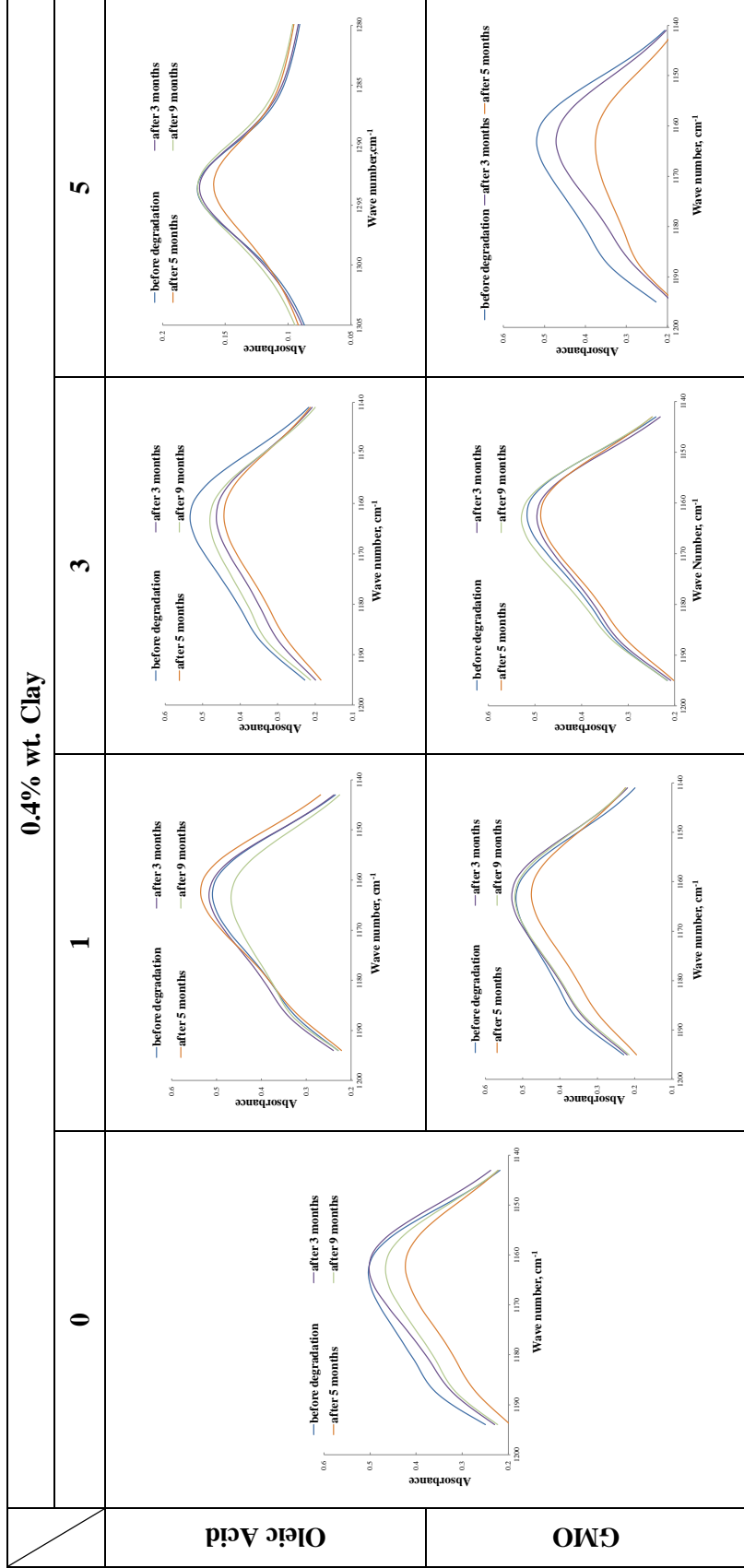


Figure M.10 Amorphous peaks of films which have 0.4 % clay with respect to increasing organic additive before soil burial degradation, after 3, 6 and 9 months.

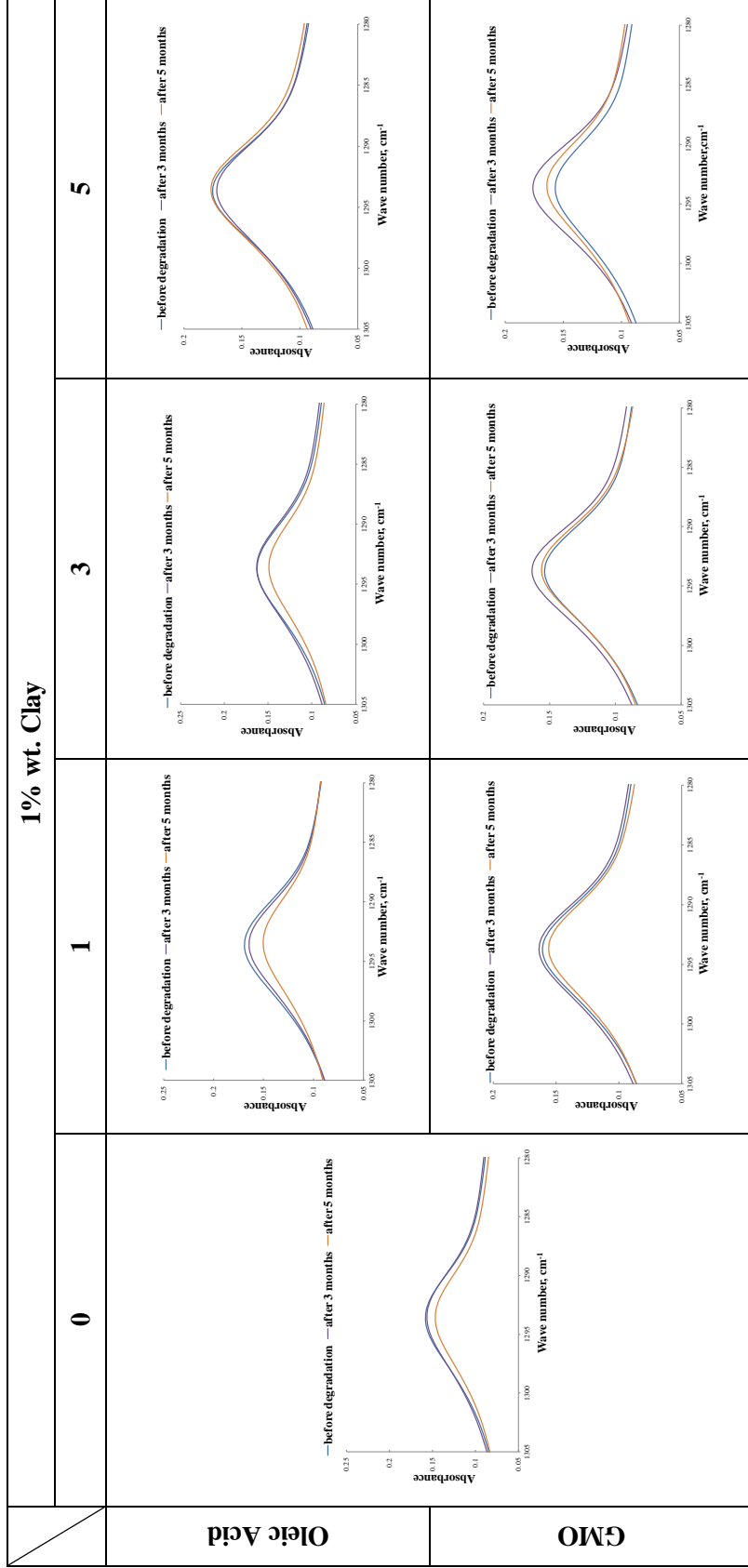


Figure M.10 Crystal peaks of films which have 1 % clay with respect to increasing organic additive before soil burial degradation, after 3, 6 and 9 months.

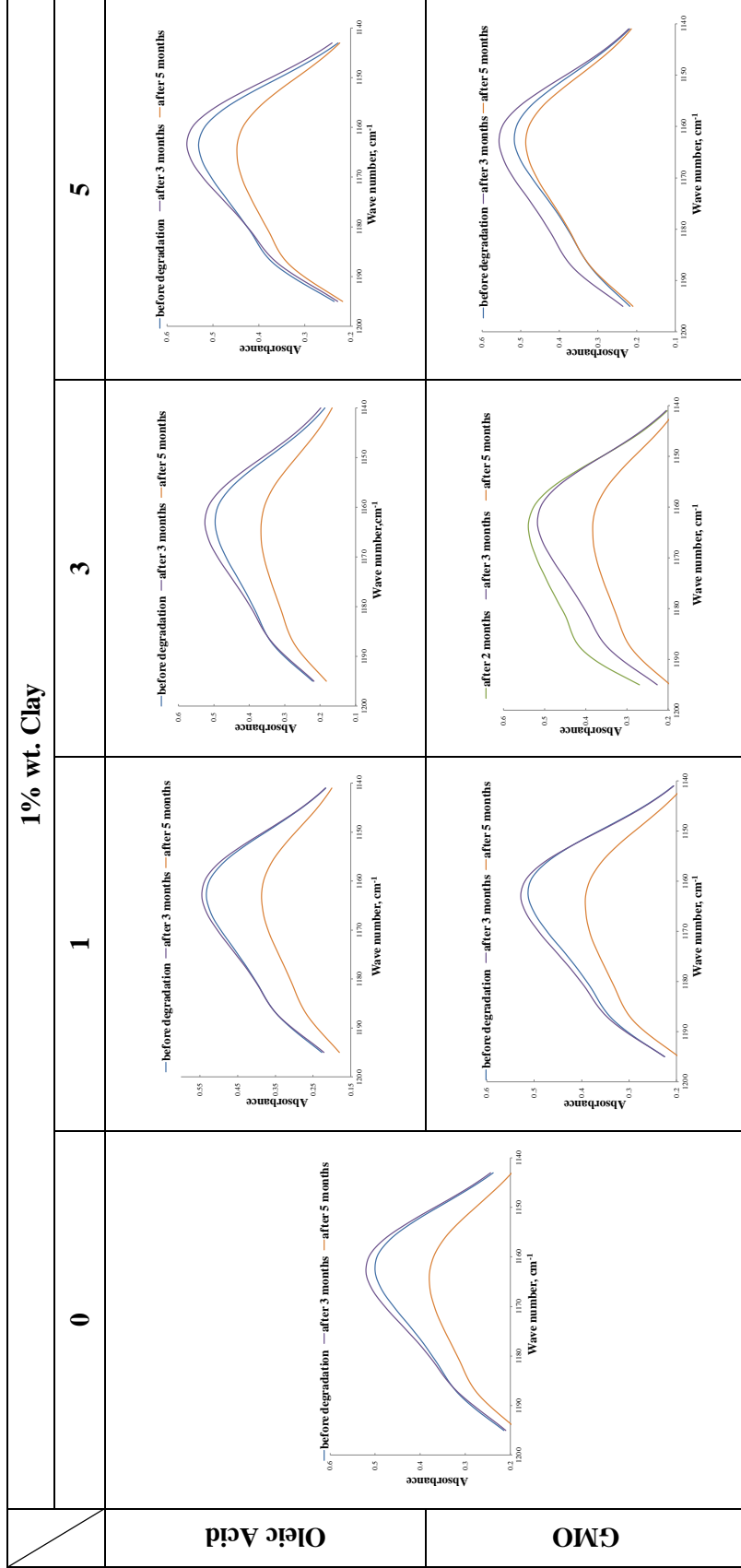


Figure M.1.1 Amorphous peaks of films which have 1 % clay with respect to increasing organic additive before soil burial degradation, after 3, 6 and 9 months.

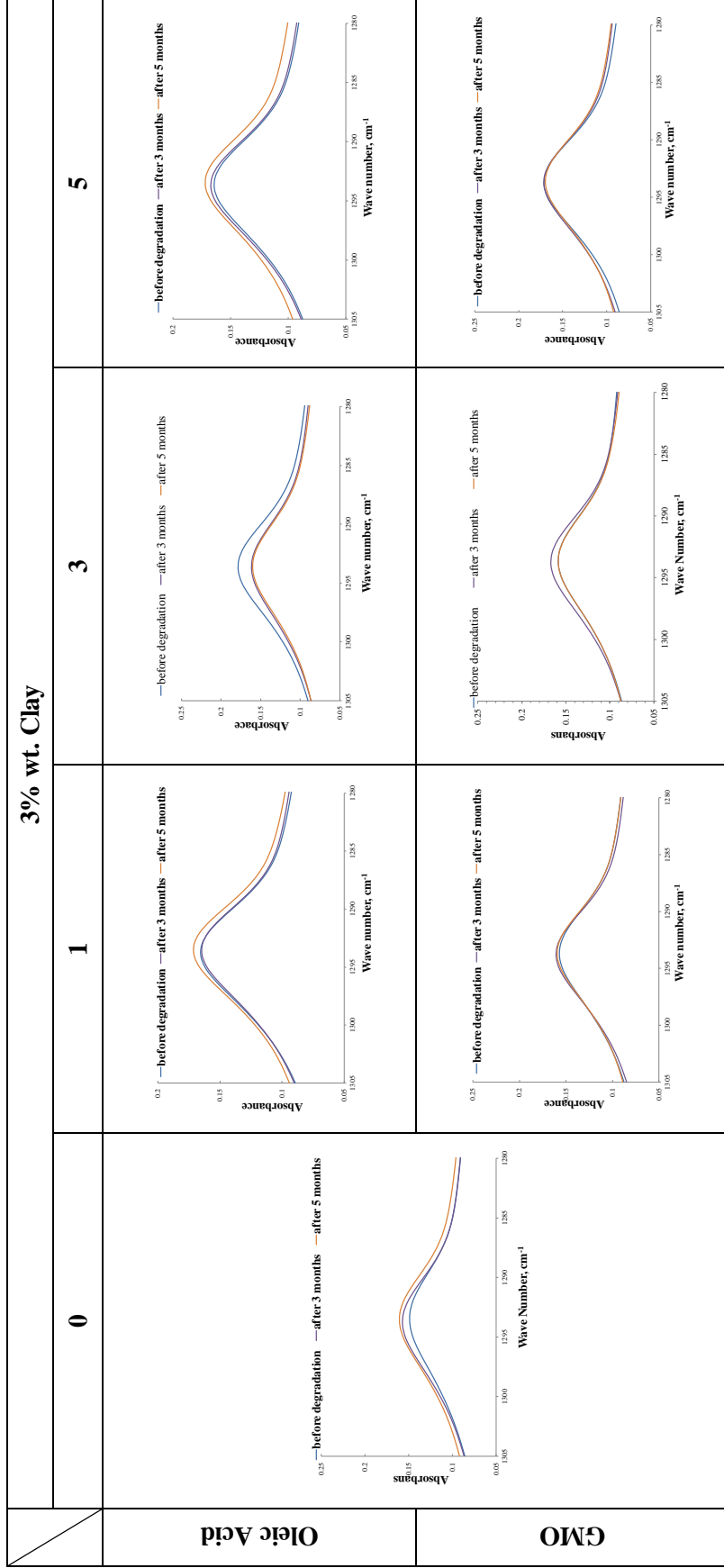


Figure M.12 Crystal peaks of films which have 3 % clay with respect to increasing organic additive before soil burial degradation, after 3, 6 and 9 months.

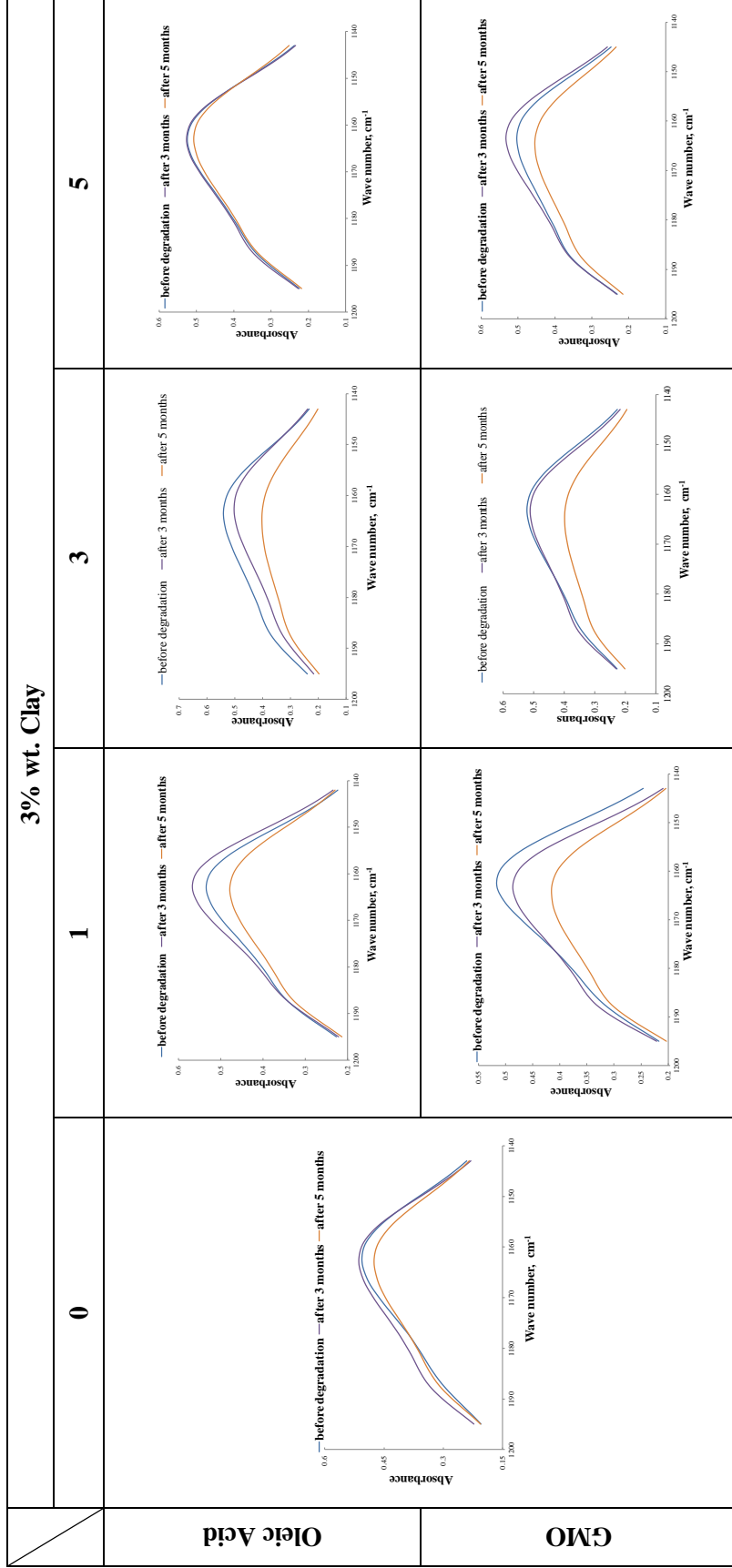


Figure M.1.3 Amorphous peaks of films which have 3 % clay with respect to increasing organic additive before soil burial degradation, after 3, 6 and 9 months.